UNCLASSIFIED

AD NUMBER
AD395707
CLASSIFICATION CHANGES
TO: unclassified
FROM: confidential
LIMITATION CHANGES
TO: Approved for public release, distribution unlimited
FROM: Distribution authorized to U.S. Gov't. agencies and their contractors; Administrative/Operational Use; Jan 1969. Other requests shall be referred to AFRPL [RPOR/STINFO] Edwards AFB, CA 93523.
AUTHORITY
Air Force Rocket Propulsion ltr, 15 Mar 1971; Air Force Rocket Propulsion ltr, 5 Feb 1986

THIS PAGE IS UNCLASSIFIED

AFRPL-TR-69-3-VOL II

CONFIDENTIAL

[illegible]
FRDC SUB-CONTROL STA. [illegible]

AD 395707

(UNCLASSIFIED TITLE)

AIR FORCE REUSABLE ROCKET ENGINE PROGRAM

XLR129-P-1

FIRST ANNUAL REPORT

R. R. ATHERTON

PRATT & WHITNEY AIRCRAFT
DIVISION OF UNITED AIRCRAFT CORPORATION
FLORIDA RESEARCH AND DEVELOPMENT CENTER

TECHNICAL REPORT
AFRPL-TR-69-3—VOL II
JANUARY 1969

GROUP 4
DECLASSIFIED AFTER 12 YEARS

PATENT SECRECY NOTICE

PORTIONS OF THIS DOCUMENT CONTAIN SUBJECT MATTER COVERED BY A U.S. PATENT OFFICE SECRECY ORDER WITH MODIFYING SECURITY REQUIREMENTS PERMIT. HANDLING SHALL BE IN ACCORDANCE WITH THE PERMIT AS DESCRIBED ON PAGE A AND INDICATED HEREIN. VIOLATORS MAY BE SUBJECT TO THE PENALTIES PRESCRIBED BY, TITLE 35, U. S. C. (1952), SECTIONS 182 AND 186.

THIS DOCUMENT CONTAINS INFORMATION AFFECTING THE NATIONAL DEFENSE OF THE UNITED STATES WITHIN THE MEANING OF THE ESPIONAGE LAWS, TITLE 18 U. S. C., SECTIONS 793 AND 794. ITS TRANSMISSION OR THE REVELATION OF ITS CONTENTS IN ANY MANNER TO AN UNAUTHORIZED PERSON IS PROHIBITED BY LAW.

D D C
[illegible]
FEB 26 1969
[illegible]

AIR FORCE ROCKET PROPULSION LABORATORY
AIR FORCE SYSTEMS COMMAND
EDWARDS AIR FORCE BASE
EDWARDS, CALIFORNIA

CONFIDENTIAL

PATENT SECRECY NOTICE

Material in this publication relating to

LAMINATED CHAMBER COOLING MEANS AND A SLOT
TUBE INJECTOR CONCEPT

reveals subject matter contained in U. S. Patent Application Serial No. 319,047 and 725,954 entitled "High Pressure Rocket and Cooling Means" and "Slot Tube Swirler Injector," respectively, which have been placed under Secrecy Orders issued by the Commissioner of Patents. These Secrecy Orders have been modified by a SECURITY REQUIREMENTS PERMIT.

A Secrecy Order prohibits publication or disclosure of the invention, or any material information with respect thereto. It is separate and distinct, and has nothing to do with the classification of Government contracts.

By statute, violation of a Secrecy Order is punishable by a fine not to exceed $10,000 and/or imprisonment for not more than two years.

A SECURITY REQUIREMENTS PERMIT authorizes disclosure of the invention or any material information with respect thereto, to the extent set forth by the security requirements of the Government contract which imposes the highest security classification on the subject matter of the application, except that export is prohibited.

Disclosure of these inventions or any material information with respect thereto is prohibited except by written consent of the Commissioner of Patents or as authorized by the permits.

The foregoing does not in any way lessen responsibility for the security of the subject matter as imposed by any Government contract or the provisions of the existing laws relating to espionage and national security.

(UNCLASSIFIED TITLE)

AIR FORCE REUSABLE ROCKET ENGINE PROGRAM

XLR129-P-1

FIRST ANNUAL REPORT

GROUP 4
DECLASSIFIED AFTER 12 YEARS

PATENT SECRECY NOTICE

PORTIONS OF THIS DOCUMENT CONTAIN SUBJECT MATTER COVERED BY A U.S. PATENT OFFICE SECRECY ORDER WITH MODIFYING SECURITY REQUIREMENTS PERMIT. HANDLING SHALL BE IN ACCORDANCE WITH THE PERMIT AS DESCRIBED ON PAGE A AND INDICATED HEREIN. VIOLATORS MAY BE SUBJECT TO THE PENALTIES PRESCRIBED BY, TITLE 35, U. S. C. (1952), SECTIONS 182 AND 186.

THIS DOCUMENT CONTAINS INFORMATION AFFECTING THE NATIONAL DEFENSE OF THE UNITED STATES WITHIN THE MEANING OF THE ESPIONAGE LAWS, TITLE 18 U. S. C., SECTIONS 793 AND 794. ITS TRANSMISSION OR THE REVELATION OF ITS CONTENTS IN ANY MANNER TO AN UNAUTHORIZED PERSON IS PROHIBITED BY LAW.

Printed in the United States of America

SECTION IV

TASK 1.1 - SUPPORTING DATA AND ANALYSIS

A. FIXED FUEL AREA PREBURNER INJECTOR

1. Introduction. 23
2. Summary, Conclusions, and Recommendations 23
3. Oxidizer Element Testing. 24
4. Preburner Rig Testing 39
5. Stability Investigation 66

SECTION IV
TASK 1.1 - SUPPORTING DATA AND ANALYSIS

A. FIXED FUEL AREA PREBURNER INJECTOR

1. Introduction

(C) The objective of the fixed fuel area preburner injector subtask was to design, fabricate, and test a fixed fuel area preburner injector that would provide a temperature profile of less than 150°R peak-to-average at an average temperature of 2325°R. The injector tested had 252 dual-orifice tangential-swirl oxidizer and fixed concentric fuel area, elements.

2. Summary, Conclusions, and Recommendations

(U) The fixed area preburner injector must operate on cold gaseous hydrogen and liquid oxygen. The gaseous fuel allows throttling the fuel while still maintaining a suitable injection velocity due to the compressible fuel density change. On the liquid oxygen side, a dual orifice principle was applied to a slot swirler element to provide suitable injection velocity over the throttle range for the essentially incompressible liquid oxygen. The slot swirler element was selected because of its excellent very fine atomization and mechanical simplicity.

(C) Initial water flow tests of the liquid oxygen injection element were conducted to determine the element discharge coefficients, cone angle, and stability during pulse testing. The originally selected element (0.095-inch inside diameter) had undesirable vortex instability characteristics at several flow levels. Similar tests of an alternative element (0.124-inch inside diameter) showed none of the undesirable features encountered with the 0.095-inch inside diameter tube. A series of water flow tests were conducted to determine the significant injection element geometry for vortex stability. These tests showed that there is a required relation of slot area to tube area for vortex stability in the injection element ($A_S/A_T < 0.5$) as well as that required for the element to meet the required ΔP of the cycle.

(C) The 0.124-inch inside diameter element was selected for the fixed area preburner injector with slot areas to provide the required engine cycle injection ΔP's.

(C) Fourteen full-scale preburner combustion tests were conducted with the fixed fuel area preburner. The preburner temperature profile was significantly improved over the results obtained with the variable area preburner injector tested during Phase I (Contract AF04(611)-11401). A peak-to-average combustion temperature profile of 76°R in a radial plane was demonstrated at an average temperature of 2388°R. Damaged oxidizer elements in a section of the injector in line with the temperature rake in a second radial plane (thermocouples No. 31 to 39) distorted the temperature profile causing a reduction in average temperature to 2325°R and subsequent increase in measured peak-to-average temperature of 215°R.

(C) Four ignition tests were conducted to determine if the preburner would ignite with a secondary helium purge flow rate and the low engine starting tank head flow rate. Successful ignition and sustained combustion occurred during all four tests. Four additional tests were programmed to simulate the engine start transients from the ignition flow rates to the 20% flow rate level. Purge timing during shutdowns was adjusted to study the best engine shutdown sequence.

(C) During testing of the preburner injector, low frequency combustion instability was encountered at thrust levels below 25% and several tests were programmed to obtain data on influential parameters. An analog model of the preburner injector, combustion chamber, and a portion of the test stand was constructed to determine the influence of various parameters on stability. Water flow tests of the injector assembly and single element test rigs were also made.

(U) It was concluded from the test data where high pressure drop orifices had been installed in the facility lines that the test facility line volumes were not the cause of the chugging. The analog model that duplicated the test results of frequency and amplitude fairly well indicated that the low secondary pressure drop and large secondary volume contributed significantly to the instability and that reducing the liquid oxygen injector secondary volume would detune this cavity eliminating the instability.

3. Oxidizer Element Testing

(U) Tangential slot swirler elements are mechanically simple, durable and provide excellent atomization. They can be easily manufactured from drawn tubing and the tangential slots accurately electric discharge machined into the tube. To meet the throttling requirements of the preburner, a second set of small "primary" tangential slots were added. At the low end of the throttling range a reasonably high injection pressure drop can still be maintained across these small "primary slots". The larger secondary tangential slots provide flow area and prevent the injection pressure drop requirement at full thrust level from being excessive for the engine cycle.

(C) Oxidizer injector element inside diameters from 0.085-inch and larger with the proper slot sizes will satisfy the cycle injection ΔP requirements. Test elements were manufactured with 0.085-, 0.095-, and 0.124-inch inside diameters, and the flow passages were sized to fit the pressure drop of the engine cycle. It appeared that the smaller tube diameters would keep the hollow vortex gas core small inside the element. Larger tubes produce larger injection cone angles and better atomization. The dimensional characteristics of these elements to meet the engine cycle ΔP are presented in Table II.

(C)(U) Table II. Element Dimensional Characteristics

Tube P/N	ID (in.)	A_s (in^2)	A_o (in^2)	A_s/A_o	Number of Slots	Primary Diameter (in.)	Primary Holes	Length (in.)
AKS-5360	0.085	0.017	0.00567	3.0	3	0.0145	2	3.090
AKS-5361	0.095	0.0103	0.00709	1.45	3	0.0145	2	3.090
AKS-5362	0.124	0.0101	0.0121	0.84	3	0.0145	2	3.090

(C) The sizing of tangential slots was based on water flow element discharge coefficient data shown plotted in Figure 1. With the element inside diameter and total secondary effective area required by the preliminary engine cycle, the total secondary physical area for an element can be obtained from the curve. Earlier experience showed that slot widths of less than 0.015 inch were difficult to manufacture with any degree of repeatability, while slot widths-to-diameter ratio (W/D) of more than 0.20 were undesirable with the required length-to-diameter ratio (L/D) because of deterioration of the element spray cone angle. With the total element secondary physical area slot width limits known, it was possible to choose the number and length of the secondary flow passages. Because of their small size, the major portion of the primary pressure drop occurs across the primary slots making the primary flow insensitive to any small changes in static pressure inside the element. Therefore, the primary passages were sized by the engine effective area requirements combined with the primary discharge coefficient experience from earlier testing.

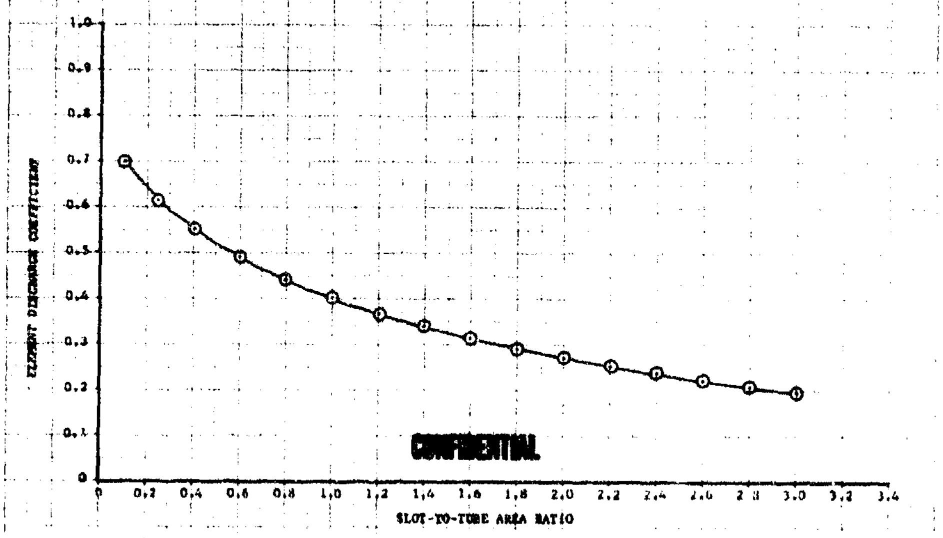

(U) Figure 1. Data From Prior Tangential Entry Oxidizer Element Testing DFC 65430

(U) The individual oxidizer elements were water flowed to determine individual effective flow area and cone angles. The flow testing required a test piece that (1) contained the individual oxygen injection element, (2) separated the primary and secondary cavities, and (3) provided manifolding in the slot areas.

(U) The first flow blocks used were welded units containing a single oxygen injection element with the primary-to-secondary cavities sealed with braze material as shown in Figure 2. The primary and secondary manifold heights were the same as the Bill-of-Material injector to simulate the pressure distribution. Pressure taps were provided inside the manifold flow cavities to ensure accurate static pressure data. For tests requiring gas core observation, the element tip was removed and replaced with an optically clear lucite adapter as shown in Figure 3. The adapter length (1.9 inches) was sufficient to enable observations of the gas core behavior. This type of flow block was used for all liquid nitrogen testing because of its positive braze seal between the primary and secondary passages, thus eliminating a static seal problem at cryogenic temperatures.

(U) For repetitive flow testing, a quick-change flow block, which is shown in Figure 4, was used. The individual primary and secondary manifolds were formed by separate steel details bolted together. Rubber O-rings were used to seal the primary from the secondary cavities. Injector primary and secondary manifolds were simulated, and pressure taps intersecting the manifolds were supplied. Injection elements to be tested were inserted into the flow block and held in place with the locking screw. Tubes tested for gas core behavior were shorter than the Bill-of-Material. Optically clear lucite adapters were bolted to the flow block to provide the additional tube length and means of gas vortex core observation.

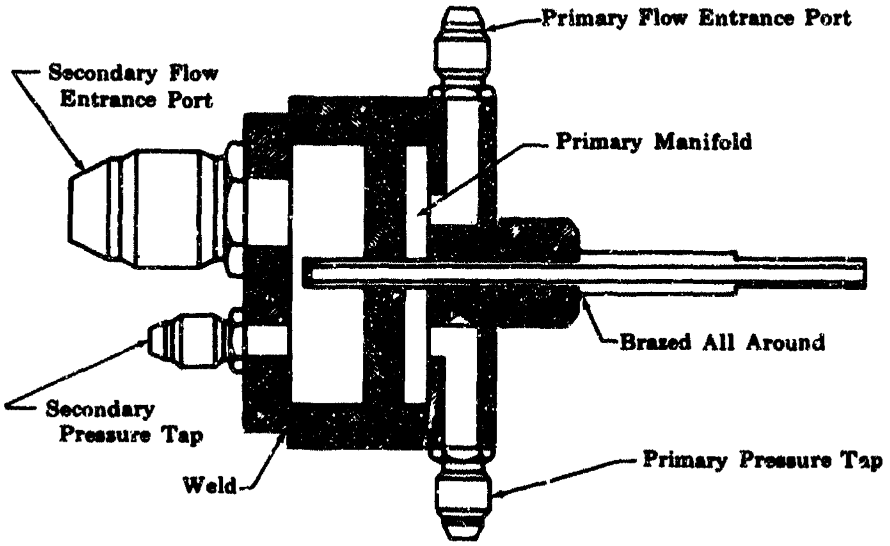

(U) Figure 2. Integral Flow Block FD 25207

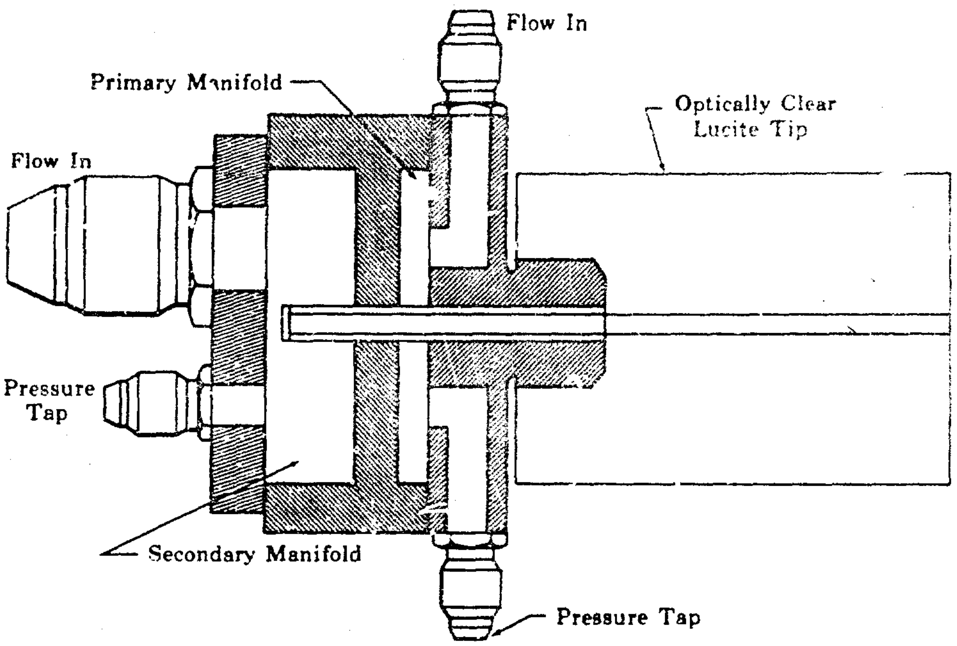

(U) Figure 3. Integral Flow Block With Optically Clear Lucite Adapter FD 25208

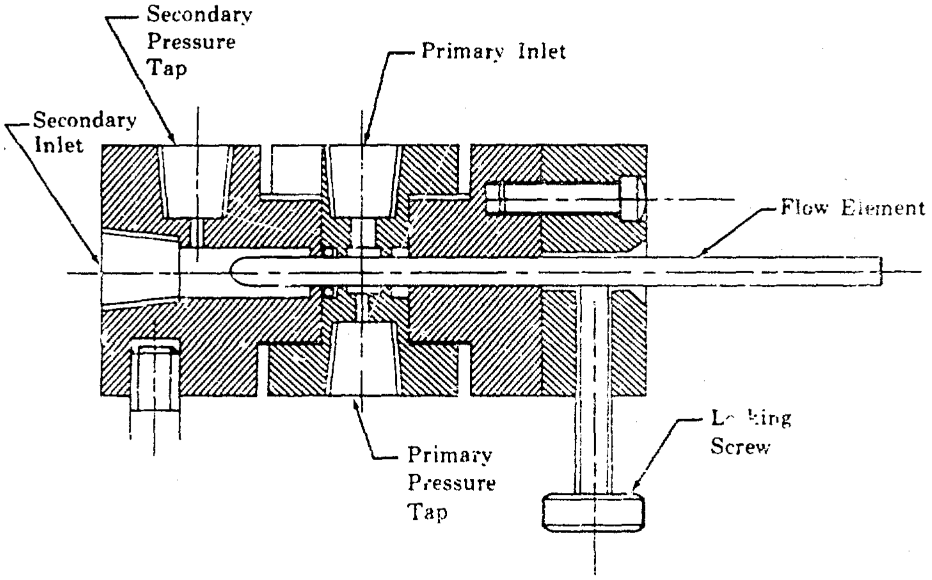

(U) Figure 4. Quick Change Flow Block FD 25209A

(U) Pulse chambers were made for water and liquid nitrogen pulsing tests. The pulse chambers were constructed so that the element flow discharged into a closed volume, which allowed pressure disturbances to be created at the element discharge. The pulse chamber used in the water flow test series was fabricated from optically clear lucite and bonded with epoxy resin. This design allowed observation of the spray cone and the gas core.

(U) The pressure disturbance, or pulse, was created inside the pulse chamber by a burst of gaseous nitrogen supplied through an electrical solenoid valve. The magnitude and time of the pulse was regulated by trial and experience adjustment of the valve cycle time and upstream nitrogen pressure. Figure 5a shows a typical water pulse test setup.

(U) The liquid nitrogen pulse tests were conducted at a chamber back pressure of 100 psig created with gaseous helium. The back pressure requirement, plus possible thermal stresses from the liquid nitrogen bath, required that the liquid nitrogen pulse chamber be fabricated from stainless steel. Pulsing of the chamber was accomplished by a burst of gaseous helium supplied through an electrical solenoid valve. The magnitude and time of the pulse was regulated by trial and experience adjustment of the valve cycle time and upstream helium pressure. Figure 5b shows a typical liquid nitrogen pulse test setup.

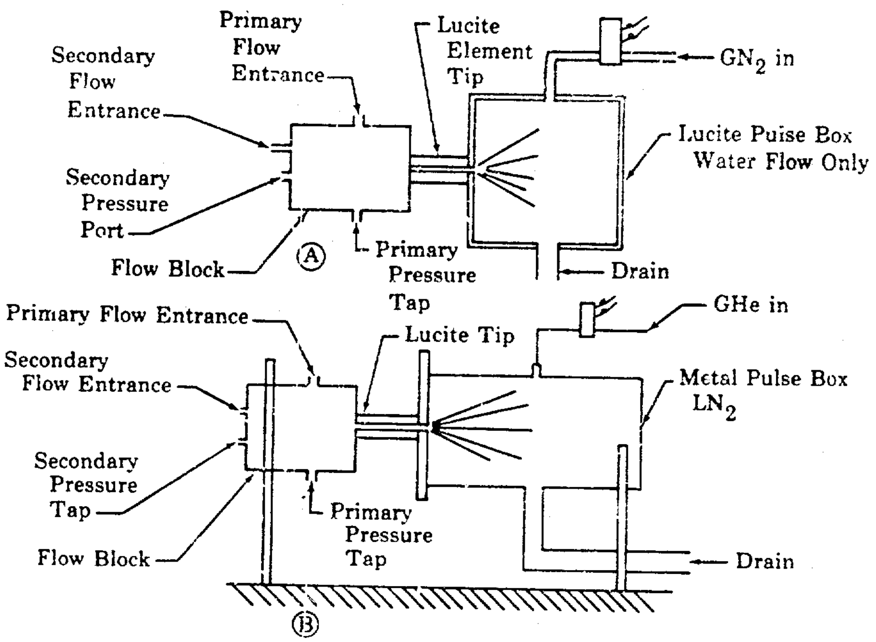

(U) Figure 5. Pulse Chambers

FD 25210A

(C) The discharge coefficient data of the primary and secondary on the selected elements were obtained by varying the element pressure drops from 25 to 300 psi in 25 psi increments. The dual flow discharge coefficients were obtained by setting the primary-to-total mass flow rate ratios ($\dot{w}_p/\dot{w}_t$) between 0 and 100%. The single and dual flow calibrations for the 0.095- and 0.124-inch inside diameter elements are shown in Figures 6 and 7, respectively.

(C) To verify that the sizing of the 0.095-, 0.124-, and 0.085-inch inside diameter flow passages were in accordance with Figure 1, which was based on earlier dual tangential entry data, test data from these elements were plotted as shown in Figure 8.

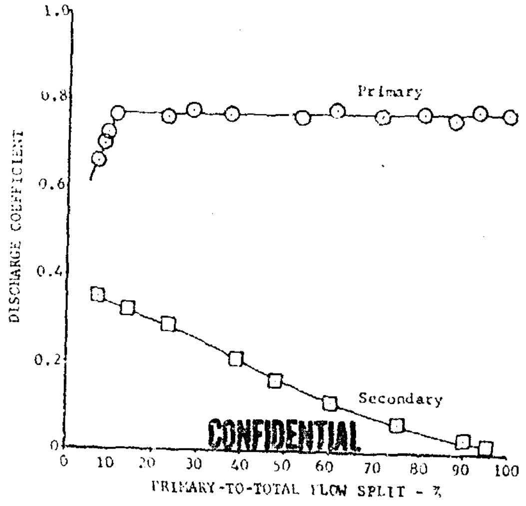

(C) Figure 6. Flow Calibrations for 0.095-Inch Tube DFC 65431

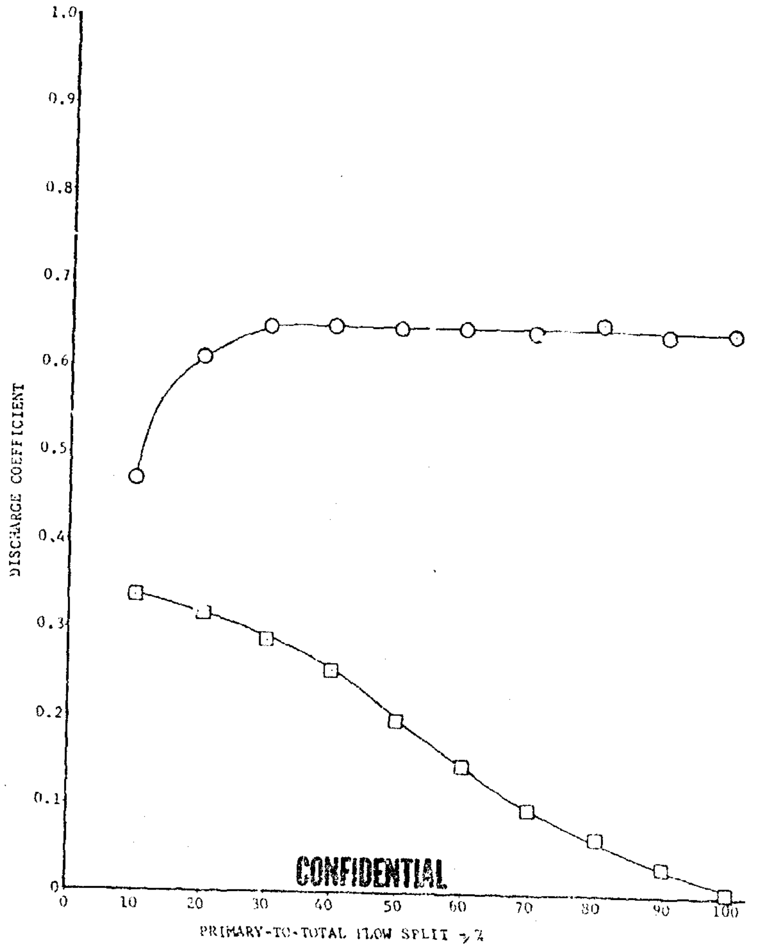

(C) Figure 7. Flow Calibrations for 0.124-Inch Tube DFC 65432

(C) Generally, the larger the spray cone angle of oxidizer elements the smaller the drop size of the spray. Small drop size promotes more rapid vaporization and better mixing between the oxidizer and fuel, and provides more efficient and uniform combustion. It is also desirable to have the spray cones impinge slightly prior to the establishment of the flame front. It is possible to predict analytically the maximum and minimum spray cone angle and where impingement will occur for a given thrust condition. For the fixed fuel area injector at 100% thrust, 60 degrees was the maximum cone angle, and 39 degrees the minimum. The predicted impingement was 0.680 inch from the injector face at 100% thrust, and a mixture ratio o .

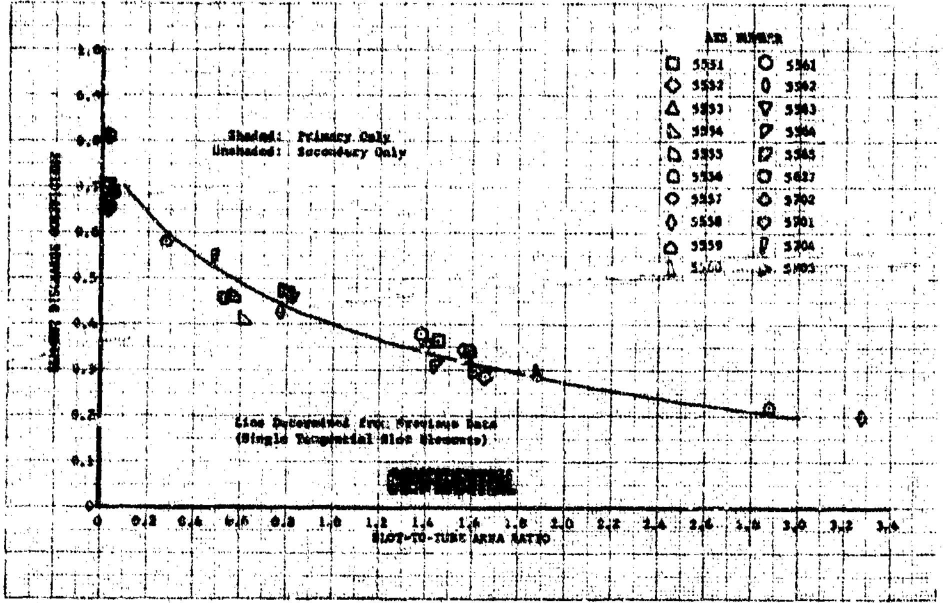

(U) Figure 8. Element Discharge Coefficient DFC 65433

(C) To verify that the predicted spray cone angles were valid, the 0.085-, 0.095-, and 0.124-inch inside diameter elements were flowed at the 20, 40, and 60% simulated thrust levels, and the angles recorded by direct observation of the spray above a graduated template. The spray cone angles of the 0.124-inch inside diameter elements are shown in Figure 9. The cone angles for this element with water were within the predicted limits at 100% simulated thrust. The spray cone angles of the 0.085- and 0.095-inch inside diameter elements were of no value because of a fluctuating gas core and cone angle.

(U) To observe the size and movement of the gas core during testing, a plexiglass tip was installed on the element. For downstream pulse testing, this tip discharged into a plexiglass box where the static pressure could be forced to rise and decay 10 psi above ambient very rapidly (250 milliseconds) by a gas pulse. High-speed movies at 300 frames per second film speed were taken to record the activity of the gas core during the pulse. The relative change of the gas core diameter gives a qualitative rating of the flow stability inside the test element.

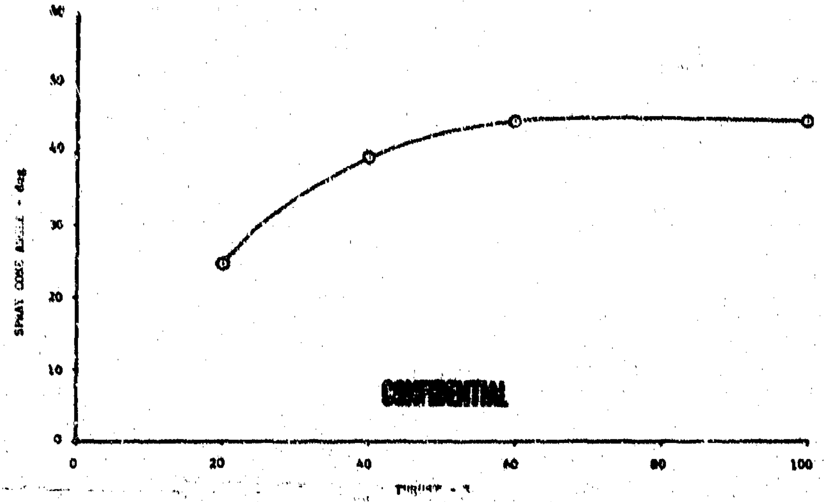

(C) Figure 9. Cone Angle vs Thrust for 0.124-Inch Element DFC 65434

(C) The 0.095-inch inside diameter element was the first element to be flowed with the plexiglass tip and pulse box. With secondary flow alone and dual flows, the spray cone angle was observed to vary from the nominal of approximately 45 degrees by as much as 30 degrees of the included angle. The secondary manifold pressure fluctuated by as much as 5 to 10 psi during large cone angle variations. It was also observed that the size and formation of the gas core were unpredictable when the primary alone was flowing at less than 250 psid, or when the secondary alone was flowing at less than 72 psid.

(C) When the 0.095-inch inside diameter element was pulse tested at 20% simulated thrust, a primary pressure drop of 320 psi and a flow ratio ($\dot{w}_p/\dot{w}_t$) of 55%, a large gas core was observed in the downstream portion of the plexiglass tip with no visible gas core in the upstream portion. The visible gas core was moving axially rapidly and erratically and appeared to be trying to form completely through the element from the discharge. When the pulse occurred, the gas core was driven upstream approximately 95% of the length of the plexiglass portion of the element. Immediately, the core moved downstream and was discharged completely before recovering.

(C) At 40% of simulated thrust on the 0.095-inch inside diameter element and at a primary pressure drop of 460 psid and flow ratio ($\dot{w}_p/\dot{w}_t$) of 27%, the same behavior observed at 20% was noted, before, during, and after the pulse, except that a very small diameter gas core was observed in the upper portion of the element.

(C) At 60% simulated thrust and at a primary pressure drop of 570 psid and flow ratio ($\dot{w}_p/\dot{w}_t$) of 17%, a large diameter, well defined gas core was observed completely through the plexiglass portion of the element.

The pulse did not visibly affect the gas core and, therefore, there was no recovery of the core.

(C) Preliminary testing on the 0.124-inch inside diameter element revealed steady, well defined spray cones and gas cores at steady-state conditions corresponding to 20, 40, and 60% simulated thrust on the pump-fed test facility. Pressure fluctuations of 1 to 1.5 psi maximum were noted in the secondary manifold. To determine if the fluctuations in secondary cavity pressure were inherent in the element or if the fluctuations were caused by the pump-fed facility, the test rig was moved to a pressure-fed test stand. The steady-state conditions and pulse testing were then repeated with no differences in the observed or recorded data.

(C) At 20% simulated thrust on the 0.124-inch inside diameter element, and at an element pressure drop of 320 psid and flow ratio ($\dot{w}_p/\dot{w}_t$) of 55%, as mentioned, the gas core was complete and well defined at steady-state. When the pulse occurred, the gas core was deformed and then recovered.

(C) At 40% simulated thrust and at an element pressure drop of 460 psid and flow ratio ($\dot{w}_p/\dot{w}_t$) of 27%, the steady-state gas core of the 0.124-inch element was well defined. The pulse had no visible effect on the gas core.

(C) At 60% simulated thrust and at an element pressure drop of 570 psid and flow ratio ($\dot{w}_p/\dot{w}_t$) of 17%, again the 0.124-inch inside element exhibited a steady, well defined gas core at steady-state. The pulse had no visible effect on this gas core.

(C) Preliminary testing of the 0.085-inch inside diameter element exhibited poorly defined or unpredictable gas cores, with rapid axial movement at all conditions. This element also exhibited 1 to 1.5 psi fluctuations in the secondary manifold. The spray cone angle varied as much as 30 degrees from the nominal of approximately 45 degrees. This element was dropped from consideration and no pulse testing was conducted.

(C) Because the water flow testing of the originally selected element design (0.095-inch ID) revealed a rapidly changing cone angle and visually unstable gas core, an effort was made to correct this element instability through modifications. This testing was qualitative in nature because a fix for the instability was sought, and not necessarily the causes of the instability. The following modifications to the original element design were tested and were unsuccessful at stabilizing the element flow:

1. Length reductions of 3, 5, 8, 11, 15, 19, 23, and 35%
2. Area reductions at the element discharge ranging from 14 to 27%

3. An area reduction of 27% at the element discharge with a reduction in length of 0.125 inch

4. An inside diameter of 0.120 inch producing an A_s/A_0 ratio of 0.965

5. An inside diameter of 0.120 inch and a 37% area reduction for the last 0.800 inch of the element

6. A 33% secondary slot area reduction by eliminating one of three secondary slots leaving two slots spaced unequally

7. A 33% secondary slot area reduction by closing 1/3 of each slot

8. A 33% secondary slot area reduction by having two equally spaced slots

9. The element with the 37% area reduction opened for the last 0.800 inch and 1/3 of each secondary slot closed

10. Top and bottom edges at the entrance to the secondary slots machined to provide a radius and a curved lead into the slots

11. All entrance edges to the secondary slots machined to provide a radius

12. Reduce wall thickness in the region of the primary and secondary slots by 9, 29, 54, and 68%

13. Inside diameter roughened 0.002-inch deep

14. A tube inserted to eliminate the gas core

15. Interchanged location of the primary holes and secondary slots

16. Replaced secondary slots with 32 holes 0.020 inch in diameter.

(C) To further investigate the effect of the secondary flow area to the element area ratio (A_s/A_0), the secondary slots were modified on two different 0.095-inch inside diameter elements to yield A_s/A_0 ratios of 0.300 and 0.542 as opposed to the A_s/A_0 ratio of 1.5 on the original 0.095-inch diameter element design. Flow from these elements were stable when tested indicating that lowering the A_s/A_0 ratio yields a stable element.

(C) To judge the stability effects of primary slot geometry, a 0.124-inch ID tube was made and tested with one primary hole of equivalent area to the two-hole original design. The element flow was stable and the cone angle was constant but the cone angle axis revolved in a circular pattern. This configuration was considered unsatisfactory because of the spray cone axis shift observed during tests.

(C) Another modification considered was a typical 0.124-inch ID tube, except for a 0.095-inch inside diameter the last 0.300 inch of tube length. This configuration proved to be essentially stable during initial tests. Pulse testing, however, showed that the gas core was momentarily eliminated at the 20% and 40% simulated thrust flow points. The core was not affected at the 60% thrust flow point. The configuration was considered unsatisfactory because of gas core behavior during pulsing.

(C) Because all the modifications attempted were unsuccessful at stabilizing the element flow, and only one alternative design (0.124-inch ID) indicated stable flow on water, a more comprehensive program was initiated to determine both the cause of element instability, and possible corrective action to the fundamental design.

(C) The first section of this program approached the cause of element instability in terms of element geometry. Past performance and analytical data had shown the influential parameters to be: slot width, slot length, element inside diameter, slot area to element area ratio (A_s/A_o), and length of element to element inside diameter ratio (L/D). Sixteen elements were fabricated to form a matrix covering these parameters at inside diameters ranging from 0.075 inch to 0.124 inch. The test matrix is provided in Table III and the dimensional characteristics of the elements investigated are provided in Table IV.

(U) Each element of the matrix was water flowed on the B-21 pressure-fed test facility. Two individual tests were conducted on each element. The first test consisted of visual observations of the spray cone angle, spray cone and gas core stability, pressure fluctuations in the primary and secondary manifolds, and flow rate fluctuations while flowing the element in the as designed length configuration. This test was then repeated with the length of each element reduced by approximately 35%. Because of geometry of the test rig, examination of the gas core could not be performed during investigation of elements in the reduced length configuration.

(C) Typical test conditions during the first test on the matrix elements included flowing at primary ΔP's corresponding to the 20%, 40%, and 60% thrust levels with secondary ΔP's varying between zero and 250 psid. Visual observations were recorded at steady-state points within this range.

(C) The second test on each of the matrix elements consisted of water flow calibration, oscillograph recording of primary and secondary manifold pressures, and high-speed movies of the spray cone and gas core while flowing the element in the Bill-of-Material length configuration. Flow calibration was performed at flow splits (primary flow rate to total flow rate, $\dot{w}_p/\dot{w}_t$) of 8.75% to 80% and high-speed movies were taken at the 20%, 40%, and 60% thrust levels while at the corresponding flow splits. Movies were also taken at steady-state points ranging above and below the fore-mentioned thrust levels.

(C)(U) Table III. Test Matrix

			Element Length										
			Short Length Configuration					Long Length Configuration					
	Nominal ID (in.)		0.075	0.085	0.095	0.110	0.124	0.075	0.085	0.095	0.110	0.124	
Slot Area	Constant Area Ratio A_s/A_o = 1.5 Nominal	0.245 Constant W/D, Slot Width to Tube Diameter	P	H	B	L	D	P	H	B	L	D	Element Letter
		0.010 Inch Min Nominal Slot Width	O	G	A	K	C	O	G	A	K	C	Element Letter
	Constant Equivalent Cycle A_{cd}	0.245 Constant W/D, Slot Width to Tube Diameter		J	B	N	F		J	B	N	F	Element Letter
		0.010 Inch Min Nominal Slot Width		I	A	M	E		I	A	M	E	Element Letter

(C)(U) Table IV. Dimensional Characteristics of Elements Tested

Element No.	Number of Secondary Slots*	Length of Slot (in.)	Width of Slot (in.)	ID of Element (in.)	Area of Slot A_s (in²)	Area of Tube A_o (in²)	Area Ratio A_s/A_o	L/D Short Configuration	L/D Long Configuration
A	3	0.361	0.0102	0.0950	0.01110	0.00710	1.563	20.31	33.80
B	3	0.150	0.023	0.0950	0.01035	0.00710	1.458	18.10	31.60
C	4	0.455	0.0110	0.1240	0.0200	0.01206	1.658	18.45	30.00
D	3	0.1997	0.0315	0.1235	0.01887	0.01198	1.575	14.31	24.70
E	2	0.328	0.0106	0.1205	0.00696	0.01138	0.612	15.75	26.35
F	2	0.108	0.032	0.1240	0.00690	0.01206	0.572	13.51	23.80
G	3	0.2734	0.0111	0.0855	0.00909	0.00571	1.592	21.58	36.60
H	3	0.085	0.0320	0.0860	0.00816	0.00580	1.407	19.25	34.10
I	4	0.4248	0.0111	0.0858	0.01884	0.00575	3.276	23.30	38.20
J	3	0.1780	0.0320	0.0870	0.01707	0.00592	2.883	20.01	34.80
K	3	0.4592	0.0129	0.1096	0.01776	0.00947	1.875	18.45	30.01
L	3	0.1676	0.0270	0.1120	0.01356	0.00983	1.379	15.50	26.90
M	3	0.2533	0.0096	0.1091	0.00729	0.00940	0.776	16.71	28.50
N	3	0.0948	0.0027	0.1095	0.00078	0.00945	0.082	15.20	26.90
O	3	0.2140	0.0102	0.0763	0.00654	0.00453	1.444	23.40	40.20
P	3	0.1420	0.0190	0.0800	0.00807	0.00500	1.614	21.40	37.40

*All elements incorporated two primary slots (0.015-inch diameter nominal) upstream of the secondary.

(C) Table V tabulates the results obtained from the test matrix section of the stability program. Figure 10 illustrates the test results tabulated in Table V. The following conclusions were made on the basis of these results:

1. Slot width is not significant to stability when the slot area to tube area ratio (A_s/A_o) is 1.5.
2. Slot width is significant in creating stability in a 0.110-inch diameter tube with an A_s/A_o ratio of 0.80.
3. Slot widths between 0.010 and 0.030 inch are stable with a 0.124-inch diameter tube at an A_s/A_o ratio of 0.542.
4. Tube diameter variation between 0.075 and 0.124 inch is not significant to stability at an A_s/A_o ratio of 1.5.
5. All tubes of 0.095-inch diameter and smaller are unstable when their A_s/A_o ratio is greater than 0.80.
6. Reduced tube length decreases the magnitude of instability.

(U) The stability investigations showed that certain elements were more stable than others. To confirm these results, it was decided to flow selected elements with liquid nitrogen. The vapor pressure, surface tension, and temperature of liquid nitrogen are similar to the corresponding properties of liquid oxygen.

(U) The liquid nitrogen flow splits and differential pressures set for the various test points were the same as the corresponding water flow tests. The element discharged into a chamber pressurized to 100 psig.

(U) After the desired liquid nitrogen flows were set, movie and oscillograph data were taken. During the data point, a 10 to 15 psig pulse of helium was flowed into the chamber.

(C) The first configuration that was flowed with liquid nitrogen was the original design 0.095-inch diameter element. These were conducted at the engine cycle primary injection pressure (primary upstream pressure to element back pressure) and secondary mass flow rate set to give the cycle primary to total mass flow rate ratio corresponding to 20%, 40%, and 60% thrust levels at an engine mixture ratio of seven. Chamber pulses of approximately 10 psi above steady-state back pressure were used.

(C)(U) Table V. Test Matrix Results

			TUBE LENGTH									
SLOT AREA			SHORT LENGTH CONFIGURATION					LONG LENGTH CONFIGURATION				
Nominal ID (in.)			0.075	0.085	0.095	0.110	0.124	0.075	0.085	0.095	0.110	0.124
Constant Area Ratio A_s/A_o = 1.5 Nom	Constant W/D, Slot Width to Tube Diameter of 0.245	Element Letter	P	H	B	L	D	P	H	B	L	D
		Spray Cone	Unstable	Unstable	Unstable	Unstable	Unstable	Unstable	Unstable	Unstable	Unstable	Unstable
		Gas Core						Unstable	Unstable	Unstable	Unstable	Stable
		Secondary Gage Fluctuation	±5 psi max	±5 psi max	±2 psi max	±5 psi max	±2 psi max	±4 psi max	±2 psi max	±2 psi max	±3.5 psi max	±2.5 psi max
		Oscilloscope Secondary ΔP Frequency & Amplitude	6 psi max 600 cps max	8 psi max Frequency not Recorded	Not Recorded	1.0 psi max at 50 cps	Not Recorded	6 psi max 300 cps max	8 psi max Frequency not Recorded	Not Recorded	1.6 psi max 100 cps max	Not Recorded
		Spray Cone Angle & Drop Size	45 to 60 deg Fine to Medium	35 to 45 deg Medium to Fine	20 to 30 deg Fine Drop Size	55 to 65 deg Fine at All Times	12 to 25 deg Fine Drop Size	20 to 40 deg Heavy to Medium	15 to 40 deg Very Heavy to Fine	20 to 50 deg Heavy to Fine	45 to 65 deg Medium to Fine	24 to 50 deg Heavy to Medium
	Slot Width of 0.010 in. min Nominal	Element Letter	O	G	A	K	C	O	G	A	K	C
		Spray Cone	Unstable	Unstable	Unstable	Unstable	Unstable	Unstable	Unstable	Unstable	Unstable	Unstable
		Gas Core						Unstable	Unstable	Unstable	Unstable	Unstable
		Secondary Gage Fluctuation	±3 psi max	±3 psi max	±3 psi max	±1.0 psi max	±0.5 psi max	±6 psi max	±4 psi max	±2 psi max	±2.0 psi max	±2 psi max
		Oscilloscope Secondary ΔP Frequency & Amplitude	2 psi max Frequency not Recorded	3.6 psi max Frequency not Recorded	Not Recorded	5 psi max Frequency not Recorded	2 psi max Frequency not Recorded	2 psi max Frequency not Recorded	3 psi max Frequency not Recorded	Not Recorded	6 psi max Frequency not Recorded	3 psi max Frequency not Recorded
		Spray Cone Angle & Drop Size	25 to 45 deg Heavy to Fine	45 to 55 deg Heavy to Fine	15 to 30 deg Medium to Fine	25 to 45 deg Heavy to Fine	40 to 65 deg Medium to Fine	20 to 30 deg Heavy to Fine	30 to 50 deg Heavy to Fine	24 to 30 deg Heavy to Fine	35 to 45 deg Very Heavy to Medium	35 to 45 deg Heavy to Fine
Constant Equivalent Cycle A_{cd}	Constant W/D, Slot Width to Tube Diameter of 0.245	Element Letter		J	B	N	F		J	B	N	F
		Spray Cone		Unstable	Same As Element "B" Above	Unstable	Stable		Unstable	Same As Element "B" Above	Unstable	Stable
		Gas Core							Unstable		Unstable	Stable
		Secondary Gage Fluctuation		±8 psi max		±6 psi max	±5 psi max		±8 psi max		±5 psi max	±4 psi max
		Oscilloscope Secondary ΔP Frequency & Amplitude		9.6 psi max at 100 cps		1 psi max Frequency not Recorded	6 psi max Frequency not Recorded		9 psi max at 200 cps		1 psi max Frequency not Recorded	5 psi max Frequency not Recorded
		Spray Cone Angle & Drop Size		50 to 65 deg Medium to Fine		30 to 45 deg Heavy to Fine	55 to 70 deg Heavy to Fine		25 to 35 deg Heavy to Medium		15 to 50 deg Heavy to Fine	35 to 45 deg Heavy to Fine
	Slot Width of 0.010 in. min Nominal	Element Letter		I	A	M	E		I	A	M	E
		Spray Cone		Unstable	Same As Element "A" Above	Stable	Stable		Unstable	Same As Element "A" Above	Stable	Stable
		Gas Core							Unstable		Stable	Stable
		Secondary Gage Fluctuation		±1 psi max		±1.5 psi max	±2 psi max		±2 psi max		±1 psi max	±5 psi max
		Oscilloscope Secondary ΔP Frequency & Amplitude		4.2 psi max at 200 cps		1 psi max at 100 cps	1 psi max Frequency not Recorded		3 psi max at 200 cps		3.2 psi max at 100 cps	5 psi max Frequency not Recorded
		Spray Cone Angle & Drop Size		60 to 65 deg Medium to Fine		55 to 65 deg Fine Drops at All Times	35 to 65 deg Medium to Fine		30 to 60 deg Heavy to Fine		40 to 55 deg Medium to Fine	25 to 50 deg Medium to Fine

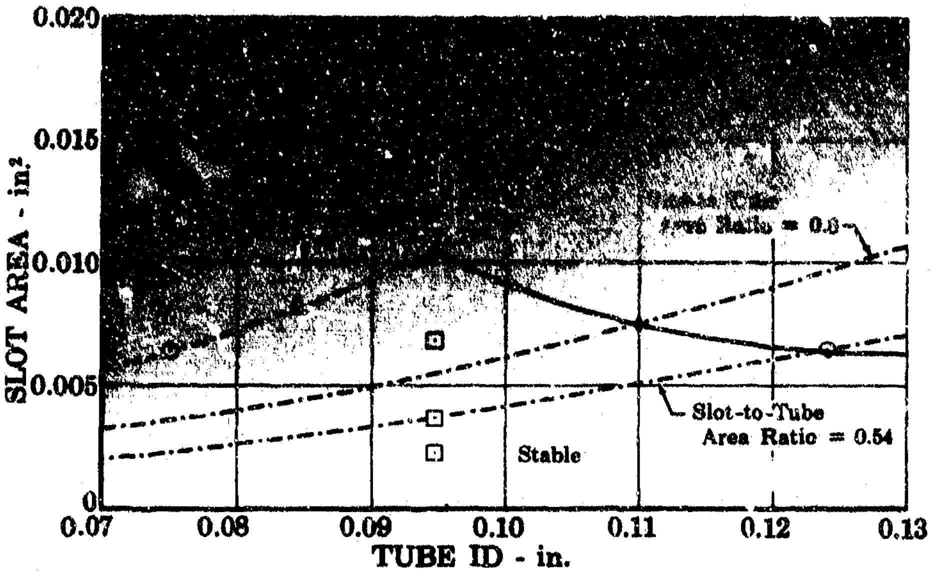

(U) Figure 10. Element Test Matrix Test Results FD 23225B

(C) The movies revealed the following facts:

1. Gas cores exist on liquid nitrogen flows
2. Cores were unstable at 20% and 40% thrust level at steady-state conditions
3. Cores were eliminated by the pulse at the 20% and 40% thrust level
4. The core was stable at 60% thrust level
5. The core was distorted but not eliminated at 60% thrust level by the pulse.

(C) The oscillograph data showed fluctuations in secondary cavity pressure of 0.5 psi at 20%, 1.0 psi at 40%, and 1.5 psi at 60% thrust level points.

(C) The second configuration tested was the alternative design; 0.124-inch inside diameter element. Tests were conducted at flow rates corresponding to 20%, 40%, and 60% thrust levels. Each thrust level was pulsed. Two other tests conducted were a 60% thrust volumetric flow and a 60% secondary sweep. The 60% thrust volumetric point consists of setting primary and secondary flows corresponding to the liquid oxygen volumetric flow rate according to the engine cycle. The 60% thrust secondary sweep consists of setting 60% thrust cycle primary injection pressure (secondary upstream pressure to element back pressure) from zero to 400 psi.

(C) The movies revealed the following facts:

1. Gas cores were large, varying from 55% of the diameter at 20% thrust points to 60% at 40% thrust volumetric point.
2. Pulsing at 20% caused an enlargement of the core by 5% of the diameter.
3. Pulsing at 40% and 60% thrust points had no effect on the cores.
4. Cores at all points were stable.

(C) The oscillograph data showed fluctuations in secondary cavity pressure of 0 psi at 20%, 0.1 psi at 40%, and 0.1 psi at 60% thrust level points.

(C) The third configuration tested was a modification to the 0.124-inch inside diameter tube. The modifications were as follows: (1) an area reduction was incorporated in the tube 0.250 inch from the exit to an inside diameter of 0.095 inch, (2) the slot areas were increased in size by 24% to accommodate the 0.095-inch diameter at the tip while keeping the overall element pressure drop as required by the engine cycle.

(C) Tests were conducted at flows corresponding to 20%, 40%, and 60% thrust levels plus secondary sweeps at 40% and 60% levels.

(C) The movies revealed the following facts:

1. Gas cores could exist upstream of the tube tip restriction.
2. The gas core at 20% was relatively small (22% of tube diameter) and slightly unstable. Pulsing momentarily eliminated the gas core.
3. The gas core at 40% was still small (28% of the tube diameter) and relatively stable. Pulsing again momentarily eliminated the gas core.
4. The gas core at 60% was small but stable. Pulsing had no visible effect on the gas core.

4. Preburner Rig Testing

a. Hardware Description

(U) An existing preburner test rig fabricated during Phase I (Contract AF04(611)-11401) was modified for use in testing the fixed fuel area preburner injector. Figure 11 shows the major details of the test rig including the oxidizer dome, preburner oxidizer valve, combustion chamber, back pressure simulator, injector assembly, and temperature rakes.

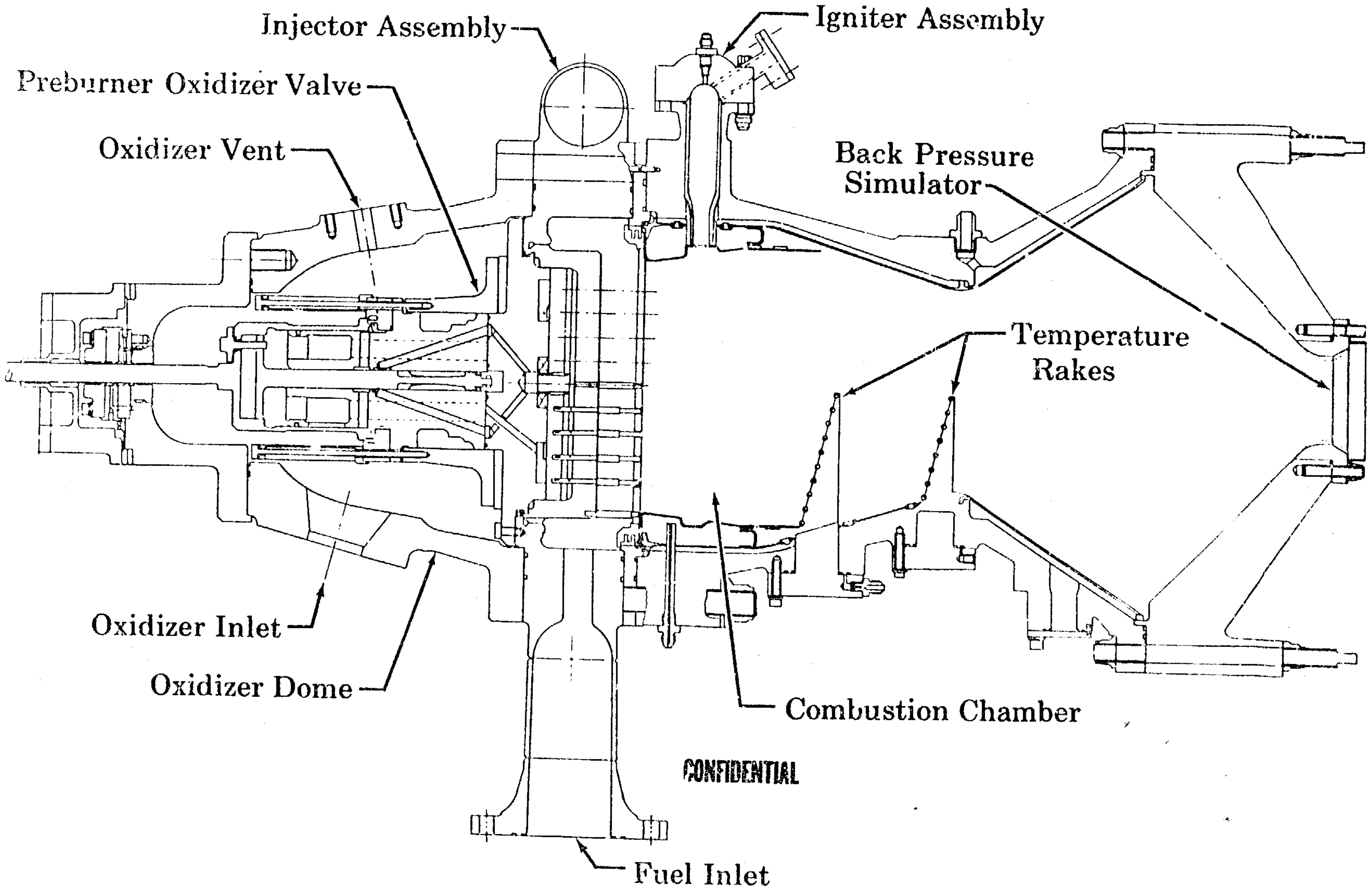

(U) Figure 11. Preburner Rig Configuration

FDC 23248B

(U) The oxidizer dome was modified to eliminate flange leakage and thus permit higher rig operating pressures than were possible during Phase I (Contract AF04(611)-11401) tests. Figure 12 shows the oxidizer dome used in these previous tests and the modified dome used in the current tests. The modifications included a thicker flange, larger seal vent area, a relief cut on the flange mating surface to move the bolt reaction more directly in line with the pressure source, and tensilized stretch studs for higher loads.

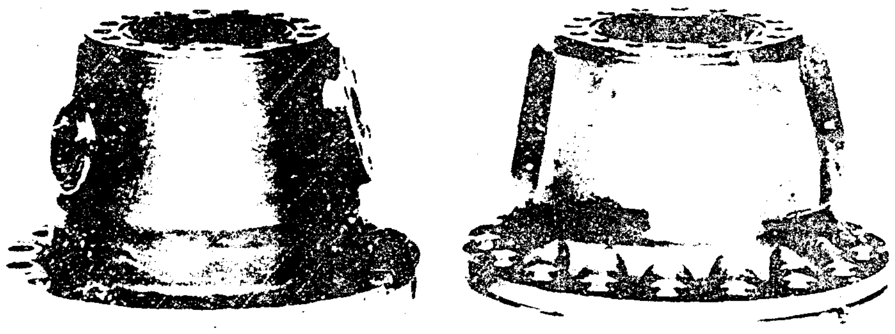

(Original Design) **(Revised Design)**

(U) Figure 12. Original and Revised Oxidizer Domes FD 23472

(U) The preburner oxidizer valve, which controls the primary-to-secondary flow split, was basically unchanged from the configuration used during Phase I (Contract AF04(611)-11401) testing, except that the upper and lower piston rings were replaced with balanced piston rings.

(U) The combustion chamber liner was modified by reducing the distance from the outermost injection element to the chamber wall to 0.5 inch.

(U) The back pressure simulator was modified to accept inserts of various inside diameters, thus allowing a wide range of simulated chamber pressures.

(U) The injector assembly was an existing variable fuel area housing that was bored and threaded to accept the fixed fuel area injector block assembly. The injector block assembly, which is shown in Figure 13, was a brazement composed of the oxidizer elements, divider plate, oxidizer block, and the Rigimesh faceplate.

(U) Temperature rakes were installed in two circumferential locations at axial distances of 7 and 11 inches from the injector face.

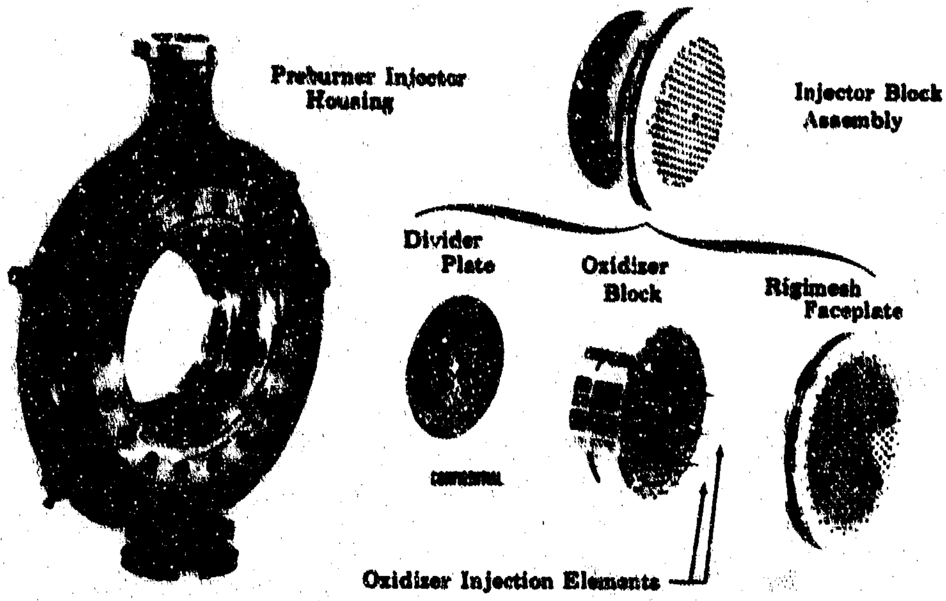

(U) Figure 13. Preburner Injector Block Assembly FDC 23221C

(U) Figure 14 is a cross section of the fixed fuel area preburner injector and the following paragraph is keyed to this figure.

(C) Fuel is supplied to the circular fuel manifold (1) by the fuel system. The fuel then flows through the feed holes (2) into the manifolding (3) behind the faceplate Rigimesh and is metered into the combustion chamber through annuli (4) around each oxidizer element (252 places). Liquid oxygen is supplied to the injector from the preburner oxidizer valve, which controls and meters the total oxidizer flow to primary (5) and secondary (6) flow passages in the injector oxidizer plate (7). The two oxidizer flows, primary and secondary, are used to maintain safe injection differential pressures at all engine cycle points. The series of flow passages (5 and 6) delivers oxidizer to the primary (10) and secondary (11) supply manifolds. Oxidizer flow is transferred to the combustion chamber through individual oxidizer elements (8). Each element has flow entries machined tangentially to the tube ID (9): rectangular slots for the secondary flow and circular holes for the primary flow. Element length is determined by the manifold heights of the fuel (3), primary oxidizer (10), and secondary oxidizer (11), and heights of each are kept to a minimum, consistent with low distribution losses.

(C) The concentric fuel annuli of this design act as fixed orifices as opposed to the variable fuel metering area design. Two injector assemblies were fabricated for this test program, each having a different fuel annulus area. The initial testing (tests No. 1.01 and 2.01) was made with a fuel annulus designed for 200 psi pressure drop at the design point of 100% thrust mixture ratio of 7. The remaining tests were made with a fuel annulus designed for 400 psi pressure drop at design point.

THIS PAGE CONTAINS SUBJECT MATTER COVERED BY A SECRECY ORDER WITH A MODIFYING "SECURITY REQUIREMENTS PERMIT" ISSUED BY U.S. COMMISSIONER OF PATENTS.

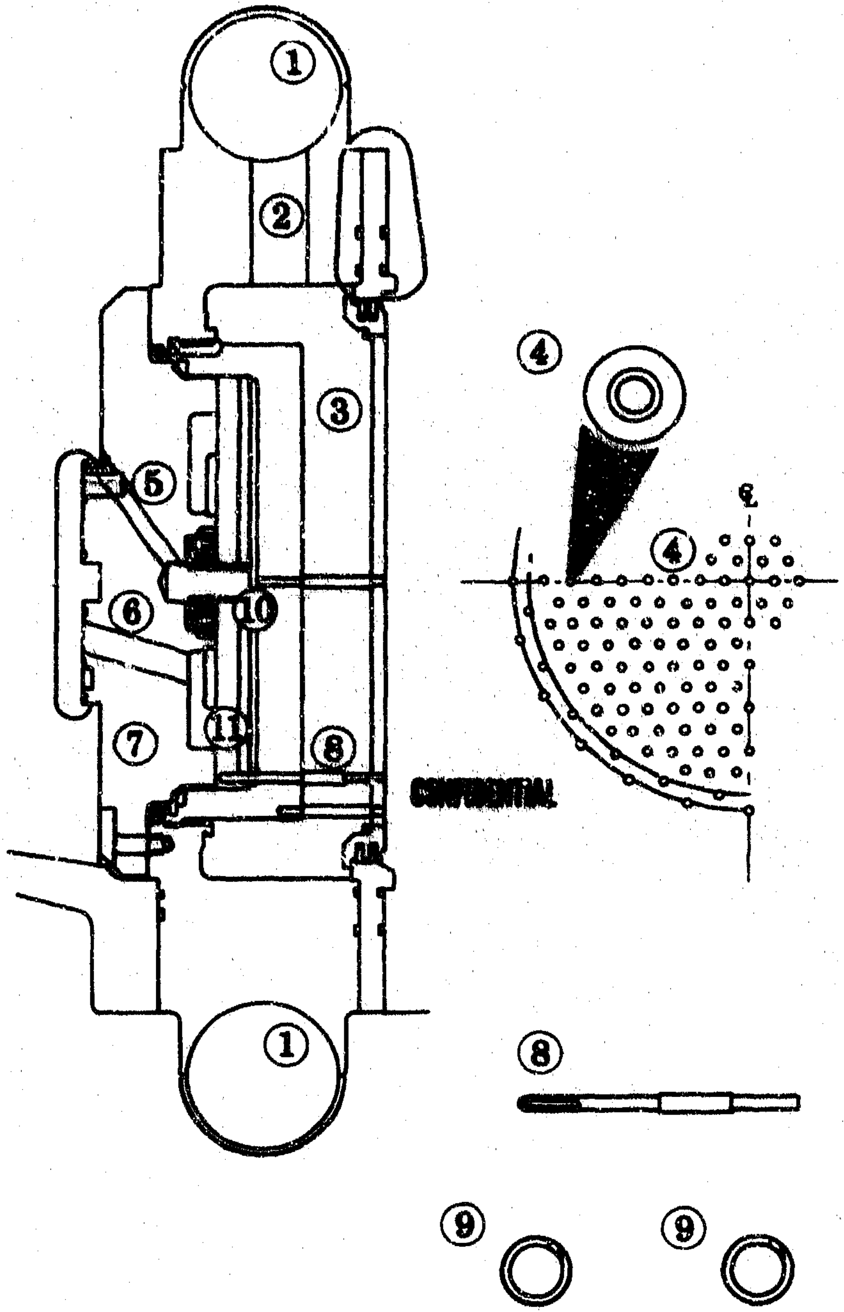

(U) Figure 14. Cross Section of Fixed Fuel Area Preburner Injector FDC 24990

b. Test Facilities and Procedures

(C) The fixed fuel area preburner injector rig was tested in the E-8 test facility. A plan view of this facility is shown in Figure 15. The E-8 test facility permits preburner testing to chamber pressures of 5000 psia. The preburner control configuration is shown in Figure 16.

(C) The preburner starting sequence was initiated by diverting the required fuel and oxidizer flows from a preset overboard condition to the injector. The diverted fuel and oxidizer were then allowed to stabilize. The combustion chamber pressure at this point was less than 1% for tank head ignition tests and 7% for other tests.

(C) After the fuel and oxidizer valves were in position and were stabilized at the 7% level, they were switched to flow control. The run tanks were then pressurized to the operating levels, and the preburner flows were ramped to the desired equivalent thrust level and combustion temperature.

(U) The fuel mixture temperature control section modulated the valves that regulated the GH_2 flow into the mixing section and provided the desired injector fuel temperature. The total fuel flow was determined by measuring both the gaseous and liquid flow rates; however, only liquid flow was controlled by the system.

(U) The oxidizer flow was also closed-loop controlled through the computer with the necessary timing to maintain the required mixture ratio during the transient.

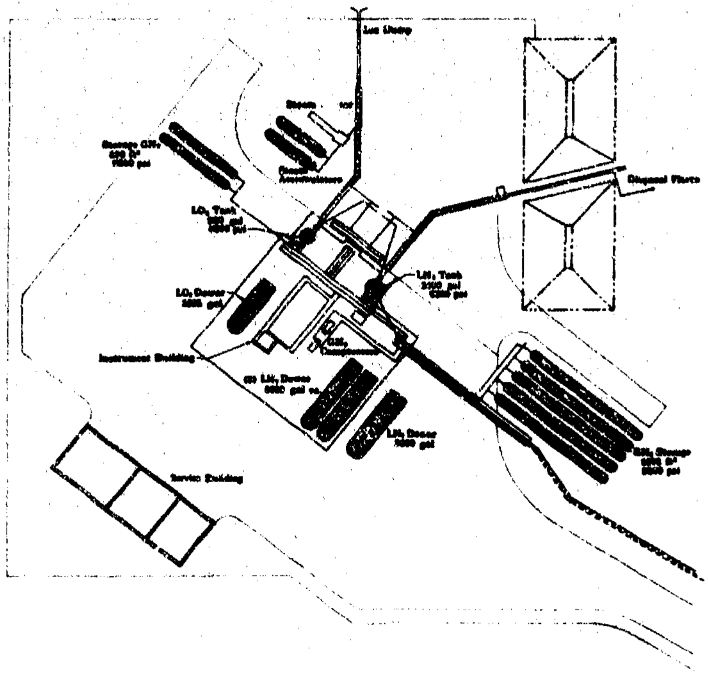

(U) Figure 15. Plan View of E-8 Test Facility FD 21139A

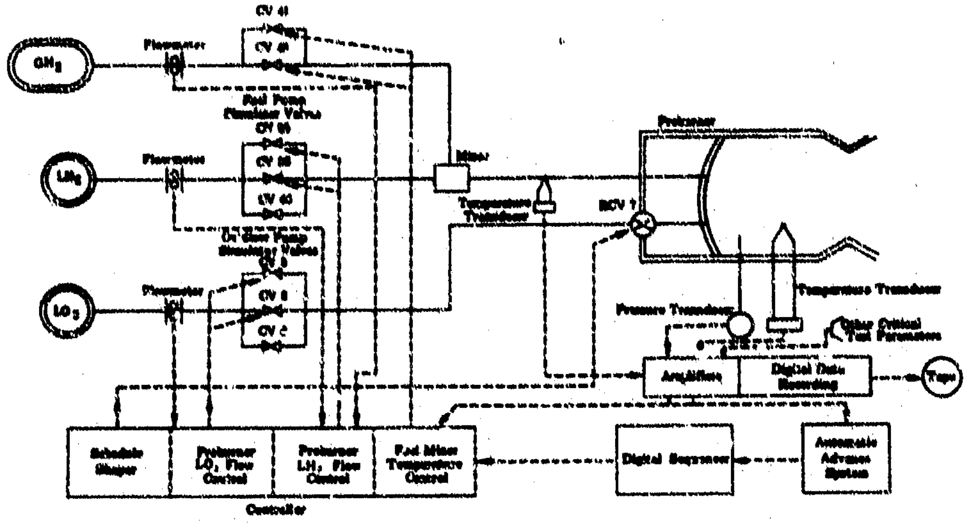

(U) Figure 16. Preburner Rig Control System FD 21136C

(U) Starting flows, automatic changes of flow levels, and test conditions other than those scheduled by power lever, were programmed in and out of the control by the digital sequencer.

c. Test Results

(C) The test objectives were to evaluate: (1) temperature profile, (2) tank head ignition and start transient, and (3) combustion stability pulsing with 80-grain charges. Both the 200 psid and 400 psid injector assemblies were tested. A low frequency chugging instability was present at thrust levels below 25% for all engine mixture ratio conditions.

(U) Pulse guns, as shown in Figure 17, were used to introduce the pressure upsets in the preburner test rig. In the combustion chamber, pressure upsets were caused by the dissipation of the high pressure gases from the gun barrel. The intensity of these gases may be regulated by charge size and burst disk rupture level.

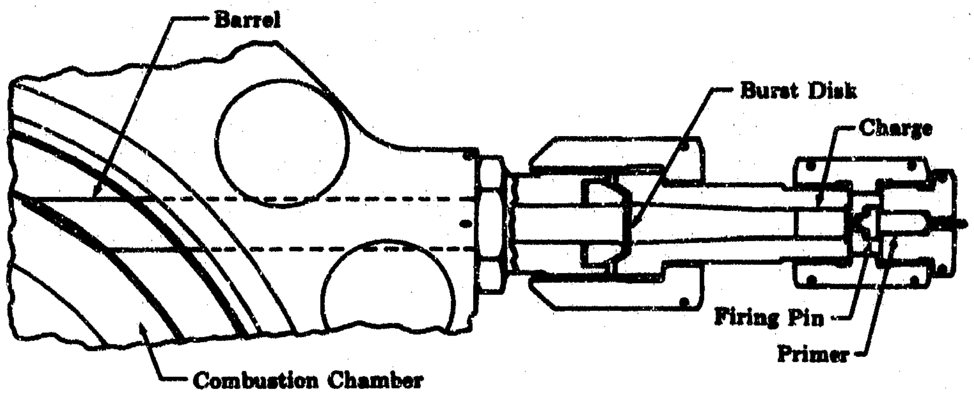

(U) Figure 17. Preburner Rig Pulse Gun FD 25307

(U) Each test is described in the following paragraphs. The measured parameters are summarised in Table VI and the calculated results are summarized in Table VII.

(C) Figure 18 shows the injector face prior to test 1.01, which was conducted on 31 May 1968. Data at five of the six planned engine cycle data points were obtained. The test was advanced before the last data point condition was reached because of excessive combustion temperature resulting from a facility oxidiser valve oucillation. Data were taken at 20% and an equivalent engine cycle condition for mixture ratios of 5, 6, and 7 and at 60% for mixture ratios of 5 and 6. The chamber was pulsed with 80-grain charges at 20% for mixture ratios of 5 and 7 and at 60% for a mixture ratio of 5.

(C) Analysis of the data from test 1.01 showed that although combustion stability was essentially insensitive to the pulse gun discharges, a low frequency (approximately 100 cps) system instability occurred on the ramp from 7% to 20% flow levels and persisted through all three mixture ratios at 20% thrust levels. The instability in chamber pressure was limited to 150 psi peak-to-peak. On ramping from 20% to 60% the instability stopped and did not recur at higher thrust levels. The maximum peak-to-average combustion temperature profile at the 20% level was 124°R at a mixture ratio of 7 as shown in Figure 19. At the 60% level and a mixture ratio of 6, one of the oxidizer pump simulator valves (CV8) was required to operate on a portion of its stroke where large effective area changes are made by small valve stroke changes. The oxidizer flow control system became unstable causing combustion overtemperature. The test sequence was automatically advanced by the overtemperature prior to attaining the 60% thrust level and mixture ratio of 7 steady-state data point. The peak-to-average combustion profile at 60% level was 119°R at an average temperature of 1848°R and a mixture ratio of 6 as shown in Figure 20.

(C) Pulse guns with 80-grain charges were fired at the 20% and 60% thrust levels on test 1.01. The pulses at the 20% and mixture ratio of 5 and 7 levels caused a chamber pressure rise of 292 and 302 psi and combustion recovered to normal levels in 10 and 6 milliseconds, respectively. The pulse at the 60% and mixture ratio of 5 level caused a chamber pressure rise of 364 psi that dissipated within 10 milliseconds. The firing of the pulse guns damaged the combustion liner in four places; however, the damaged combustion liner was suitable for use on test 2.01.

(C) Test 2.01 was conducted on 4 June 1968. The run was programmed for data points at a mixture ratio of 5 at 20% thrust and mixture ratios of 6 and 7 at 100% thrust. The run was automatically advanced during the flow ramps from the mixture ratio of 6 data point by an overtemperature.

(C)(U) Table VI. Summary of Measured Parameters During Preburner Inj

Test No.	Thrust (%)(1)	Date	Rig No. Build No.	Test Duration (sec)	Ambient Pressure (psia)	Oxidizer Injector Inlet Temperature (°R)	Fuel Injector Inlet Temperature (°F)	Liner Coolant Inlet Temperature (°R)	Oxidizer Injector Primary Inlet Pressure (psia)	Oxidizer Injector Secondary Inlet Pressure (psia)
1.01	20	31 May 1968	35117-1	35.9	14.71	191.9	129.5	129	986	713
1.01	20	31 May 1968	35117-1		14.71	192.1	144.4	144	971	699
1.01	20	31 May 1968	35117-1		14.71	192.7	150.2	150	934	667
1.01	60	31 May 1968	35117-1		14.71	189.3	154.7	155	3401	2806
1.01	60	31 May 1968	35117-1		14.71	189.3	164.2	164	3125	2660
2.01	20	4 Jun 1968	35117-1	29.4	14.49	196.0	303.2	303	901	670
2.01	100	4 Jun 1968	35117-1		14.49	181.6	188.3	188	5171	4801
3.01	20	14 Jun 1968	35117-2	62.1	14.73	195.8	134.6	135	1053	619
3.01	20	14 Jun 1968	35117-2		14.73	196.8	133.1	133	904	614
3.01	20	14 Jun 1968	35117-2		14.73	198.5	131.3	131	700	596
3.01	60	14 Jun 1968	35117-2		14.73	191.2	148.9	149	2783	2349
3.01	100	14 Jun 1968	35117-2		14.73	186.4	184.8	185	4322	4270
4.02	97	19 Jun 1968	35117-2	23.1	14.69	185.3	149.9	150	5062	4834
2.01	20	27 Jun 1968	35117-2	31.1	14.71	170.5	446.7	447	891	650
4.02	20	28 Jun 1968	35117-2	45.2	14.74	173.4	95.4	95	830	598

(1) Data point at percent equivalent engine thrust

Parameters During Preburner Injector Testing

Liner olant Inlet mperature (°R)	Oxidizer Injector Primary Inlet Pressure (psia)	Oxidizer Injector Secondary Inlet Pressure (psia)	Fuel Injector Inlet Pressure (psia)	Liner Coolant Inlet Pressure (psia)	Chamber Static Pressure (psia)	Fuel Injector ΔP (psid)	Oxidizer Injector Primary ΔP (psid)	Oxidizer Injector Secondary ΔP (psid)
129	980	713	745	745	691	32.2	278	7.6
144	971	699	729	729	685	34.4	285	10.8
15[illegible]	934	667	694	694	652	50.0	284	10.2
155	3401	2806	2868	2868	2653	106	692	87.4
164	3125	2660	2682	2682	2534	85.4	585	90.4
303	901	670	753	753	644	73.4	246	7.2
188	5171	4801	4618	4618	4285	168.7	929	403
135	1053	619	663	663	608	80.3	447	8.4
133	904	614	665	665	611	80.0	307	6.6
131	700	596	666	666	611	76.1	111	3.9
149	2783	2349	2485	2485	2210	217.8	549	76.1
185	4322	4270	4397	4397	3911	388	424	283
150	5062	4854	5092	5092	4406	526	587	317
447	891	650	892	892	639	237	242	4.0
95	830	598	626	626	589	35.1	220	6.8

(C)(U) **Table** VII. Summary of Calculated Parameters During

Test No.	Date	Rig No. Build No.	Total Combined Flow Rate (lb_m/sec)	Total Fuel Flow Rate (lb_m/sec)	Total Oxidizer Flow Rate (lb_m/sec)	Upper Liner Fuel Coolant Flow Rate (lb_m/sec)	Lower Liner Fuel Coolant Flow Rate (lb_m/sec)	Total Liner Flow Rate (lb_m/sec)	Overall Mixture Ratio	Injector Mixture Ratio(1)	Ideal Temperature (°R)
1.01	31 May 1968	35117-1	23.72	14.46	9.26	0.21	0.21	0.42	0.64	0.66	1285
1.01	31 May 1968	35117-1	21.65	12.35	9.30	0.17	0.18	0.35	0.75	0.78	1504
1.01	31 May 1968	35117-1	19.84	10.57	9.27	0.15	0.16	0.32	0.88	0.90	1728
1.01	31 May 1968	35117-1	85.04	46.63	38.41	0.73	0.54	1.27	0.82	0.85	1628
1.01	31 May 1968	35117-1	77.95	39.63	38.32	0.55	0.48	1.02	0.97	0.99	1881
2.01	4 Jun 1968	35117-1	23.04	14.43	8.61	0.21	0.19	0.40	0.60	0.61	1390
2.01	4 Jun 1968	35117-1	142.81	65.32	77.49	0.99	0.69	1.68	1.19	1.22	2272
3.01	14 Jun 1968	35117-2	23.58	14.40	9.18	0.19	0.28	0.47	0.64	0.66	1290
3.01	14 Jun 1968	35117-2	23.74	14.56	9.18	0.19	0.28	0.47	0.63	0.65	1276
3.01	14 Jun 1968	35117-2	23.88	14.62	9.26	0.20	0.29	0.48	0.63	0.65	1281
3.01	14 Jun 1968	35117-2	77.77	39.85	37.92	0.80	0.71	1.51	0.95	0.99	1861
3.01	14 Jun 1968	35117-2	128.57	57.52	71.05	1.22	0.94	2.16	1.24	1.28	2369
4.02	19 Jun 1968	35117-2	152.08	75.98	76.10	1.66	1.13	2.79	1.00	1.04	1950
12.01	27 Jun 1968	35117-2	24.76	15.51	9.25	0.29	0.26	0.55	0.60	0.62	1552
14.02	28 Jun 1968	35117-2	23.96	14.77	9.19	0.17	0.26	0.43	0.62	0.64	1215

(1) Injector fuel flow rate = total fuel flow rate - total liner coolant flow rate

(2) Based on injector mixture ratio

(3) ΔT = maximum temperature - average temperature at 11-inch location

(4) η_c^* = (average temperature/ideal temperature)$^{0.5}$ x 100

(5) Measured temperature based on rake No. 3

(6) Throat Effective Area = 6.620 in.^{2}

(7) Throat Effective Area = 7.573 in.^{2}

(8) Throat Effective Area = 8.00 in.^{2}

ed Parameters During Preburner Injector Testing

ll re o	Injector Mixture Ratio(1)	Ideal Temperature(2) (°R)	Average Combustion Temperature (°R)	ΔT Profile at 11 in.(3) (°R)	$\eta_{c^*_1}$	η_{c^*} at 11 in.(4) (%)	Fuel Injection Velocity (ft/sec)	Oxidizer Injection Velocity (ft/sec)	Fuel/Oxidizer Momentum Ratio
	0.66	1285	1268	72	98.0(6)	99.3	495	131	5.8
	0.78	1504	1716	94	101.6(6)	103.9	555	133	5.4
	0.90	1728	1823	124	101.6(6)	102.8	545	132	4.6
	0.85	1628	1589	107	98.0(6)	98.8	579	145	4.7
	0.99	1881	1849	119	98.2(6)	99.1	547	137	4.0
	0.61	1390	1552(5)	25(5)	102.0(7)	105.4(5)	1163	132	14.4
	1.22	2272	2388(5)	76(5)	99.0(7)	102.5(5)	690	246	2.8
	0.66	1290	1322	310	99.3(7)	101.3	813	221	5.6
	0.65	1276	1326	260	99.4(7)	102.0	805	160	7.7
	0.65	1281	1266	144	98.7(7)	99.4	780	70	17.0
	0.99	1861	1793	211	99.0(7)	98.2	828	136	6.2
	1.28	2369	2325	215	99.7(7)	99.0	1022	198	4.0
	1.04	1950	1920	115	99.0(7)	99.2	1074	213	4.9
	0.62	1552	1676	58	94.3(8)	103.9	2088	119	28.3
	0.64	1216	1140	255	96.9(7)	96.9	437	113	6.0

perature based on rake No. 3

tive Area = 6.620 in.^{2}

tive Area = 7.573 in.^{2}

tive Area = 8.00 in.^{2}

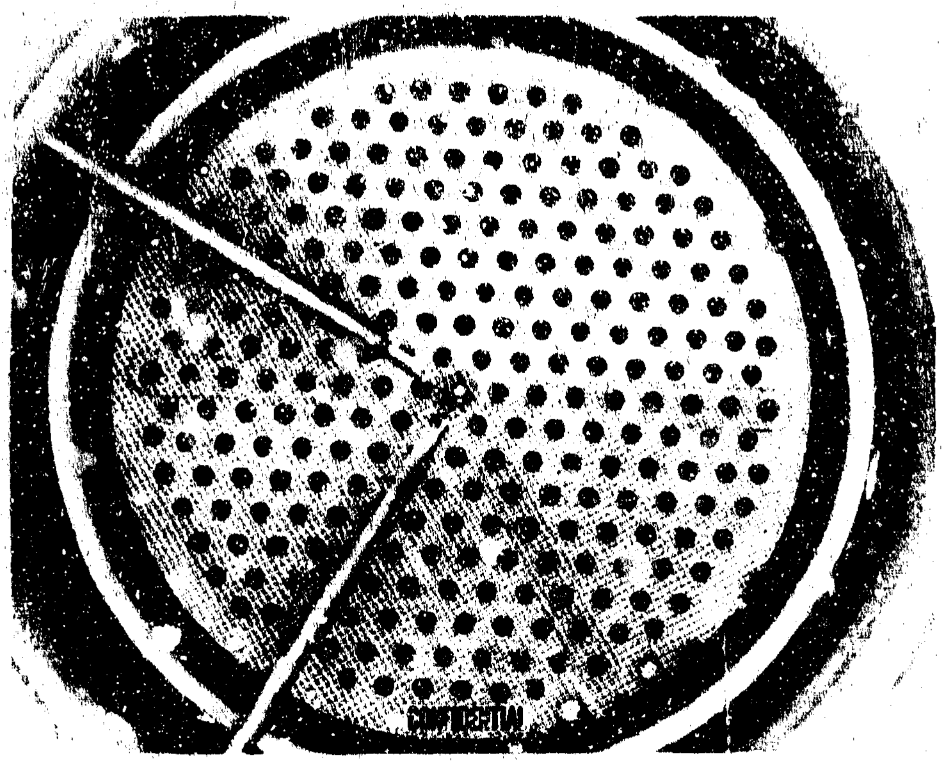

(U) Figure 18. Injector Face Prior to Test 1.01 FE 77800

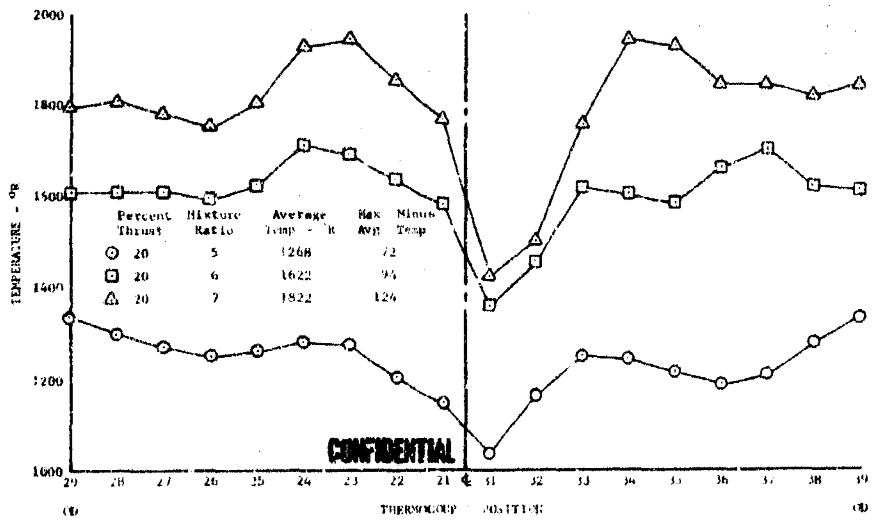

(U) Figure 19. Preburner Temperature Profile, Rig 35117-1, Test 1.01, 11-Inch Rake DFC 65190

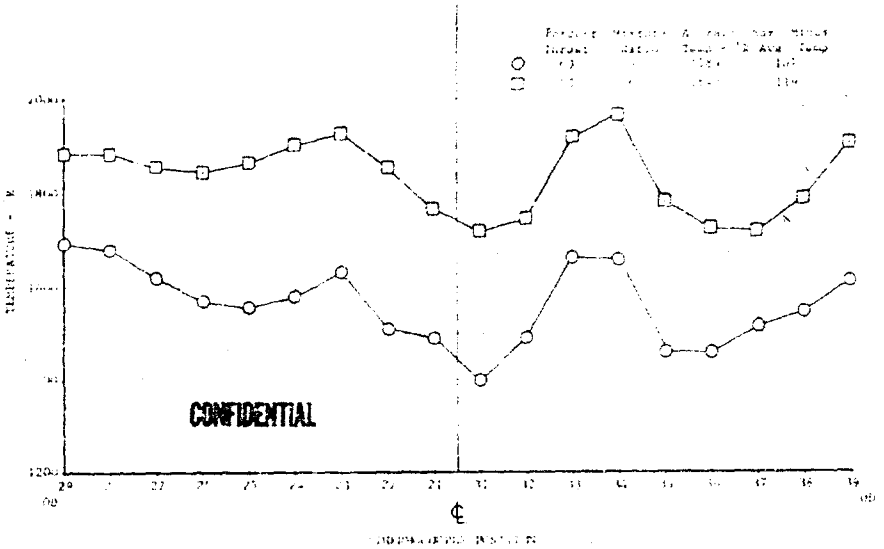

(U) Figure 20. Preburner Temperature Profile, Rig 35117-1, Test 1.01, 11-Inch Rake DFC 65191

(C) The acceleration to mixture ratio of 5 and 20% thrust level was made with the fuel inlet temperature held constant at 300°R instead of being ramped to 127°R as in test 1.01. This was an attempt to determine the effect of fuel temperature on the system instability. During the ramp from 7% to 20%, system instability was encountered. The instability persisted through the 20% data point and disappeared on the ramp to 100%. The peak-to-average temperature on the acceptable temperature rake (thermocouples No. 21 to 29) at a mixture ratio of 5 and 20% level was 25°R, and at a mixture ratio of 6 and 100% it was 75°R as shown in Figure 21. During the ramp to the mixture ratio of 7 at 100%, the run was automatically advanced because of high combustion temperature. This was caused by the large oxidizer valve (CV5) being at a portion of the stroke where little or no effective area change was made with stroke changes. As a result, even though the oxidizer valve was closing as scheduled, the oxidizer flow was not reducing as required to match the reducing fuel flow for the mixture ratio of 7 set point at 100% level.

(U) On test 2.01, two of the combustion temperature rakes in the same radial plane at 7- and 11-inch axial planes (thermocouples No. 31 to 39 on 11-inch rake shown in Figure 21) indicated a reduction in temperature toward the chamber outside diameter. These rakes had not shown a temperature reduction during test 1.01, which indicated that the injector had been damaged on the first test.

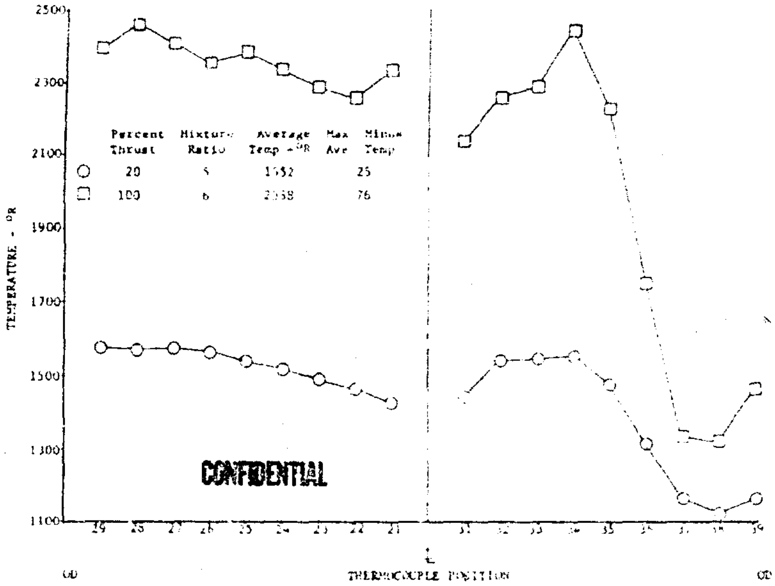

(U) Figure 21. Preburner Temperature Profile, Rig 35117-1, Test 2.01, 11-Inch Rake DFC 65192

(U) The teardown inspection revealed approximately 35 oxidizer elements burned in the secondary area. Figure 22 shows the injector face after test 2.01, and Figure 23 shows the secondary burning. The burned elements in most instances reduced the secondary flow area. The burned elements were concentrated in an area directly in line with the temperature rakes that showed a reduction in temperature at the chamber outside diameter. Consequently, these temperature rakes are not representative of the actual injector profile. The burning of the oxidizer elements was attributed to aspirating fuel into the cavity during the extended fuel lag shutdown. To prevent this from recurring, the shutdown fuel lag was reduced and increased oxidizer cavity purges were provided.

(C) The preburner rig was rebuilt using the backup injector, which was the same as the original injector, except that the fuel size was designed for a pressure drop of 400 psid at mixture ratio of 7 and 100% thrust level, instead of 200 psid. Figure 24 shows the face of the backup injector prior to test 3.01.

(C) Test 3.01 was conducted on 14 June 1968. This test was programmed for data points at a mixture ratio of 5 at 20% thrust level, a mixture ratio of 6 at 60% thrust level, and a mixture ratio of 7 at 100% thrust level.

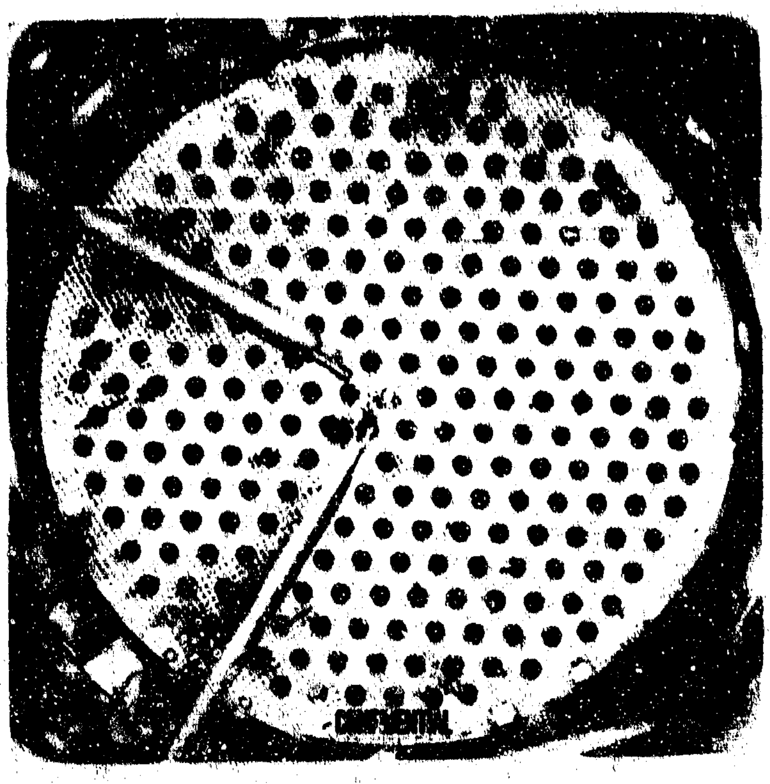

(U) Figure 22. Injector Face After Test 2.01 FE 77966

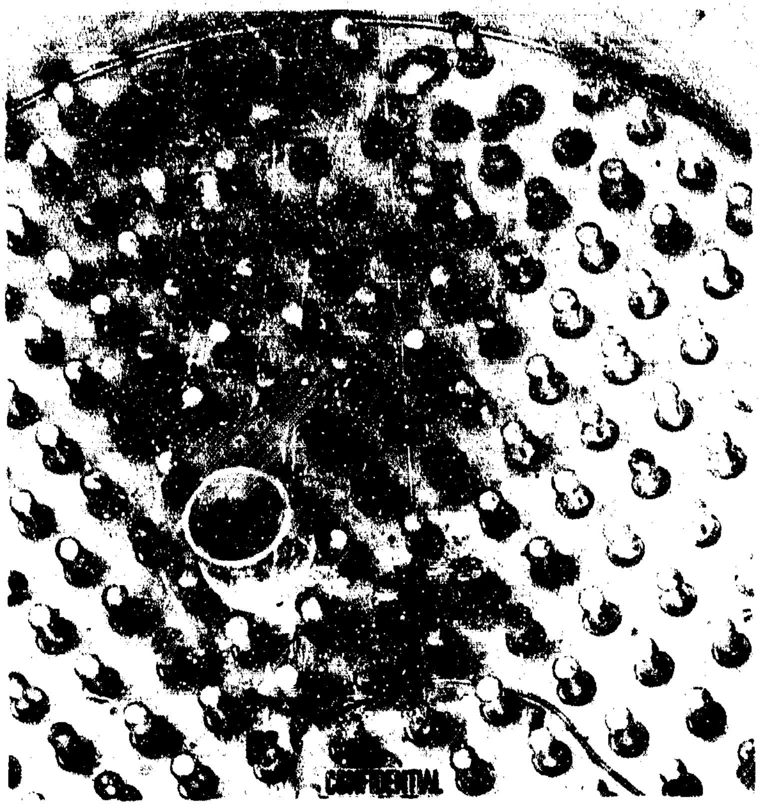

(U) Figure 23. Injector Secondary Burned Area After Test 2.01 FE 77998

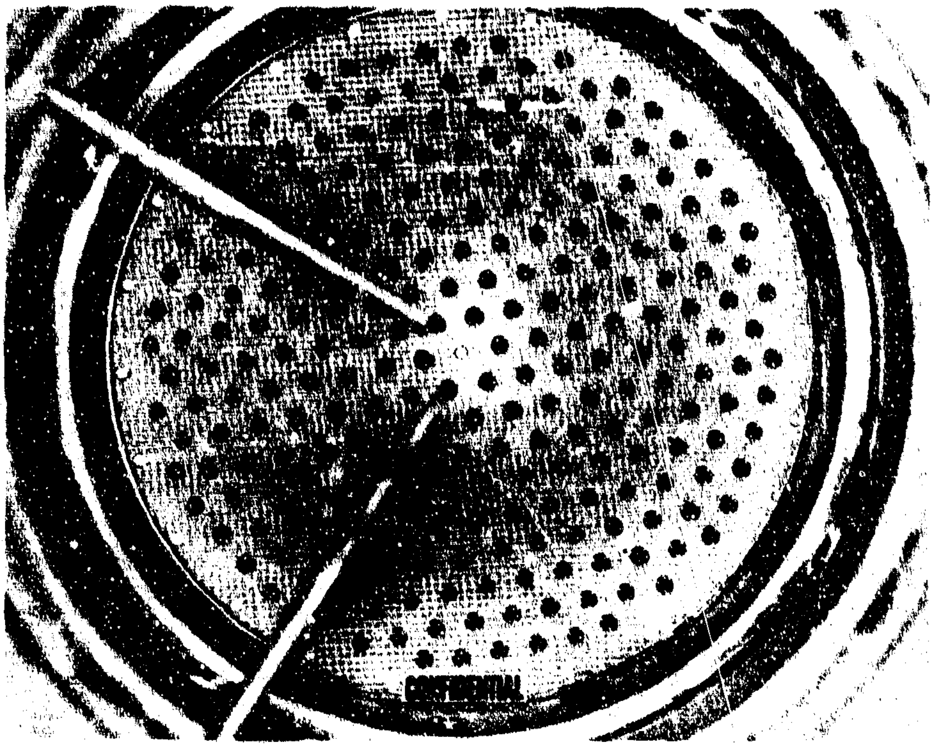

(U) Figure 24. Face of Backup Injector Prior to Test 3.01 FE 78185

(C) Low frequency (approximately 100 cps) system instability developed after the 20% level flow rates had been attained while the fuel temperature was being lowered to cycle set point. While at the steady-state 20% thrust levels, the preburner oxidizer valve was moved to give primary-to-total oxidizer flow splits of 86% to 45% at a constant cycle point fuel temperature. The system instability persisted during this preburner oxidizer valve excursion. The instability ceased after ramping away from the 20% thrust level flow rates toward 60% set point.

(C) The maximum-to-average temperature at a mixture ratio of 5 and 20% thrust level was 144°R at an average temperature of 1266°R; however, the temperature profile deteriorated with an increasing flow split as shown in Figure 25. This effect of flow split on the temperature profile is attributed to the result of built-in injector distribution, which is a function of the match of individual oxidizer primary flow area to the corresponding fixed fuel annulus area. This is substantiated by the fact that the profile was not symmetrical. The injector was assembled by matching the oxidizer total element area with the fuel annuli based on the water calibration of the individual elements prior to assembly. Oxidizer element primary area variation was 17% total span with 76% of the elements falling in a 6% band. No attempt was made to match the primary area to its respective fuel annulus thus explaining the deterioration in profile with increasing flow split.

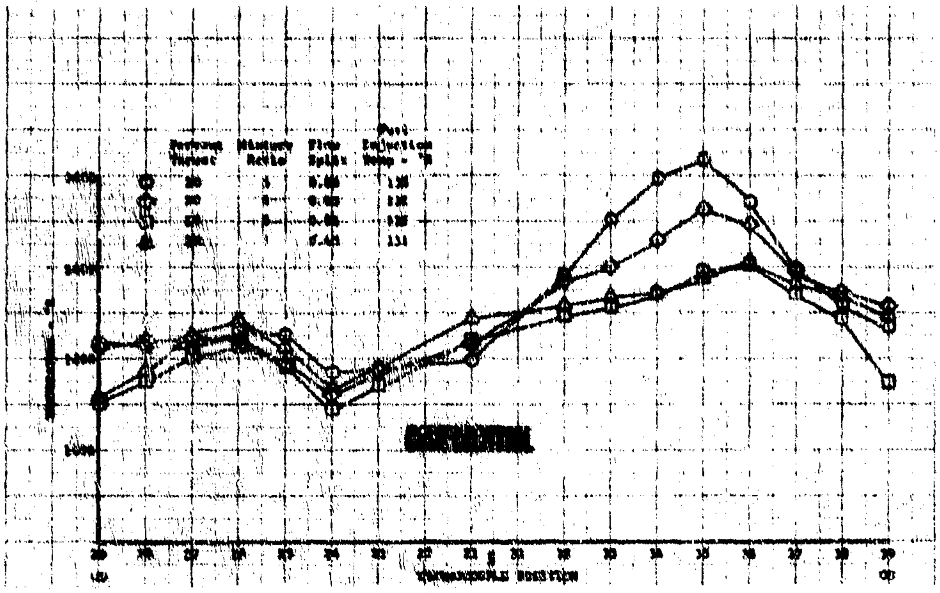

(U) Figure 25. Preburner Temperature Profile With Primary-to-Total Oxidizer Flow Split Variation, Rig 35117-2, Test 3.01, 11-Inch Rake DFC 66774

(C) The maximum-to-average temperature at a mixture ratio of 6 and 60% thrust level was 211°R at an average temperature of 1793°R. The maximum-to-average temperature at a mixture ratio of 7 and 100% thrust level was 215°R at an average temperature of 2325°R. (See Figure 26.)

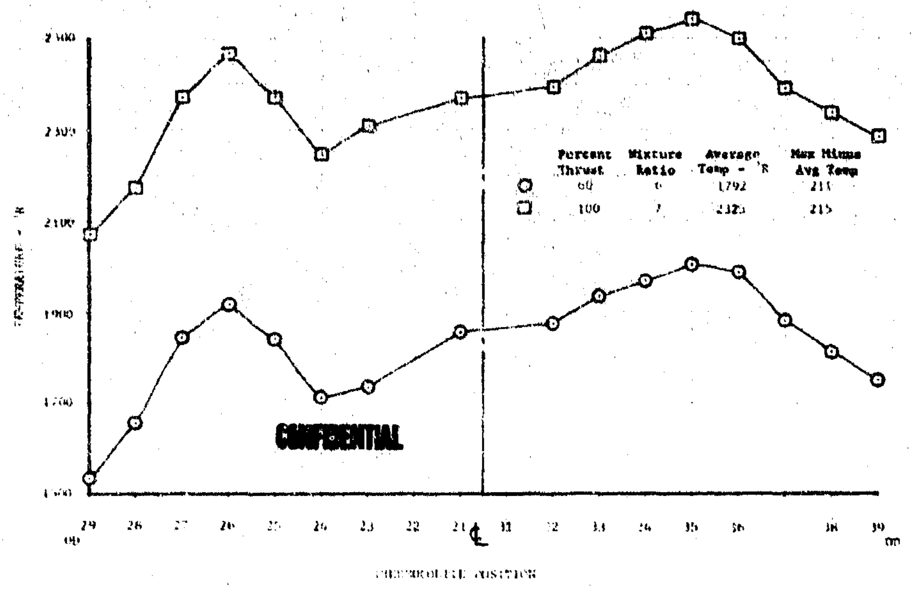

(U) Figure 26. Preburner Temperature Profile, Rig 35117-2, Test 3.01, 11-Inch Rake DFC 65193

(U) The magnitude of the peak-to-average temperature may be attributed to fuel leakage around the faceplate piston rings causing low combustion temperature at the outside on one of the rakes. The modified shutdown and purge procedure worked properly with no indication of hardware damage. The procedure used was to bring on a 2 lb/sec GH_2 supply and a 0.6 lb/sec GHe supply to the fuel side at shutdown. A small GN_2 supply was opened to the primary and secondary oxidizer injector cavities at shutdown. One and a half seconds after shutdown, the small GN_2 purge was calculated to have cleared the majority of oxidizer out of the injector, and at this time, a 0.25 lb/sec GHe purge was opened to the primary and secondary cavities to create approximately 10 psid across the elements without causing excessive overtemperature. At 2 seconds after shutdown, the 2.0 lb/sec GH_2 purge was turned off to clear the rig of any fuel.

(C) Test 4.02 was programmed for 100% thrust at a mixture ratio of 5 including the firing of a pulse charge. The test was automatically advanced by a high combustion temperature just after the top of the propellant ramps to the set point. The pulse charge was not fired. The test was advanced because the liquid hydrogen run tank was depleted, which caused the fuel temperature to rise. The gaseous hydrogen control valves, which are on fuel temperature control, started closing in an attempt to reduce fuel temperature. This combination of events delivered low fuel flow to the rig causing a high combustion temperature advance. The cause of liquid hydrogen depletion was insufficient topping off of the liquid hydrogen tank.

(C) The maximum-to-average temperature on test 4.02 was 115°R with an average temperature of 1920°R, at 97% thrust and a mixture ratio of 5. (See Figure 27.)

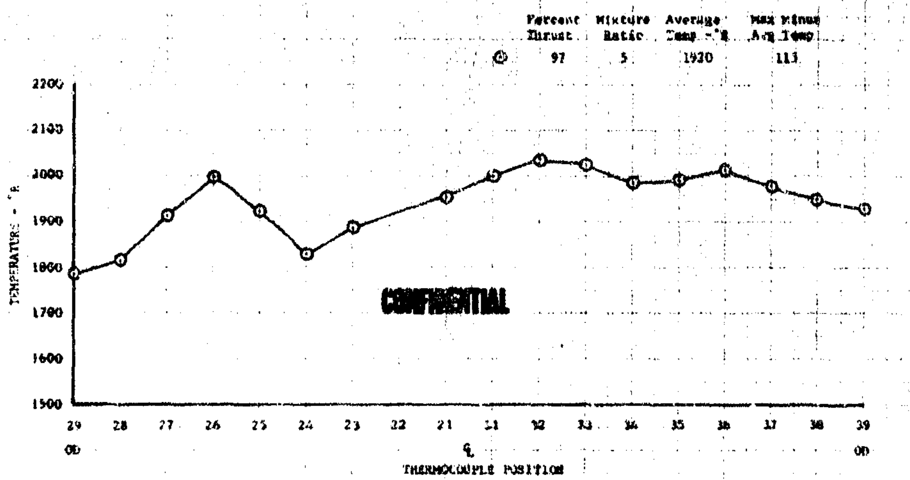

(U) Figure 27. Preburner Temperature Profile, Rig 35117-2, Test 4.02, 11-Inch Rake DFC 66720

(C) Tests 5.12, 6.01, 7.01, and 8.01 were ignition checks to determine if the preburner would ignite with a secondary helium purge flow rate (0.20 lb/sec) and the low engine tank head flow rate. The ignition fuel and oxygen flow rates were both below 1.0 lb/sec. All four ignition tests successfully ignited and sustained combustion. In tests 5.12 and 6.01 the oxygen was programmed to lead the fuel by 2 seconds. Test 7.01 was a repeat of test 6.01 with the oxygen and fuel flows opened to the rig simultaneously. These two tests showed that the oxygen to fuel timing did not influence ignition within this time span. Tests 7.01 and 8.01 were run at essentially constant total propellant flow rate and constant helium flow rate with mixture ratio variations from 1.0 during test 7.01 to 0.5 during test 8.01. The flow rates for tests 7.01 and 8.01 are provided in Table VIII.

(C)(U) Table VIII. Flow Rates for Tests 7.01 and 8.01

Test No.	He (lb/sec)	O_2 (lb/sec)	H_2 (lb/sec)
7.01	0.205	0.56	0.56
8.01	0.202	0.35	0.71

(C) Tests 9.01, 9.02, and 9.03 were liquid oxygen cold flows to determine the response of oxidizer flow to the rig with a programmed 420 millisecond ramp of the oxidizer pump simulator valves and the oxidizer tank pressurized to 1700 psia. The delivered flow rate from these cold flows was matched with the fuel flow rate for the simulated engine start transient from ignition flow rates to the 20% flow rates.

(C) Tests 9.04, 10.01, 11.01, and 12.01 were programmed to simulate the engine start transients from ignition flow rates to the 20% flow rate level, plus a fuel temperature excursion from ambient temperature to cycle temperature of 127°K and back to ambient temperature. The rig shutdowns for these tests omitted the initial low flow rate nitrogen purges to the primary and secondary cavities, but instead used the 0.20 lb/sec helium supply to purge the liquid oxygen. The shutoff valve for the primary and secondary helium supply, which previously had been approximately 40 feet away, was close coupled to the rig on tests 9.04, 10.01, and 11.01.

(U) Test 9.04 was automatically advanced by high combustion temperature after 2.75 seconds. Test 10.01 was automatically advanced by a low combustion temperature after 2.0 seconds. The rig ignited, but failed to sustain combustion. Test 11.01 was manually advanced by a low combustion temperature after 3.60 seconds. Again, the rig ignited but failed to sustain combustion. These tests showed that helium was being delivered much earlier to the injector with the helium valve close coupled to the rig. The early arrival of helium influences the ignition process causing unsustained combustion.

(C) Test 12.01 was made with the helium valve that opens the helium start purge located in its original position, approximately 40 feet from the rig. Because of the large volume between the helium valve and the rig, the helium flow rate arrives at the rig after ignition has taken place and thus does not affect the ignition process. Test 12.01 ran successfully through to the programmed shutdown. The required rapid chamber pressure rise that simulates an engine start was attained. The chamber pressure rise rate was approximately 4400 psi/sec. System instability was encountered at the 20% flow rates as the fuel temperature was lowered from the ambient to cycle set point. The instability began at approximately 290°R fuel temperature. The instability disappeared at 230°R as the fuel temperature was ramped up from 126°R to ambient. The effect of fuel injection temperature on the temperature profile is shown in Figure 28, which shows a reduction in profile with increasing fuel temperature. The valve that opens the helium shutdown purge to the primary and secondary cavities was close coupled to the rig as in tests 9.04, 10.01, and 11.01. The close-coupled valve delivered the full helium purge flow rate to the rig rapidly, which caused a high temperature spike just after shutdown on test 12.01.

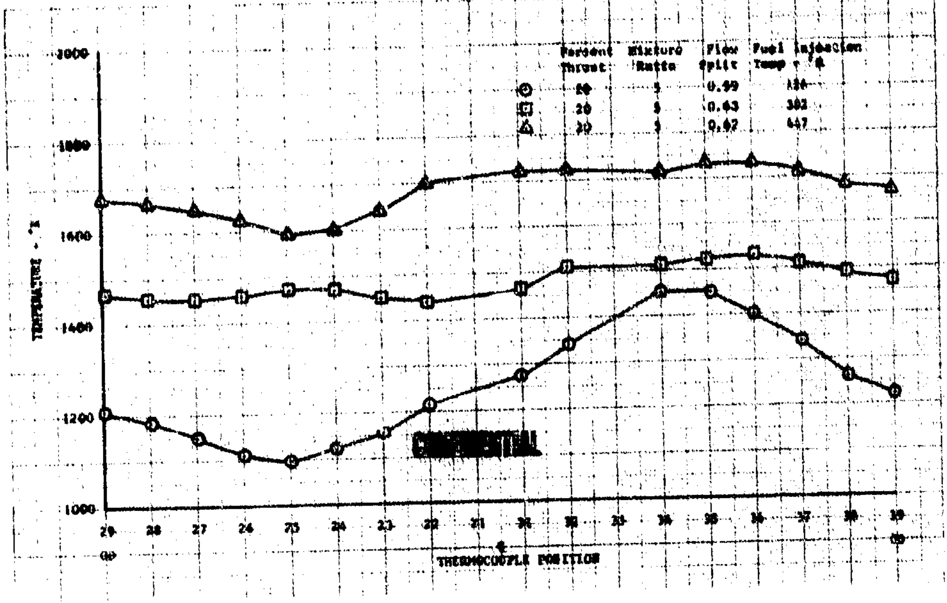

(U) Figure 28. Preburner Temperature Profile, Rig 35117-2, Test 12.01, 11-Inch Rake DFC 66721

(C) Tests 13.01, 13.02, 13.04, 14.01, and 14.02 were programmed for fuel temperature excursions from 300°R to 85°R and flow divider valve excursions from 90% to 40% primary-to-total oxidizer flow splits while at the 20% flow rates. For these tests, orifices were installed in the fuel and oxidizer stand run lines just upstream of the rig. The orifices create a high-pressure drop in an effort to isolate the volumes in the stand run lines from the injector cavities. In an attempt to correct the high temperature spikes encountered during shutdown purge of test 12.01, these tests were made with the close-coupled helium valve opening the primary and secondary purges after approximately 0.100 second delay. The delay was to allow more time for chamber pressure to decline and the fuel line to bleed in an attempt to drive the mixture ratio above stoichiometric and thus reduce the shutdown temperature spike.

(C) Tests 13.01 through 14.01 were unsuccessful attempts because of various control and operational problems. Test 14.02 was a successful test to the programmed shutdown. System instability was encountered at the 20% level as fuel temperature was ramped down past 290°R to the cycle set point of 127°R. The preburner oxidizer valve excursions at cycle temperature did not correct the system instability. The instability remained as the fuel temperature was ramped from 127°R to 290°R. The shutdown on test 14.02 had a high temperature spike even with the delayed opening of the shutdown helium purge. Figure 29 shows the injector face at the conclusion of test 14.02.

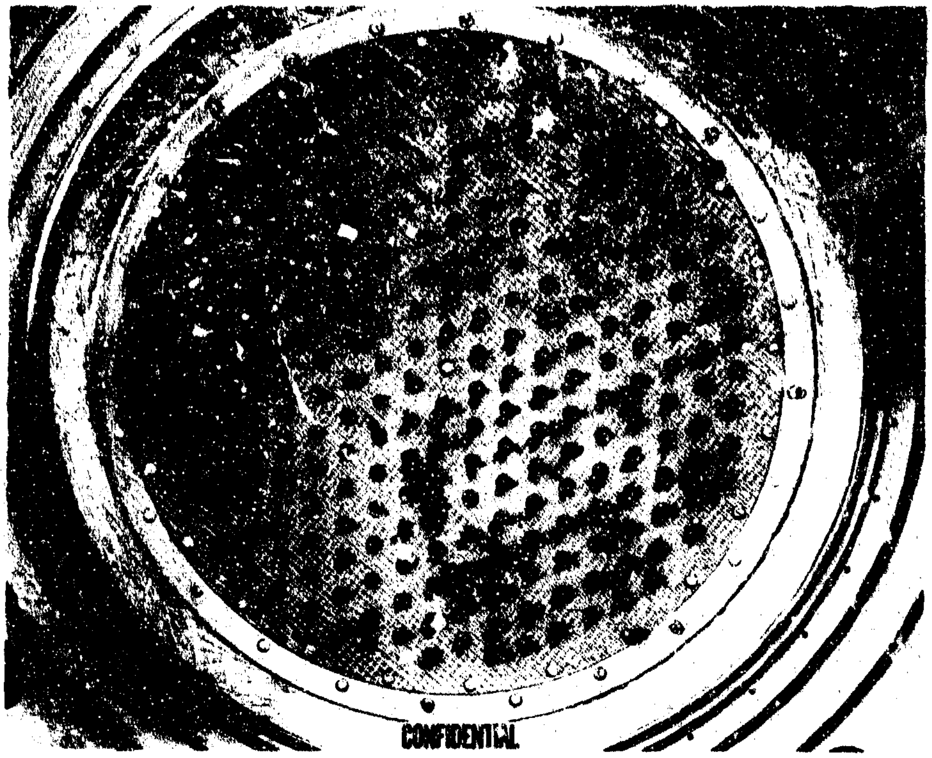

(U) Figure 29. Injector Face After Test 14.02 FE 78445

d. Performance Calculations

(C) The characteristic velocity efficiency computed from rig pressures and flow rates had an average value of approximately 99.5% as shown in Figure 30. Figures 31 and 32 show the characteristic velocity efficiency based on the average combustion temperature at the 7 inch and 11 inch locations, respectively. The results of both indicate an average η_c* of approximately 100% with a scatter band of ±4. The agreement of η_c* calculated from measured combustion temperatures and that calculated from rig pressure and flow rates tends to verify the validity of combustion temperatures and the method used to calculate average combustion temperature.

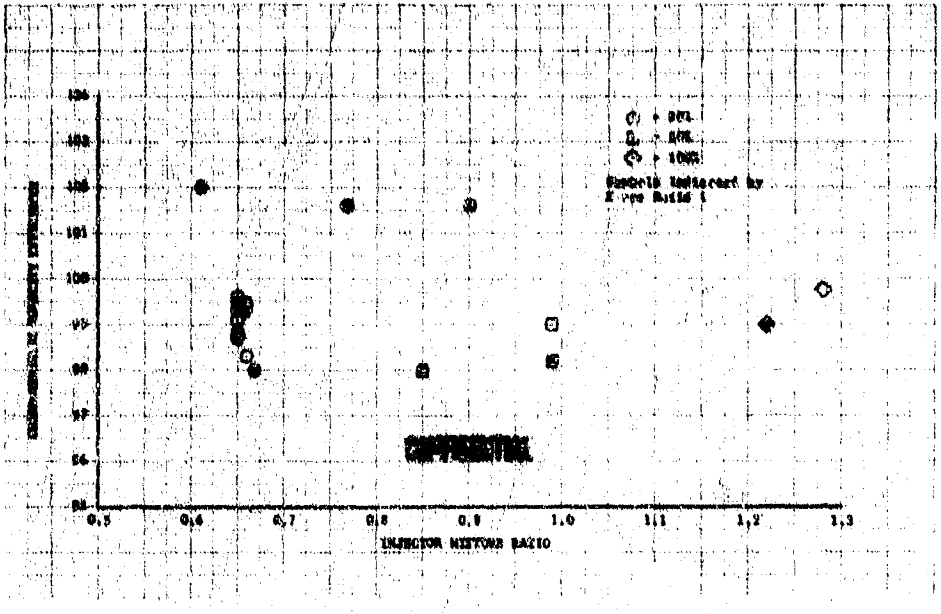

(U) Figure 30. Characteristic Velocity Efficiency Based on Rig Pressures and Flow Rates DFC 66722

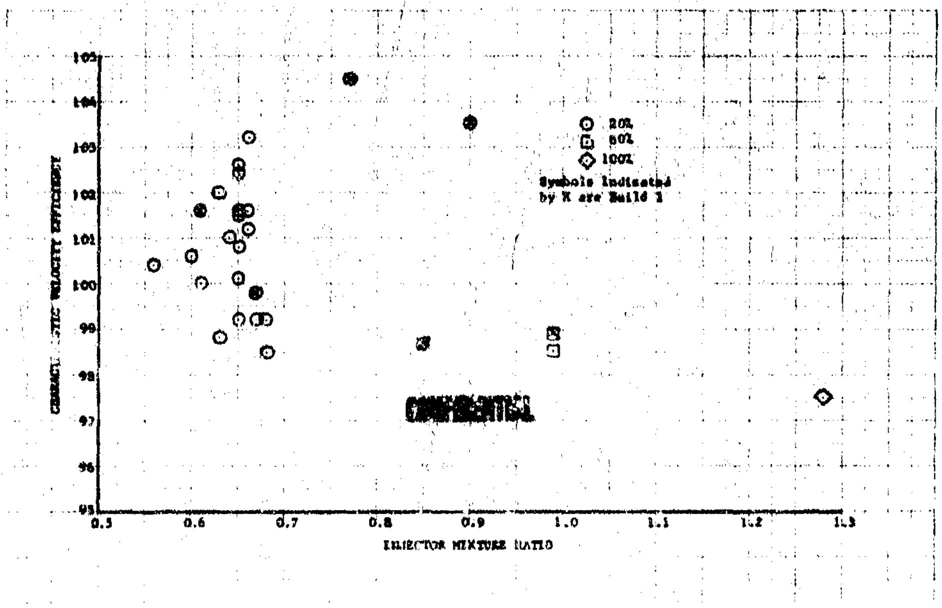

(U) Figure 31. Characteristic Velocity Efficiency Based on Combustion Temperatures at the 7-Inch Rake DFC 66723

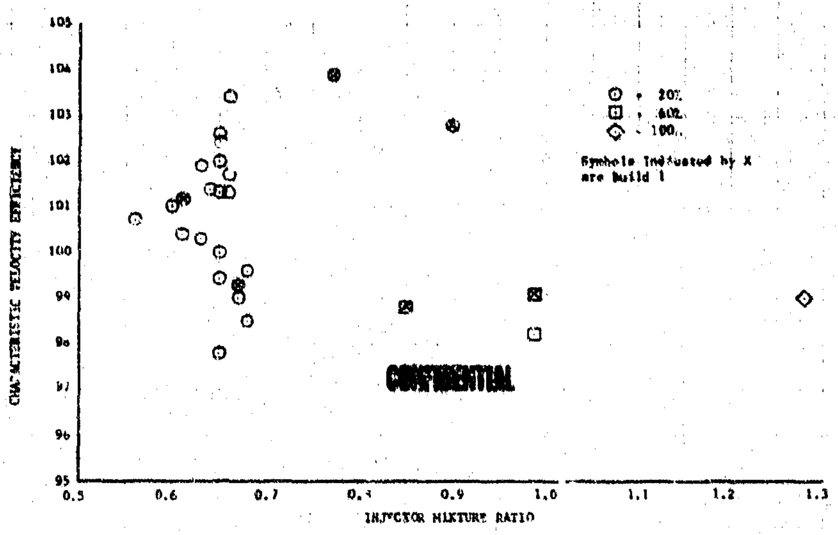

(U) Figure 32. Characteristic Velocity Efficiency Based on Combustion Temperatures at the 11-Inch Rake DFC 66768

(U) The oxidizer injector secondary effective area compared well with the predicted levels determined from water flow tests of the individual elements and showed the same effect of flow split on effective area. A comparison between preburner rig results and the levels predicted from water flows of individual tubes are shown in Figure 33. Combustion rig data and water bench calibrations indicate that the injector used on Build 1 had a secondary effective area about 7% smaller than the injector used on Build 2.

(U) The calculated primary effective area had a large amount of scatter, particularly at low flow splits. This would be expected because slight errors in the estimated flow split will result in proportionately larger errors in the primary flow and primary effective area. The flow split for the preburner rig tests was estimated from the measured preburner oxidizer valve pressure drop and the water calibration of the preburner oxidizer valve. The agreement between the preburner rig test data and the predicted shape of the secondary effective area versus flow split curve indicated that the flow divider valve calibration provided an acceptable method of determining secondary flow rate.

(C) The oxidizer secondary effective area increased slightly with an increasing fuel to oxidizer momentum ratio as shown in Figure 34. Data from tests 3.01, 12.01, and 14.02 were used with data points corresponding to 20% thrust and a mixture ratio of 5. All points were obtained with a constant preburner oxidizer valve position to minimize the effect of flow split on effective area. A slight increase in flow split did result, however, when momentum ratio was increased as shown in Figure 35. This makes the increase in secondary effective area with momentum ratio slightly larger than is indicated. The increase in oxidizer effective area with increasing momentum ratio was contrary to the trend expected and that experienced during Phase I (Contract AF04(611)-11401) testing. No change in the primary effective area with changing momentum ratio was observed as shown in Figure 36.

(C) Two fuel injectors were tested. Build 1 (tests 1.01 and 2.01) had an injector sized to provide a 200 psi pressure drop at an engine thrust of 100% and a mixture ratio of 7. Build 2 had an injector sized to provide a 400 psi pressure drop at the same conditions. The calculated effective areas are shown in Figure 37. The scatter in the Build 1 data was caused by unexplained injector instrumentation variations.

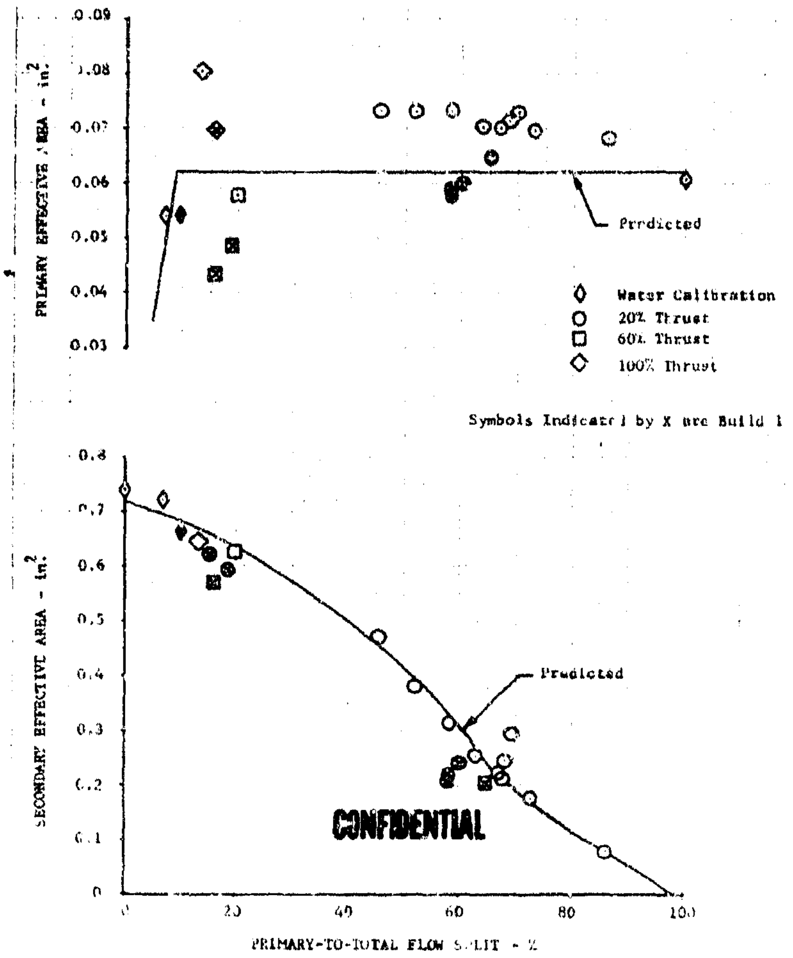

(U) Figure 33. Oxidizer Injector Calibration DFC 66769

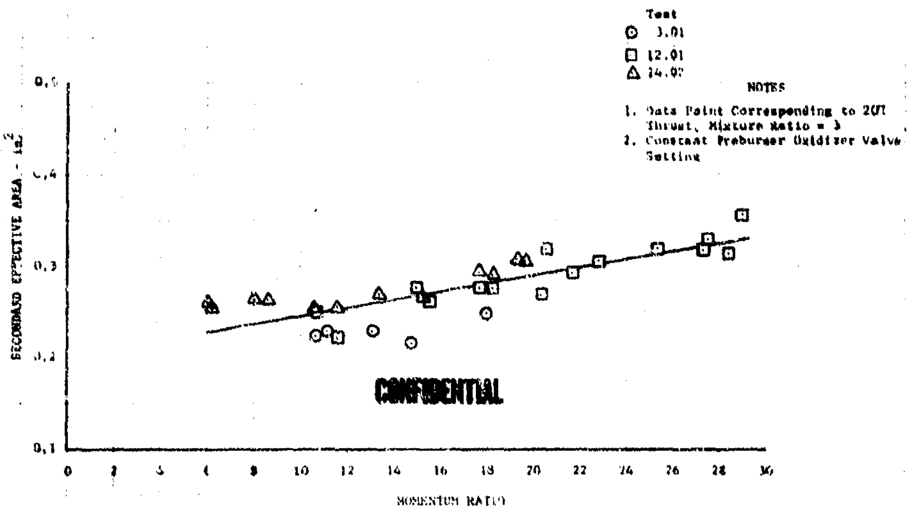

(U) Figure 34. Secondary Effective Area vs Momentum Ratio DFC 66770

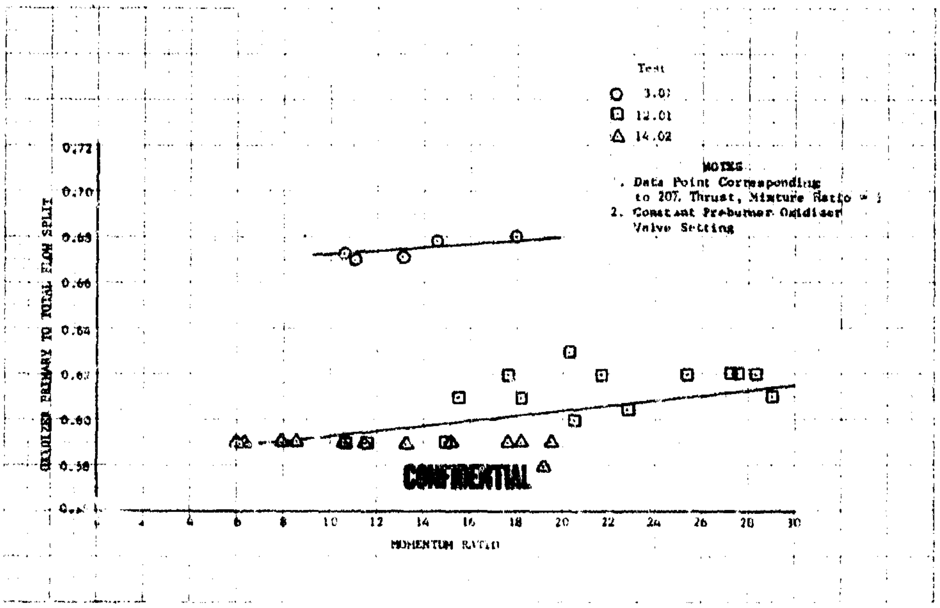

(U) Figure 35. Primary-to-Total Flow Split vs Momentum Ratio DFC 66771

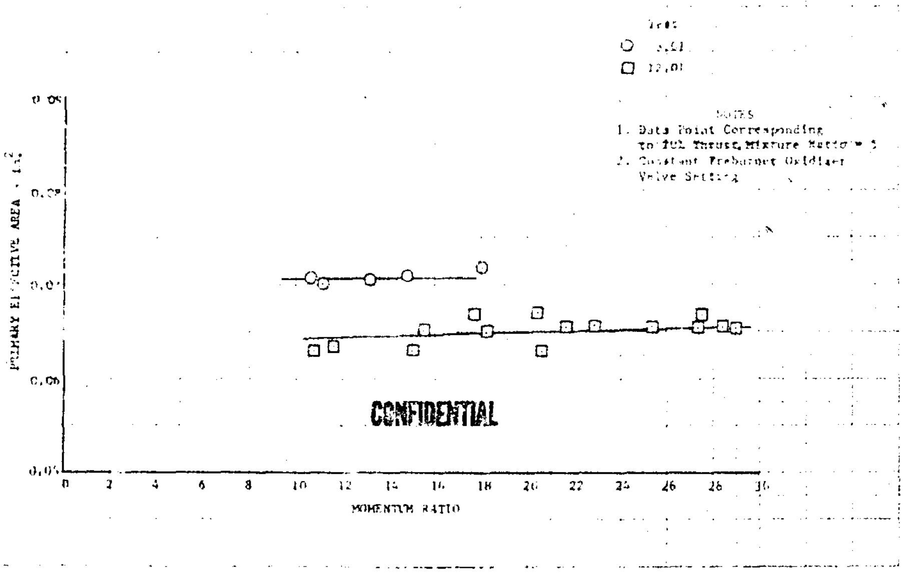

(U) Figure 36. Primary Effective Area vs Momentum Ratio DFC 66773

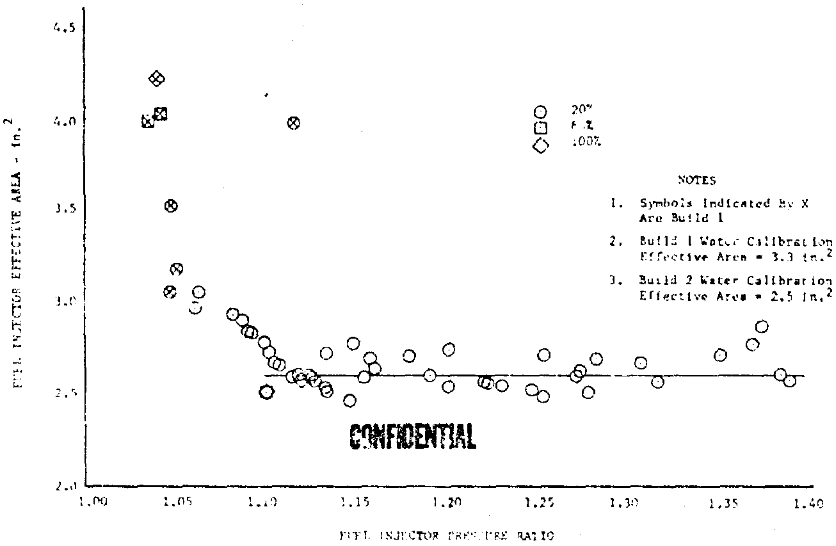

(U) Figure 3 . Fuel Injector Effective Area DFC 66772

5. Stability Investigation

(C) During testing of the preburner injector, low frequency combustion instability was encountered while operating at the 20% thrust level. To evaluate the cause of the combustion instability, several tests were programmed to obtain data on the suspected influential parameters. An analog model of the preburner injector, combustion chamber, and a portion of the test stand was constructed to determine the influence of various parameters on stability. Also, water flows of the injector assembly and single element test rigs were made in an attempt to relate hot firings to water flow tests.

a. Special Preburner Rig Tests

(U) Of the the possible causes of combustion instability, three of the conditions could be controlled to some extent in a typical preburner test without compromising the basic test objective. The three conditions were (1) liquid oxygen flow split between the primary and secondary, (2) fuel temperature, and (3) separation of the test stand propellant volumes from the preburner rig. Portions of preburner rig tests were scheduled to vary these parameters.

(1) Flow Split Evaluation

(C) At the 20% thrust cycle conditions during tests 3.01 and 14.02, the oxidizer primary-to-total flow split was varied from approximately 30% to 90% as shown in Figure 38. This change had no significant effect on the combustion instability even though the percent effective oxidizer pressure drop varied from 4% to 57% of preburner pressure as shown in Figure 39. In the injector designed during Phase I (Contract AF04(611)-11401), it was possible to eliminate combustion instability by increasing the percent effective oxidizer pressure drop above 4%. Because this was not true with the current injector, it was concluded that this fully tangential dual orifice element does not achieve the momentum addition at the secondary slot. Therefore, with the vapor core in the center of the element, the oscillations in the preburner pressure bypass the high pressure drop primary stream and come into direct contact with the low pressure drop secondary.

(U) The range of primary and secondary pressure drop is shown as a percent of chamber pressure in Figures 40 and 41, respectively. The primary pressure drop is across a large range, but the secondary pressure drop varies only between 0.6 and 1.7% of chamber pressure. The primary pressure drop is always well above the range where instability occurs when compared to past experience. The secondary pressure drop, however, is always lower than that required for stable operation. It was concluded that the low secondary pressure drop contributes significantly to the instability and the high primary pressure drop does not influence the instability.

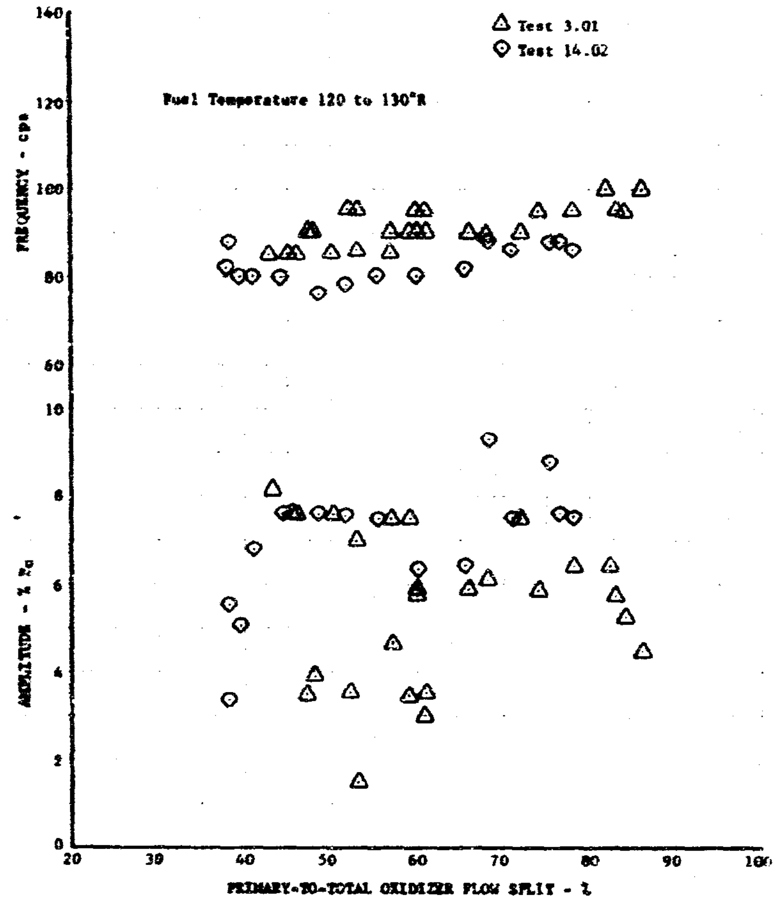

(U) Figure 38. Flow Split Variation DF 66711

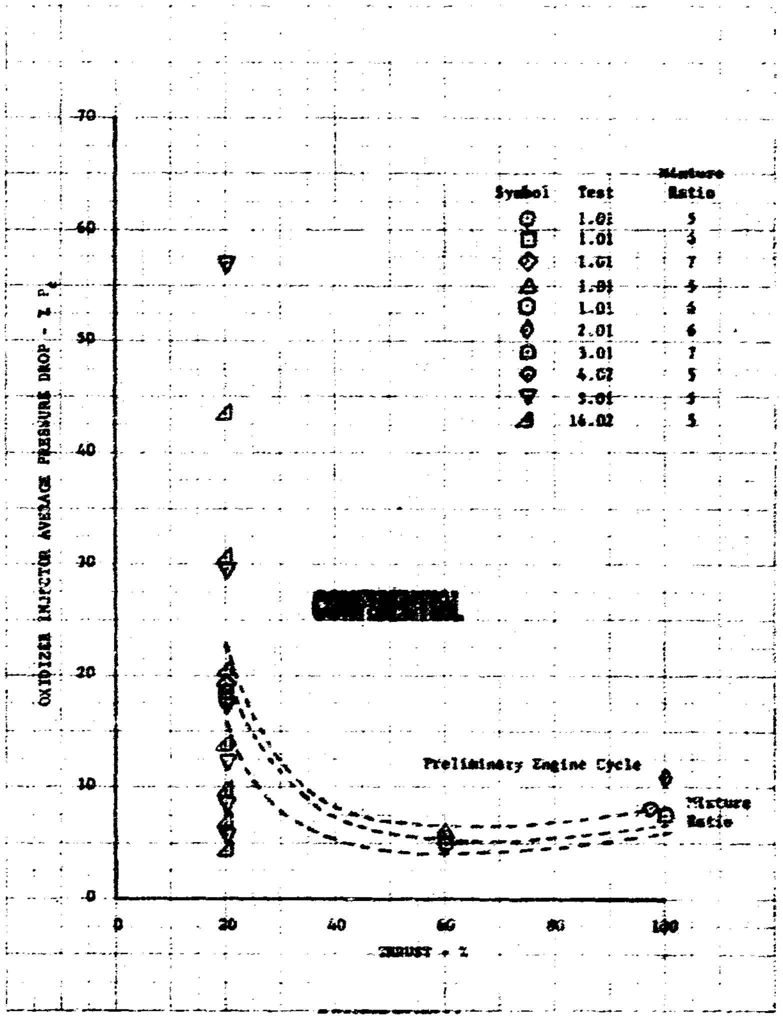

(U) Figure 39. Oxidizer Injector Percent Pressure Drop vs Percent Thrust DFC 66710

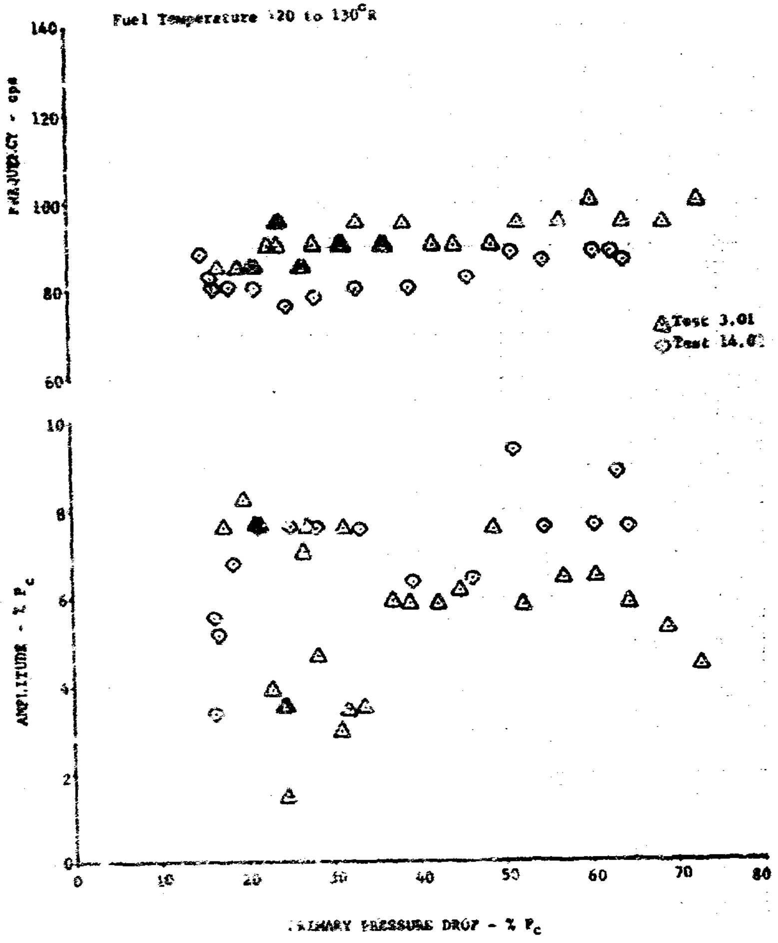

(U) Figure 40. Primary Pressure Drop as a Percent of Chamber Pressure DF 66712

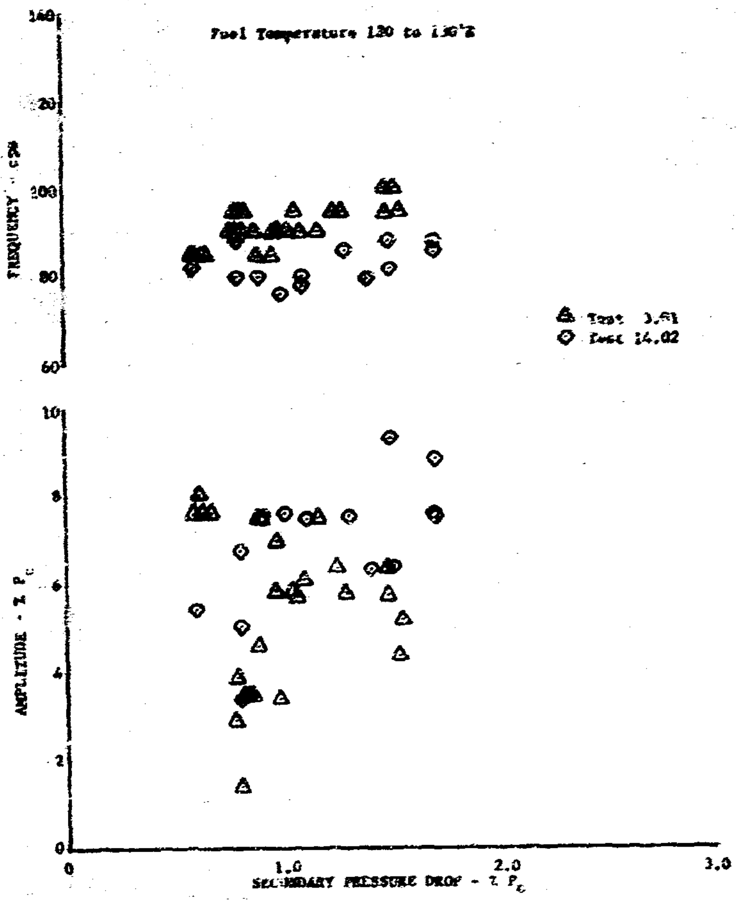

(U) Figure 41. Secondary Pressure Drop as a Percent of Chamber Pressure DF 66713

(U) Some oscillations in the oxidizer injector almost always exist either because of inherent instabilities in the injector cavities or the possible interaction between the oxidizer spray cone and the surrounding fuel flow. The repeatable effect on the frequency by changing the oxidizer primary-to-total flow split shown in Figure 38 indicates the oxidizer injector affects the instability to some extent.

(2) Fuel Temperature Evaluation

(U) Increasing the fuel injection temperature consistently eliminated the combustion instability as shown in Figure 42. Changing the fuel injector effective area at constant temperature by changing from the low pressure drop to the high pressure drop fuel plate did not affect the combustion instability as shown in Figure 43. Therefore, it was concluded that the fuel temperature, and not the fuel pressure drop or velocity, eliminates the combustion instability.

(U) The most probable theory on how the fuel temperature affects the combustion instability is that the increase in fuel temperature decreases the combustion delay enough to uncouple the preburner combustion from the oxidizer injector.

(C) During test 12.01, the fuel injector temperature at 20% thrust was varied extensively. Figures 44, 45, and 46 are traces that show the path and the effects of fuel temperature on the amplitude and frequency of the combustion instability. The phase relationships are also indicated in Figures 44, 45, and 46. The only two consistent phase relationships observed were that the secondary oxidizer cavity is in phase with the chamber oscillations and the fuel manifold is 180 degrees out of phase with the combustion chamber. It is not understood what bearing this particular phase relationship has on the stability problem. However, the frequency of the parameters was not always equal at a particular fuel temperature. When frequencies are not equal, the phase relationship between the parameters is constantly changing, which lessens the significance of phase relationships. Another significant item is the large reduction in combustion chamber amplitude at fuel temperatures above 180°R.

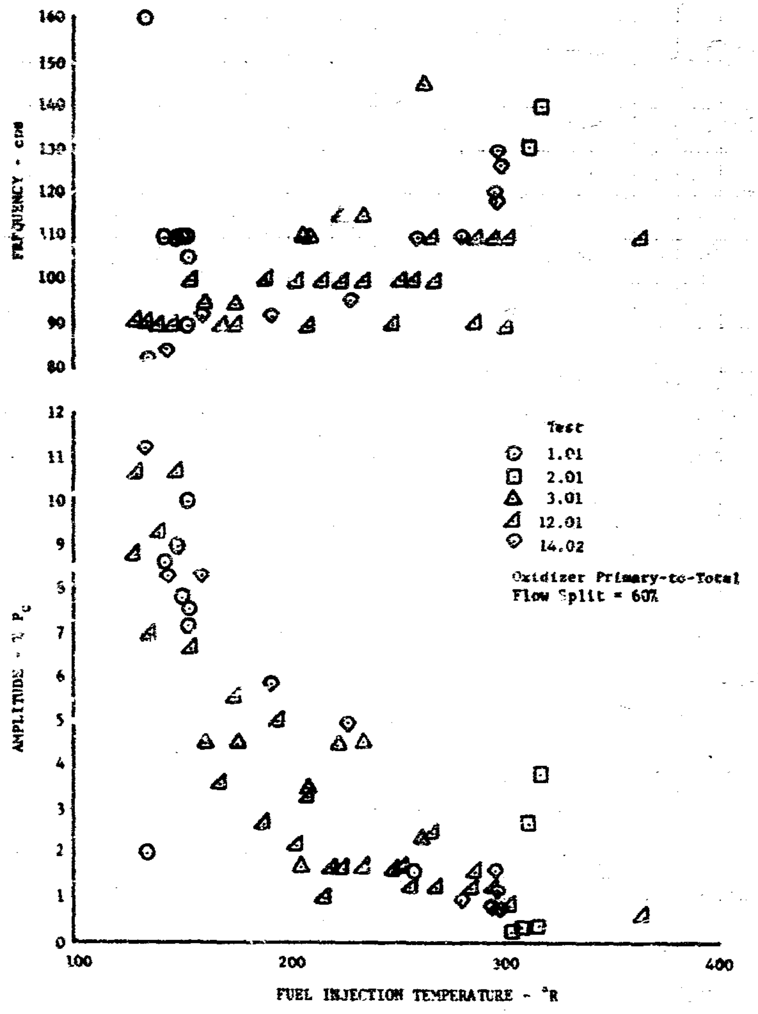

(U) Figure 42. Effect of Fuel Injection Temperature DF 66714

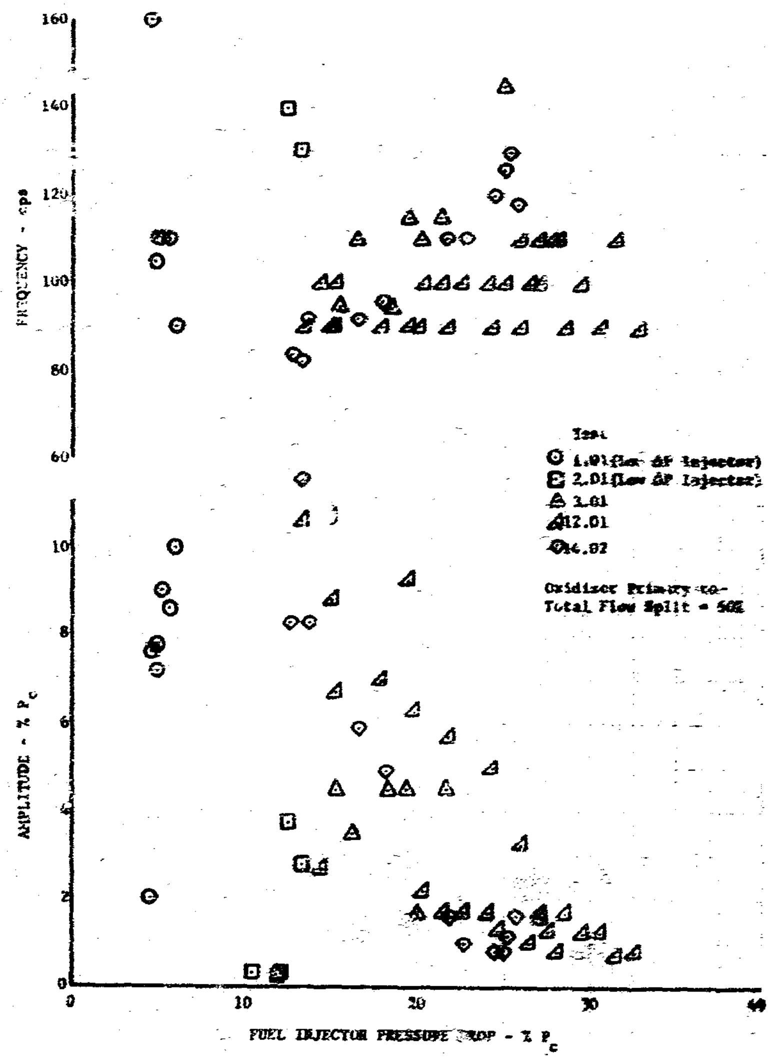

(U) Figure 43. Effect of Fuel Injector Pressure Drop DF 66715

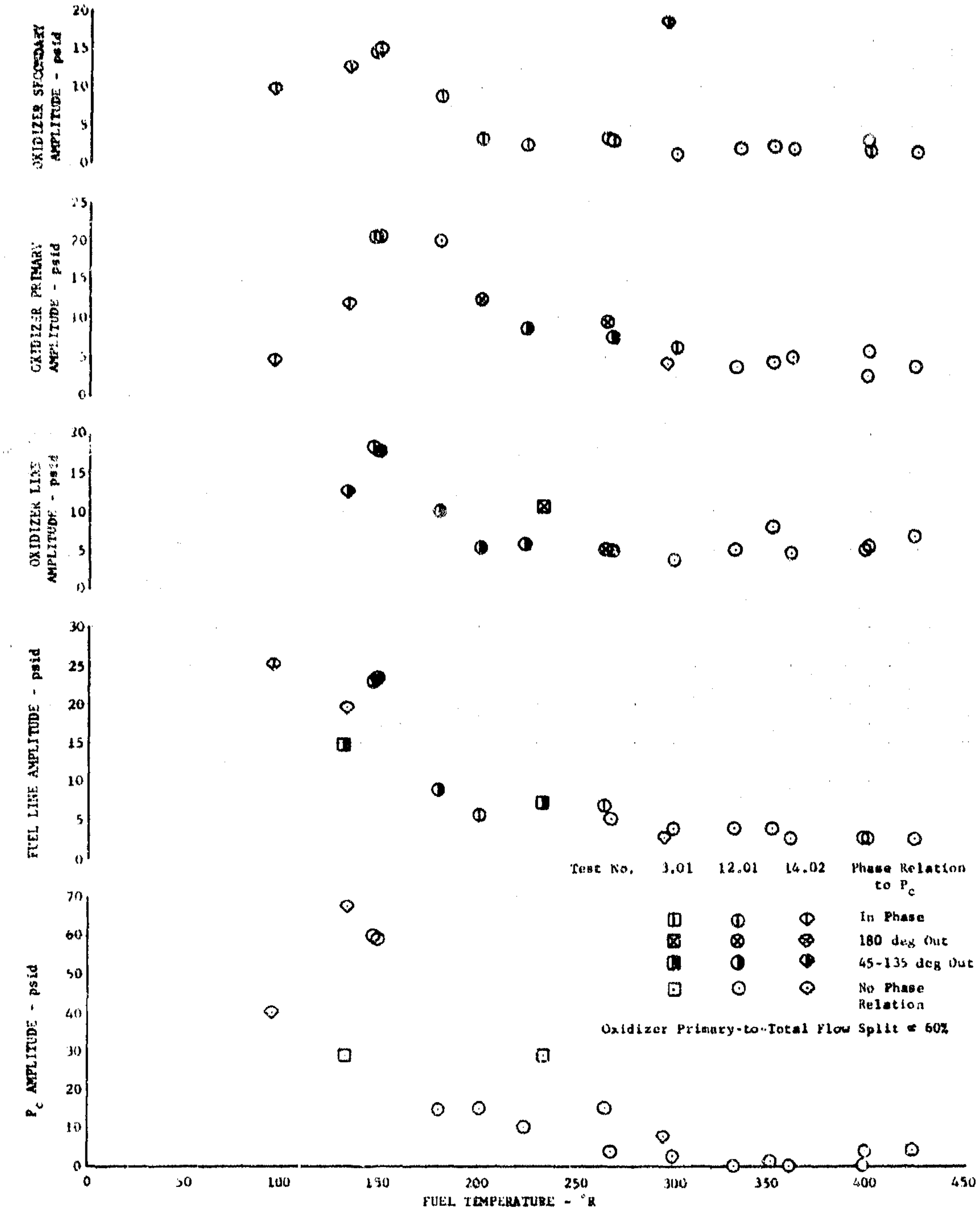

(U) Figure 44. Fuel Temperature Effect on Amplitude DF 66716

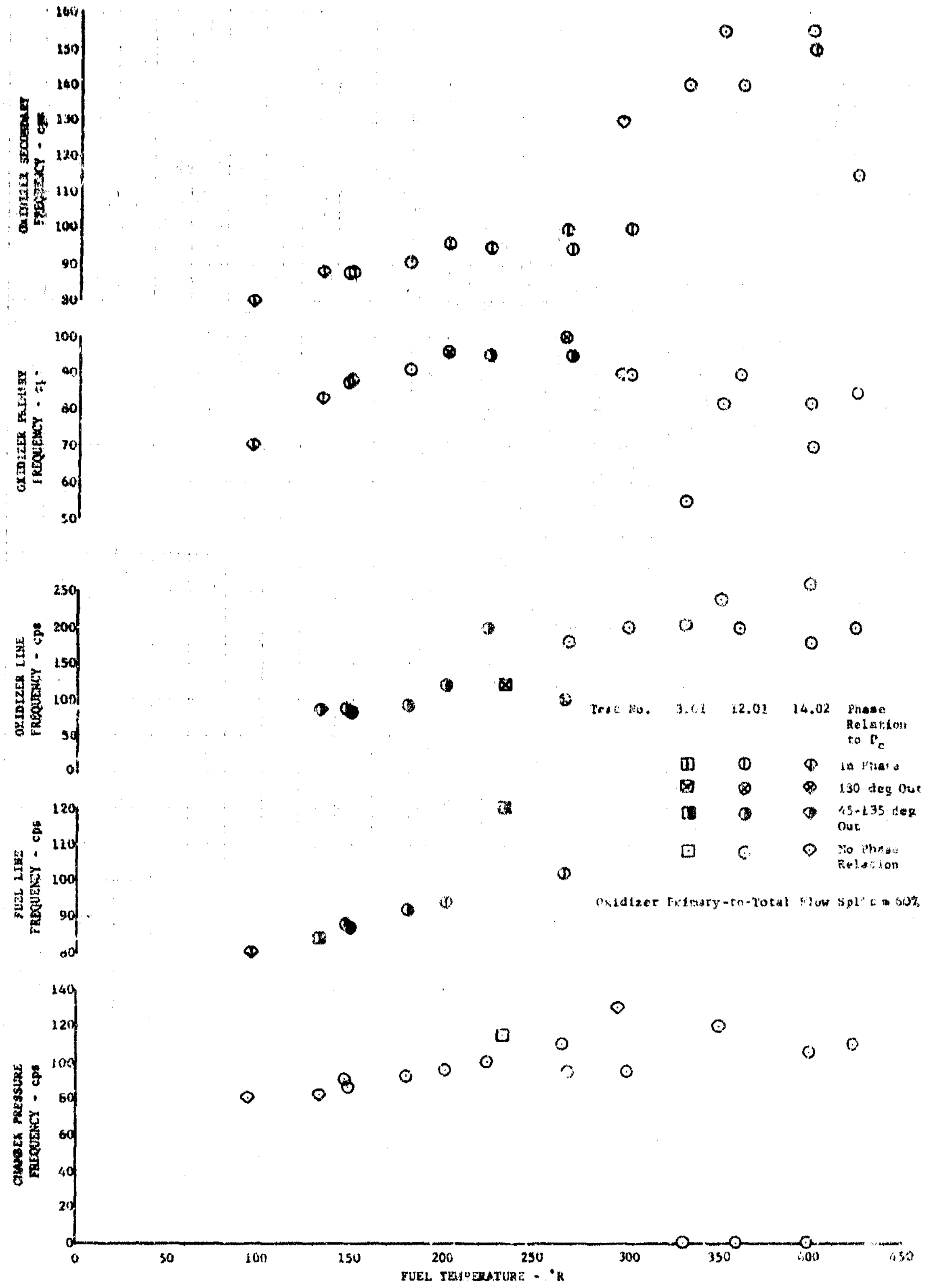

(U) Figure 45. Fuel Temperature Effect on Frequency DF 66717

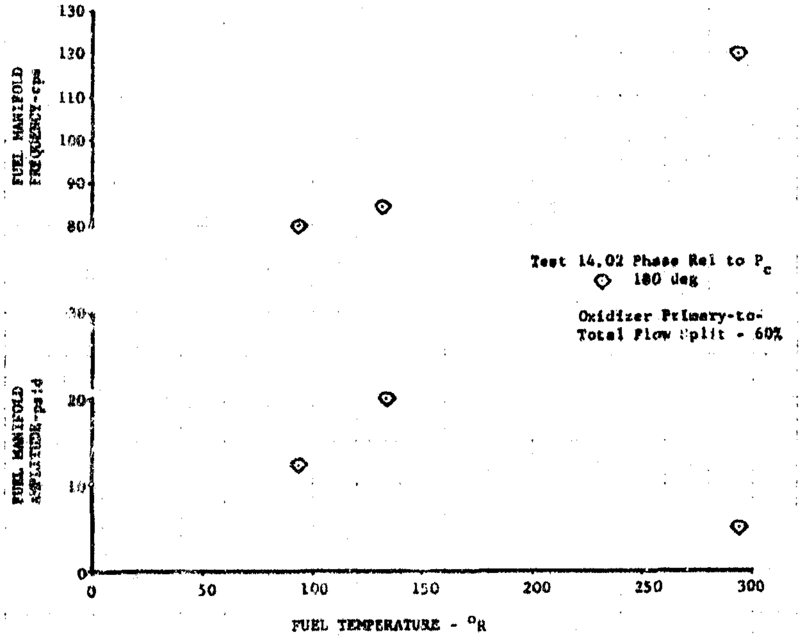

(U) Figure 46. Fuel Temperature Effect on Fuel Manifold Amplitude and Frequency DF 66709

(3) Evaluation of Test Stand Volumes

(U) During test 14.02, high pressure drop orifices $\left(\frac{\Delta P}{P} > 0.6\right)$ were installed in the stand lines just upstream of the rig in an attempt to isolate the test facility from the rig. There was no significant change in either the amplitude or the frequency of the combustion instability.

(U) Preburner injector testing during Phase I (Contract AF04(611)-11401) showed stable combustion at approximately the same flow rates, pressures, and temperatures with the identical test facility. Table IX compares a previous test with cold fuel temperatures with a recent test.

(C)(U) Table IX. Preburner Test Comparison

Item	Phase I (Contract AF04(611)-11401) Testing	Current Testing
Rig	33447-5	35117-2
Test No.	49.01	12.01
Primary Oxidizer Pressure Drop (psid)	50.7	235
Secondary Oxidizer Pressure Drop (psid)	15.0	9.3
Fuel Injector Pressure Drop (psid)	73.3	83.0
Fuel Temperature (°R)	118	147
Fuel Flow (lb_m/sec)	11.9	14.1
Oxidizer Flow (lb_m/sec)	3.7	9.1
Oxidizer Primary-to-Total Flow Split	0.22	0.59
Preburner Chamber Pressure (psia)	474	560
Chamber Pressure Amplitude (psid)	0	±60
Chamber Pressure Frequency (cps)	-	90

(U) Based on these observations it was concluded that the combustion instability was not caused by the test facility.

b. Analog Model of Preburner Test Rig

(U) Many variables that could strongly influence the combustion instability could not be readily controlled in a special test or changed in the existing hardware. An analog model was therefore constructed in which the suspected variables were investigated to show the relative influence of each variable.

(1) Model Formulation

(U) A mathematical representation of dual-orifice oxidizer, fixed fuel area preburner rig was formulated and programmed on the analog computer. The formulated system is illustrated in Figure 47. The simulation included the preburner injector, preburner oxidizer valve, combustion chamber, and a segment of the stand propellant lines feeding the injector. The propellant feed lines having a large L/D (fuel = 6[illegible], oxidizer = 70) were formulated as a distributed system. The injectors with their concentrated volumes and low L/D were represented as a lumped parameter system. The combustion chamber dynamics were represented by a gas residence time constant and an oxidizer vaporization delay.

(2) Program Verification

(U) The program was set up at idle thrust (T_{fuel} = 125°R) to attempt to match with the instability of tests 12.01 and 14.02. The input contained the oxidizer injector effective area vs flow split variation in Figure 33 and the oxidizer vaporization delays shown in Figure 48. The injector effective area characteristic was obtained from test data and the vaporization delay was derived from a relationship from NASA TN D-851 and modified as influenced by oxidizer velocity.

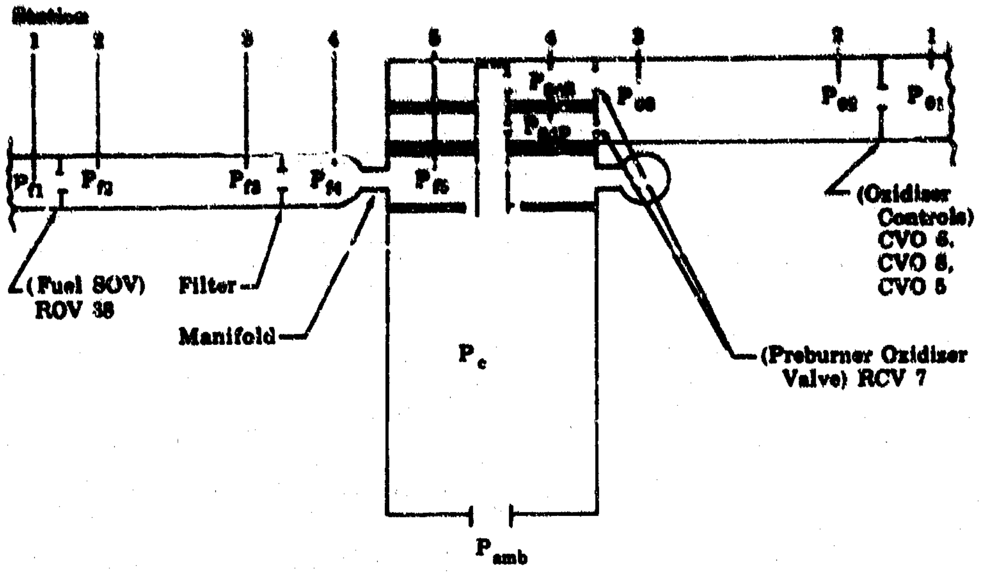

(U) Figure 47. Preburner Injector Analog Stability Model FD 25235

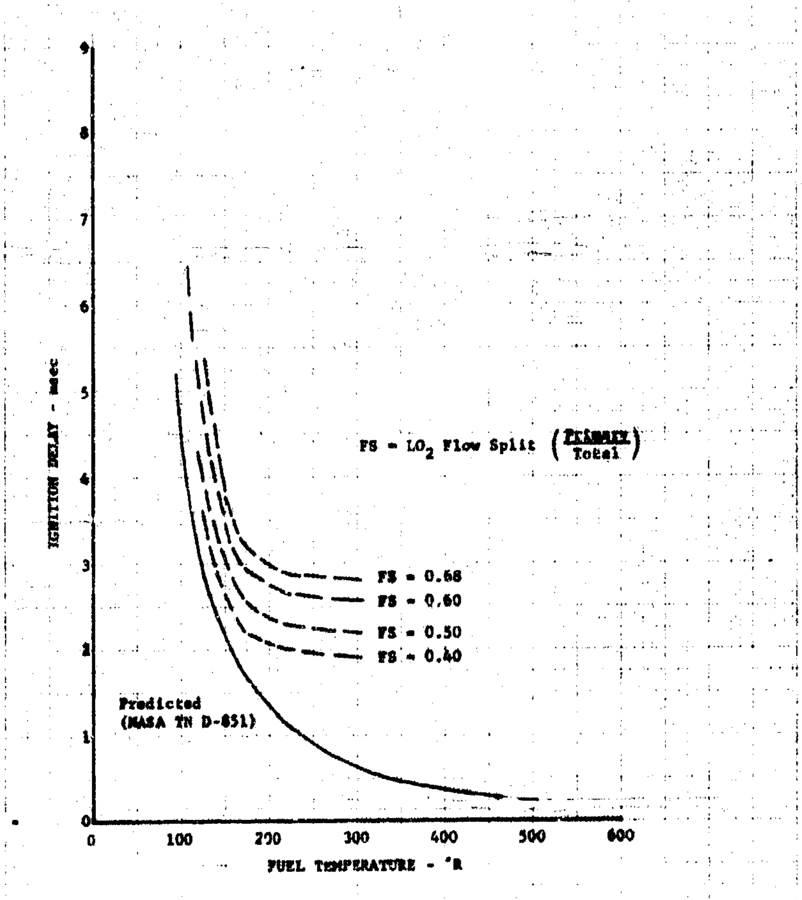

(U) Figure 48. Oxidizer Vaporization Delay DF 66779

(U) A flow split and fuel temperature excursion was run on the analog simulation with the results presented in Figures 49 and 50. The analog frequency trend as a function of flow split agreed with the test data with a slight increase with increasing flow split. No correlation of amplitude with the test data could be made: however, the analog showed an increasing then decreasing amplitude with flow split. As previously discussed, no conclusions were drawn from phase relationships. The analog results as a function of fuel temperature agreed with the test data as shown in Figure 50.

(U) Phase angles (relative to chamber pressure) differed somewhat between the test and the analog. The test data showed that the oxidizer secondary was always in phase with chamber pressure. The analog showed the oxidizer secondary was in phase at low fuel temperature (high combustion delay), but the phase angle increases with fuel temperature, reaching 100 degrees at 300°R fuel. The oxidizer primary phase angle varied from 0 to 180 degrees during test with no apparent correlation. The analog showed the oxidizer primary varied 50 to 160 degrees as fuel temperature is increased and combustion delay decreased. During test, the fuel manifold was consistently 180 degrees out of phase with chamber pressure. The analog fuel manifold had a phase lag of 60 degrees. A comparison of phase angles is presented in Table IX.

(U) The inability to obtain a closer match of phase angles could be influenced by the fact that the high response instrumentation was not flush-mounted in the injector cavities. Instrumentation passages were drilled through the injector housing, which created volumes and could affect the indicated pressure recording.

(3) Injector Cavity Volumes

(U) The primary, secondary, and fuel injector volumes were varied in the analog to determine the effects on the instability. The results show that a 20% reduction in secondary volume will stabilize the process as shown in Figure 51. Variations in the primary and fuel volumes had only minor effects on the instability.

(4) Injector Effective Areas

(U) The secondary and fuel effective areas were varied to determine the effect on instability. (See Figure 52.) A reduction in secondary area did influence the instability; however, a reasonable change in area (for cycle considerations) will not eliminate the instability. A reduction in fuel area has no significant influence on the instability, while an increase of approximately 60% causes the analog to stabilize.

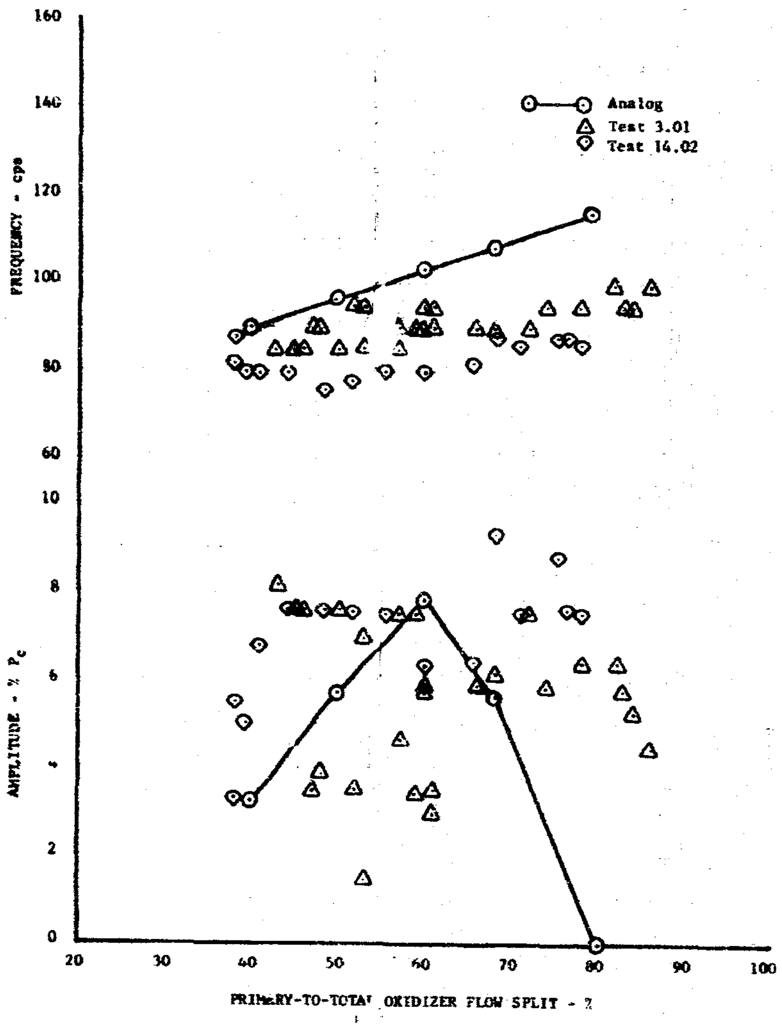

(U) Figure 49. Analog Simulation of Flow Split Variation DF 66780

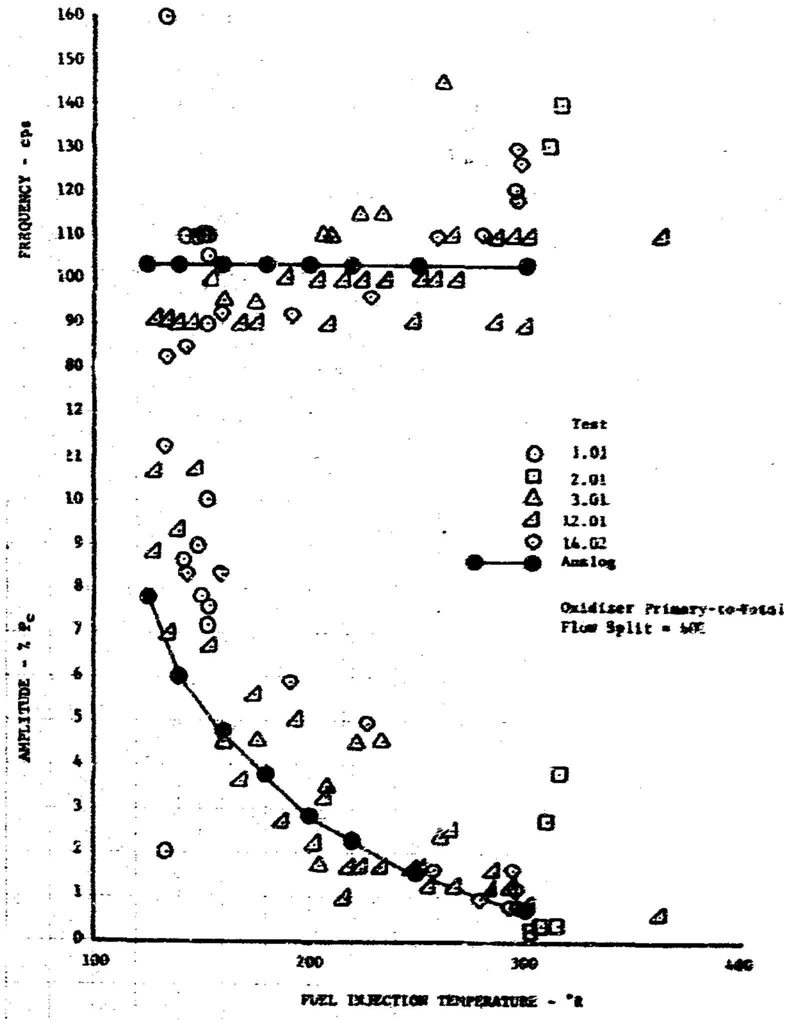

(U) Figure 50. Analog Simulation of Fuel Temperature Variation DF 66781

(U) Table X. Phase Angle Comparison

	Test	Analog
Fuel Injector (deg)	180	60
Fuel Line (deg)	0 to 180	75
Primary (deg)	0 to 180	50 to 160
Secondary (deg)	0	25 to 100
Oxidizer Line (deg)	0 to 180	70 to 180

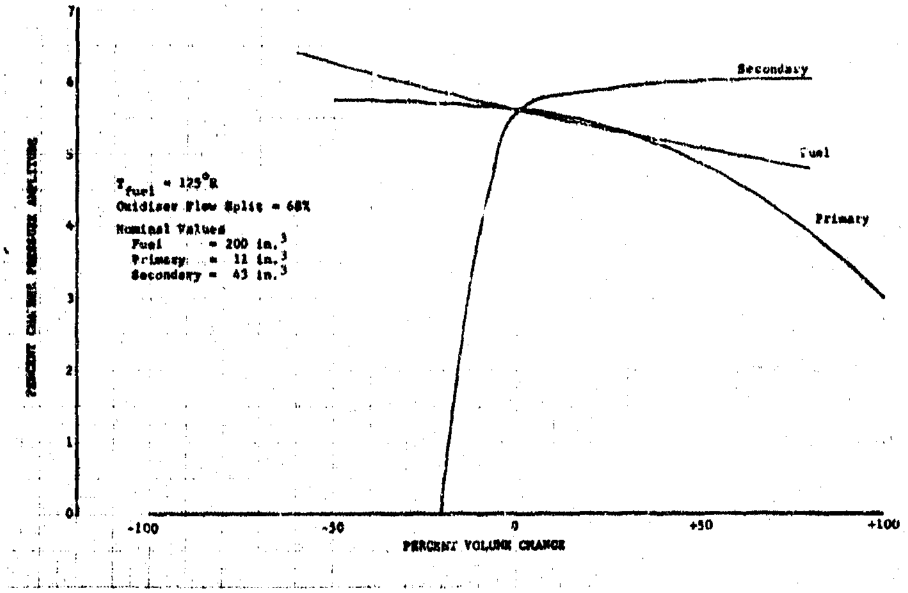

(U) Figure 51. Predicted Volume Influence on Preburner Stability DF 66766

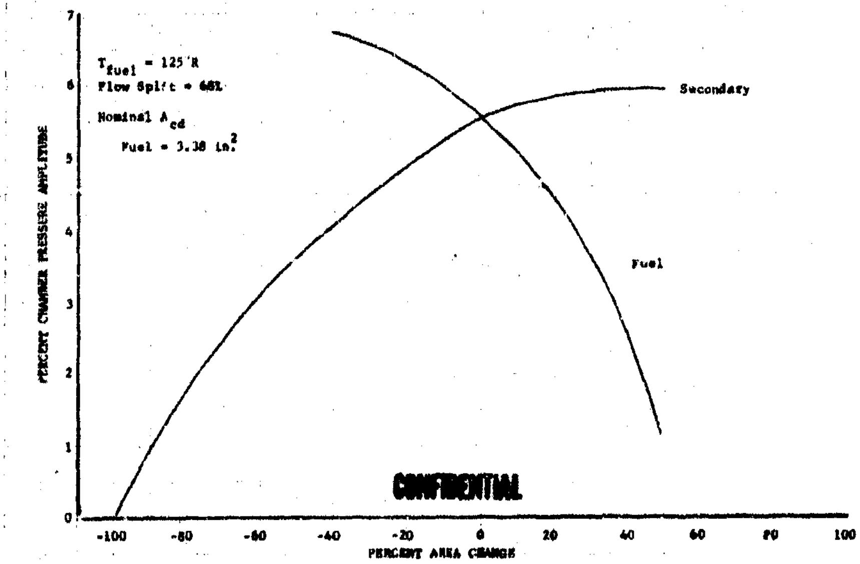

(U) Figure 52. Influence of Effective Areas on Preburner Stability DFC 66767

(5) Effect of Instability on Engine Operations

(U) A mathematical simulation of the 250K engine, which was programmed on the analog computer during Phase I (Contract AF04(611)-11401), was used to determine what effects preburner injector instability would have on engine operation. This engine simulation was developed to study control systems, therefore it contains the necessary system dynamics (turbopump acceleration, heat exchanger dynamics, etc.) that affect starting, throttling, and shutdown. The simulation is complete in that it contains all the turbopumps, heat exchangers, propellant lines, combustors, etc.

(C) The engine was trimmed at idle thrust and nominal mixture ratio. A sine wave was superimposed on preburner combustion pressure of such magnitude to produce an instability of ±70 psi (±9%) amplitude. The frequency of this sine wave was varied from 1 to 200 cps to investigate the effects on the engine. The external forcing sine wave applied to the preburner chamber pressure was used to obtain the preburner instability and was present in the system throughout the investigation. Engine feedback to the preburner reduced the instability such that the forcing function always had to be greater than the resulting instability.

(U) The results of this investigation are shown as amplitude-frequency plots of some of the major engine parameters. These plots are included as Figures 53 and 54. Frequencies of 75 to 150 cps were experienced during tests of the preburner. At this frequency level, most of the engine variables have attenuated to an amplitude of approximately 1%. The exception to this are those variables directly associated with the preburner injector flows, mixture ratio, combustion products, etc.

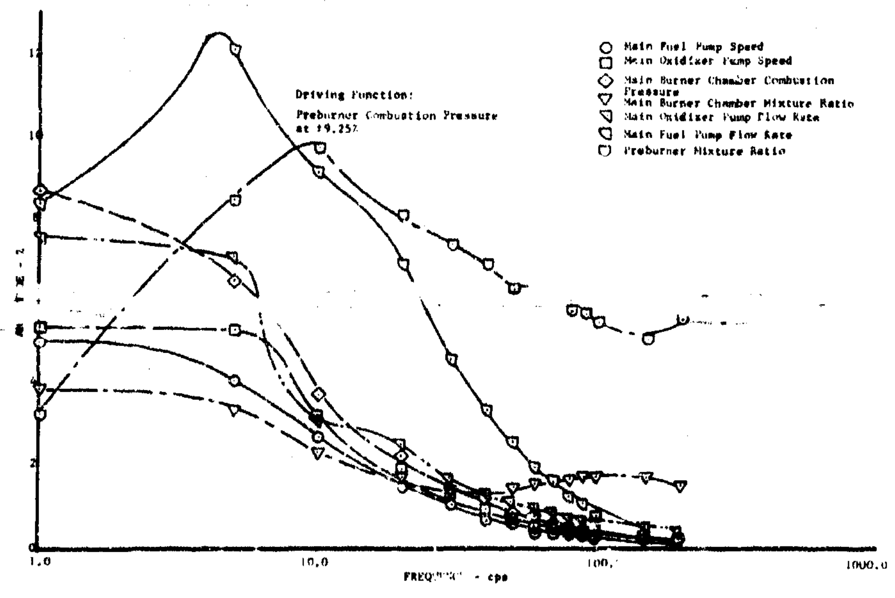

(U) Figure 53. Predicted Frequency Response DF 66718

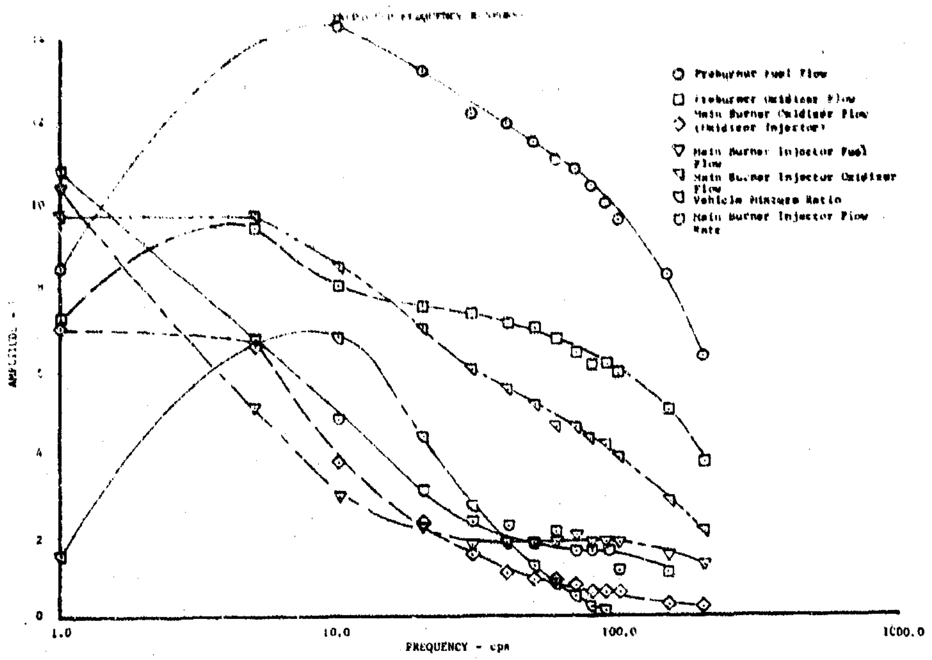

(U) Figure 54. Predicted Frequency Response DF 66719

c. Water Flow Correlation

(U) Water flow tests were conducted on the injector assembly and single element flow blocks in attempts to correlate water flow with hot firing instability through pressure fluctuations. The following paragraphs describe these tests.

(1) Injector Assembly

(U) After the preburner test series, the entire preburner injector was water flowed with high response instrumentation. High-frequency and high-amplitude oscillations existed in all fuel and oxidizer cavities. Further investigation showed that these instabilities were present in the stand system (B-21) even when the injector was removed. The injector effective area was simulated by hand valves in the stand supply lines. Water was flowed through the test stand just as had been done previously with the injector in place. Pressure oscillations with high frequencies and amplitudes were recorded. Table XI presents these data. It is concluded that no direct correlation could be made between preburner hot firing instability and preburner injector water flows.

(U) Table XI. Injector Water Flow Test Results

OXIDIZER INJECTOR ONLY

Primary Pressure Transducer			Secondary Pressure Transducer			Primary Kistler		Secondary Kistler	
Level (psi)	Amplitude (psi)	Frequency (cps)	Level (psi)	Amplitude (psi)	Frequency (cps)	Amplitude (psi)	Frequency (cps)	Amplitude (psi)	Frequency (cps)
72	3.6	50	0	-	-	19.8	150	0	-
253	9.6	135	0	-	-			0	-
430	6.0	230	0	-	-			0	-
460	4.8	270	0	-	-	17.2	830	0	-
447	6.2	200	0	-	-	21.0	630	0	-
460	6.7	240	39	0.82	135	26.0	830	8	480
420	4.8	240	38	0.60	140	29.7	730	7	500

FUEL INJECTOR ONLY

Fuel Pressure Transducer			Fuel Kistler	
Level (psi)	Amplitude (psi)	Frequency (cps)	Amplitude (psi)	Frequency (cps)
16	0	-	10	60
26	0.6	-	15	56
49	1.5	22	149	510
67	1.8	40	257	570
75	4.0	32	297	610
87	5.0	35	228	720
92	6.0	40	257	760
94	5.0	38	248	850
95	5.0	38	257	900
94	5.0	38	218	900
95	5.0	40	238	920

FEED LINE ONLY

Primary Feed Line Pressure Transducer			Secondary and Fuel Feed Line Pressure Transducer			Primary Feed Line Kistler		Secondary and Fuel Feed Line Kistler	
Level (psi)	Amplitude (psi)	Frequency (cps)	Level (psi)	Amplitude (psi)	Frequency (cps)	Amplitude (psi)	Frequency (cps)	Amplitude (psi)	Frequency (cps)
15	4.0	200	0	0	-	5.0	730	0	-
200	12.0	645	0	0	-	45.0	3300	0	-
375	17.3	670	0	0	-	40.0	3600	0	-
440	20.0	730	40	4.1	5	56.0	5100	2.5	130
440	14.6	670	210	13.3	190	65.0	5600	32.0	463
440	20.0	750	235	16.6	250	65.0	5500	48.0	445
440	14.6	730	230	12.5	230	60.0	5300	25.5	520

(2) Individual Elements

(U) Even though a direct correlation between water flow frequencies and amplitudes did not exist, the possibility remained that a shift in pressure oscillations away from a base line water flow would indicate a combustion stability shift. With this in mind, individual element water flow tests were designed to determine if the vena contracta at the secondary tangential slot could be shifting and thus causing the pressure oscillations. To change the vena contracta characteristics, the secondary slot entrances were rounded in steps as shown in Figure 55. The element was water flowed in condition 1 (Bill-of-Material) to establish a baseline frequency and amplitude of secondary cavity pressure fluctuation. The secondary cavity pressure oscillated at 150 cps and an amplitude of 3 psid. The element slot was reoperated to the shape of condition 2. Water flow revealed a secondary pressure fluctuation of 2.5 psid at 150 cps. With the slot revised as shown in condition 3 the cavity pressure was 2 psid at 150 cps. The final configuration, shown as configuration 4, gave cavity pressure oscillations of 2 psid at 150 cps.

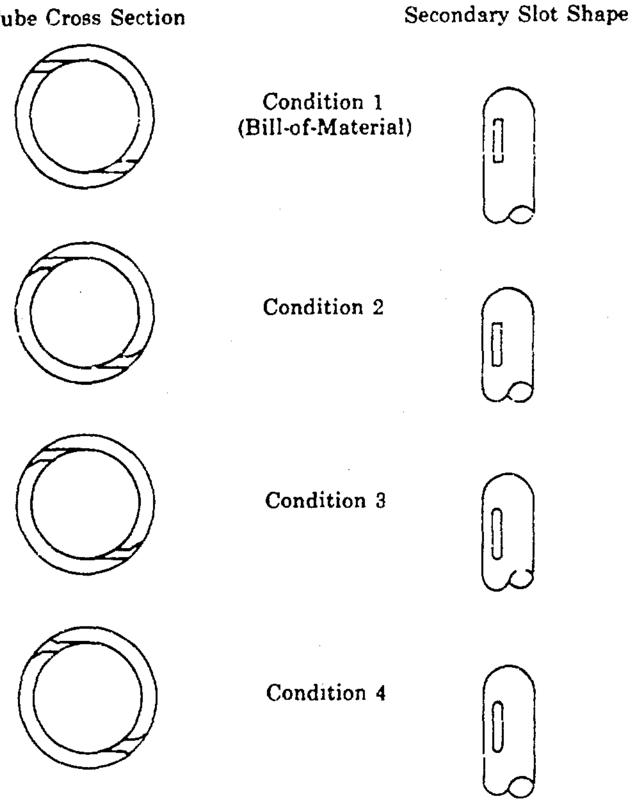

(U) Figure 55. Oxidizer Element Slot Modifications for Water Flow Testing FD 25236

(U) An individual element GN_2-water flow rig that discharged into a pressurized chamber was fabricated. The pressurized chamber allows the adjustment of the density of the GN_2 to approach that of hydrogen in the preburner. Fuel-to-oxidizer momentum ratios could be equated with GN_2-to-water momentum ratios with the GN_2 flow remaining unchoked. Flow conditions were varied to produce a range of momentum ratio from 0 to 20% and a primary-to-total flow split range from 0 to 100% about the nominal conditions. The conditions provided in Table XII were established as nominal test conditions.

(C)(U) Table XII. Nominal Test Conditions

	E-8 Combustion Tests	B-21 Flow Tests
Primary pressure drop (psid)	235.0	235.0
Secondary pressure drop (psid)	9.3	9.3
Fuel side pressure drop (psid)	83.0	83.0
Fuel temperature (°R)	147.0	540.0
Fuel flow (lb/sec/element)	14.1/252*	14.1/252*
Oxidizer flow (lb/sec/element)	9.1/252*	9.1/252*
Primary-to-total oxidizer flow split	0.59	0.59
Chamber pressure (psia)	560.0	145.0
Momentum ratio (fuel/oxidizer)	12.7	12.7

*Total injector flow/no. injector elements

(C) A base primary and secondary effective area was established by calibrating the element with no GN_2 flowing through the fuel injector. The calibration was made over a primary-to-total flow split range of 0 to 100%. This calibration is presented in Figure 56. The momentum ratio was varied by varying the primary, secondary, and fuel side pressure drops. This effect of momentum ratio on primary and secondary effective area is shown in Figure 57. The primary area change at nominal momentum ratio (12.7) is a 1.0% area change for an 8.0% momentum ratio change. For the primary alone to produce an instability in chamber pressure of 10% amplitude, it was calculated that the primary flow must change 26.5%. This results in a momentum ratio change of 19.8%. This slope is also presented in Figure 57. Comparison of these two slopes indicate that it was not possible for the momentum influence alone to have caused the observed combustion instability. The momentum ratio has the effect of increasing the primary area over the base area. This could be caused by a lowering of the static pressure at oxidizer discharge by the fuel velocity. Data from the combustion tests show that the primary injector, operating under nominal conditions, also had an area increase of approximately 15% above base calibrated area. Increasing the momentum ratio has the effect of decreasing the secondary area. At nominal momentum ratio (12.7) the secondary area is being reduced at the rate of 1% area change for 16% momentum ratio increases. For the secondary alone to produce 10% amplitude in chamber pressure, secondary flow must change 40%. This requires a momentum ratio change of 4.3%. This slope is also presented in Figure 57. Comparison of these slopes shows that it would not be possible for this interaction of the secondary alone to cause the instability.

(U) The fuel injector was calibrated with GN_2 with no flow through the oxidizer element. Momentum ratio was varied by varying primary, secondary, and fuel pressure drops. The chamber pressure was maintained as necessary to prevent the fuel pressure ratio from exceeding critical pressure ratio. The momentum was found to have no influence on fuel effective area as seen in Figure 58; therefore changes in fuel area could not cause injector instability. Upon introduction of oxidizer element flow, the fuel area reduces 5% and remains at this level throughout the momentum ratio range. This phenomenon is unexplained but is not considered to have any bearing on the instability.

(U) Dynamic pressure instrumentation was installed in the water-GN_2 flow rig (primary, secondary, fuel, and chamber) to measure any instability that might occur. This instrumentation indicated that instabilities of the frequency and amplitude observed during hot firings were not present.

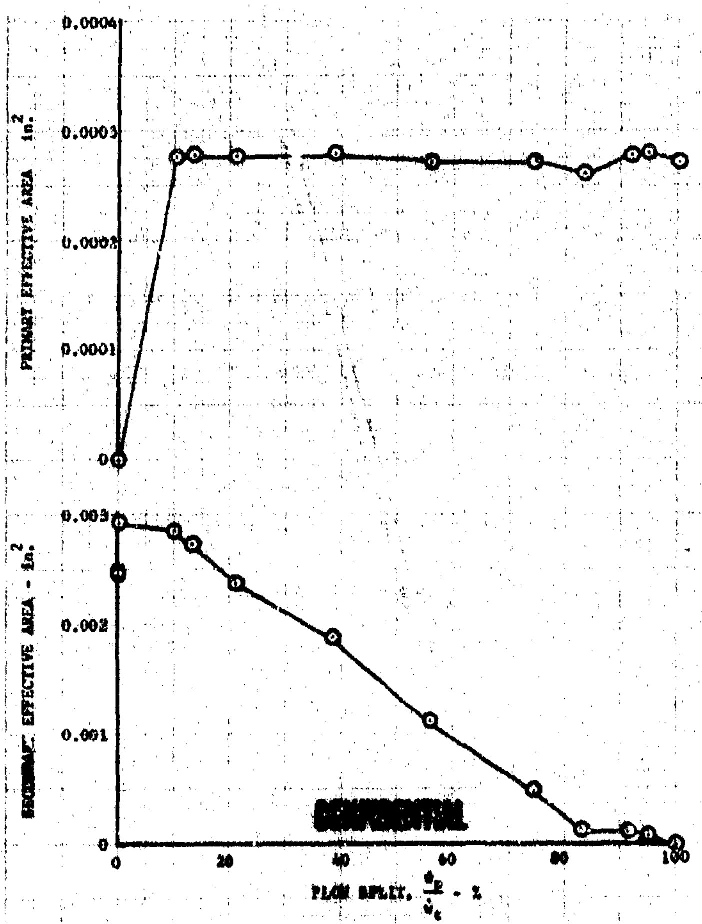

(U) Figure 56. Oxidizer Element Calibration for Injector Flow Tests

DFC 68229

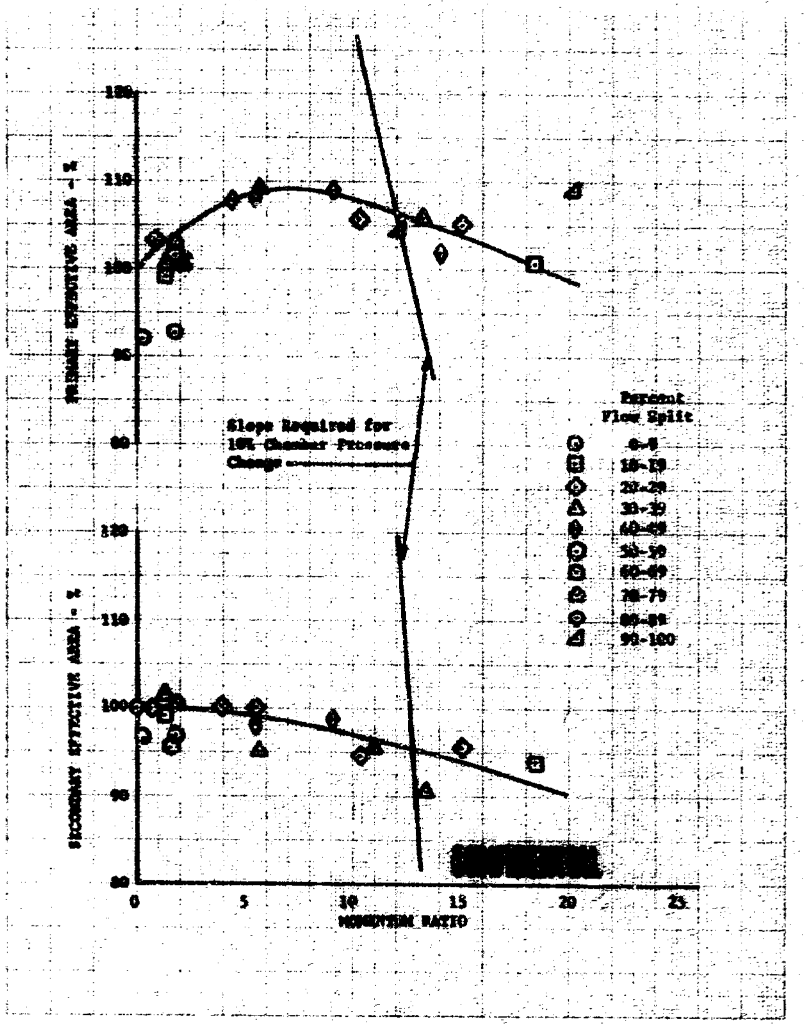

(U) Figure 57. Effect of Momentum Ratio on Primary and Secondary Effective Area DFC 68230

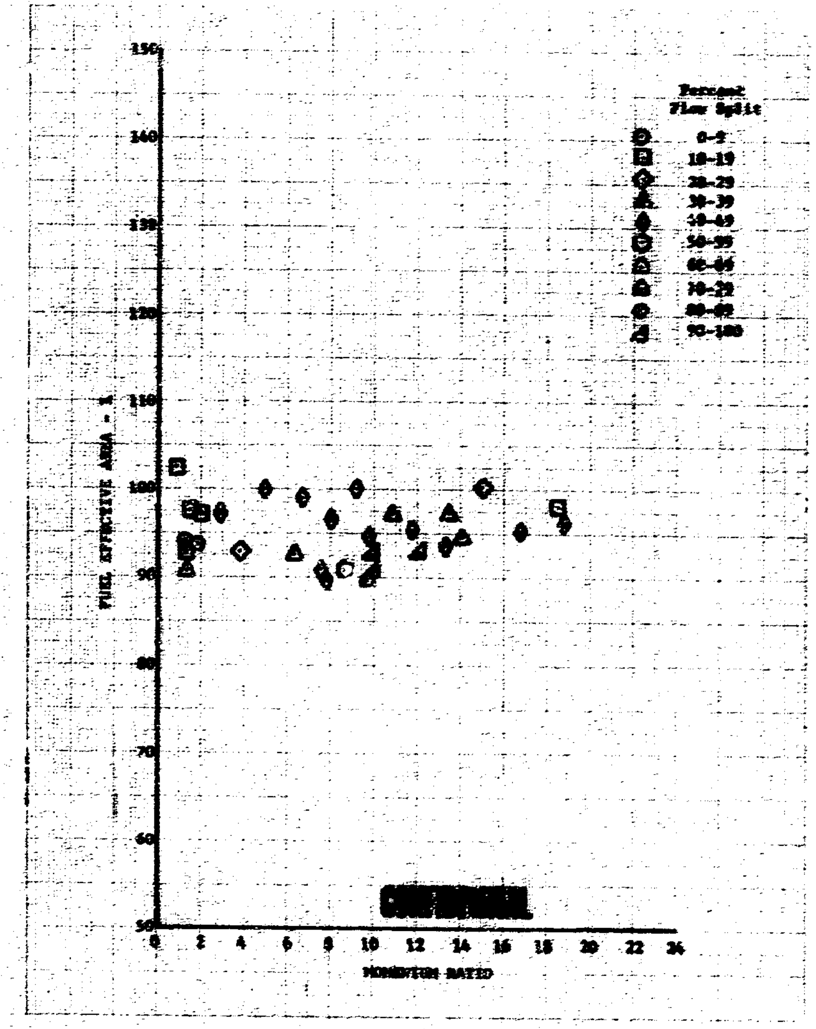

(U) Figure 58. Effect of Momentum Ratio on Fuel Effective Area DFC 68231

(C) Table XIII presents the test results of the injector area change per momentum ratio change as well as the required change to give 10% chamber pressure amplitude.

(U) Table XIII. Injector Area Change Per Momentum Ratio Change

	Test Results (%/%)	Required for 10% Chamber Pressure Change (%/%)
Primary	1.0/-8.0	26.5/-19.8
Secondary	1.0/-16.0	40.0/-4.3
Fuel	None	--

(U) The following conclusions were made from the flow test:

1. The secondary oxidizer injector effective area is affected by fuel flow but the simulated effect was not large enough to produce the observed instability.
2. The primary injector effective area is also affected by fuel flow, but the effect is not predicted to be large enough to cause the instability.
3. The fuel effective area is not significantly influenced by oxidizer flow and does not cause the instability.

B. ROLLER BEARING DURABILITY TESTS

1. Introduction. 87
2. Summary, Conclusions, and Recommendations 87
3. Analysis. 93
4. Hardware Description. 96
5. Test Results. 100

B. ROLLER BEARING DURABILITY TESTS

1. Introduction

(C) The objective of the roller bearing durability program was to evaluate 55 x 96.5 mm roller bearings for use in the 250K fuel turbopump. Testing was conducted with liquid hydrogen cooling at a shaft speed of 48,000 rpm and with a 1700-lb radial load. The radial load requirement resulted from design studies of bearing loads based on hydraulic and vehicle maneuver loading, and the pump speed was established by the engine cycle studies. Preliminary bearing tests, during Phase I (Contract AF04(611)-11401), indicated that it was feasible to operate a roller bearing at these conditions, but that roller end wear and skewing could affect bearing repeatability and durability. The current program investigated the effects of roller length-to-diameter ratio, roller crowning, internal clearance, and roller-to-side rail clearance on roller end wear and bearing durability. The ultimate objective of the program is to conduct 10 hour endurance tests on ten sets of bearings.

2. Summary, Conclusions, and Recommendations

(C) During the current program, which accumulated 58.1 hours of test time at 48,000 rpm, tests were conducted to evaluate the effects of roller length-to-diameter ratio, roller end-to-side rail clearance, internal clearance, and roller crowning on roller end wear and bearing durability. The test matrix, shown in Figure 59 graphically shows the four variables and the bearing configurations evaluated. Table XIV is a summary of the bearing tests conducted to date on this program. During all the tests, a 1700-lb radial load was applied to the load bearing resulting in an approximate 1445-lb radial load on the reaction bearing. Five bearing configurations (matrix points 3, 22, 23', 27', and 43') surpassed the 10-hour goal test duration at the design operating conditions.

(U) Because of the limited scope of the bearing program and the many variables being evaluated, conclusions were necessarily made based on a single test of a particular bearing configuration unless abnormal test conditions indicated that a repeat test on a configuration was required. This technique was used to indicate the direction on the test matrix for subsequent tests in an effort to reduce the investigation to the more promising area.

(C) Based on the roller bearing tests, it appears that both roller end wear and skewing can be minimized or eliminated by increasing the negative diametral internal clearance and increasing the side rail clearance over the normally used values. The 0.005-inch tight fit of the outer race on the rollers is the negative diametral clearance required to maintain a load on the rollers on the unloaded side of the bearing, when the bearing is operating at design conditions and fabricated from stainless steel alloy (AMS 5630). Roller skewing, which accounted for most of the bearing failures during the current program, was not found to be related to roller end wear or roller end-to-side rail clearance if sufficient negative internal clearance was incorporated in the bearing.

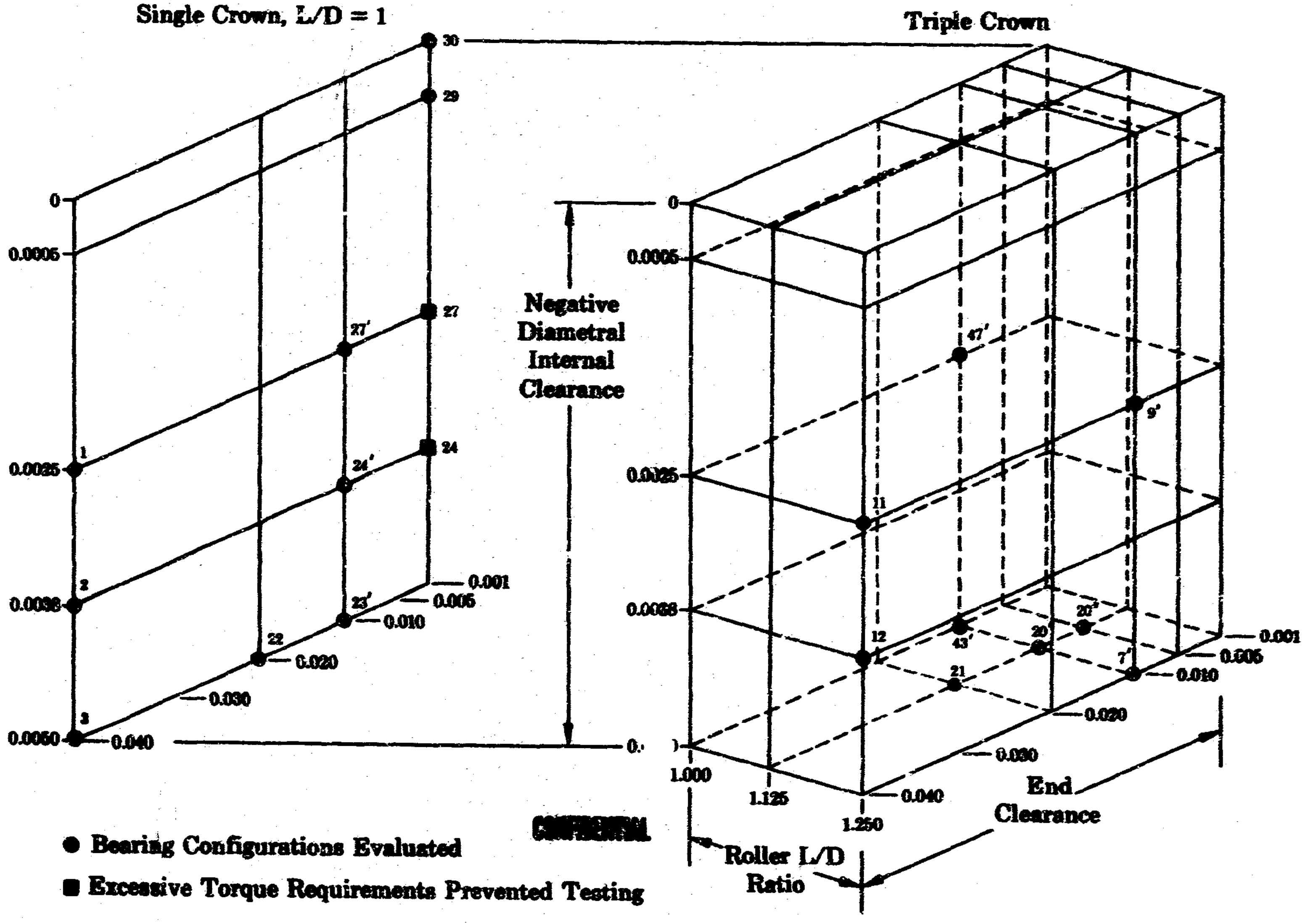

(U) Figure 59. Roller Bearing Test Matrix

FDC 24391D

(C)(U) Table XIV. Summary of Roller Bearing Tests

Build No.	Date of Testing(1)	Identification		Internal Clearance	Configuration		Roller Crown	Accumulated Time At Speed (hr/cycles)	Total Accumulated Time (hr/cycles)	Radial Load (lb)	Cooling Flow (gpm)	Roller End Wear (in.)		Remarks
		S/N	Matrix Point		End Clearance	L/D						Total Average	Maximum	
17	15-3-68	V-1	1	-0.0027	0.0395	1.000	Single	1.1/2	2.0/3	1445	30	None-Scuffing On Turbine End	-	Bearing condition excellent. Rig rebuilt because of moisture.
	18-3-68	V-2	2	-0.0038	0.0402	1.000	Single	1.1/2	2.0/3	1700	30	None-Scuffing On Rear End	-	
18	26-3-68	V-1	1	-0.0027	0.0395	1.000	Single	1.2/3	2.4/4	1445	28	Same as Build 17	-	Bearing condition excellent. Rig rebuilt because of failed slave bearing.
		V-2	2	-0.0035	0.0402	1.000	Single	1.2/3	2.4/4	1700	32	Same as Build 17	-	
19	10-4-68	V-1	1	-0.0027	0.0395	1.000	Single	1.2/3	2.4/5	1445	15	None-Scuffing On Both Ends	-	Testing terminated during acceleration to test speed because of unequal cooling flow through test bearings. Flow split was balanced by adjusting valve in load bearing discharge line but rig would not rotate. Rig rebuilt because of jammed rollers and to change shaft thrust loading.
		V-2	2	-0.0038	0.0402	1.000	Single	1.2/3	2.4/5	1700	48	None-Scuffing On Both Ends	-	
20	8-5-68	V-1	1	-0.0027	0.0395	1.000	Single	1.3/4	2.6/6	1170	16	None-Scuffing On Both Ends	-	Test terminated because of rising slave bearing outer race temperature and high vibration on turbine end. Rig rebuilt to increase tie bolt load by incorporating new design tie bolt.
		V-2	2	-0.0038	0.0402	1.000	Single	1.3/4	2.6/6	1375	29	None-Scuffing On Both Ends	-	
21	20-5-68	V-1	1	-0.0027	0.0395	1.000	Single	1.3/4	2.6/6	N/A	N/A	None-Scuffing On Both Ends	-	Rig would not rotate when cold after two rotations during cooldown. Locked up at ambient. Freed. Tried cooldown again without rotation, then tried again. Locked up cold and at ambient. Rebuilt with slave bearing not loaded at ambient.
		V-2	2	-0.0038	0.0402	1.000	Single	1.3/4	2.6/6	N/A	N/A	None-Scuffing On Both Ends	-	
22	27-5-68	V-1	1	-0.0027	0.0395	1.000	Single	2.2/7	4.3/11	1445	25	0.0006	0.0008	Completed three accelerations to speed. Test terminated by rising outer race temperature on reaction bearing. One roller in reaction bearing failed after 2.2 hours at design speed.
	28-5-68	V-2	2	-0.0038	0.0402	1.000	Single	2.2/7	4.3/11	1700	25	0.0009	0.0011	
23	6-6-68	W-1	30	+0.0001	0.0007	1.000	Single	2.0/4	2.8/5	1680	32	0.0064	0.0121	Completed four accelerations to rated speed. Test terminated because of rise in slave bearing outer race temperature and turbine vibration. Slave bearing, turbine, and shaft replaced and balance procedure revised to incorporate a final assembly balance of the rotor assembly on the test bearings.
	7-6-68	W-2	29	-0.0006	0.0007	1.000	Single	2.0/4	2.8/5	1740	26	0.0031	0.0062	
24	27-6-68	W-1	30	+0.0001	0.0007	1.000	Single	2.9/7	4.2/11	1445	25	0.0091	0.0143	Completed three accelerations to speed. Test was terminated by rise in load bearing outer race temperature. One roller and inner race side rails in load bearing failed after 2.9 hours at design speed.
		W-2	29	-0.0006	0.0007	1.000	Single	2.9/7	4.2/11	1700	27	0.0082	0.0123	
25A	12-7-68	X-1	27'	-0.0026	0.0090	1.000	Single	9.7/17	10.0/17	1445	30	0.0010	0.0013	Completed 17 accelerations to speed. Testing was terminated because of rapid increase in vibration level. Both races of the load bearing were broken but no rollers had skewed. Reaction bearing was in good condition.
	18-7-68	X-2	24'	-0.0037	0.0097	1.000	Single	9.7/17	10.0/17	1700	30	0.0003 (Heavy Impact Damage)	0.0017	
26	23-7-68	Y-1	11	-0.0025	0.0388	1.250	Triple	0.2/1	0.2/1	1440	15	None(2)	0.007	Testing terminated after 0.2 hours at design speed of first cycle because of increase in reaction bearing outer race temperature and vibration levels. One roller of reaction bearing was beginning to skew and was wedged in side rails. Inner race of reaction bearing was not properly seated on shaft. Load bearing in good condition.
		Y-2	12	-0.0038	0.0414	1.250	Triple	0.2/1	0.2/1	1700	15	None	N/A	

NOTE: Number 1 bearing is reaction bearing, Number 2 bearing is at load position.

(1) All test speeds were run at 48,000 rpm except Build No. 19, which was at 20,000 rpm.

(2) No. 15 roller had begun skewing and turbine end of roller had worn a 0.007 in. bevel at corner radius.

(C)(U) Table XIV. Summary of Roller Bearing Tests (Continued)

Build No.	Date of Testing	Identification S/N	Identification Matrix Point	Configuration Internal Clearance	Configuration End Clearance	Configuration L/D	Roller Crown	Accumulated Time At Speed (hr/cycles)	Total Accumulated Time (hr/cycles)	Radial Load (lb)	Cooling Flow (gpm)	Roller End Wear (in.) Total Average	Roller End Wear (in.) Maximum	Remarks
27	29-7-68	Y-1A Y-2	11 12	-0.0023 -0.0038	[illegible] 0.0414	1.250 1.250	Triple Triple	0.3/2 0.5/3	0.3/2 0.5/3	1440 1700	15.5 15.5	0.0004 0.0001	0.0005 0.0003	Reaction bearing incorporated new rollers and cage load bearing same as previous test. Testing was terminated early in second cycle because of rise in reaction bearing outer race temperature and erratic speed. One roller in reaction bearing had chewed and rubbed against adjacent roller. Load bearing in good condition.
28	2-8-68 6-8-68	Z-1 Z-2	47' 43'	-0.0026 -0.0051	0.0098 0.0097	1.000 1.000	Triple Triple	6.4/14 6.4/14	6.7/14 6.7/14	1440 1700	30 30	0.0039 0.0026	0.0075 0.0070	Testing terminated after 1 minute at design speed of cycle 14 because of increase in reaction bearing outer race temperature and vibration levels. One roller in reaction bearing had skewed. Load bearing in good condition.
29	12-8-68 14-8-68	AA-1 AA-2	9' 7'	-0.0027 -0.0049	0.0097 0.0095	1.250 1.250	Triple Triple	3.1/6 3.1/6	3.2/6 3.2/6	1440 1700	31 31	0.0037 0.0004	0.0220 0.0010	Testing terminated after 0.1 hour at design speed of 6th cycle because of increase in reaction bearing outer race temperature and vibration levels. The rollers in reaction bearing were beginning to skew. Load bearing in good condition.
30	16-8-68 20-8-68	X-1 Z-2	27' 45'	-0.0028 -0.0049	0.0090 0.0097	1.000 1.000	Single Triple	16.0/27 12.8/24	16.5/27 13.2/24	1445 1700	31 31	0.0021 0.0032	0.0029 0.0095	Testing terminated after 6.3 hours at design speed when load bearing had accumulated 12.8 hours; reaction bearing accumulated 16 hours. Both bearings in excellent condition.
31	23-8-68 26-8-68	BB-1 BB-2	20' 20"	-0.0051 -0.0050	0.0038 0.0048	1.125 1.125	Triple Triple	1.0/1 1.0/1	1.0/1 1.0/1	1440 1700	29 29	0.0092 (3)	0.0005 (3)	Testing terminated after first cycle. Shaft locked when attempted to start second cycle and after six attempts to free shaft and start rig. Shaft locked tight. Teardown revealed the load bearing rollers were wedged between the side rails and the rollers were heavily scored on both ends. Pitting was evident on roller OD and on roller tracks on inner and outer races. Reaction bearing in good condition except for cracked outer race.
32	29-8-68 30-8-68	CC-1 CC-2	23' 22	-0.0049 -0.0052	0.0099 0.0199	1.000 1.000	Single Single	(4)2.3/6 (4)2.3/6	(4)2.4/6 (4)2.4/6	1445 1700	29 29	0.0016 0.0013	0.0021 0.0020	Testing terminated after 0.1 hour on 6th cycle because of increase in vibrations, increase in slave bearing temperature, and decay in speed. Teardown inspection showed turbine end of shaft had cracked and bent causing heavy rub of turbine on housing. Test bearings in good condition except for cracked outer race on reaction bearing.
33	10-9-68 11-9-68	DD-1 DD-2	20' 21	-0.0050 -0.0051	0.0098 0.0198	1.125 1.125	Triple Triple	1.3/5 1.3/5	1.4/5 1.4/5	1440 1700	30 30	None-Scuffing On Turbine Ends None-Scuffing On Turbine Ends	0.0002 0.0001	Testing terminated after 1 minute on 5th cycle because of a decay in coolant flows, and an increase in vibrations and slave bearing outer race temperature. Teardown inspection showed the bellows seal had failed, the slave bearing inner race was spalled, and there was light rub on the turbine and turbine lab seal. Test bearings in good condition except for cracked outer race on reaction bearing.

(3) Severe scoring on both ends of rollers prevented any meaningful end wear measurements.

(4) Conglomerate bearings. CC-1 high time roller had 1.5 hours, 3 cycles before Build 32 tests. CC-1 cage had 0.3 hour, 1 cycle. CC-1 races were unused. CC-2 rollers had 2.2 hours, 7 cycles before Build 32 tests. CC-2 cage had 0.3 hour, 1 cycle. CC-2 races were unused.

(C)(U) Table XIV. Summary of Roller Bearing Tests (Continued)

Build No.	Date of Testing	Identification		Configuration			Roller Crown	Accumulated Time At Speed (hr/cycles)	Total Accumulated Time (hr/cycles)	Radial Load (lb)	Cooling Flow (gpm)	Roller End Wear (in.)		Remarks
		S/N	Matrix Point	Internal Clearance	End Clearance	L/D						Total Average	Maximum	
34	20-9-68	EE-1	23'	(A)-0.0039	0.0105	1.000	Single	(5)2.3/6	(5)2.4/6	N/A	N/A	N/A	N/A	Test bearings identical to CC-1 and CC-2 except for new outer races which are made from steel alloy, (AMS 6260) carburized on the ID. Testing terminated during initial turbine pressurization because of failure of turbine housing. No data had been accumulated at time of failure. Turbine and turbine housing replaced on next build.
		EE-2	22	(B)-0.0042	0.0204	1.000	Single	(5)2.3/6	(5)2.4/6	N/A	N/A	N/A	N/A	
35	25-9-68	EE-1	23'	(A)-0.0039	0.0105	1.000	Single	(5)6.4/15	(5)6.8/16	1445	36	0.0017	0.0045	Testing terminated after 0.2 hour on 9th cycle because of speed shift, and increase in slave bearing temperature. Teardown inspection showed that the bellows seal had failed and the slave bearing was severely damaged. The turbine was undamaged and the labyrinth showed moderate rub. The test bearings were in good condition and were in the next build.
	26-9-68	EE-2	22	(B)-0.0042	0.0204	1.000	Single	(5)6.4/15	(5)6.8/16	1700	24	0.0027	0.0047	
36	3-10-68	EE-1	23'	(A)-0.0039	0.0105	1.000	Single	(6)14.9/31	(6)15.5/32	1445	(7)	0.0020	0.0072	Same test bearings as previous build. Testing terminated after 6.4 hours at design speed when outer races had a cumulated 12.6 hours. Both test bearings in good condition.
	8-10-68	EE-2	22	(B)-0.0042	0.0204	1.000	Single	(6)14.9/31	(6)15.5/32	1700	(7)	0.0044	0.0068	
37	18-10-68	FF-1	3	(C)-0.0040	0.0392	1.000	Single	3.9/3	4.3/7	1440	33	0.0011	0.0022	Test bearings similar to previous build except for wider races and cages. The test rig was modified to replace the bellows seal with a labyrinth seal. The coolant flow revised to provide a series flow system. Testing was terminated after 0.1 hour on 3rd cycle because of increase in slave bearing temperature and vibrations. The slave bearing failed and was severely damaged. The test bearings were in good condition except for some thermal cracking on both outer races outside the roller path. Both bearings were reused in the next built.
	21-10-68	FF-2	22	(D)-0.0041	0.0196	1.000	Single	3.9/3	4.3/7	1700	33	0.0002	0.0004	
38	25-10-68	FF-1	3	(C)-0.0040	0.0392	1.000	Single	6.2/4	6.7/8	1440	(8)45	0.0010	0.0021	Testing terminated after 2.3 hours of 1st cycle because of increase in reaction and slave bearing outer race temperatures. The slave bearing cage was beginning to fail. The test bearing outer races showed some increase in thermal cracks but were reused in next build.
		FF-2	22	(D)-0.0041	0.0196	1.000	Single	6.2/4	6.7/8	1700	(8)45	0.0003	0.0005	
39	30-10-68	FF-1	3	(C)-0.0040	0.0392	1.000	Single	9.9/6	10.6/12	1440	33	0.0011	0.0019	Test rig modified to provide slave bearing inner race cooling. Testing terminated after 2 hours of the 2nd cycle because of increase in vibrations and load bearing outer race temperature and speed shift. The load bearing outer race cracked directly under the point of radial loading. The reaction bearing was in good condition except for increased thermal cracking on outer race. Slave bearing and turbine end of rig in good condition.
	31-10-68	FF-2	22	(D)-0.0041	0.0196	1.000	Single	9.9/6	10.6/12	1700	33	0.0003	0.0004	

(5) Conglomerate bearings from Build 32. EE-1 high time roller had 3.8 hours, 9 cycles after Build 32 tests. EE-1 cage had 2.5 hours. 7 cycles. EE-1 and EE-2 inner race have 2.3 hours, 6 cycles. EE-1 and EE-2 outer races are new parts of steel alloy (AMS 6260). EE-2 rollers had 4.5 hours, 13 cycles after Build 32 tests. EE-2 cage had 2.5 hours, 7 cycles.

(6) Conglomerate bearings from Build 35. EE-1 high time rollers had 16.4 hours, 34 cycles after Build 36 tests. EE-1 and EE-2 inner races had 14.9 hours, 31 cycles. EE-1 and EE-2 outer races had 12.6 hours, 25 cycles. EE-2 rollers had 17.0 hours, 38 cycles. EE-1 and EE-2 cages had 15.1 hours, 32 cycles.

(7) Load bearing load ring coolant seal failed causing coolant leak around load bearing negating flow split determination. Total test bearing coolant supply flow was 60 gpm and bearing outer race temperatures were normal.

(8) Higher than normal cooling flow was used to maintain slave ball bearing outer race temperature within operating limits.

(A) Equivalent to -0.0049 fit of stainless steel (AMS 5630) outer race
(B) Equivalent to -0.0052 fit of stainless steel (AMS 5630) outer race
(C) Equivalent to -0.0050 fit of stainless steel (AMS 5630) outer race
(D) Equivalent to -0.0051 fit of stainless steel (AMS 5630) outer race

(C)(U) Table XIV. Summary of Roller Bearing Tests (Continued)

Build No.	Date of Testing	Identification S/N	Identification Matrix Point	Internal Clearance	Configuration End Clearance	Configuration L/D	Roller Crown	Accumulated Time At Speed (hr/cycles)	Total Accumulated Time (hr/cycles)	Radial Load (lb)	Cooling Flow (gpm)	Roller End Wear (in.) Total Average	Roller End Wear (in.) Maximum	Remarks
40	6-11-68	GG-1	3	(A)-0.0028	0.0411	1.000	Single	1.6/1	1.6/1	1440	36	0.0001	0.0005	Test bearings incorporated Inconel 718 (AMS 5663) outer races. Testing terminated after 1.5 hours of the 1st cycle because of increase in load bearing outer race temperature and vibrations. Teardown revealed that the load bearing outer race had failed and the rollers and inner race were heavily damaged. The reaction bearing was in good condition except for material spalling in the roller track of the outer race.
		GG-2	3	(B)-0.0031	0.0386	1.000	Single	1.6/1	1.6/1	1700	36	(*)	(*)	
41	18-11-68	HH-1	3	(C)-0.0036	0.0391	1.000	Single	10.0/6	10.0/6	1440	31	0.0082	0.0120	Test bearings incorporated steel alloy (AMS 6265) outer races. Testing terminated after 1 minute of the 6th cycle when a speed shift was detected and the reaction bearing outer race temperature increased. Teardown revealed a skewed roller in the reaction bearing. Slight inner race side rail chipping and moderate thermal cracks in the outer race were noted. The load bearing was in good condition and can be reused.
	19-11-68	HH-2	3	(D)-0.0040	0.0393	1.000	Single	10.0/6	10.0/6	1700	31	0.0021	0.0048	
42	2-12-68 5-12-68	JJ-1	22	(E)-0.0044	0.0202	1.000	Single	15.3/305	15.4/305	1440	31	0.0070	0.0098	Test bearings similar to previous build except for increased fits and decreased end clearance. After completion of 125% of the goal duration a coolant reduction survey was performed. This indicated that the bearing outer race temperature was not affected when coolant flow was reduced to approximately 10 gpm. Cooling flow was returned to normal operating level and 295 additional acceleration cycles were completed to conclude the program. Teardown inspection revealed all parts in excellent condition except for surface thermal cracks on the outer races in the cage contact areas.
		JJ-2	22	(F)-0.0043	0.0202	1.000	Single	15.3/305	15.4/305	1700	31	0.0005	0.0014	

(A) Equivalent to -0.0048 fit of stainless steel (AMS 5630) outer race
(B) Equivalent to -0.0051 fit of stainless steel (AMS 5630) outer race
(*) Heavy impact damage of rollers prevented any meaningful end wear measurements
(C) Equivalent to -0.0046 fit of stainless steel (AMS 5630) outer race
(D) Equivalent to -0.0050 fit of stainless steel (AMS 5630) outer race
(E) Equivalent to -0.0054 fit of stainless steel (AMS 5630) outer race
(F) Equivalent to -0.0053 fit of stainless steel (AMS 5630) outer race

(C) The increased length-to-diameter ratio, triple crown rollers did not demonstrate the anticipated improvement in resistance to roller skewing over L/D = 1.000 single crown rollers. The longer L/D rollers demonstrated more skewing tendency than the L/D = 1.0 rollers with the same internal clearance and side rail clearance as indicated by a comparison of matrix points 1 and 11. Comparing matrix points 9', 47', and 27' as well as 7', 43', and 23' confirms this trend. (Refer to Table XIV.)

(C) The durability of a bearing configuration with a 0.005-inch negative diametral fit (matrix point 43') was initially demonstrated on Build 30. The three subsequent tests on bearings with the 0.005-inch negative diametral fit were terminated permaturely because of cracking of the reaction bearing outer race. An analysis of the cracked races indicated that the failures were the result of flexing stress cycles. The solution to the outer race cracking problem appears to be adjusting the ring design to keep the inside diameter in compression or to use a material with more elongation and fracture toughness than the stainless steel (AMS 5630). An outer race design fabricated from steel alloy (AMS 6260 with the inner diameter carburized and hardened has demonstrated 12.6 hours on two bearings without failure, and 9.9 hours on two other bearings before the outer race of the load bearing failed. The most promising bearing configuration tested used stainless steel (AMS 5630) inner race and rollers; an outer race guided Armalon cage; a steel alloy (AMS 6265) outer race, single crown, L/D = 1.0 rollers with 0.020 inch roller end-to-inner race side rail clearance and 0.0043 inch negative diametral internal clearance. It is recommended that bearings of this configuration be used in the fuel turbopump.

3. Analysis

(C) Based upon experience gained during the fuel pump technology program under Contract NAS8-11714, a roller bearing configuration was selected for the 250K fuel turbopump. The spring rate and capacity requirements of the pump design necessitated a roller bearing to provide high radial stiffness to minimize instabilities associated with rotor bouncing or rocking modes. The design speed of 48,000 rpm and a shaft diameter of 55 mm selected for the fuel turbopump resulted in a bearing DN requirement of 2.64×10^6. A preliminary calculation of the radial bearing loads indicated that the maximum loading occurs on the front fuel turbopump bearing and is approximately 1700 lb. Analytical studies indicated that 55 x 96.5 mm roller bearings should have a life in excess of the 10-hour life requirement at this value of load as shown in Figure 60. The 55 x 96.5 mm bearing is the same as bearing B in Figure 60 except that the outer race has been thinned to 96.5 mm outside diameter.

(U) After conducting screening tests on several roller bearing and cage configurations during the Phase I (Contract AF04(611)-11401) program, the bearing configuration selected for test evaluation was a 55 x 96.5 mm bearing with races and rollers of stainless steel (AMS 5630) and a cage fabricated from Armalon. The roller bearing is an inner race flanged configuration and the cage is outer race piloted. The outer race is a thin ring design that was sized to permit an outside diameter clearance in the housing at operating conditions and is retained by a lateral load across the end faces. This feature provided a stiff spring shaft supporting arrangement. The flexible outer race permitted the incorporation of a negative internal fit on the rollers, which is desirable to permit more load sharing among the rollers, thereby reducing the roller loads and ensuring that the rollers are never completely unloaded. This negative internal clearance also provides more rotor restraint and reduces the hydraulic-mechanical vibrator interchange on the turbopump.

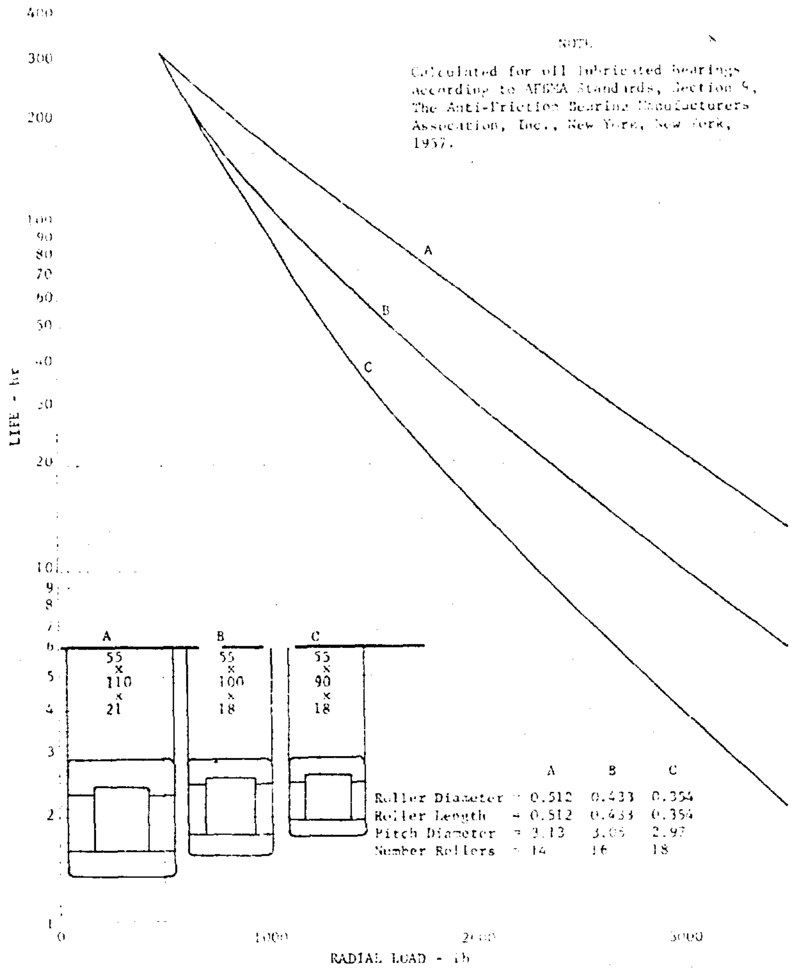

(U) Figure 60. Roller Bearing Fatigue Life vs Radial Load (50,000 rpm) DF 52756

(C) The initial testing with roller bearings operating at these high shaft speeds and radial loads indicated that roller end wear was most probably the failure mode that would prevent obtaining the goal duration. Subsequent testing showed that roller end wear could be significantly reduced if the inner race side rail-to-roller end clearance was increased from the normally used 0.001 inch to 0.040 inch; however, roller skewing resulted.

(U) It was theorized that if the outer race could be used as the guiding mechanism by using its deflection to conform to the roller crown, and if the rollers were always in contact with both the inner and outer races, that skewing could be eliminated. Because the existing bearing analysis programs were not applicable to this unique bearing configuration, a computer program was formulated to aid in the understanding of the bearing elements. A complete description of the computer program is included in the Appendix.

(C) This new computer program indicated that a radial internal fit of approximately 0.005 inch at ambient assembly conditions with stainless steel, rollers and races was required to maintain sufficient contact between the rollers and both races in the unloaded zone when the 1700-lb radial load was applied. This ambient assembly fit is adjusted when other race materials are used to provide an equivalent operating condition. Testing with this internal fit has eliminated roller skewing, and roller end wear values of approximately 0.001 inch have been obtained after 10 hours of testing. This tight internal fit has caused failure of some outer races and it is believed that these failures can be eliminated by using a material with improved fracture toughness and elongation such as carburized steel alloy (AMS 6260 or AMS 6265) or an outer race that is maintained with a compressive surface by shrinking a ring over the outside diameter of the hardened roller track material. The first of these approaches was investigated, and six bearings surpassed the goal duration with excellent results. Two others completed 9.9 hours before one outer race failed in the area of thermal checks caused by the cage contact.

(U) The effect of surface hardness on calculated radial roller bearing life is based on the following equation:

$$L = \left(\frac{C'}{Fe}\right)^{10/3}$$

when hardness is less than 58

$$C' = C\left(\frac{Rc}{58}\right)^{3.6}$$

when hardness is over 58

$$C' = C$$

where:

Rc = Rockwell Hardness
C = Basic Dynamic Capacity
Fe = Equivalent Radial Load
L = Revolutions x 10^6

This equation is from T.A. Harris, Rolling Bearing Analysis, John Wiley & Sons, 1966, and indicates that as the bearing contact surface hardness is decreased from a Rockwell Hardness of 58 that the calculated bearing life is also decreased. Because the carburized surface hardness of the steel alloy (AMS 6260) outer races is in the Rc 59 to 61 range it is anticipated that the life of these races should be approximately the same as the stainless steel (AMS 5630) races, which have a hardness in the Rc 56 to 62 range.

4. Hardware Description

a. Bearing Test Rig

(U) The rig that was used for these tests was the same rig that was used in the tests during Phase I (Contract AF04(611)-11401) except that modifications were made to the load bearing mounting and to the drive turbine labyrinth seal areas. These modifications were made to improve the alignment of the load bearing and to improve control of the thrust load on the turbine ball bearing.

(C) As shown in Figure 61, the test rig consists of four housings that enclose a shaft driven by a radial inflow gaseous nitrogen turbine. The shaft is supported by a 35-mm ball bearing (slave bearing) at the turbine drive end and a 55-mm roller bearing (reaction bearing) at the opposite end. The test load is applied through another 55-mm test bearing (load bearing) that is located adjacent to the reaction bearing. This bearing test rig has the versatility required to test roller bearings with length-to-diameter ratios of 1.000, 1.125, and 1.250.

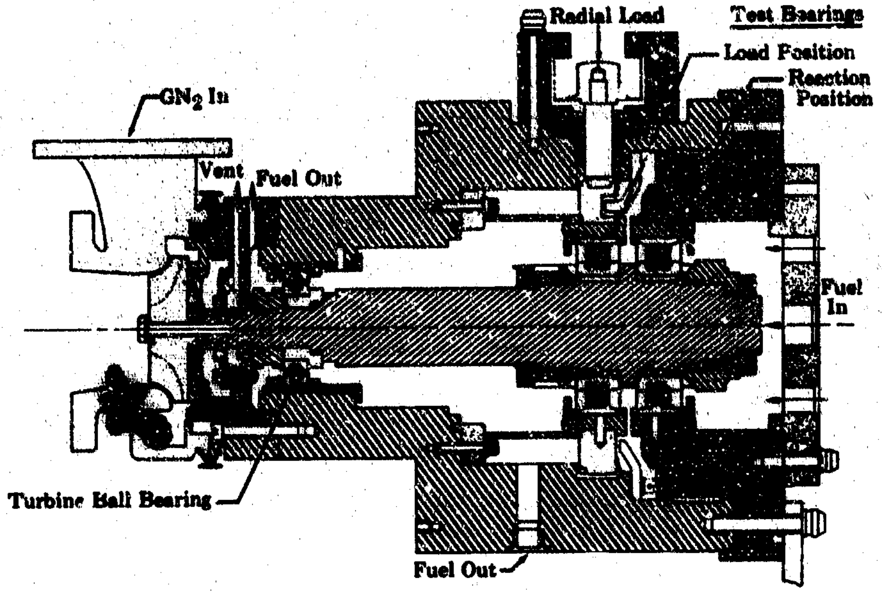

(U) Figure 61. Roller Bearing Test Rig Cutaway FD 19278H

(C) The test rig is operated at a shaft speed of 48,000 rpm with a 1700-lb radial load applied to the shaft through the load bearing. The load bearing is mounted in a flexure unit that provides axial stiffness and bearing alignment while offering radial flexibility when subjected to actuator loads. The radial load is applied by a pneumatic actuator through the load bearing. The reaction test bearing, which is just aft of the load bearing, absorbs 85% of the applied radial load and the turbine ball bearing supports the balance of the load (15%).

b. Bearing Configuration

(U) Figure 62 shows the basic bearing configuration used during these tests. A common width was used on the inner and outer races to minimize the changes required to the test rig rotor when different L/D ratio rollers were tested. The roller track width on the inner races was adjusted by grinding the side rails to establish the desired roller-to-side rail clearance with each of the different roller configurations. Some tests were conducted with inner and outer races that were 0.8268-inch wide instead of 0.935-inch wide because these races were available from the Phase I (Contract AF04(611)-11401) program. These narrow races were used on the following bearings: S/N V-1, V-2, W-1, W-2, X-1, X-2, CC-1, CC-2, EE-1, and EE-2.

(C) Four types of stainless steel (AMS 5630) rollers were used in the bearing program. Single crown rollers with a length-to-diameter ratio of 1.000, and triple crown roller with length-to-diameter ratio of 1.000, 1.125, and 1.250 have been tested. These roller configurations are shown in Figure 63.

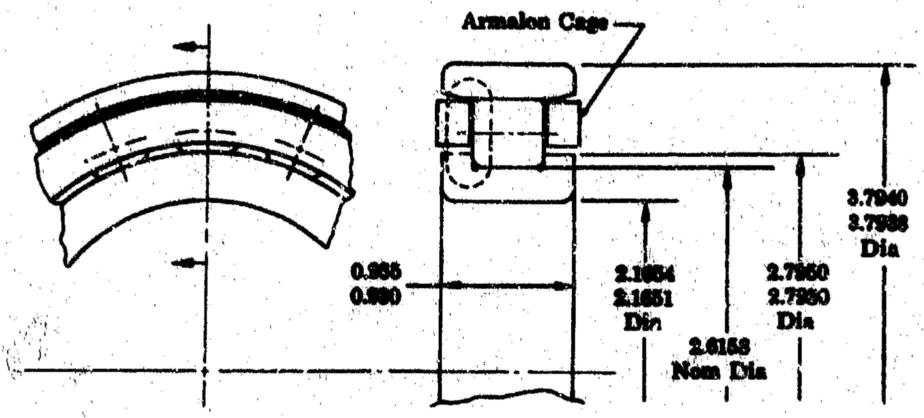

RBEC-5 Grade

(U) Figure 62. 250K Roller Bearing Configuration FD 25522

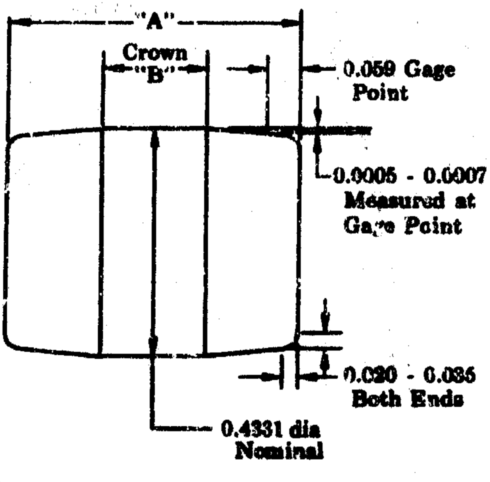

Single Crown	"A" (Nominal)	"B"
L/D = 1.000	0.4331	0.217-0.260
Triple Crown		
L/D = 1.000	0.4331	0.130-0.180
L/D = 1.125	0.4872	0.146-0.202
L/D = 1.250	0.5414	0.162-0.224

RBEC-5 Grade

(U) Figure 63. Roller Configurations FD 25523A

(C) Roller length-to-diameter ratio, the roller end-to-side rail clearance, the amount of negative diametral internal clearance, and the amount of roller crowning were the variables to be evaluated during the current program testing before the final bearing design could be selected. The negative diametral clearance of 0.005 inch was found to minimize the roller end wear and to effectively control roller skewing. By maintaining a load on all of the rollers, the beam structure of the outer race deformed around the elements providing roller alignment and skewing restraint. However, the negative diametral fit did adversely affect the outer race durability because of the sensitivity of this hard material to particle ingestion and irregularities in the microstructure. Substitute outer race material of steel alloy (AMS 6260 and AMS 6265) was selected. The inside diameter of the outer race was carburized to a depth of approximately 0.043 inch and hardened to a value of Rc 60. The core of the outer race was maintained at a hardness value of Rc 40. This outer race configuration was selected because it could be carburized and hardened, which offered a hard-wear resistant roller track, and it put the inside diameter in compression to minimize the effects of bearing loads. The notch sensitivity and impact resistance of the outer race was improved significantly with this material.

c. Test Facility

(U) Testing of the roller bearing test rig is being conducted on the B-13 test stand shown schematically in Figure 64. Gaseous nitrogen is supplied for rig purging, for turbine drive, and for actuating the pneumatic load piston. Gaseous hydrogen is used as the final prerun rig purge and liquid hydrogen is used as the bearing coolant. Test parameters such as bearing outer race temperature, speed, vibration levels, coolant flow rate, coolant supply and discharge conditions, and load are monitored and recorded.

d. Test Procedures

(U) The general test procedures that were used on this test program were as follows:

1. The test rig was purged and temperature conditioned to a liquid hydrogen environment.
2. The radial load was applied in increments as the rig was accelerated to 48,000 rpm.
3. The abort parameters of vibrations and outer race temperatures are monitored to ensure that vibration levels remained below 15g and to detect sudden rises in bearing outer race temperature, either of which could indicate a bearing failure.

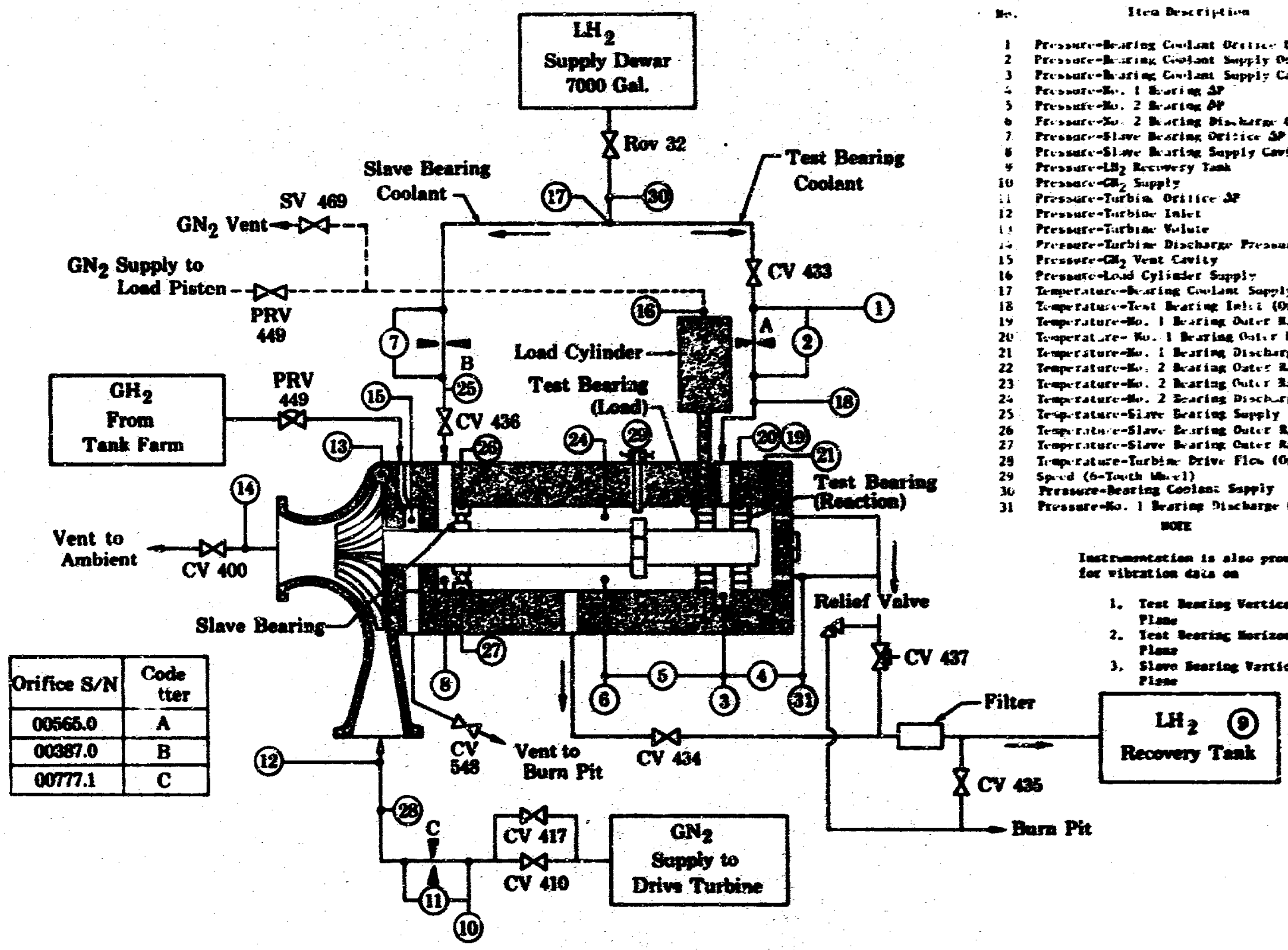

Orifice S/N	Code tter
00565.0	A
00387.0	B
00777.1	C

No.	Item Description
1	Pressure-Bearing Coolant Orifice Upstream
2	Pressure-Bearing Coolant Supply Orifice ΔP
3	Pressure-Bearing Coolant Supply Cavity
4	Pressure-No. 1 Bearing ΔP
5	Pressure-No. 2 Bearing ΔP
6	Pressure-No. 2 Bearing Discharge Cavity
7	Pressure-Slave Bearing Orifice ΔP
8	Pressure-Slave Bearing Supply Cavity
9	Pressure-LH$_2$ Recovery Tank
10	Pressure-GN$_2$ Supply
11	Pressure-Turbine Orifice ΔP
12	Pressure-Turbine Inlet
13	Pressure-Turbine Volute
14	Pressure-Turbine Discharge Pressure
15	Pressure-GH$_2$ Vent Cavity
16	Pressure-Load Cylinder Supply
17	Temperature-Bearing Coolant Supply
18	Temperature-Test Bearing Inlet (Orifice D/S)
19	Temperature-No. 1 Bearing Outer Race
20	Temperature- No. 1 Bearing Outer Race
21	Temperature-No. 1 Bearing Discharge Cavity
22	Temperature-No. 2 Bearing Outer Race
23	Temperature-No. 2 Bearing Outer Race
24	Temperature-No. 2 Bearing Discharge Cavity
25	Temperature-Slave Bearing Supply
26	Temperature-Slave Bearing Outer Race
27	Temperature-Slave Bearing Outer Race
28	Temperature-Turbine Drive Flow (Orifice D/S)
29	Speed (6-Tooth Wheel)
30	Pressure-Bearing Coolant Supply
31	Pressure-No. 1 Bearing Discharge Cavity

NOTE

Instrumentation is also provided for vibration data on

1. Test Bearing Vertical Plane
2. Test Bearing Horizontal Plane
3. Slave Bearing Vertical Plane

(U) Figure 64. B-13 Test Stand Schematic

FD 25315

5. Test Results

(C) During this program, tests were conducted on the roller bearing test rig to evaluate the bearing configurations listed in Table XIV. Eight test bearings surpassed the goal test duration of 10 hours at design conditions, and four other bearings completed 9.0 hours or more.

(C) The same test bearings were incorporated during Builds 17 to 21 and accumulated 1.2 hours and 4 cycles. These builds were used primarily to evolve build procedures on the modified test rig, to optimize the facility, and to develop test procedures. The initial roller bearing testing of the current program was with Build 17 of the bearing test rig. The configuration of the test bearings was the same as that used on the last Phase I (Contract AF04(611)-11401) endurance test, i.e., test matrix points 1 and 2. This configuration was selected to establish a new baseline following the rig modifications that changed the load bearing mount arrangement and the thrust load on the ball bearing. Both test bearings incorporated single crown stainless steel (AMS 5630) rollers with an L/D of 1.000 stainless steel (AMS 5630) races, 0.040-inch roller end-to-side rail clearance and outer-land-guided Armalon cages. Negative internal clearance was incorporated between the rollers and races; namely, 0.0038 inch on the load bearing and 0.0027 inch on the reaction bearing at ambient conditions.

(U) The initial test of the current roller bearing program, Build 17, began on 15 March 1968 and was terminated on 18 March 1968 when the shaft locked on the third cycle after cooldown to liquid hydrogen temperature. The teardown inspection revealed moisture contamination of the rig. The test rig was cleaned and reassembled as Build 18, and testing was initiated on 26 March 1968. The facility and rig purge procedures were modified to prevent moisture contamination between tests and during cooldown. Testing of Build 18 was terminated after 0.1 hour at design speed on the first test cycle because of high vibrations at the turbine end of the rig. The teardown inspection showed that the slave bearing had failed.

(U) The test rig was reassembled with the same test bearings used in Builds 17 and 18 and with a new slave bearing. Testing of Build 19 began on 10 April 1968. After the rig was accelerated to 20,000 rpm, to permit final flow settings prior to accelerating to design speed, it was determined that the flow split to the test bearings was unequal and the test was terminated. Before resuming, test facility modifications were made to the bearing coolant vent systems to permit better control of the coolant flow split. Attempts to resume testing were unsuccessful because of a locked shaft. The teardown inspection did not reveal any reason for this malfunction, except for the possibility that the roller ends were jammed against the inner race side rails. There was some fretting on the outside diameter of the outer race of both test bearings and some scuffing of the roller ends, but no measurable roller end wear. A series of assembly and inspection checks on the test rig was completed in an attempt to isolate the reason for this malfunction. The tests indicated that roller bearings with tight internal fits tend to track with the rollers in the center of the races if they are assembled in that position. If a thrust load is applied to the shaft, the shaft will shift axially by an amount equal to the internal clearance of the turbine slave bearing and lock up with the rollers of the reaction bearing against the side rail. When this thrust load is released, and shaft rotation is continued, the shaft returns to the original position with the rollers and races centered. If the bearings are assembled with the rollers against the side rails, there is a tendency for the rig to lock up before the rollers become aligned in the center of the races. The assembly procedure for the test rig was changed so that the rig was assembled with the rollers of both bearings aligned in the center of the races and with the turbine slave bearing in its rearward position to maintain the shaft in this aligned condition.

(U) During all tests conducted prior to this time, the turbine discharge had been throttled to provide a back pressure on the turbine and a thrust load on the shaft in a direction away from the turbine end. Because this back pressure on the turbine was maintained by manual adjustment of the test stand valves by the test operator, this procedure was not repeatable, and there were periods of operation when the shaft thrust loading was not in the desired direction or of the desired magnitude. The slave bearings from Builds 17 to 19 showed tracks on both sides of the inner race indicating a change in thrust load on the shaft. It was determined that if the rig was operated without throttling the turbine discharge, the thrust loading on the shaft would be in the direction toward the turbine as a result of the pressure from the bearing cooling flow and the shaft areas. If additional thrust in this direction was desired, it could be obtained by applying pressure in the bellows seal vent compartment.

(U) As a result of these findings, Build 20 was assembled with the rollers and races centered and the turbine slave bearing positioned with the thrust load toward the turbine. The direction of shaft thrust loading was reversed from that previously used to allow better control of the shaft thrust loading by regulating the pressure in the seal cavity. The outside diameter of the outer races of the roller bearings were silver flashed in an effort to reduce the fretting at these locations.

(U) Testing of Build 20 was initiated on 8 May 1968. The bearing rig was accelerated to design speed but was shut down after recording a set of data because there were high turbine vibrations and the turbine slave bearing outer race temperature was rising. A teardown inspection indicated fretting of the shaft spacers on the turbine end of the rig and one area of rub on the turbine labyrinth seal. The vibration data showed that the synchronous vibration (one per revolution) increased with the rig speed. The evidence indicated that the turbine tie bolt did not have sufficient stretch to keep the stackup tight at operational conditions. The turbine tie bolt torque was within the blueprint limits on teardown; therefore, it appears that thermal and/or centrifugal effects cause the tie bolt to loosen during rig operation.

(U) On Build 21, the rig was rebuilt with the same test bearings that were used on the previous tests, a new slave bearing, and a new design turbine tie bolt. A titanium (AMS 4928) stretch-type tie bolt was incorporated to replace the Inconel 718 (AMS 5663) bolt. Testing on Build 21 was attempted on 20 May 1968. During the cooldown of the rig, two rotational checks were completed successfully and free rotation was verified. After the cooldown was complete the rig would not rotate and it remained locked even when warmed to ambient temperature. The shaft was freed by rotating it backward. Another attempt was made to test the rig, but without the rotational checks during the cooldown, and the same results were experienced. A series of ambient tests was then made that revealed that if the shaft was in the rearward position on shutdown that the turbine did not have sufficient breakaway torque to start the rig. If the shaft was in the forward or normal operating position on shutdown, the rig would start up easily with the turbine drive. The rig was returned to assembly for a teardown inspection, which revealed no change from the previous build.

(C) On Build 22, the rig was reassembled with the test bearings centered and the slave bearing 0.007 inch from the front loaded position to compensate for the thermal differences between the shaft and housings when the rig was cooled down for operation. Thus, both the slave bearing and the test bearings would be in their normal operating position after rig cooldown. Testing of Build 22 was initiated on 27 May 1968 and terminated on the third test cycle to design speed when a temperature rise on the reaction bearing outer race was detected. A total of 0.9 hour test time at design speed was accumulated during Build 22 with a total of 7 cycles and 2.2 hours accumulated on the test bearings.

(U) The teardown inspection revealed one skewed roller in the reaction bearing as shown in Figure 65. All of the other rollers were in good condition, as shown in Figure 66, with an average roller end wear of 0.0004 inch and 0.0008 inch on the roller with the maximum wear. The load bearing was in good condition, as shown in Figure 67, with an average roller end wear of 0.0009 inch and 0.0011 inch on the roller with the maximum wear.

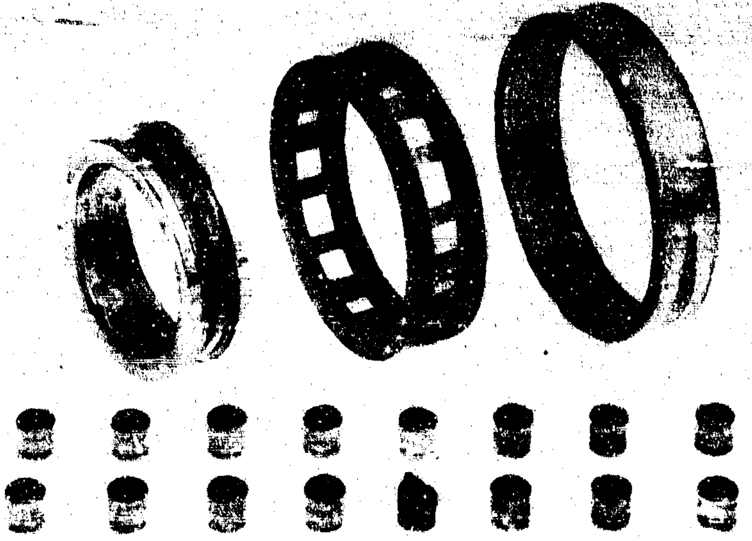

(U) Figure 65. Disassembly Condition of Reaction Bearing (S/N V-1) With Turbine End of Rollers Up (Build 22) FE 77884

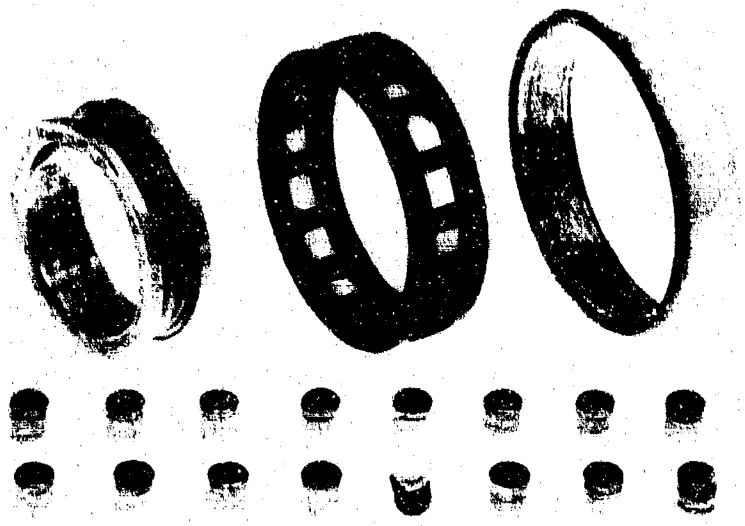

(U) Figure 66. Disassembly Condition of Reaction Bearing (S/N V-1) With Rear End of Rollers Up (Build 22) FE 77883

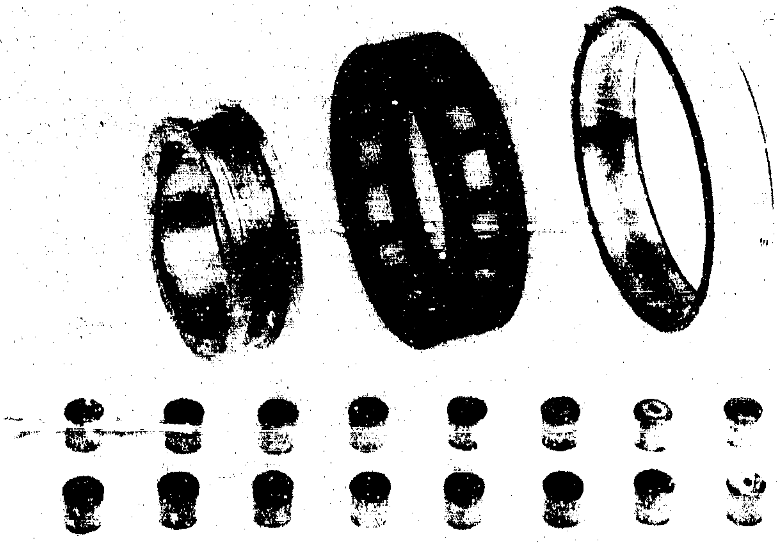

(U) Figure 67. Disassembly Condition of Load Bearing (S/N V-2) With Turbine End of Rollers Up (Build 22) FE 77891

(C) Because the reaction bearing from Build 22, which was identical in configuration to the only Phase I (Contract AF04(611)-11401) bearing to surpass the 10-hour goal duration, did not repeat the durability evaluation, the subsequent testing through Build 30 was used primarily to determine a configuration that would prevent roller skewing. This series of tests ended with Build 30 when both test bearings surpassed 12.8 hours at design operating conditions.

(C) Build 23 of the bearing test rig incorporated test bearings with stainless steel (AMS 5630) rollers and races, Armalon outer-race-guided cages, and the standard roller end-to-side rail clearance (0.0007 inch). The load bearing internal clearance was 0.0006-inch tight and the reaction bearing internal clearance was 0.0001-inch loose, (matrix points 29 and 30, respectively). Build 23 was tested on 6 and 7 June 1968 and testing was terminated after accumulating four cycles and 2.0 hours at design speed when the outer race temperature on the turbine slave bearing and the vibration level on the turbine end increased. The teardown inspection revealed that the slave bearing had failed. The roller bearings were in good condition, although there was high roller end wear. The average roller end wear was 0.0031 inch on the load bearing with 0.0062 inch on the roller with maximum end wear. The average roller end wear on the reaction bearing was 0.0064 inch with 0.0121 inch on the roller with maximum end wear.

(C) Build 24 of the roller bearing test rig included the test bearings from Build 23 and a new slave bearing. Build 24 testing was conducted on 27 June 1968 and was terminated after accumulating three cycles and 0.9 hour at design speed when the outer race temperature on the load bearing increased. The teardown inspection revealed that one roller in the load bearing had failed (skewed), as shown in Figure 68, and that the inner race side rails had heavy spalling as shown in Figure 69. Spalling was also found on four rollers, and two additional rollers showed heavy end scuffing. The average load bearing roller end wear was determined to be 0.0082 inch (not including the failed roller) with 0.0123 inch on the roller with maximum end wear. The reaction bearing had two rollers with moderate spalling and the average end wear was 0.0091 inch. The roller in the reaction bearing exhibiting the greatest end wear had 0.0143-inch wear and was one of the two rollers spalled as shown in Figure 70. The roller end wear was on the turbine end of the load bearing rollers and on the rear end of the reaction bearing rollers. The high end wear is attributed to the coolant flow pressure drop across the bearings. The accumulated total cycles and time for the bearings used during Builds 23 and 24 (matrix points 29 and 30) are 7 cycles and 2.9 hours at design speed.

(C) Build 25 of the roller bearing test rig contained stainless steel (AMS 5630) rollers and races, Armalon outer-race-guided cages, and 0.0016 inch roller end-to-side rail clearances. The load bearing internal clearance was 0.0037-inch tight and the reaction bearing internal clearance was 0.0026-inch tight (matrix points 24 and 27, respectively). During final torque checks of the rotor prior to final balancing, it was determined that excessive torque was required to rotate the shaft and the required torque exceeded the drive turbine capability. The rig was disassembled and roller drag on the inner race side rails was confirmed to have been the cause of the high drive torque requirement.

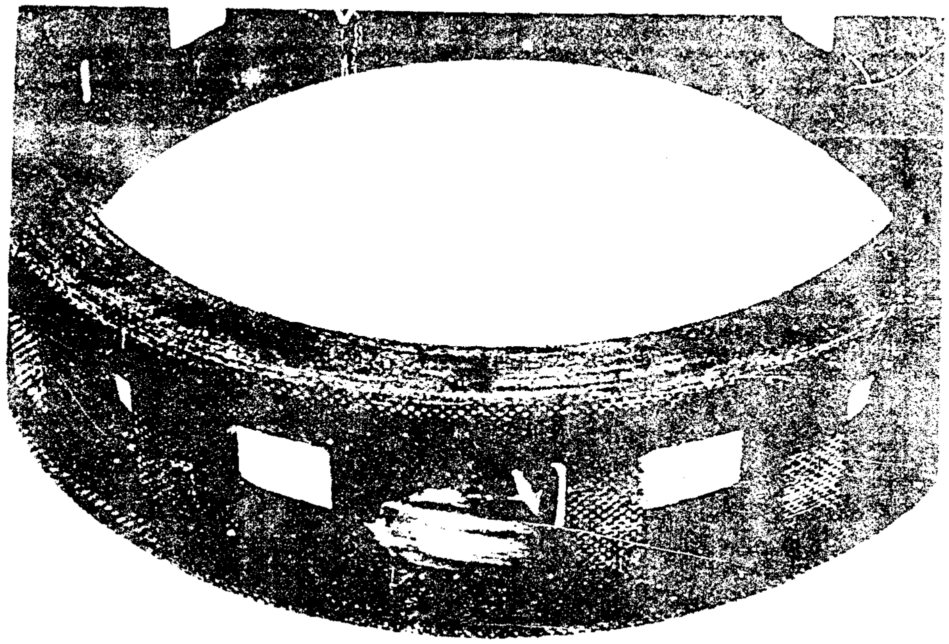

(U) Figure 68. Teardown Condition of Failed Roller (No. 4) and Cage from Load Bearing S/N W-2 FE 78430

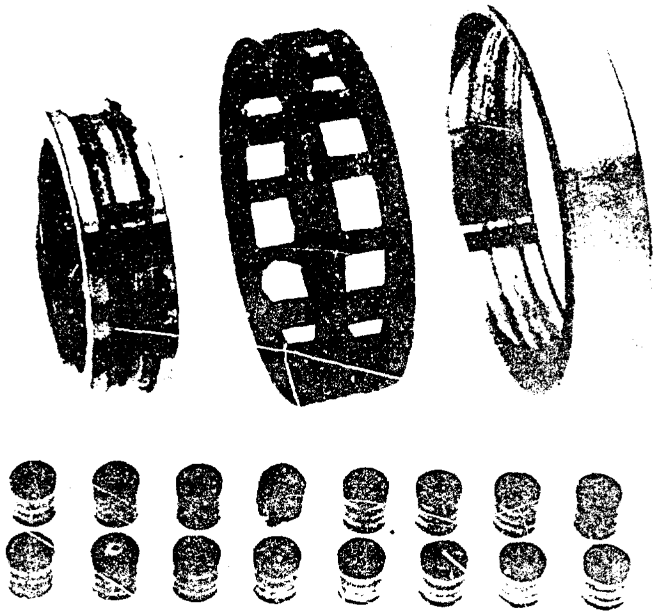

(U) Figure 69. Disassembly Condition of Load Bearing (S/N W-2) With Turbine End of Rollers Up (Build 24) FE 78433

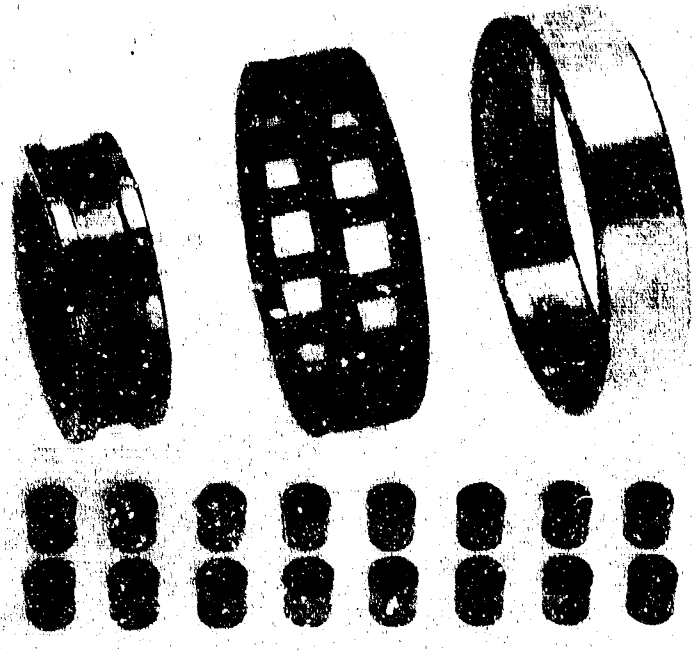

(U) Figure 70. Disassembly Condition of Reaction Bearing (S/N W-1) With Rear End of Rollers Up (Build 24) FE 78431

(C) The configuration of Build 25A was identical to Build 25, except the roller end-to-side rail clearances were increased to 0.0097 inch on the load bearing and 0.0090 inch on the reaction bearing (matrix points 24' and 27', respectively). Build 25A testing began 12 July 1968. The first test cycle of 0.8 hour duration at rated speed was successfully completed. On the next two acceleration attempts of the rig, the shaft would not rotate. The shaft was freed by rotation in the reverse direction and required a break-away torque of 80 in.-lb. After being freed, the rotating torque was determined to be 5 to 7 in.-lb in the direction of normal rotation. Testing was continued and no further torque problems were encountered during the subsequent 16 cycles. Testing was concluded on 18 July 1968, after accumulated 17 cycles and 9.7 hours. During the final test cycle, all three vibration readouts increased suddenly and the load bearing outer race temperature increased. The teardown inspection revealed that the load bearing inner and outer races had failed, as shown in Figures 71 and 72. The load bearing rollers were severely impact damaged, as shown in Figure 73, and one roller and its cage pocket exhibited some of the characteristics noted on rollers that had skewed during previous tests. Sufficient roller end surface remained on 12 of the load bearing rollers to permit end wear measurements and an average of 0.00034 inch and a maximum of 0.0017 inch were recorded on these rollers. The reaction bearing was in excellent condition, as shown in Figure 74, and was reusable. The average roller end wear of the reaction bearing was 0.00095 inch with 0.0013 inch on the roller with maximum end wear. A metallurgical analysis of the inner and outer races did not reveal any microstructure void or inclusions, nor could any evidence of fatigue failure be determined. From the appearance of the inner race side rail chipping, it appears that this damage was caused by roller impacts on the side rails. Displaced side rail material could then have been ingested through the bearing, causing the inner and outer races to crack because of the increased loading and possible stress concentration resulting from these chips.

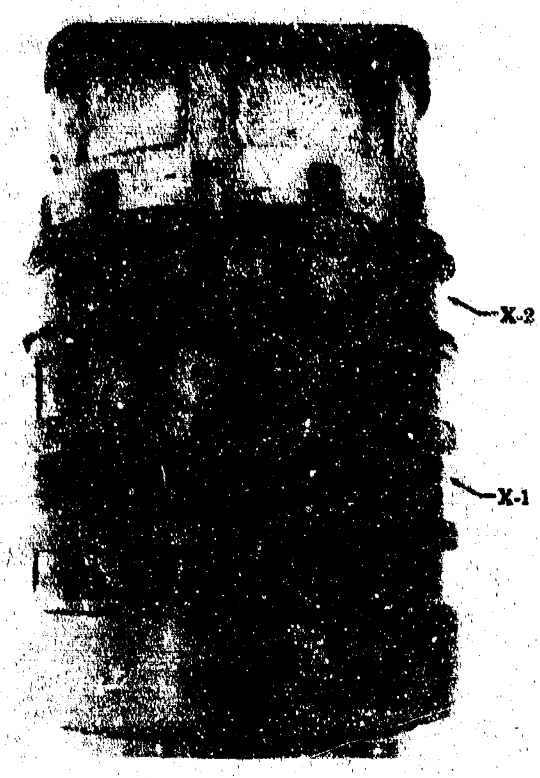

(U) Figure 71. Inner Races of Bearings S/N X-1 and X-2 Following Test of Build 25A FD 24458

(U) Figure 72. Outer Race Failure in the Unloaded Zone of Load Bearing (S/N X-2) Following Test of Build 25A

FE 78744

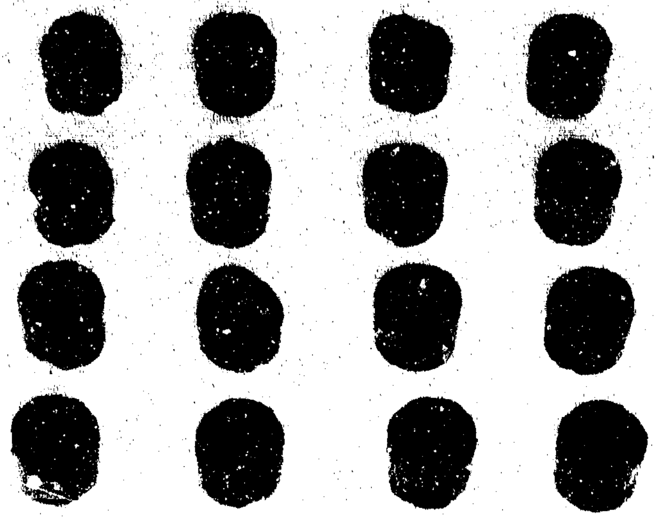

(U) Figure 73. Rollers from Load Bearing (S/N X-2) Showing Impact Damage to Turbine End of Rollers (Build 25A)

FE 78748

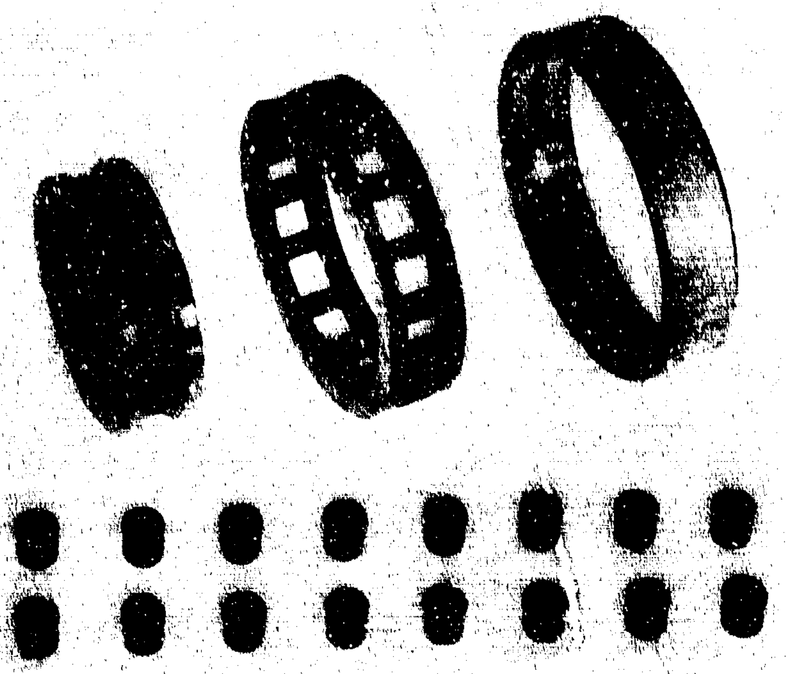

(U) Figure 74. Disassembly Condition of Reaction Bearing (S/N X-1) With Turbine End of Rollers Up (Build 25A)

FE 78782

(C) Build 26 of the roller bearing test rig incorporated the new triple-crown rollers. This build configuration also included stainless steel (AMS 5630) rollers and races, L/D of 1.250 rollers, Armalon outer-race-guided cages, and roller end-to-side rail clearances of 0.040 inch. The load bearing internal clearance was 0.0038-inch tight and the reaction bearing internal clearance was 0.0025-inch tight (matrix points 12 and 11, respectively). Testing of Build 26 was conducted on 23 July 1968. After 11 minutes operation at design speed of the first test cycle, the reaction bearing outer race temperature and the vibration readouts increased suddenly. The teardown inspection revealed that one roller in the reaction bearing had begun to skew as shown in Figure 75 and was wedging between the side rails. The probable cause of this failure was found to be the result of the reaction bearing inner race not being fully seated, resulting in approximately 0.025-inch misalignment between the inner and outer races. No measurable roller end wear was detected on either bearing except for the wedged roller, which exhibited approximately 0.0007-inch wear.

(U) The configuration of Build 27 of the roller bearing test rig was the same as Build 26, except the reaction bearing rollers and cage were replaced with new parts of the same configuration. Testing of Build 27 was completed on 29 July 1968 when, after 2 minutes operation at design speed on the second cycle, erratic speed indications and excessive reaction bearing outer race temperature were detected. The teardown inspection showed that one roller in the reaction bearing had skewed and had worn through the cage rib and was in contact with the adjacent roller as shown in Figure 76. Except for the damaged roller and cage described above, the remaining parts were in good condition. The average reaction bearing roller end wear was 0.00035 inch with 0.0005 inch on the roller with the maximum wear. The average load bearing roller end wear was 0.0001 inch with 0.0003-inch wear on the roller with the maximum wear. Figures 77 and 78 show the teardown condition of the reaction bearing and load bearing.

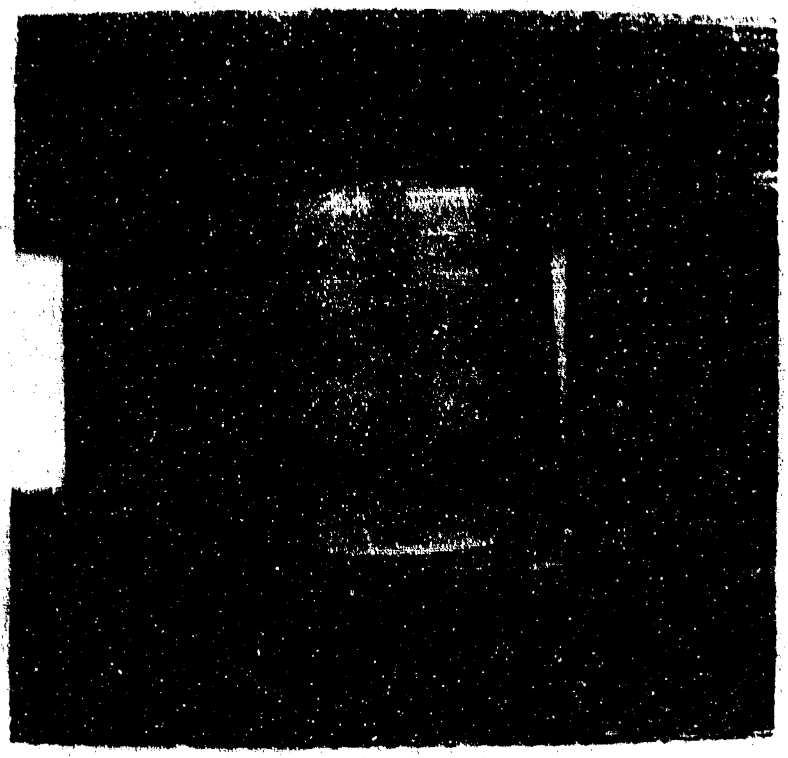

(U) Figure 75. Disassembly Condition of Reaction Bearing (S/N Y-1) Showing Skewed Position of Roller (Build 26) FE 79085

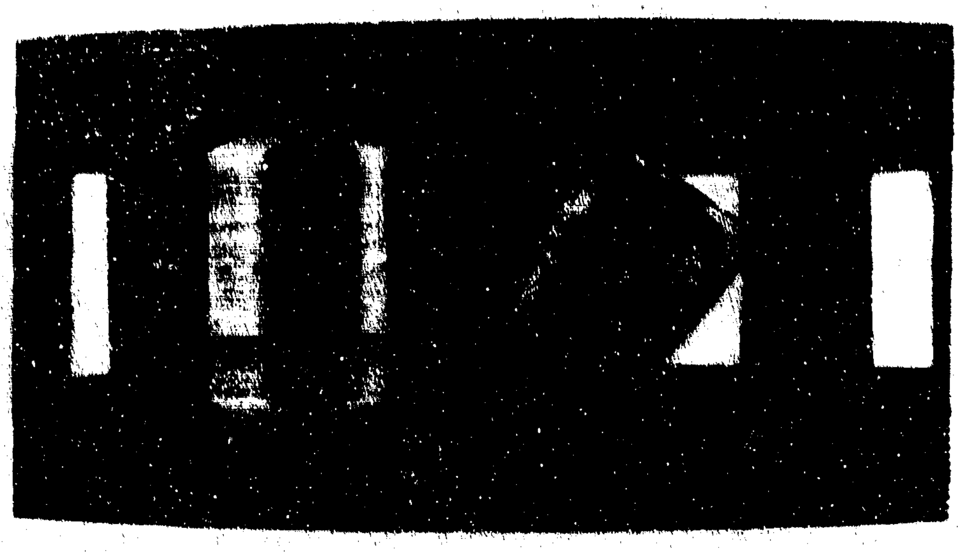

(U) Figure 76. Disassembly Condition of Reaction Bearing (S/N Y-1A) Showing Skewed Position of Roller (Build 27) FE 78915

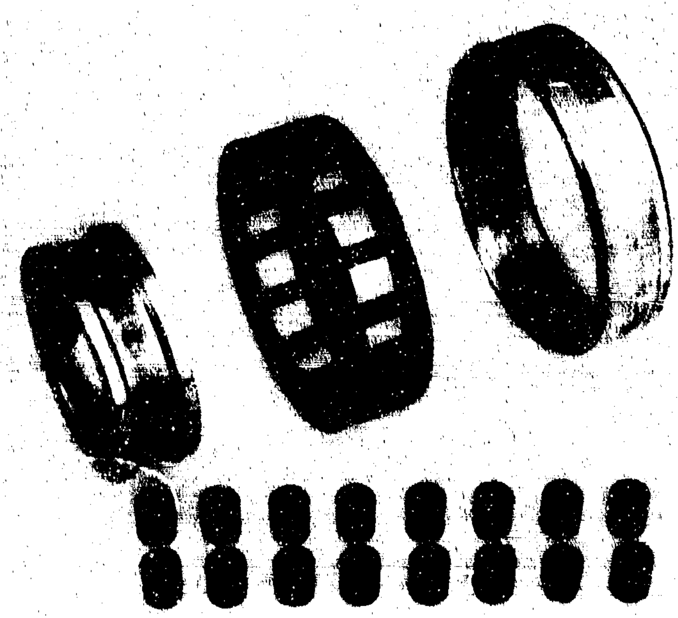

(U) Figure 77. Disassembly Condition of Reaction Bearing (S/N Y-1A) With Turbine End of Rollers Up (Build 27) FE 78959

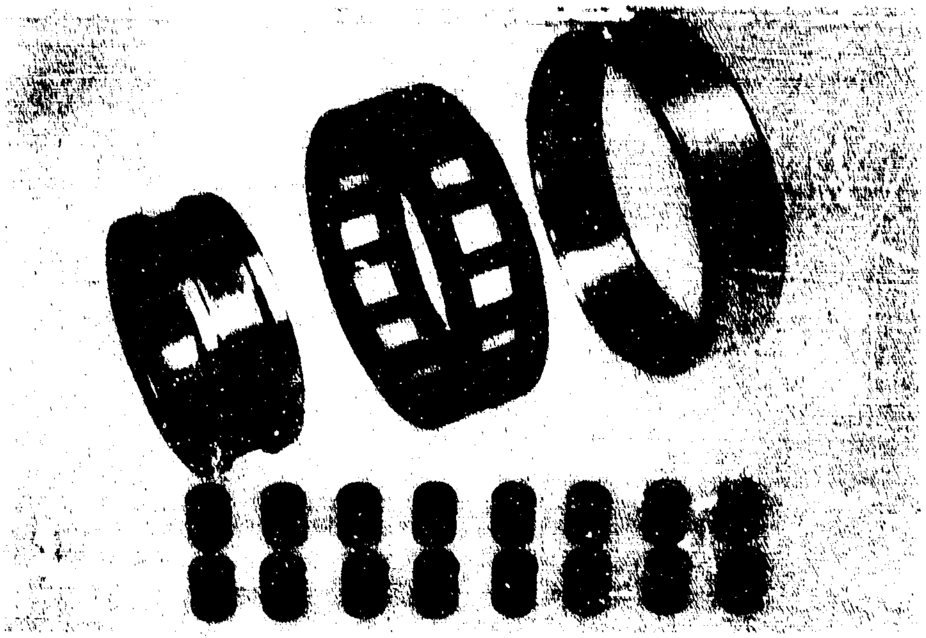

(U) Figure 78. Disassembly Condition of Load Bearing (S/N Y-2) With Turbine End of Rollers Up (Build 27) FE 78907

(C) The test bearings incorporated in Build 28 were triple-crown, L/D of 1.0 rollers, stainless steel (AMS 5630) rollers and races, Armalon outer-race-guided cages, and 0.010-inch roller end-to-side rail clearance. The load bearing internal clearance was 0.0051-inch tight and the reaction bearing internal clearance was 0.0026-inch tight (matrix points 43' and 47', respectively). Testing of Build 28 was completed on 6 August 1968. After 1 minute of design speed operation on the 14th cycle, the reaction bearing outer race temperature and the vibration levels increased suddenly, and the test was terminated. Approximately 6.5 hours had been accumulated at this time. The teardown inspection of Build 28 revealed that one roller in the reaction bearing had skewed as shown in Figure 79. Except for the skewed roller and related cage pocket damage, the remaining parts of the reaction bearing end wear was 0.00385 inch with 0.0075 inch on the roller with maximum wear. All the wear was on the turbine end of the rollers. The load bearing was in good condition and was reused in Build 30. Figure 81 shows the post-test condition of the load bearing. The average load bearing end wear was 0.00257 inch with 0.007 inch on the roller with the maximum wear. All the wear was on the turbine end of the rollers.

(U) Figure 79. Disassembly Condition of Reaction Bearing (S/N Z-1) Roller No. 5 (Build 28) FE 79271

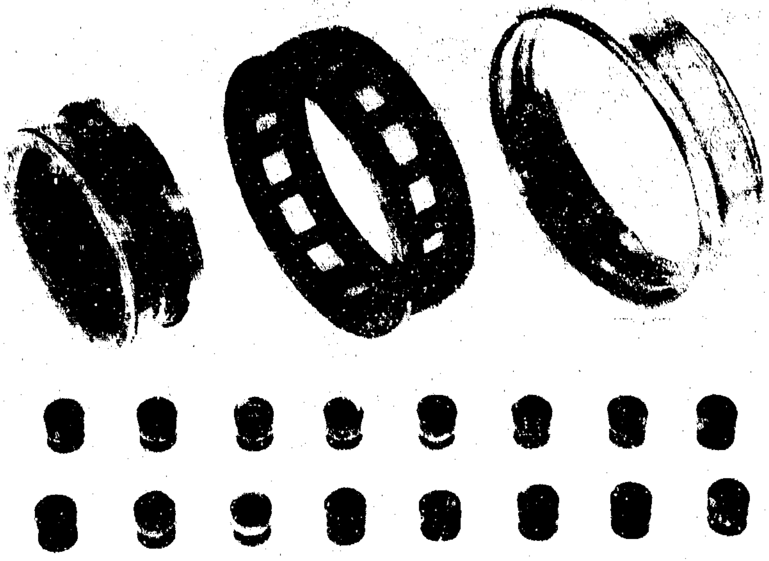

(U) Figure 80. Disassembly Condition of Reaction Bearing (S/N Z-1) With Turbine End of Rollers Up (Build 28) FE 79269

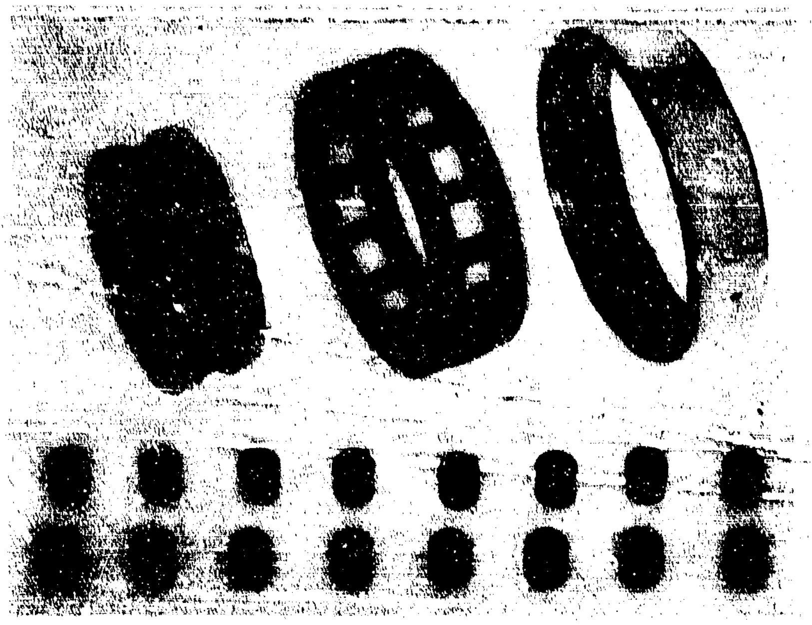

(U) Figure 81. Disassembly Condition of Load Bearing (S/N Z-2) With Turbine End of Rollers Up (Build 28) FE 79267

(C) Build 29 of the roller bearing test rig incorporated test bearings with stainless steel (AMS 5630) races and triple-crown L/D of 1.250 rollers. A roller end-to-side rail clearance of 0.010 inch was used in both bearings. The load bearing internal clearance was 0.0049-inch tight, and the reaction bearing internal clearance was 0.0027-inch tight (matrix points 7' and 9', respectively). Armalon outer-race-guided cages were used in both bearings. Testing of Buile 29 was started on 12 August 1968 and completed on 14 August 1968. Testing was terminated after 0.1 hour at design speed on the sixth cycle because of an increase in the reaction bearing outer race temperature and vibration levels. At the time that testing was suspended, approximately 3.1 hours had been accumulated. The teardown inspection of Build 29 showed that two rollers in the reaction bearing had begun to skew and had high end wear because of wedging with the inner race side rails. The primary wear on the reaction bearing was on the rear end of the rollers with an average wear of 0.0037 inch. The maximum end wear was 0.022 inch on one of the skewed rollers and the other skewed roller had 0.018-inch end wear. The post-test condition of the reaction bearing is shown in Figure 82. The load bearing was in good condition with only light wear on the turbine end of the rollers. The average load bearing roller end wear was 0.00037 inch with 0.0098 inch on the roller with maximum wear. Figure 83 shows the condition of the load bearing.

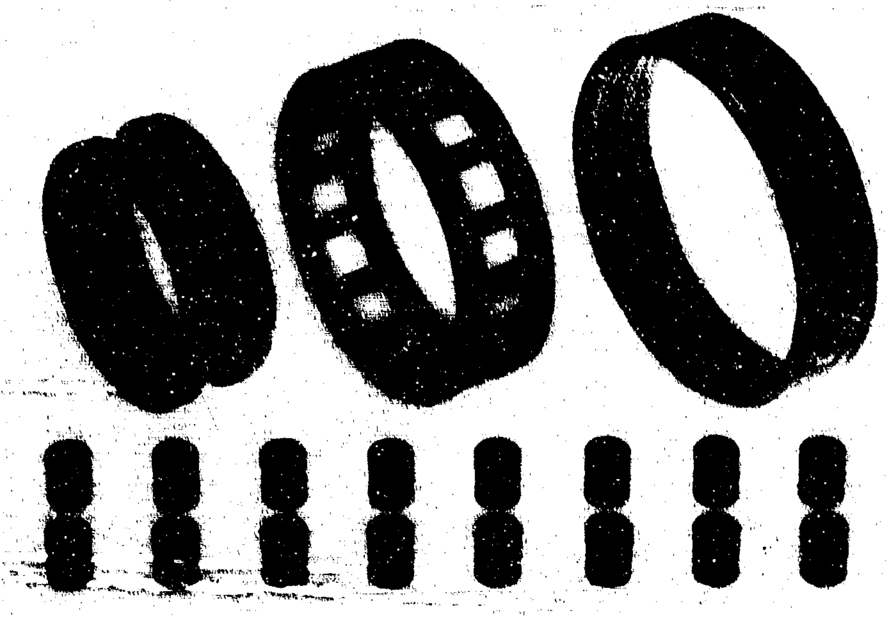

(U) Figure 82. Disassembly Condition of Reaction Bearing (S/N AA-1) With Turbine End of Rollers Up (Build 29) FE 79334

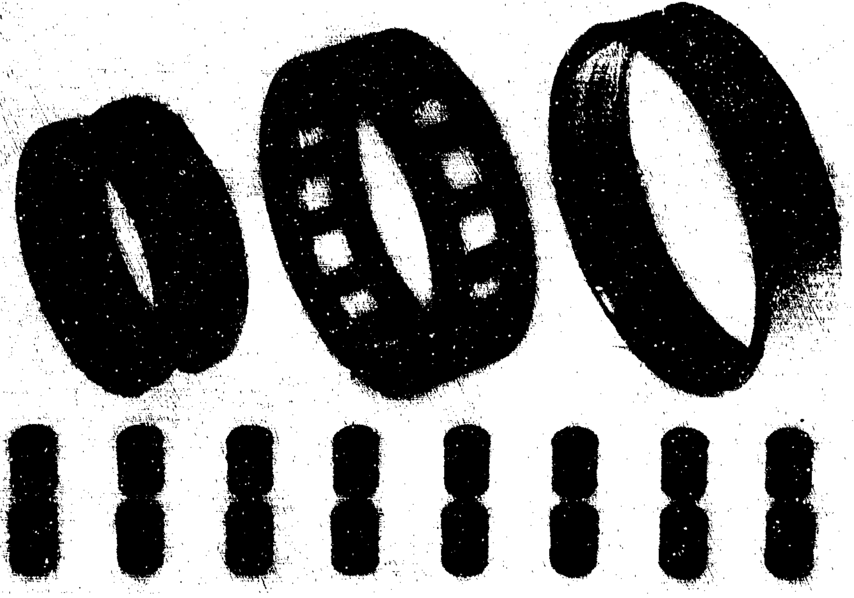

(U) Figure 83. Disassembly Condition of Load Bearing (S/N AA-2) With Turbine End of Rollers Up (Build 29) FE 79336

(C) Build 30 of the roller bearing rig incorporated test bearings used in previous testing. The reaction bearing (matrix point 27') was from Build 25A and had accumulated approximately 9.7 hours. The load bearing (matrix point 43') was from Build 28 and had accumulated approximately 6.5 hours. The reaction bearing incorporated in Build 30 consisted of single-crown rollers with an L/D ratio of 1.0, 0.009-inch roller end-to-side rail clearance, and a 0.0028-inch tight internal clearance. The primary end wear was on the turbine side of the reaction bearing rollers with an average wear of 0.00095 inch before testing on Build 30. The load bearing consisted of triple-crown rollers with an L/D ratio of 1.0, 0.0097-inch roller end-to-side rail clearance, and a 0.0049-inch tight internal clearance. The average load bearing roller end wear was 0.00257 inch nearly evenly distributed on both ends of the rollers before Build 30 testing. Build 30 testing began on 16 August and was concluded on 20 August 1968 after 12.8 hours had been accumulated on the lower time, load bearing. During Build 30, ten test cycles were completed with 6.3 hours test time at design conditions. The load bearing had accumulated a total of 24 cycles with 12.8 hours of operation at design conditions, and the reaction bearing had a total of 27 cycles with 16.0 hours. The teardown inspection revealed that both test bearings were in good condition and could be used for additional testing. The average reaction bearing end wear was 0.00213 inch with 0.0029 inch on the roller with maximum wear. Both ends of the reaction bearing rollers were worn nearly evenly. Figures 84 and 85 show the post-test condition of the reaction bearing. The average load bearing end wear was 0.00318 inch with 0.0095 inch on the roller with maximum wear that was the same roller that had 0.007-inch end wear before testing on this build. All load bearing wear was on the turbine end of the rollers. Figures 86 and 87 show the post-test condition of the load bearing.

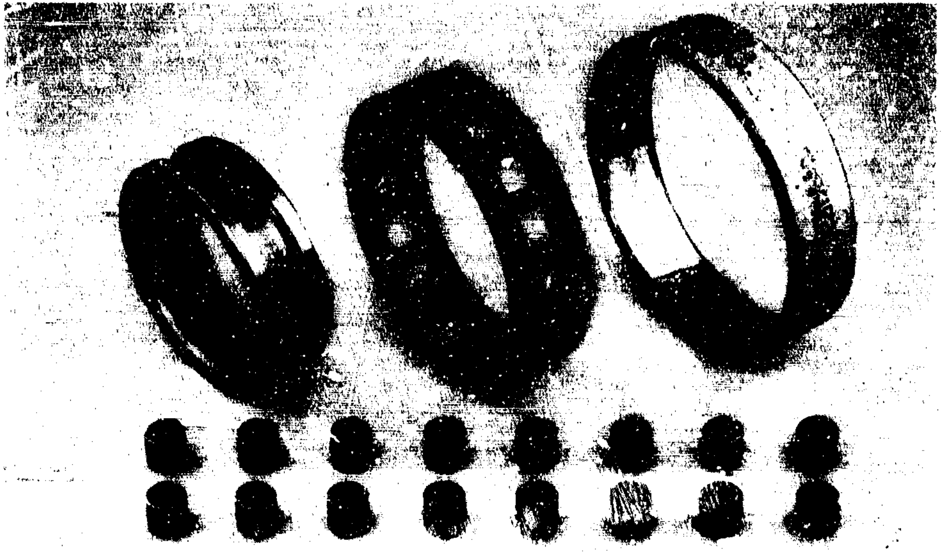

(U) Figure 84. Disassembly Condition of Reaction Bearing (S/N X-1) With Rear End of Rollers Up (Build 30) FE 79420

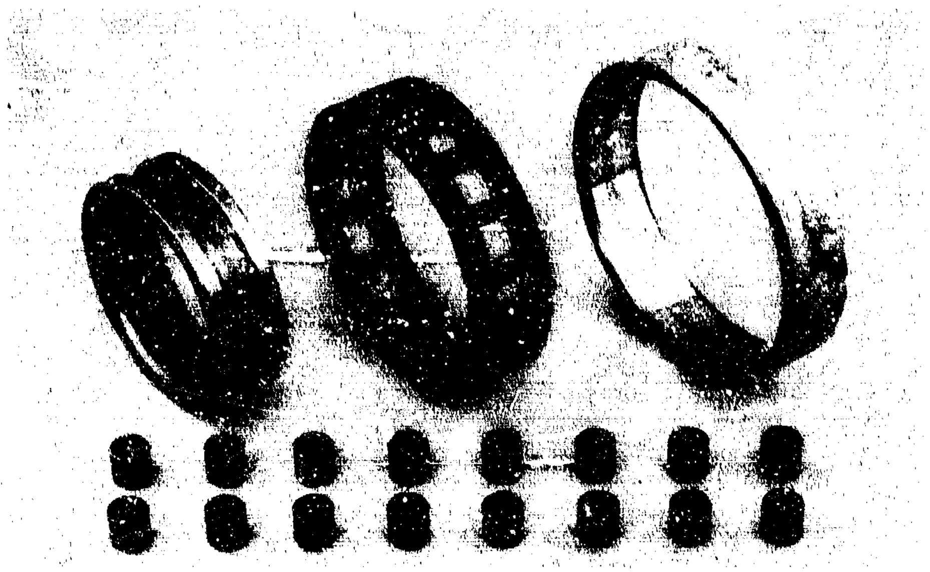

(U) Figure 85. Disassembly Condition of Reaction Bearing (S/N X-1) With Turbine End of Rollers Up (Build 30) FE 79421

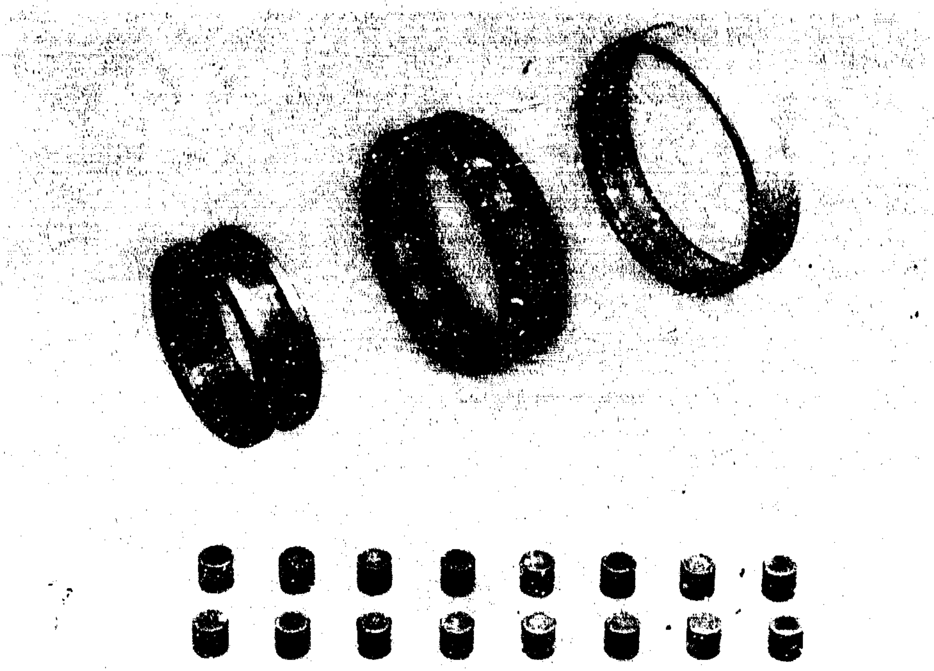

(U) Figure 86. Disassembly Condition of Load Bearing (S/N Z-2) With Rear End of Rollers Up (Build 30) FE 79491

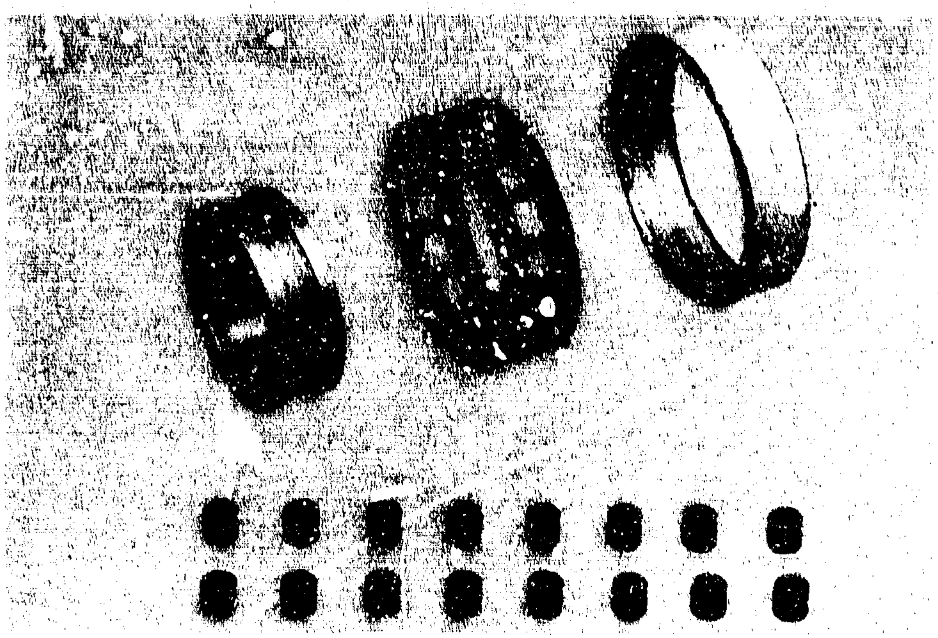

(U) Figure 87. Disassembly Condition of Load Bearing (S/N Z-2) With Turbine End of Rollers Up (Build 30) FE 79492

(C) Both roller bearings incorporated in Build 31 consisted of triple-crown, L/D of 1.125, stainless steel (AMS 5630) rollers and races. The reaction bearing (matrix point 20') had a 0.0051-inch tight internal clearance and a roller end-to-side rail clearance of 0.0098 inch. The load bearing (matrix point 20") had a 0.005-inch tight internal clearance and a roller end-to-side rail clearance of 0.0048 inch. Testing of Build 31 began on 23 August 1968. A high turbine drive pressure was required to start rotation, however, operational parameters were normal during the first cycle as soon as the design speed level was obtained. One hour at design speed were accumulated during the first cycle. The second test cycle was started on 26 August 1968, but the rig failed to rotate. Six attempts were made to accelerate the rig with the drive turbine after the shaft had been freed by rotation in the reverse direction, but on each attempt the shaft locked. On the seventh attempt, the shaft locked tight and could not be freed by turning in either direction.

(U) During disassembly of the test rig, it was determined that the locked shaft was caused by the load bearing rollers wedging into the inner race side rails. Scoring on both ends of the load bearing rollers was very heavy, as shown in Figures 88 and 89, and prevented the measurement of end wear. Figure 90 shows a comparison of typical rollers from the reaction bearing (matrix point 20') and the load bearing (matrix point 20"), which were configured identically, except that the load bearing roller end-to-side rail clearance was half that of the reaction bearing. The inner race side rails of the load bearing also showed heavy scoring. The reaction bearing was in good condition, except for an axial crack in the outer race, which is shown in Figure 91. The primary end wear of the reaction bearing was on the rear side of the rollers with an average wear of 0.00018 inch and 0.0005 inch on the roller with maximum wear. Figure 92 shows the overall condition of the load bearing (matrix point 20") and Figure 93 shows the condition of the reaction bearing (matrix point 20).

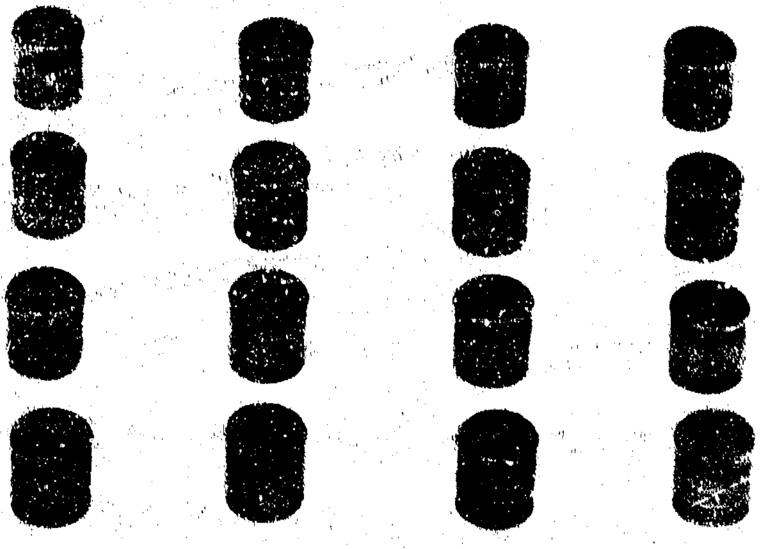

(U) Figure 88. Rollers from Load Bearing (S/N BB-2) Showing Heavy Scoring on Turbine End of Rollers (Build 31) FE 79574

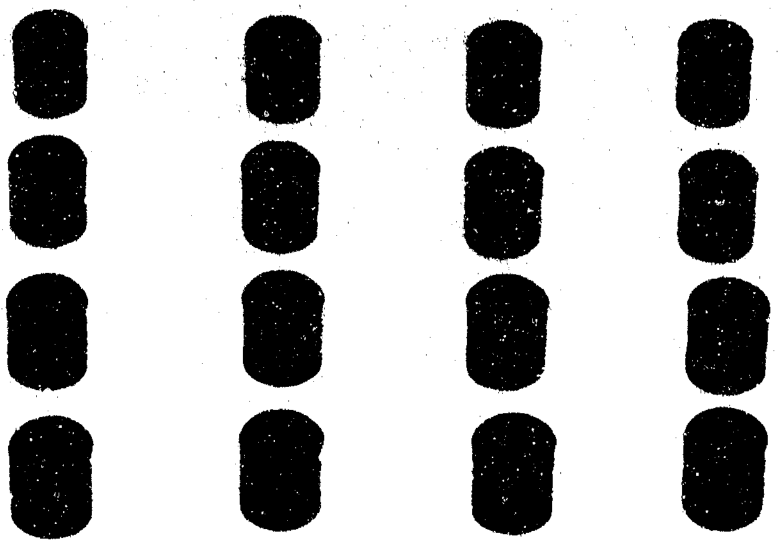

(U) Figure 89. Rollers from Load Bearing (S/N BB-2) Showing Heavy Scoring on Rear End of Rollers (Build 31) FE 79575

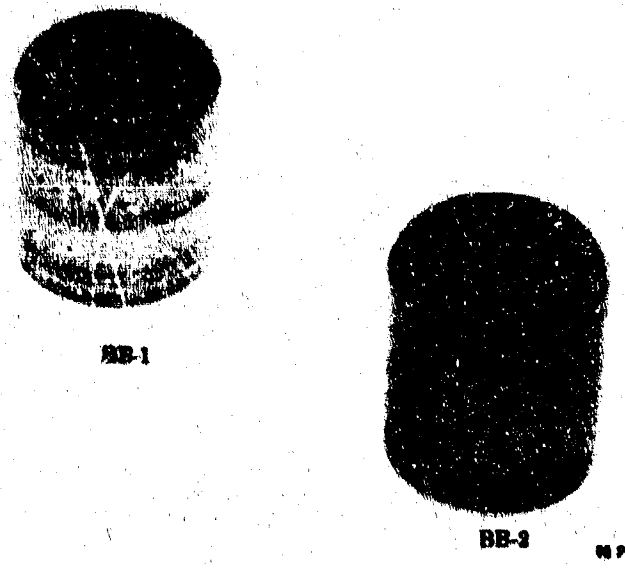

(U) Figure 90. Comparison of Post-Test Condition of a Typical Roller from Reaction Bearing (S/N BB-1) and Load Bearing (S/N BB-2) of Build 31 FD 24500

(U) Figure 91. Cracked Outer Race from Reaction Bearing (S/N BB-1) of Build 31 FE 79499

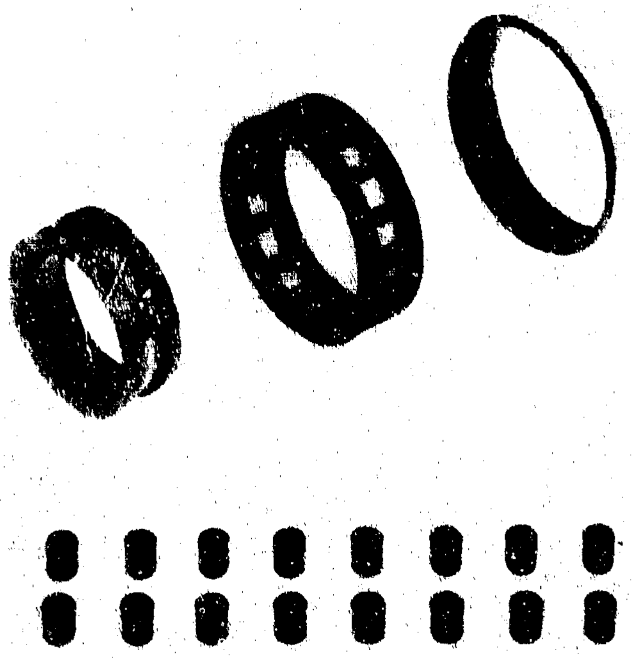

(U) Figure 92. Disassembly Condition of Load Bearing (S/N BB-2) With Turbine End of Rollers Up (Build 31) FE 79496

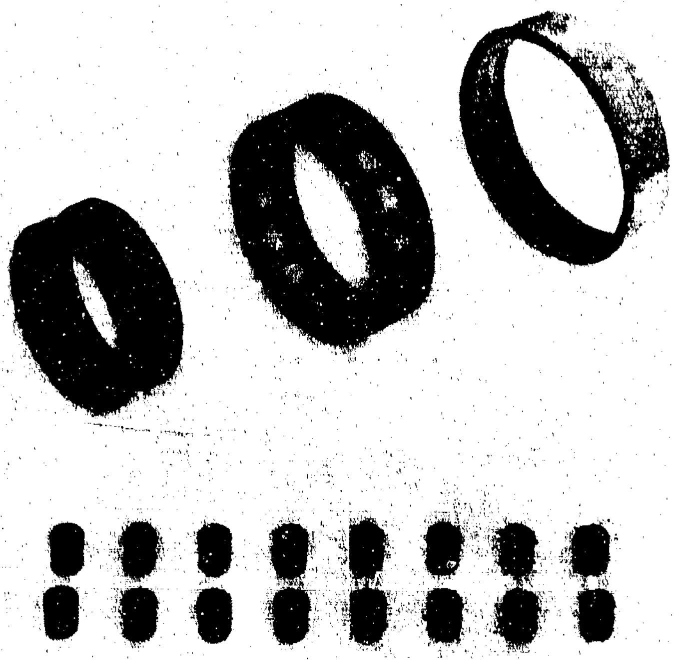

(U) Figure 93. Disassembly Condition of Reaction Bearing (S/N BB-1) With Turbine End of Rollers Up (Build 31) FE 79494

(C) Build 32 of the roller bearing test rig incorporated bearing elements used in the previous tests. The load bearing incorporated rollers from Build 22 that had accumulated 2.2 hours, and the cage was from Build 6 (Phase I (Contract AF04(611)-11401) program) that had 0.3 hour of test time. Both inner and outer races were new. The reaction bearing had rollers selected from Phase I (Contract AF04(611)-11401) test bearings (Builds 12 and 15) with 1.5 hours on the maximum time rollers; the cage was from Build 6 and had 0.3 hour of test time. The inner race was from Build 5 with no test time at rated conditions, and the outer race was new. Both test bearings incorporated single-crown, L/D of 1.0 rollers, stainless steel (AMS 5630) rollers and races with outer-race-guided Armalon cages. The load bearing (matrix point 22) had a 0.0052-inch tight internal clearance and a roller end-to-side rail clearance of 0.0199 inch. The reaction bearing (matrix point 23') had a 0.0049-inch tight internal clearance and a roller end-to-side rail clearance of 0.0099 inch. Build 32 testing began on 29 August and ended on 30 August 1968. Testing was terminated after 0.1 hour at design speed on the sixth cycle when the vibration levels and the slave bearing outer race temperature increased, and the operating speed dropped off significantly. At the time of shutdown, 6 cycles and 137 minutes of testing at design speed had been accumulated. The teardown inspection revealed that the shaft had cracked halfway through in the necked-down section on the turbine end. The crack allowed the turbine end of the shaft to deflect during operation allowing the turbine to rub heavily on the turbine housing. The labyrinth seals and the turbine spacer were also damaged by rubbing. The test bearings were in good condition except for the reaction bearing outer race, which was cracked in the same location as the previous test (Build 31), as shown in Figure 94. The greatest wear was on the rear end of the rollers in the reaction bearing, while the load bearing rollers wore on both ends in nearly equal amounts in a random manner. The roller end wear measurements are shown in Table XV. Except for the outer races, both roller bearings were reused in Builds 35 and 36 of the test rig. Figure 95 shows the overall condition of the reaction bearing (matrix point 23') and Figure 96 shows the condition of the load bearing (matrix point 22).

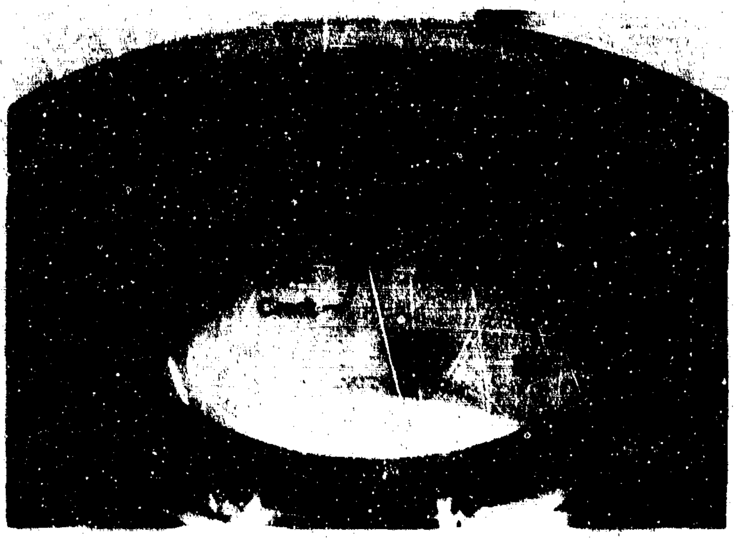

(U) Figure 94. View Showing Crack in Outer Race of Reaction Bearing S/N CC-1 (Build 32) FD 25098

(C)(U) Table XV. End Wear Summary (Matrix Points 22 and 23')

	Before Build 32 Testing	After Build 32 Testing	After Build 35 Testing	After Build 36 Testing
Reaction Bearing Rollers (23')				
Accumulated time and cycles at design speed	1.5 hours 3 cycles	3.8 hours 9 cycles	7.9 hours 18 cycles	16.4 hours 34 cycles
Average End Wear (in.)	0.0006	0.0016	0.0017	0.0020
Maximum End Wear (in.)	0.0012	0.0021	0.0045	0.0072
Load Bearing Rollers (22)				
Accumulated time and cycles at design speed	2.2 hours 7 cycles	4.5 hours 13 cycles	8.6 hours 22 cycles	17.0 hours 38 cycles
Average End Wear (in.)	0.0009	0.0013	0.0027	0.0044
Maximum End Wear (in.)	0.0011	0.0020	0.0047	0.0068

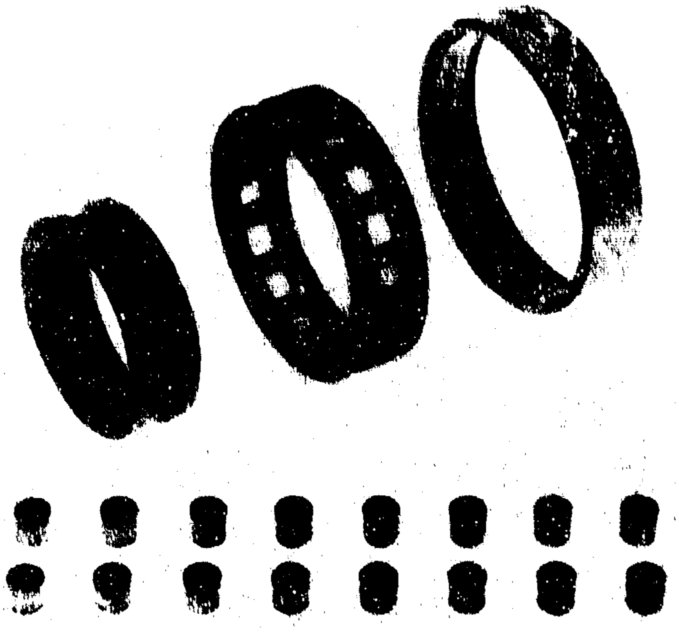

(U) Figure 95. Disassembly Condition of Reaction Bearing (S/N CC-1) With Rear End of Rollers Up (Build 32) FE 79593

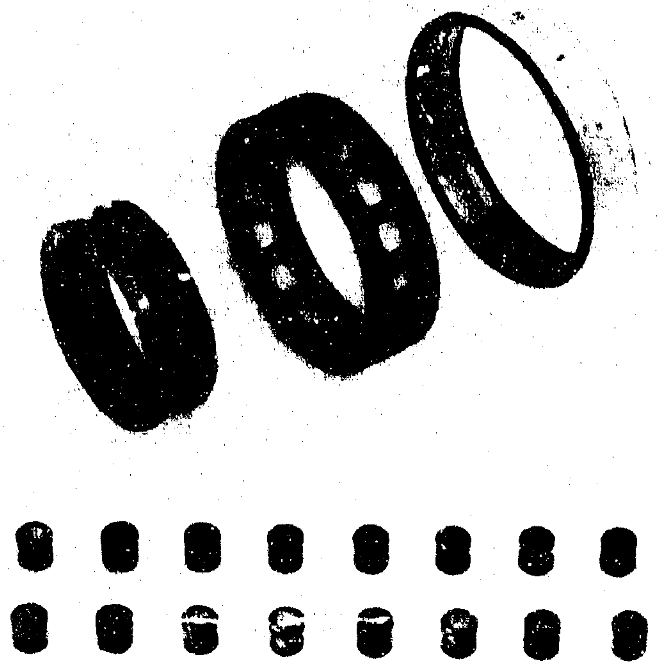

(U) Figure 96. Disassembly Condition of Load Bearing (S/N CC-2) With Rear End of Rollers Up (Build 32) FE 79598

(C) In the investigation to determine the cause of the reaction bearing outer race failures on Builds 31 and 32, a metallurgical examination of the fracture faces indicated that the point of origin was a small surface depression on the inside diameter of the race on Build 31 and was a small crack, approximately 0.0025-inch deep, on the outside diameter surface on Build 32. Metallurgical analysis also indicated that the failures resulted from flexing stress cycles and they were not associated with fatigue spalling. With bearing operation at 48,000 rpm, a given point on the race is subjected to 400,000 roller passing cycles per minute. After consultation with the bearing vendor and with the P&WA bearing group at East Hartford, it was decided that the thin outer ring inside diameter should be in compression to withstand the cycling stresses induced with the tight internal fit and high shaft speed. The compressive stresses could be induced by means of a microstructure change such as carburizing the inside diameter of the ring; by shot peening the inside surface, or by outside diameter restraint.

(U) The similarity of the angular orientation of the cracked outer races on Builds 31 and 32, coupled with the fact that the surface depressions found at the origin of the fatigue failures were less severe than observed on previously successful bearing outer races, indicated that stresses in excess of the normal operating levels were involved in these failures. The bearing test rig housings were reassembled for a bearing support alignment check. This inspection showed that the reaction bearing outer race carrier was misaligned by approximately 0.006 inch in the plane of the outer race failure, and was loose from the rear housing restraining pins. The damaged reaction bearing carrier was replaced and it was both pinned and weld attached to the rear housing. In addition, a stress relief heat treat cycle was instituted after the final grind operation, which established the desired internal clearance on the bearing, to minimize residual stresses that may be present.

(C) Build 33 of the roller bearing test rig incorporated test bearings with triple-crown, L/D 1.125, stainless steel (AMS 5630) rollers and races. The reaction bearing (matrix point 20') had a 0.005-inch tight internal clearance and a roller end-to-side rail clearance of 0.0098 inch. The load bearing (matrix point 21) had a 0.0051-inch tight internal clearance and a roller end-to-side rail clearance of 0.0198 inch. Testing of Build 33 began on 10 September 1968 and ended the next day. Testing was terminated after 1 minute at design speed on the fifth cycle when a decay in coolant flows and an increase in vibrations and in slave bearing outer race temperature was observed. At the time of failure, 5 cycles and 1.3 hours of testing at design speed had been accumulated. The teardown inspection of Build 33 revealed that the liquid hydrogen bellows seal had failed. The test bearings were in good condition except for a crack in the reaction bearing outer race. The crack was located approximately 180 degrees from the two previous failures as shown in Figure 97. The rollers from both test bearings were in excellent condition with negligible end wear, but did exhibit moderate scuffing on the turbine end as shown in Figures 98 and 99. Failure analysis of the reaction bearing outer race fracture faces again showed a brittle-failure originating in a small depression in the roller track.

(C) Build 34 of the roller bearing test rig incorporated the inner races, single-crown, L/D of 1.000 rollers, and Armalon outer-race guided cages from Build 32. New outer races were fabricated from steel alloy (AMS 6260) with the inside diameter carburized to a depth of approximately 0.043 inch and heat treated to provide a hard surface in the roller contact area. The reaction bearing (matrix point 23') internal clearance was 0.0039-inch tight and the roller end-to-side rail clearance was 0.0105 inch. The load bearing (matrix point 22) internal clearance was 0.0042-inch tight and the roller end-to-side rail clearance was 0.0204 inch. These internal clearances correspond to values of 0.0049 and 0.0051 inch, respectively, for the stainless steel (AMS 5630) races when adjusted for the difference in coefficient of expansion between steel alloy (AMS 6260) and stainless steel (AMS 5630). Build 34 of the bearing test rig was mounted and ready for test on 20 September 1968. During the initial start sequence the turbine housing failed as the turbine pressure was applied to start rotation of the test rig. The housing failed in the thin section below the Marmon clamp flange and caused damage to the turbine wheel and tie bolt. A detailed inspection revealed that the outer parts were in good condition.

(C) Build 35 of the bearing test rig incorporated the same test bearings that were used in Build 34. A new tie bolt, turbine, and turbine housing were used on this build. Testing of Build 35 of the roller bearing test rig began on 25 September 1968 and was ended on the next day. Testing was terminated on the ninth test cycle at design speed when, after 0.2 hour of operation, a speed shift was detected and the slave bearing outer race temperature increased. Build 35 testing accumulated 4.1 hours and nine cycles at design speed. The teardown inspection revealed that the slave ball bearing had failed. The test bearings were in good condition and were incorporated in the next build to continue testing of this configuration. End wear measurements summarizing the condition of the bearings after Builds 32 and 35 are listed in Table XV.

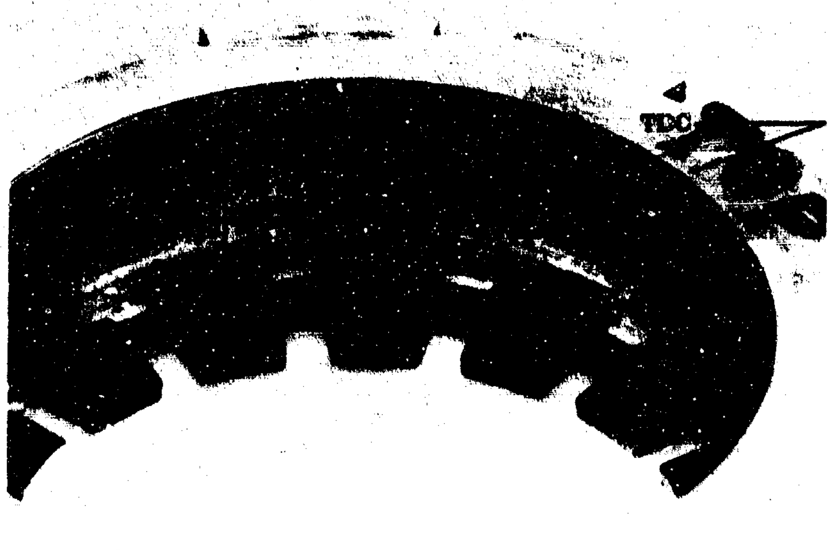

(U) Figure 97. View Showing Crack in Outer Race of Reaction Bearing (Build 33) FD 25268

(U) Figure 98. View Showing Moderate Scuffing on Turbine End of Rollers from Reaction Bearing (Build 33) FE 79866

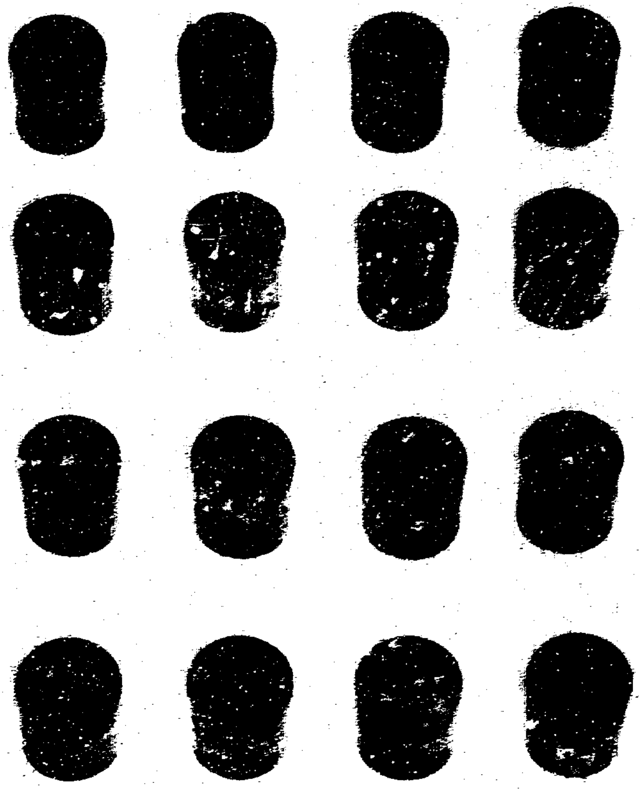

(U) Figure 99. View Showing Moderate Scuffing on Turbine End of Rollers from Load Bearing (Build 33) FE 79870

(C) Build 36 of the roller bearing test rig incorporated test bearings from Build 35. Testing of Build 36 began on 3 October 1968 and ended 8 October 1968. Testing was terminated after 8.4 hours at design speed when outer races had accumulated 12.6 hours. The teardown inspection of Build 36 revealed that both test bearings were in good condition and could have been used for additional testing. Figures 100 and 101 show the post-test condition of the reaction bearing, (matrix point 23'). Figures 102 and 103 show the post-test condition of the load bearing, (matrix point 22). Table XV summarizes the roller end wear on both test bearings after testing on Builds 32, 35, and 36.

(C) Build 37 of the bearing test rig was configured similar to Build 36 to provide a repeatability test on the load bearing (matrix point 22) and to evaluate the effects of increased roller end clearance on the reaction bearing by doubling the largest Build 36 end clearance. Increased end clearance is desirable for the 250K fuel pump to accommodate the hydrostatic thrust piston travel and the difference in thermal contraction between the housings and the rotor assembly. Build 37 also used wider races and the reaction bearing roller-end-to-side rail clearance was increased to 0.040 inch. The test bearings had single crown L/D of 1.000 rollers, stainless steel (AMS 5630) rollers and inner races, and steel alloy (AMS 6260) outer races carburized and hardened similar to the outer rings in Build 36. The races were 0.108-inch wider than the races in the previous build and the cage width was increased accordingly. The reaction bearing (matrix point 3) had a 0.0040-inch tight internal fit and the load bearing (matrix point 22) had a 0.0041-inch tight internal fit. The load bearing roller end-to-side rail clearance was 0.020 inch. Revisions were made to the test rig in this build to provide a double labyrinth seal with a vent cavity to replace the carbon bellows seal, thereby increasing rig durability.

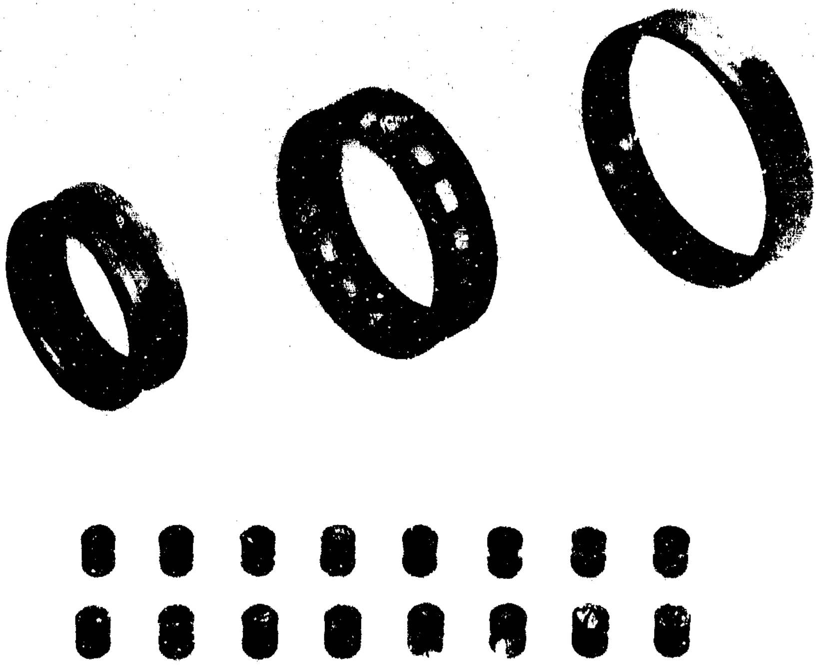

(U) Figure 100. Disassembly Condition of Reaction Bearing (S/N EE-1) With Rear End of Rollers Up (Build 36)   FE 80637

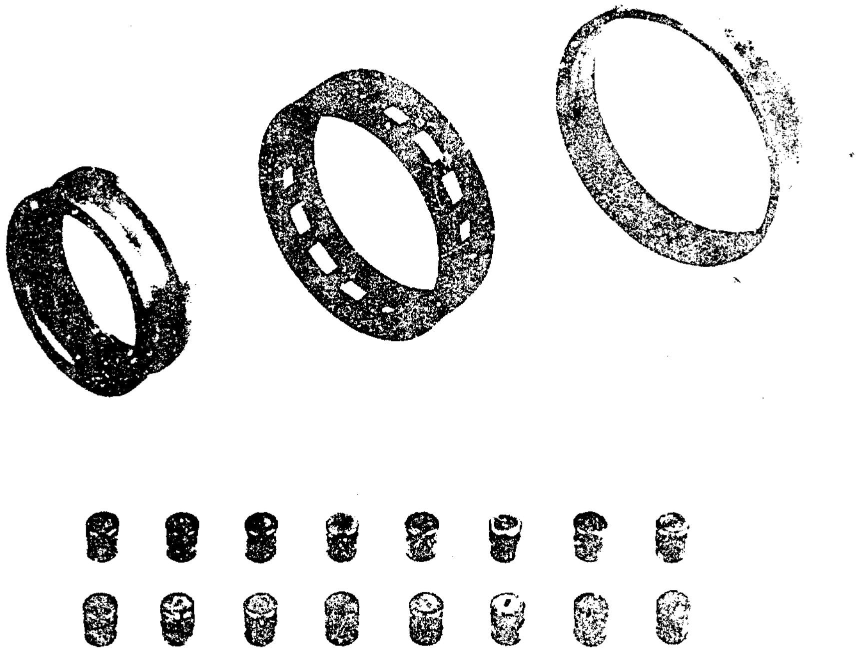

(U) Figure 101. Disassembly Condition of Reaction Bearing (S/N EE-1) With Turbine End of Rollers Up (Build 36) FE 80638

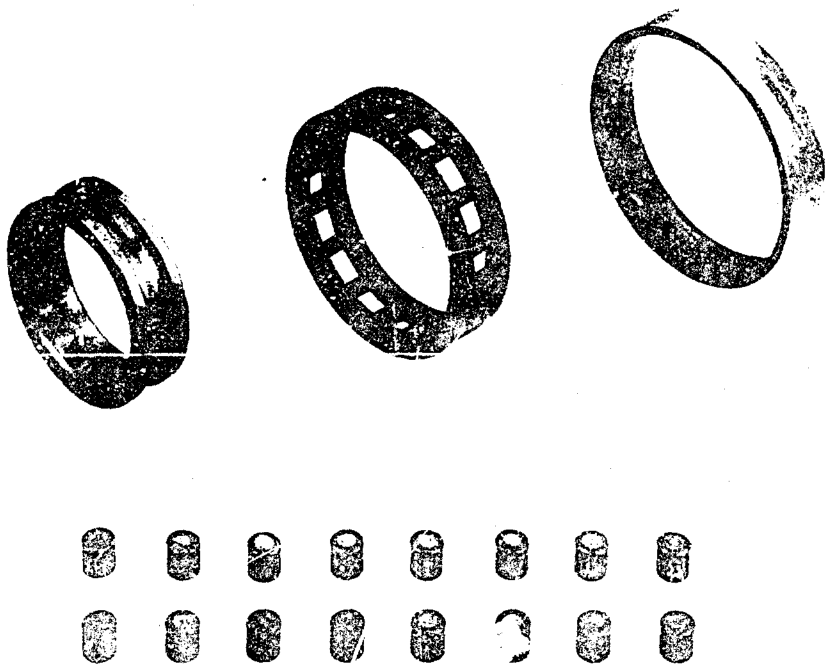

(U) Figure 102. Disassembly Condition of Load Bearing (S/N EE-2) With Rear End of Rollers Up (Build 36) FE 80639

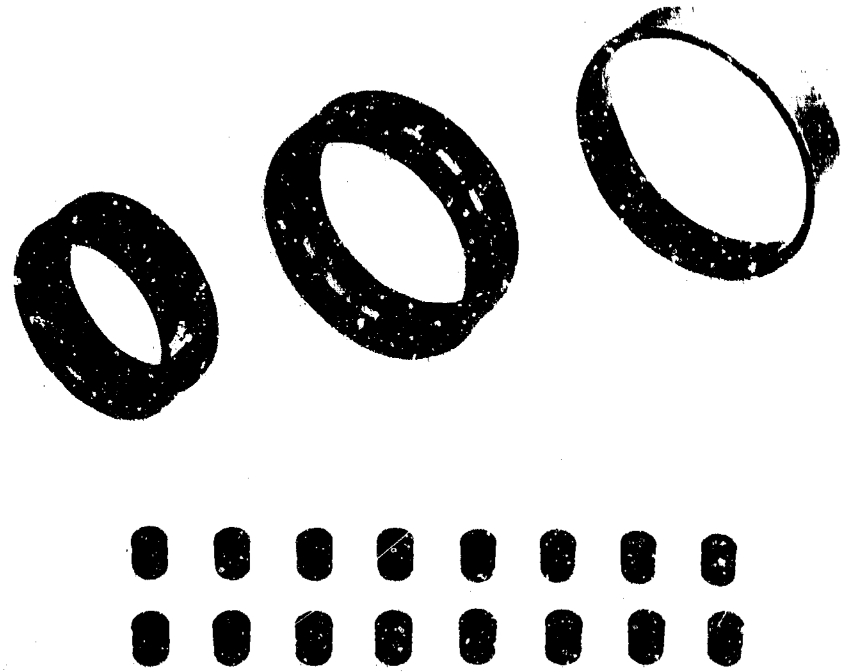

(U) Figure 103. Disassembly Condition of Load Bearing (S/N EE-2) With Turbine End Rollers Up (Build 36) FE 80640

(C) Prior to testing Build 37 of the bearing test rig, the bearing coolant system was revised to provide a series coolant flow arrangement to reduce the coolant consumption. The coolant was supplied to the reaction bearing, and after cooling the two test bearings, it was split to provide flow control through the slave bearing. Testing of Build 37 began on 18 October 1968 and ended on 21 October. Testing was terminated after 2 minutes on the third cycle to rated speed because of high slave bearing outer race temperatures and increased vibrations. Build 37 testing had accumulated 3.9 hours of operation at design conditions. The teardown inspection revealed that the slave bearing had failed but that the test bearings were in good condition. Slight thermal cracking was seen on both outer races outside the roller track in the area of cage contact. The average reaction bearing end wear was 0.0011 inch with 0.0022 inch on the roller with maximum wear. The average load bearing end wear was 0.0002 inch with 0.0004 inch on the roller with maximum wear. The wear was on the turbine end of the rollers for both bearings with moderate scoring on the rear end of both.

(C) Build 38 of the roller bearing test rig included the same test bearings as Build 37 and a new slave bearing. Testing of Build 38 was performed on 25 October and the test was terminated after 2.3 hours of the first cycle because of an increase in the reaction bearing and the slave bearing outer race temperature that could not be reduced by increasing the coolant flow rate. The teardown inspection revealed no appreciable damage to the test bearings other than increased thermal cracking on the outer races as shown in Figures 104 and 105. One crack had extended into the roller track but it was considered acceptable for continued testing. No measurable change was noted in the roller end wear for either test bearing. The slave bearing cage ball pockets showed wear from the differential pressure across the cage and from ball excursion.

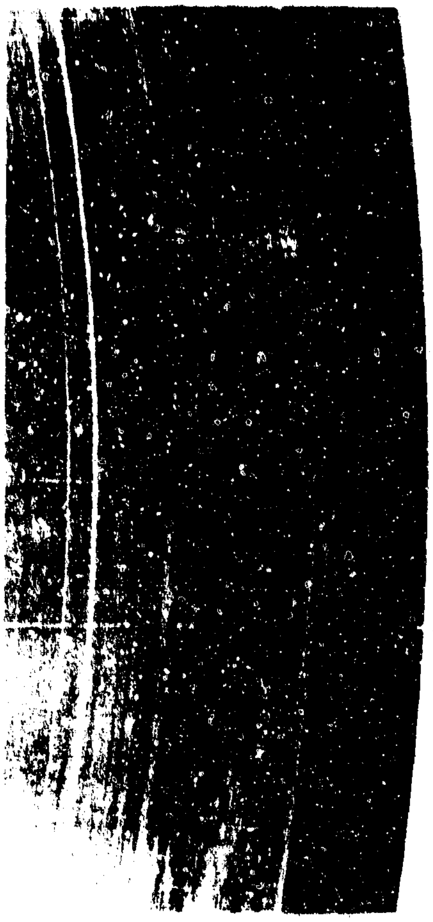

(U) Figure 104. Reaction Bearing (S/N FF-1) Outer Race ID Showing Thermal Cracks (Build 38) FE 80934

(U) Figure 105. Load Bearing (S/N FF-2) FE 80935
Outer Race ID Showing
Thermal Cracks (Build 38)

(C) Build 39 of the roller bearing test rig included the same test bearings as Build 38 and a new ball bearing with a Salox cage instead of Rulon as used previously. Revisions were incorporated in the rig build to provide bearing coolant flow under the inner race of the slave bearing in addition to the normal flow path through the bearing cage. Testing of Build 39 began on 30 October and ended on 31 October. Testing was terminated after 2 hours of the second cycle to rated speed because of increase in vibrations, decrease in speed, and increase in the load bearing outer race temperature. The test bearings had accumulated a total time of 9.9 hours. The teardown inspection revealed that the outer race of the load bearing had cracked at the loaded side with the fracture faces coincident with the thermal cracks as shown in Figure 106. Except for the thermal cracks on the outer races, both test bearings were in good condition and the roller end wear was found to be nearly identical with the previous build measurements. The average roller end wear on the reaction bearing was 0.0011 inch with 0.0019 inch on the roller with maximum wear. The average load bearing end wear was 0.0003 inch with 0.0004 inch on the roller with maximum wear. Figures 107 and 108 show the post-test condition of the reaction bearing (matrix point 3) and load bearing matrix point 22).

(C) Build 40 of the roller bearing test rig incorporated single crown L/D = 1.000, stainless steel (AMS 5630) rollers and stainless steel (AMS 5630) inner races with outer race guided Armalon cages. The load bearing cage had lateral cooling slots 0.055-inch wide (circular diameter) and 0.035-inch deep machined between the pockets. The outer races were fabricated from Inconel 718 (AMS 5663). The reaction bearing, matrix point 3, had a 0.0028-inch tight internal clearance and a roller end-to-side rail clearance of 0.0411 inch. The load bearing, matrix point 3, had a 0.0031-inch tight internal clearance and a roller end-to-side rail clearance of 0.0386 inch. These diametral fits are equivalent to the 0.005-inch tight fit used with the stainless steel (AMS 5630) outer races when adjusted for the difference in thermal expansion coefficients of the two materials.

(C) Testing of Build 40 was completed on 6 November 1968. The test was terminated after 1.5 hours of the first cycle when there was a speed shift and an increase in the load bearing outer race temperature and vibration level.

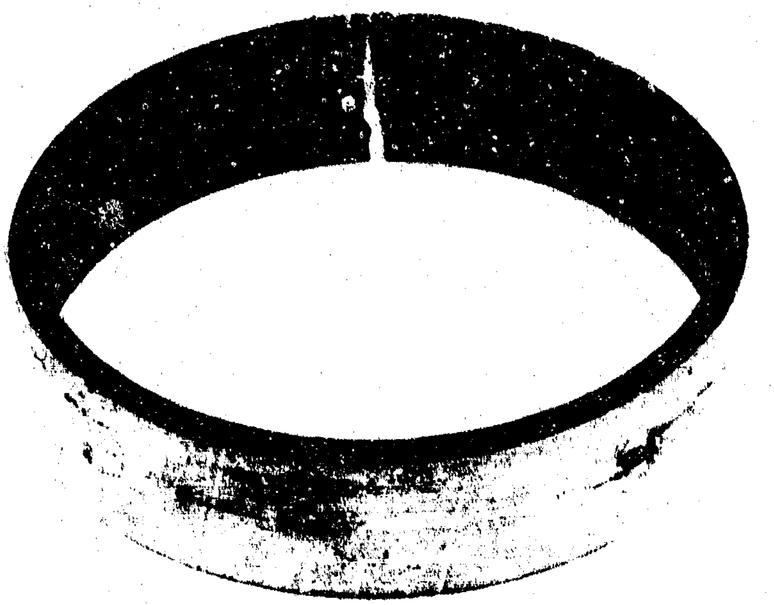

(U) Figure 106. Condition of Load Bearing (S/N FF-2) Outer Race (Build 39) FE 81074

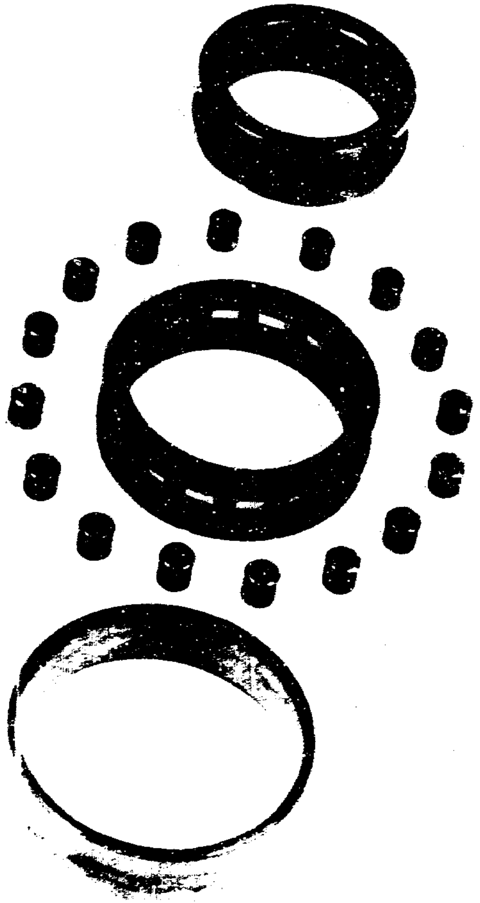

(U) Figure 107. Disassembly Condition of Reaction Bearing (S/N FF-1) With Turbine End of Rollers Up (Build 39) FE 81183

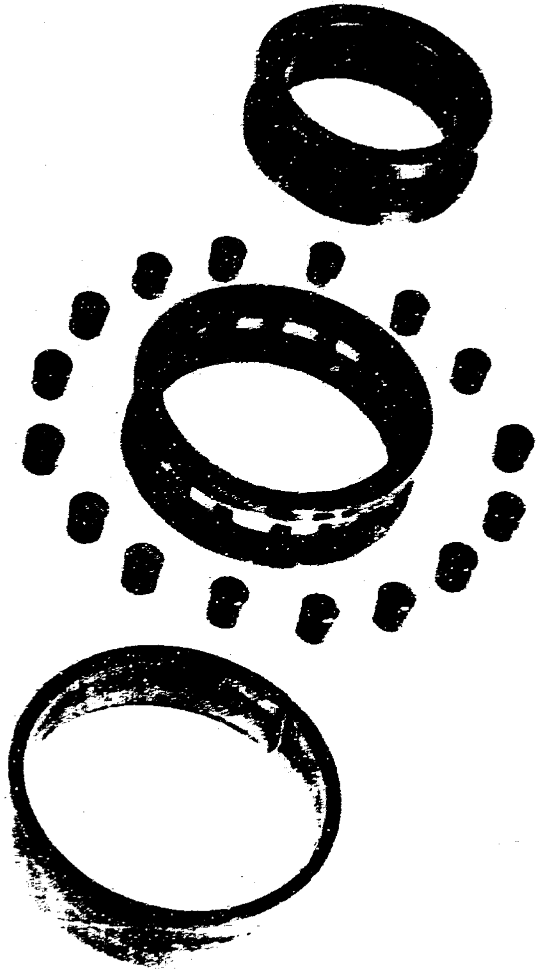

(U) Figure 108. Disassembly Condition of Load Bearing (S/N FF-2) With Turbine End of Rollers Up (Build 39) FE 81088

(C) A teardown inspection revealed that the load bearing outer race had cracked in two places in the loaded zone and the roller path was severely spalled and deformed as shown in Figure 109. The rollers suffered severe impact damage particularly on the rear end as shown in Figures 110 and 111. The inner race side rails were heavily spalled as a result of the rollers impacting with the rear rail, this condition is shown in Figure 112. The cage sustained severe abrasive damage as a result of particle ingestion from the rollers and races as shown in Figure 113. The overall condition of the load bearing (matrix point 3) is shown in Figures 114 and 115. The heavy damage on the load bearing rollers prevented measurement of roller end wear. The reaction bearing was in good condition except for some spalling on the outer race roller path in the loaded area as shown in Figure 116. The rollers exhibited an average end wear of 0.0001 inch with 0.0005 inch on the roller with maximum wear. All wear was on the turbine end of the rollers. The overall condition of the reaction bearing (matrix point 3) is shown in Figure 117.

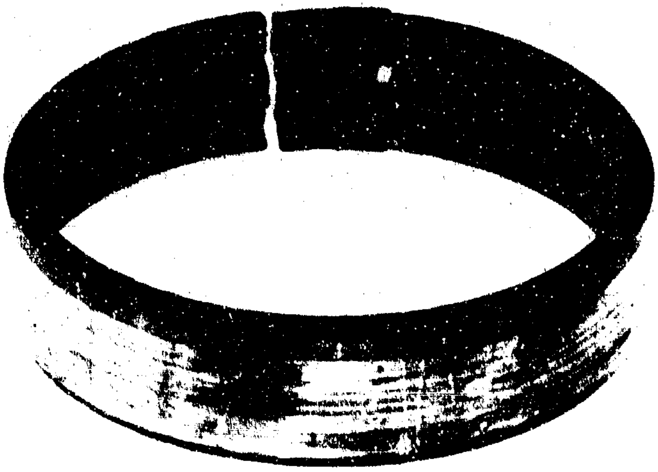

(U) Figure 109. View Showing Condition of Load Bearing Outer Race (S/N CG-2) After Test of Build 40 FE 81239

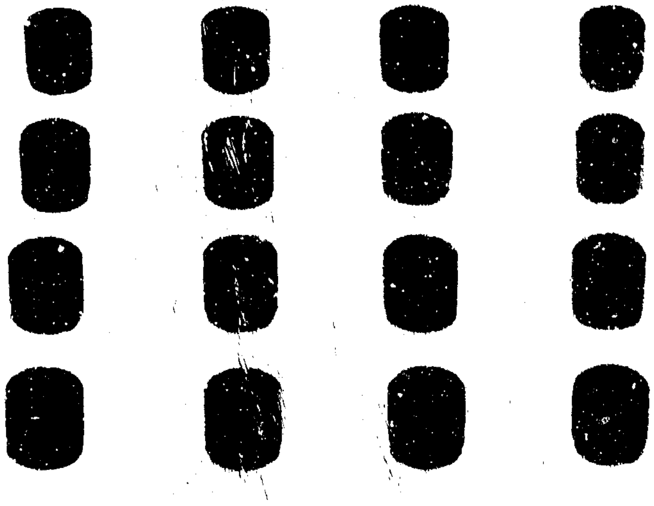

(U) Figure 110. View Showing Condition of Load Bearing Rollers (S/N GG-2), Turbine End Up (Build 40) FE 81245

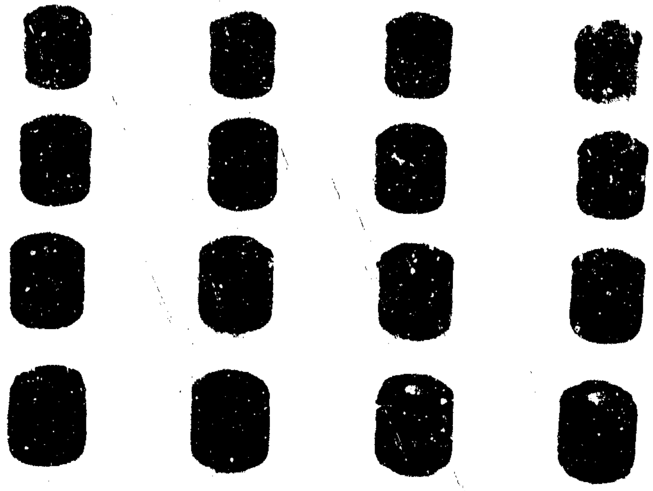

(U) Figure 111. View Showing Condition of Load Bearing Rollers (S/N GG-2), Rear End Up (Build 40) FE 81244

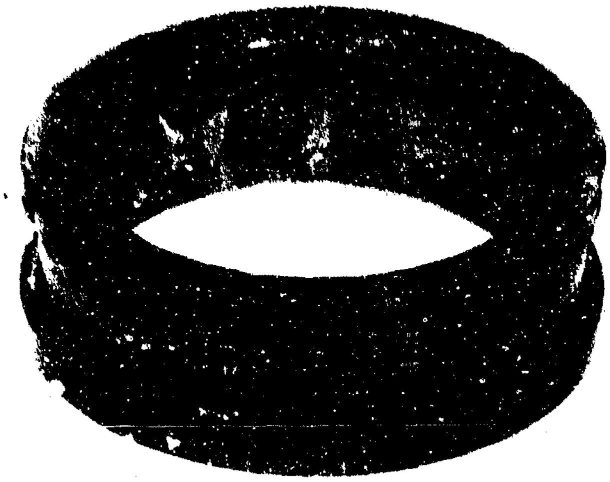

(U) Figure 112. View Showing Condition of Load Bearing Inner Race (S/N GG-2) After Test of Build 40 FE 81241

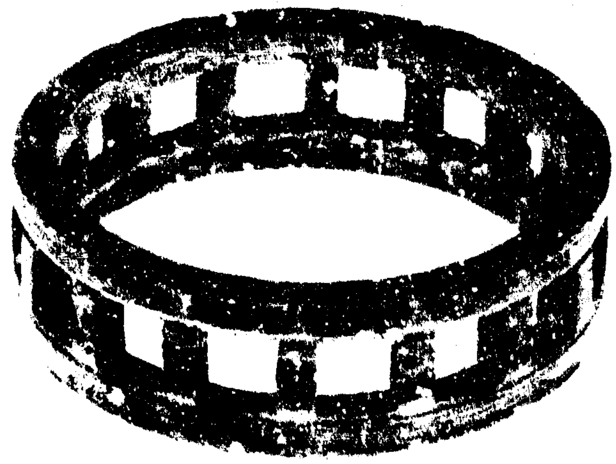

(U) Figure 113. View Showing Condition of Load Bearing Cage (S/N GG-2) After Test of Build 40 FE 81247

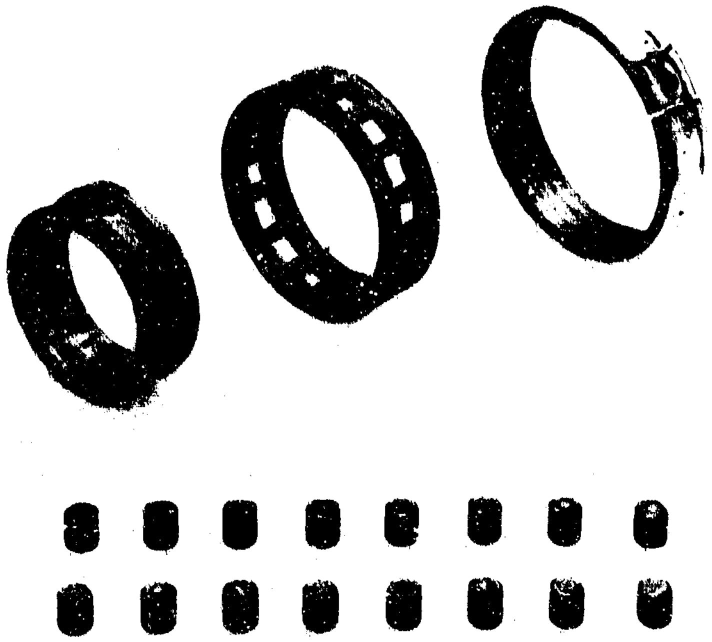

(U) Figure 114. View Showing Overall Condition of Load Bearing (S/N GG-2), Rear End Up (Build 40) FE 81234

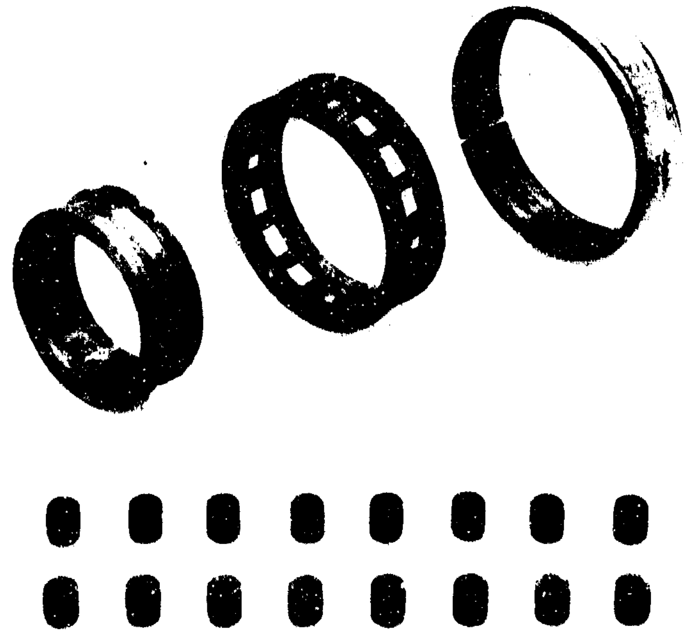

(U) Figure 115. View Showing Overall Condition of Load Bearing (S/N GG-2) Turbine End Up (Build 40) FE 81233

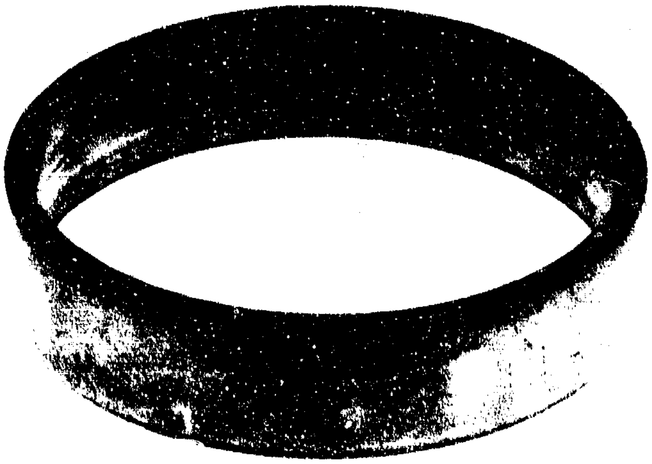

(U) Figure 116. View Showing Condition of Reaction Bearing Outer Race (S/N GG-1) After Test of Build 40 FE 80830

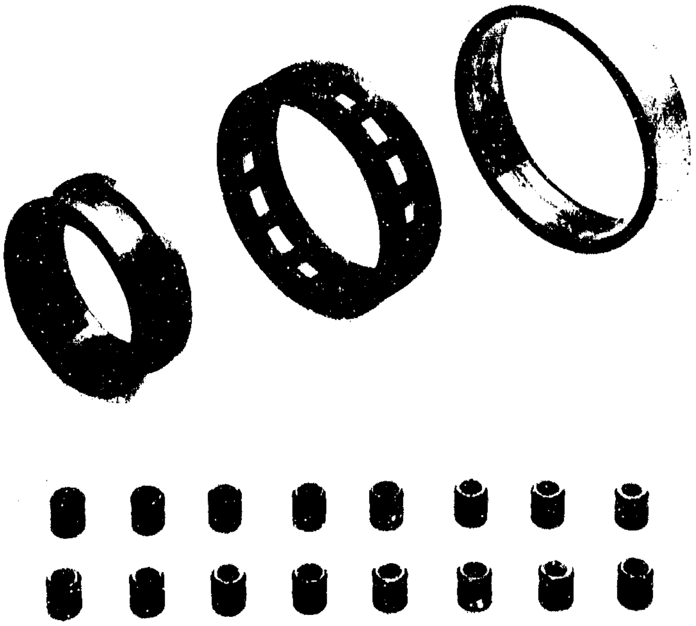

(U) Figure 117. View Showing Overall Condition of Reaction Bearing (S/N GG-1), Turbine End Up (Build 40) FE 81231

(U) Metallurgical analysis of the failed outer race from the Build 40 load bearing indicates that the Inconel 718 (AMS 5663) race was severely overloaded, which can be attributed to the mechanical deformation in the roller track. Heat generation from the deformed roller track appears to have permitted further plastic deformation until the failure was completed with the lateral cracks seen in the plastically deformed area. Metallurgical examination revealed that the microstructure in the failed zone had transformed to a cast structure. The less heavily loaded reaction bearing had begun spalling in the loaded zone and it is viewed as preliminary to the failure encountered with the load bearing. It appears that the hardness of Rc 44 on these races is not sufficient for the loads and life required in this bearing application.

(C) Build 41 of the bearing test rig consisted of test bearings with single crown L/D = 1.000 stainless steel (AMS 5630) rollers, stainless steel (AMS 5630) inner races, Armalon outer race guided cages with lateral coolant slots, and steel alloy (AMS 6265) outer races. The reaction bearing, matrix point 3, had a 0.0036-inch tight internal clearance and a roller end-to-side rail clearance of 0.0391 inch. The load bearing, matrix point 3, had a 0.0040-inch tight internal clearance and a roller end-to-side rail clearance of 0.0393 inch. These diametral fits are equivalent to a 0.0046- and 0.0050-inch tight fit, with stainless steel (AMS 5630) outer races respectively, when adjusted for the difference in coefficient of expansion.

(U) Build 41 testing, was begun on 18 November 1968 and was ended the next day after accumulating 10.1 hours. Testing was terminated after 1 minute of the 6th test cycle when a speed shift and an increase in the reaction bearing outer race temperature were observed.

(C) A teardown inspection revealed that one roller in the reaction bearing had skewed as shown in Figure 118. The cage pocket from another roller showed the characteristic "dog bone" wear pattern associated with insufficient roller preload. The equivalent negative internal clearance on this bearing, 0.0046 inch, was the lowest value tested recently. The inner race showed light chipping on both side rails with the turbine end more heavily damaged. Moderate thermal cracking of the outer race was detected in the cage contact areas on each side of the roller track. The average roller end wear was 0.0082 inch with 0.012 inch on the roller with the maximum wear. The turbine end of the rollers exhibited the heaviest wear. The post-test condition of the reaction bearing is shown in Figure 119 with detail views of the rollers, inner race and outer race shown in Figures 120, 121, and 122, respectively. The load bearing was in excellent condition as shown in Figure 123 and could be used for further testing. The average load bearing roller end wear was 0.021 inch with 0.0048 inch on the roller with the maximum wear. Both ends of the rollers exhibited some wear with the maximum wear on the rear end.

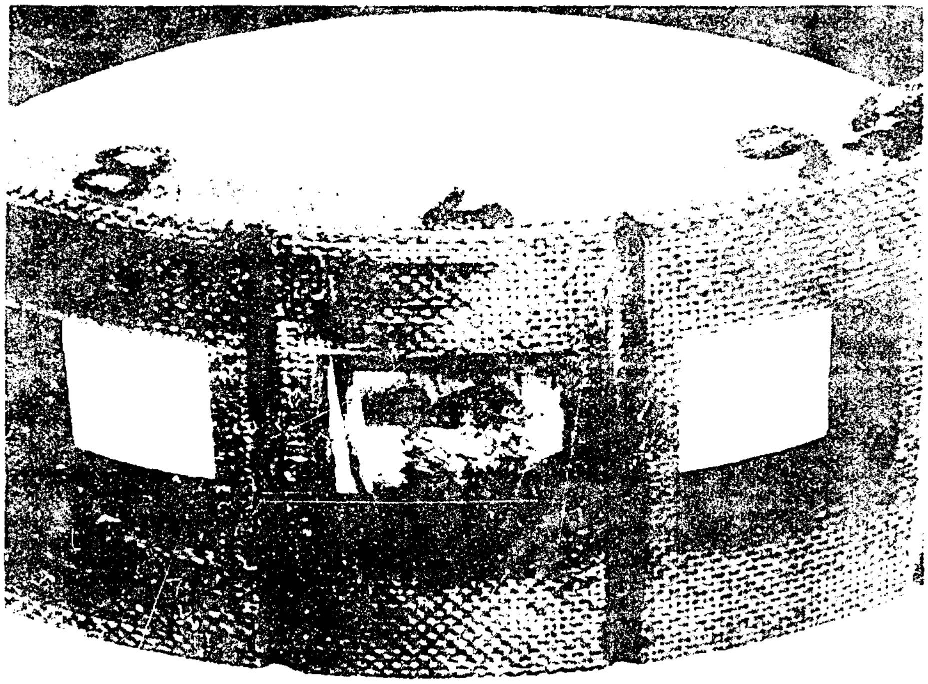

(U) Figure 118. View Showing Skewed Position of Roller No. 7 in Reaction Bearing Cage (S/N HH-1) After Test of Build 41 FE 8148

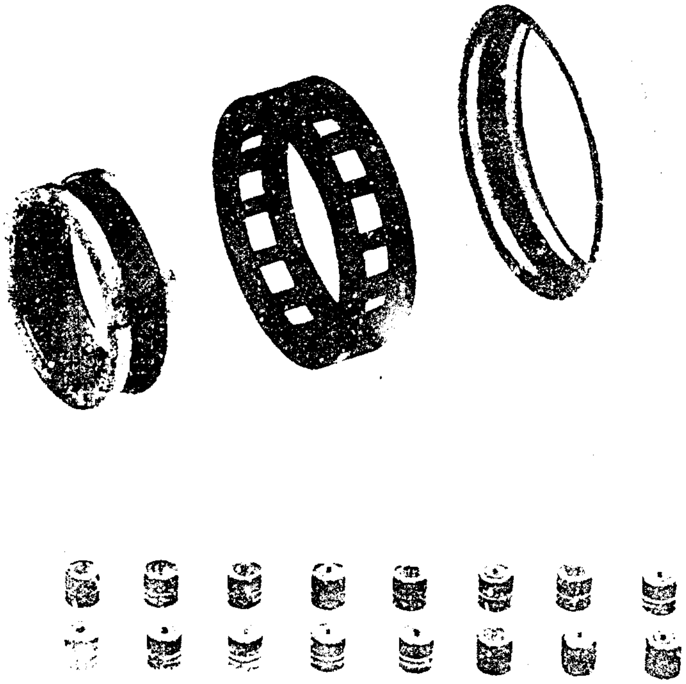

(U) Figure 119. View Showing Overall Condition of Reaction Bearing (S/N HH-1), Turbine End Up (Build 41) FE 81214

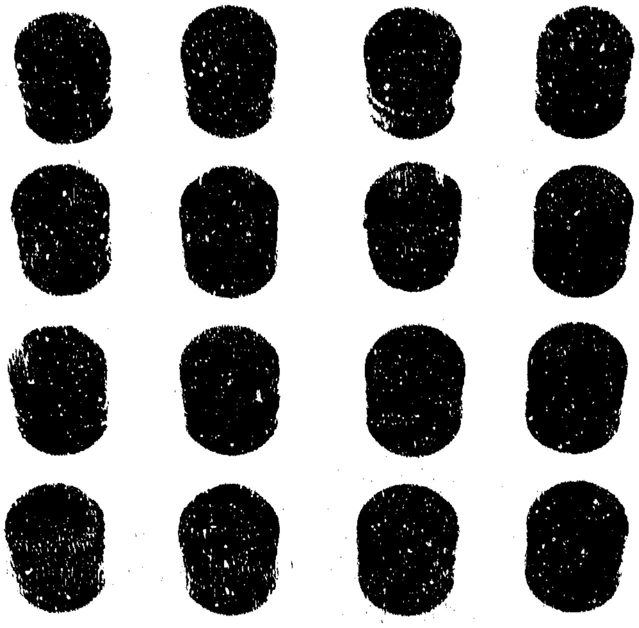

(U) Figure 120. View Showing Condition of Reaction Bearing Rollers (S/N HH-1), Turbine End Up (Build 41) FE 81478

(U) Figure 121. View Showing Condition of Reaction Bearing Inner Race (S/N HH-1) After Test of Build 41 FE 81475

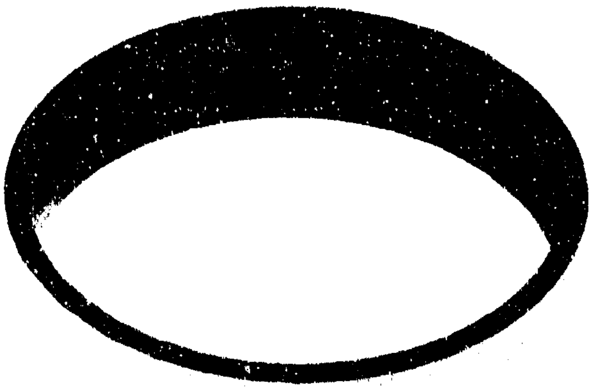

(U) Figure 122. View Showing Condition of Reaction Bearing Outer Race (S/N HH-1) After Test of Build 41 FE 81473

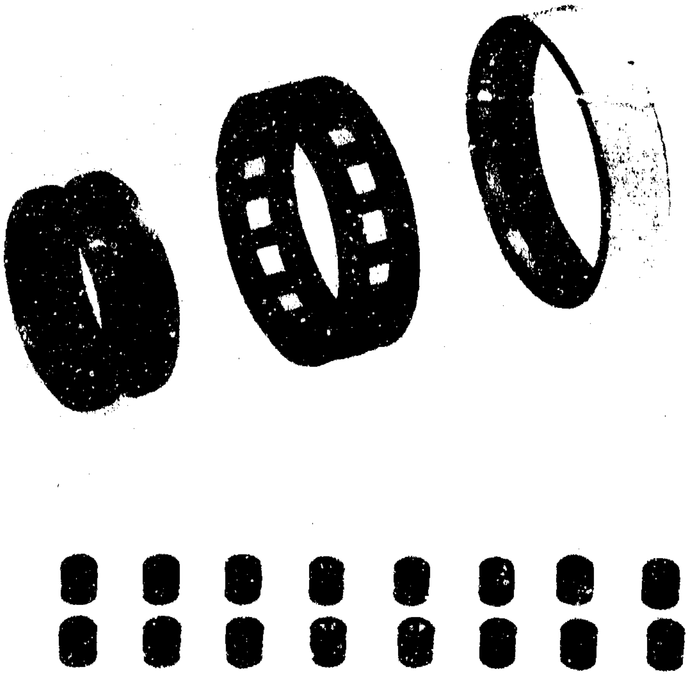

(U) Figure 123. View Showing Overall Condition of Load Bearing (S/N HH-2), Turbine End Up (Build 41) FE 81216

(C) Build 42 of the roller bearing test rig incorporated single crown L/D = 1.000 stainless steel (AMS 5630) rollers, stainless steel (AMS 5630) inner races, Armalon outer-race-guided cages with lateral cooling slots, and outer races fabricated from steel alloy (AMS 6265) with the inside diameter carburized. Both test bearings had a roller end-to-side rail clearance of 0.0202 inch and a negative diametral internal clearance of 0.0043 inch. This fit corresponds to a 0.0053-inch internal clearance with a stainless steel (AMS 5630) outer race.

(C) Testing of Build 42 began on 2 December and was concluded on 5 December 1968. During the test program, 15.3 hours of bearing operation at maximum load and speed condition, and 305 acceleration cycles were accumulated. A bearing coolant reduction survey was also conducted. No increase in outer race temperature was observed when the coolant flow was reduced from 31 gpm to 10 gpm in increments of approximately 5 gpm. Below 10 gpm coolant flow, a rapid increase in bearing outer race temperature was observed and the coolant flow was increased back to 31 gpm where the outer race temperature again stabilized. After completing all program objectives the test rig was pulled from the test stand to permit teardown inspection of the bearings.

(U) Post-test inspection of the roller bearings revealed that both bearings were in good condition and could have undergone further testing. The only discrepancy noted was thermal cracking of the outer races in the areas of cage contact as shown in Figure 124. End wear measurements showed moderate wear on the reaction bearing and extremely light wear on the load bearing. The wear on the reaction bearing was on the turbine end with an average wear of 0.0070 inch and 0.0098 inch on the roller with the maximum wear. Figures 125 and 126 show the condition of the reaction bearing rollers. The wear on the load bearing was on the rear end with an average wear of 0.0005 inch and 0.0014 inch on the roller with the maximum wear. Figures 127 and 128 show the condition of the load bearing rollers. The overall condition of the reaction bearing is shown in Figures 129 and 130, and the load bearing is shown in Figures 131 and 132. The roller bearing qualification test program was concluded with the completion of the Build 42 best.

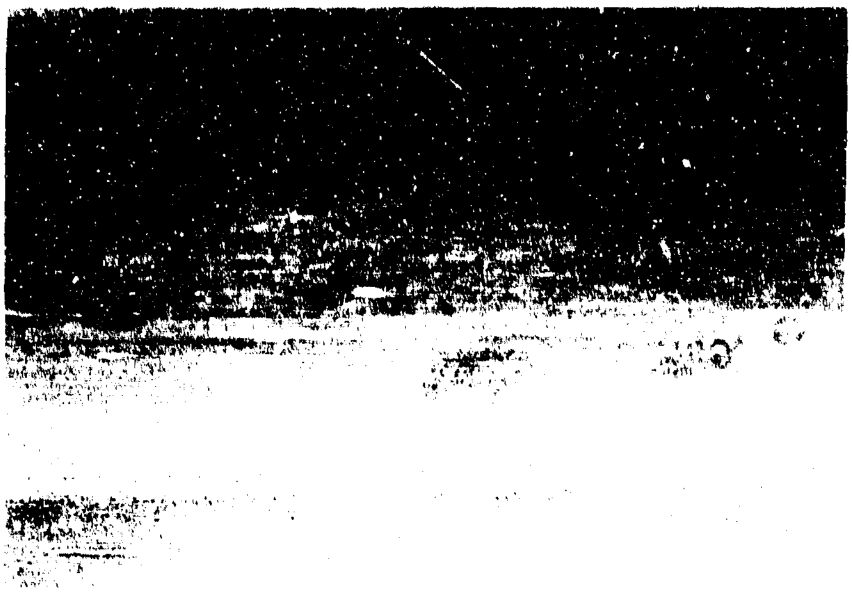

(U) Figure 124. Enlarged View of ID of Outer Race Showing Numerous Thermal Cracks FAL 14328

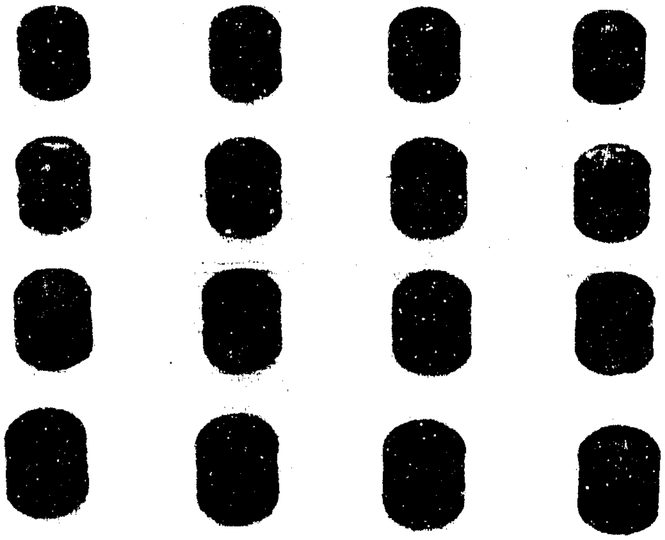

(U) Figure 125. View Showing Condition of Reaction Bearing Rollers (S/N JJ-1) With Rear End Up (Build 42) FE 81801

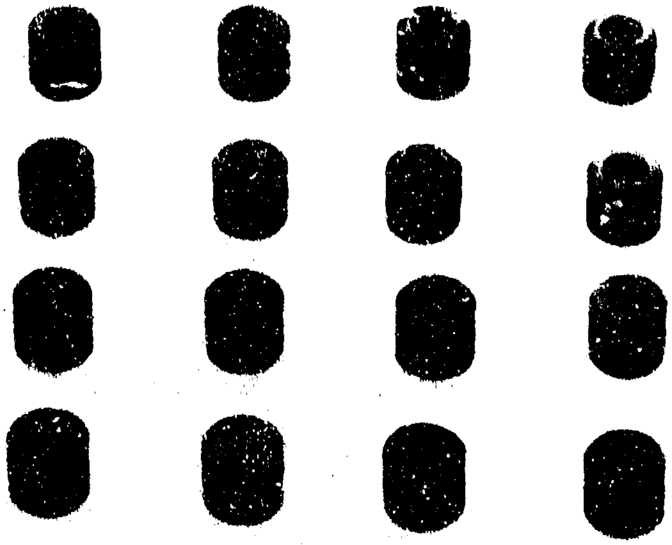

(U) Figure 126. View Showing Condition of Reaction Bearing Rollers (S/N JJ-1) With Turbine End Up (Build 42) FE 81802

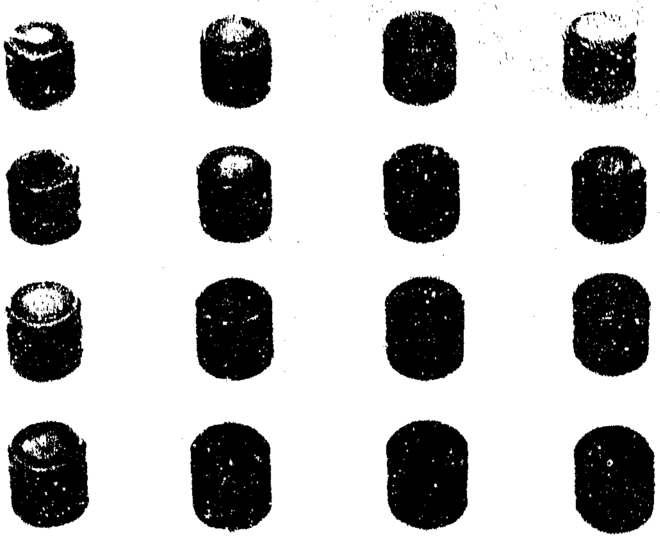

(U) Figure 127. View Showing Condition of Load Bearing Rollers (S/N JJ-2) With Rear End Up (Build 42) FE 81803

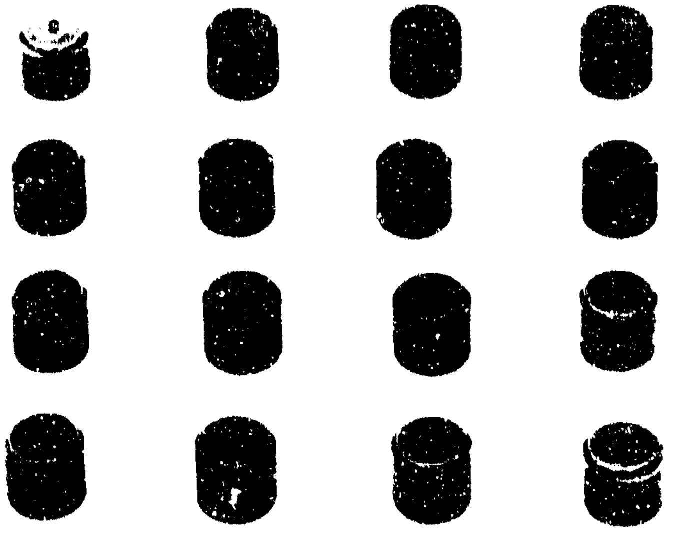

(U) Figure 128. View Showing Condition of Load Bearing Rollers (S/N JJ-2) With Turbine End Up (Build 42) FE 81804

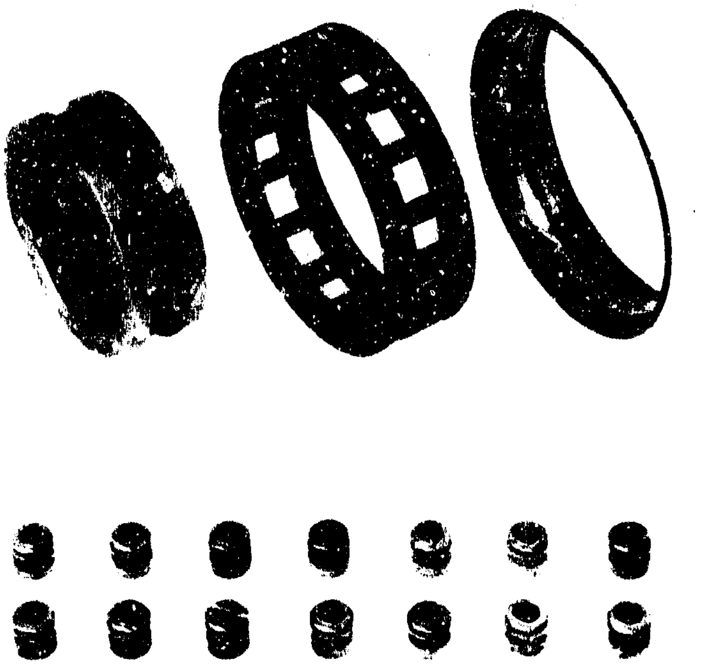

(U) Figure 129. View Showing Overall Condition of Reaction Bearing (S/N JJ-1) Turbine End Up (Build 42) FE 81794

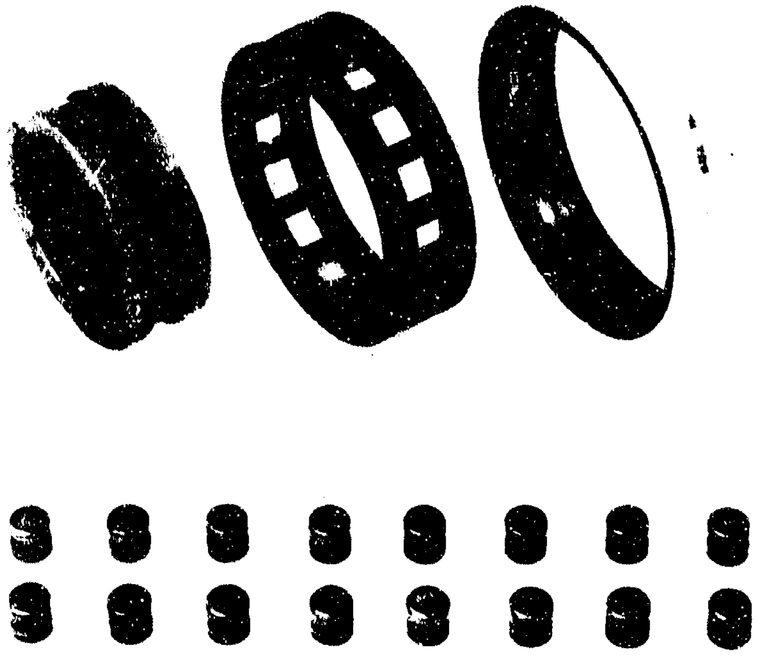

(U) Figure 130. View Showing Overall Condition of Reaction Bearing (S/N JJ-1) Rear End Up (Build 42) FE 81793

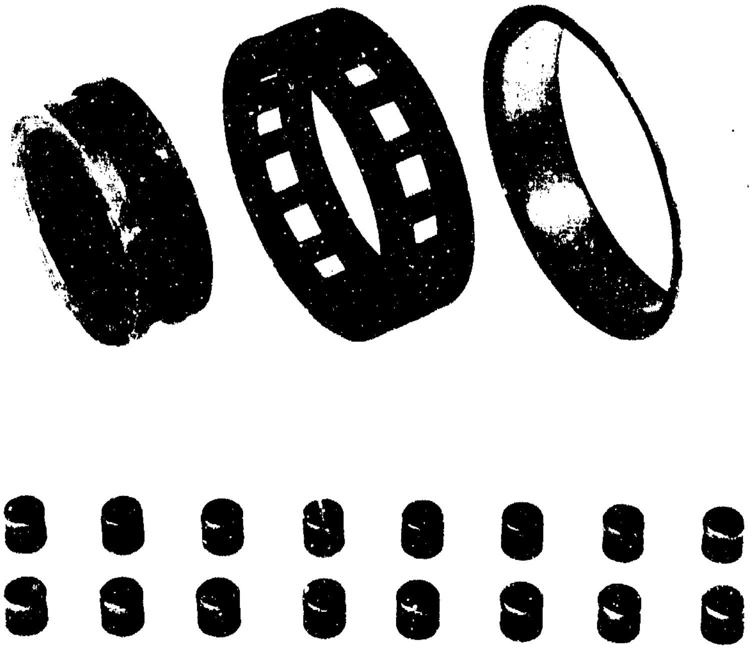

(U) Figure 131. View Showing Overall Condition of Load Bearing (S/N JJ-2) Turbine End Up (Build 42) FE 81796

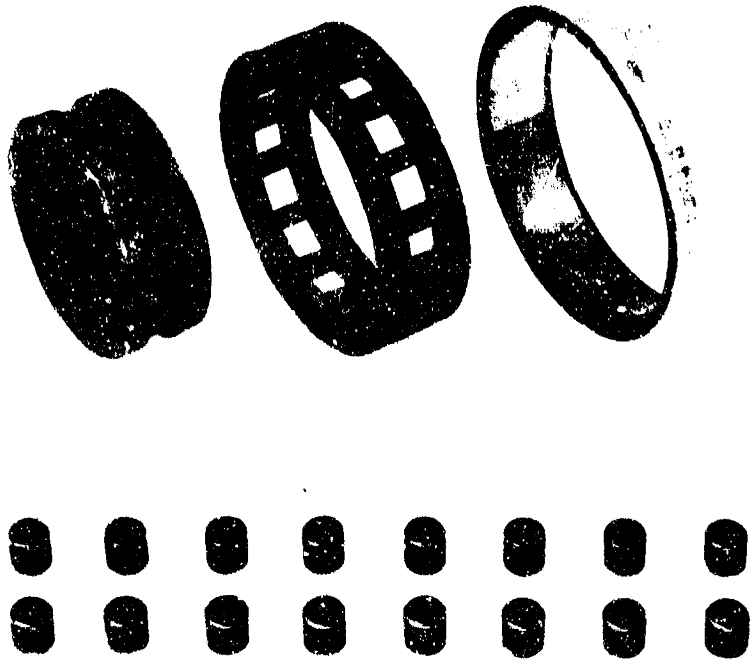

(U) Figure 132. View Showing Overall Condition of Load Bearing (S/N JJ-2) Rear End Up (Build 42) FE 81795

C. PUMP INLET EVALUATION

1. Introduction. 151
2. Summary, Conclusions, and Recommendations 151
3. Testing 153
4. Analysis. 158

C. PUMP INLET EVALUATION

1. Introduction

(U) The objective of this test program was to obtain supporting data for the design of the inlet configuration to be used on the liquid hydrogen and liquid oxygen turbopumps. Because of engine packaging considerations, the proposed demonstrator engine has a flow distributor at the inlet to each main turbopump as shown in Figure 133. The effect of an inlet flow distributor on the head-flow and suction characteristics of the inducer was investigated using water as the test fluid. These data are being used to design a suitable pump inlet configuration within the demonstrator engine envelope.

(U) Figure 133. Proposed Demonstrator Engine Showing Inlet Flow Distributors at the Fuel and Oxidizer Inlets (Circled Areas) GS 7466A

2. Summary, Conclusions, and Recommendations

(U) Nine inlet configurations were evaluated during the preliminary study as shown in Figure 134. Electrical analog studies of these candidate configurations were performed and the head loss coefficients shown in Figure 134 resulted from this study.

NO.	INLET DESCRIPTION	INLET CONFIGURATION	HEAD LOSS COEFFICIENT	HEAD LOSS* psi
1	90 Deg Elbow With Guide Vanes and R/D = 0.75	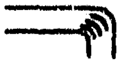	0.06	1.6
2	90 Deg Miter With Guide Vanes	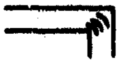	0.20	5.5
3	90 Deg Elbow Without Guide Vanes and R/D = 0.75	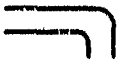	0.26	7.2
4	Double Inlet Without Line Branch Loss (Double Discharge Boost Pump)		0.40	11.1
5	Single Inlet Without Guide Vanes		0.50	13.9
6	Single Inlet With Guide Vanes		0.45	12.5
7	Stepanoff		0.70	19.4
8	Scroll		0.75	20.8
9	90 Deg Miter Without Guide Vanes	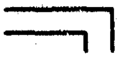	1.20	33.1

*Assuming an Inlet Velocity Head of 27.7psi

(U) Figure 134. Candidate Inlets and Predicted Pressure Loss FD 23194A

(U) Two configurations were selected as a result of this electrical analog study for evaluation on the water test loop. These were a short radius elbow with turning vanes and a single inlet without guide vanes similar to configurations No. 1 and 5 of Figure 134. Although an elbow inlet with guide vanes was the best design analyzed from a head loss and velocity distribution standpoint, it was less suitable for the fuel pump because of the severe space limitations. The single inlet without guide vanes was a more flattened design that would satisfy the envelope requirements of the fuel pump and was selected as the second candidate for evaluation on the water test loop.

(U) Three inlet configurations were tested on the water loop using an existing 350K oxidizer pump inducer fabricated under Contract NAS8-20540. These were: (1) a straight inlet to establish baseline inducer performance, (2) a 112-degree elbow inlet with turning vanes, and (3) a 112-degree flattened pancake inlet.

(U) Suction characteristics of the 350K inducer with the straight inlet compared favorably with predicted levels. Peak suction specific speed was near 25,000 rpm $(gpm)^{1/2}/ft^{3/4}$.

(U) Suction performance with the elbow inlet compared favorably with that of the straight inlet and with predicted suction performance levels. Maximum demonstrated suction specific speed was 24,000 rpm $(gpm)^{1/2}/ft^{3/4}$.

(U) Suction performance with the pancake inlet also compared favorably with that of the straight inlet and with predicted levels of suction performance. Maximum demonstrated suction specific speed was 23,500 rpm $(gpm)^{1/2}/ft^{3/4}$.

(U) Indicated noncavitated performance with the straight inlet was about 15% lower than determined during oxidizer pump tests under Contract NAS8-20540 using LO_2 and LN_2 as the pumped fluids.

(C) The noncavitated head coefficient versus flow coefficient slope was steeper with the elbow inlet and the head coefficients were higher at low flow coefficients than obtained with the straight inlet. The head coefficient flow coefficient characteristic with the pancake inlet was approximately the same level as with the straight inlet, but had a discontinuity between flow-to-speed ratios of 0.16 and 0.18.

(U) Higher noise levels emanate from the pancake inlet at low flow-to-speed ratios and also at high speeds indicating a possible structural problem.

(U) Large static pressure losses occur in the inlet section of both the elbow and pancake housings at low flow-to-speed ratios. These losses appear to be pump related and are accompanied by severe inlet pressure oscillations.

(U) The various inlet configurations were tested over the range of flow-to-speed ratios expected in the engine throttling range; however, maximum speed and flow rates were restricted by test stand limitations to about 40% of design. It is believed, however, that the test results can be extrapolated to design conditions.

(U) The elbow inlet appears to be superior to the pancake inlet and is recommended for both the fuel and liquid oxygen pumps although some slight modification to the inlet may be required to fit this configuration into the engine envelope on the fuel pump inlet.

3. Testing

(U) The pump inlet evaluation test program was conducted using the existing closed loop water test facility in test stand D-34, which is shown in Figure 135. This facility includes a 250-hp d-c motor gearbox unit capable of closely controlled speeds up to 9000 rpm. The test stand has one 5-inch and two 8-inch parallel loops with flow measurement capability from zero to 4000 gpm. A schematic of the D-34 test stand is shown in Figure 136. The test rig incorporated an existing 350K liquid oxygen turbopump inducer, which demonstrated a suction specific speed capability of 23,000 rpm $(gpm)^{1/2}/ft^{3/4}$ in liquid oxygen during the 350K Liquid Oxygen Program, Contract NAS8-20540.

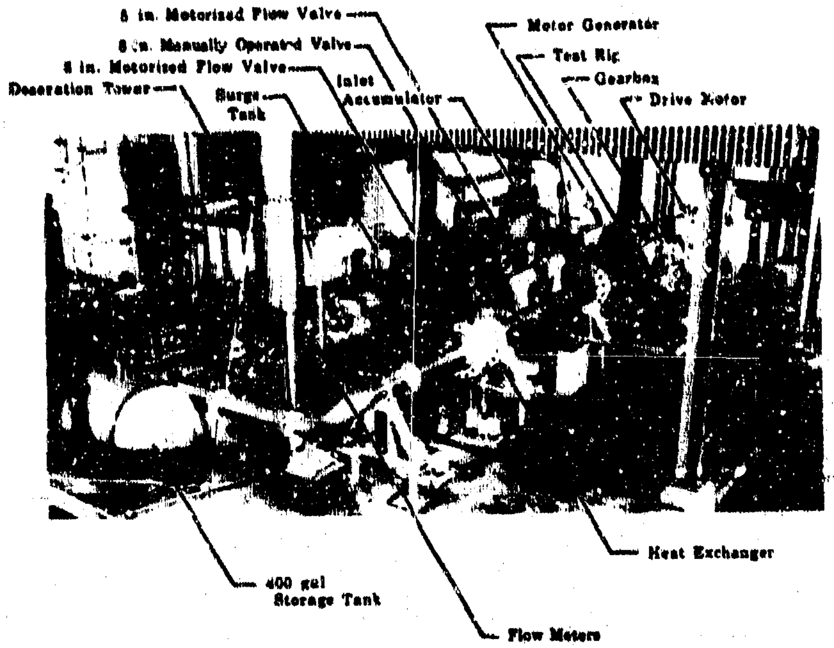

(U) Figure 135. Closed Loop Water Test Facility FD 19643A

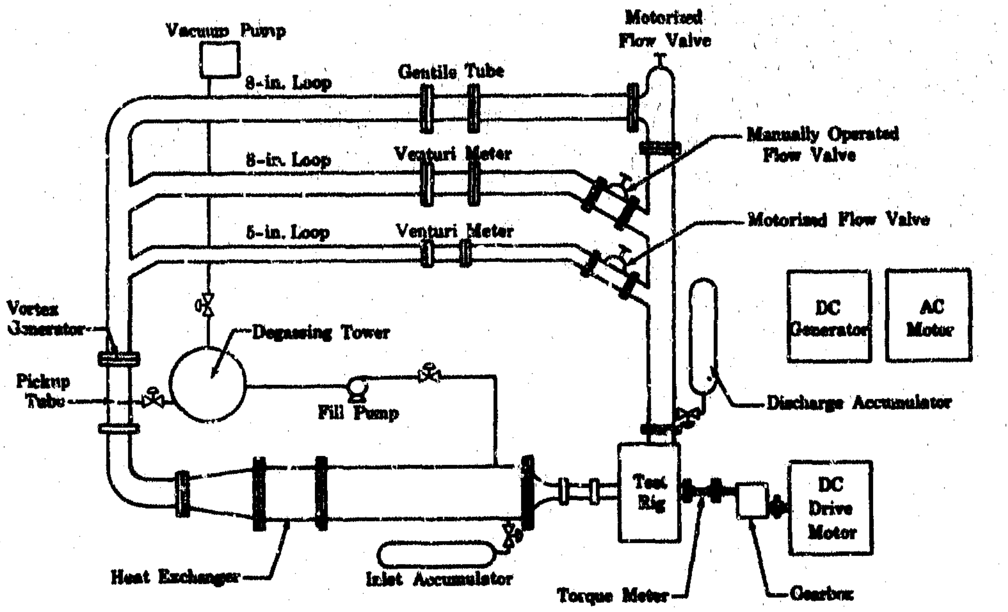

(U) Figure 136. Water Test Stand Schematic FD 19703

(U) Water testing of a straight inlet section, shown in Figure 137, was conducted to establish a baseline. Testing was then conducted on a short radius elbow with turning vanes (Figure 138) and a pancake inlet (Figure 139). Each of these configurations was constructed with transparent windows to permit taking photographs of the flow patterns at the inducer inlet. However, the lucite material was easily damaged by inducer tip cavitation as shown in Figure 140 and little useful information was obtained. In each configuration, damage to the viewing section necessitated replacing the window with a steel insert or fiberglassing over the window.

(U) Testing was conducted by setting a positive inlet pressure at the rig and then accelerating to the desired speed. Flow rate was varied to determine the head-flow characteristics, and inlet pressure was reduced until cavitation occurred to determine suction performance. The test results are summarized in Table XVI.

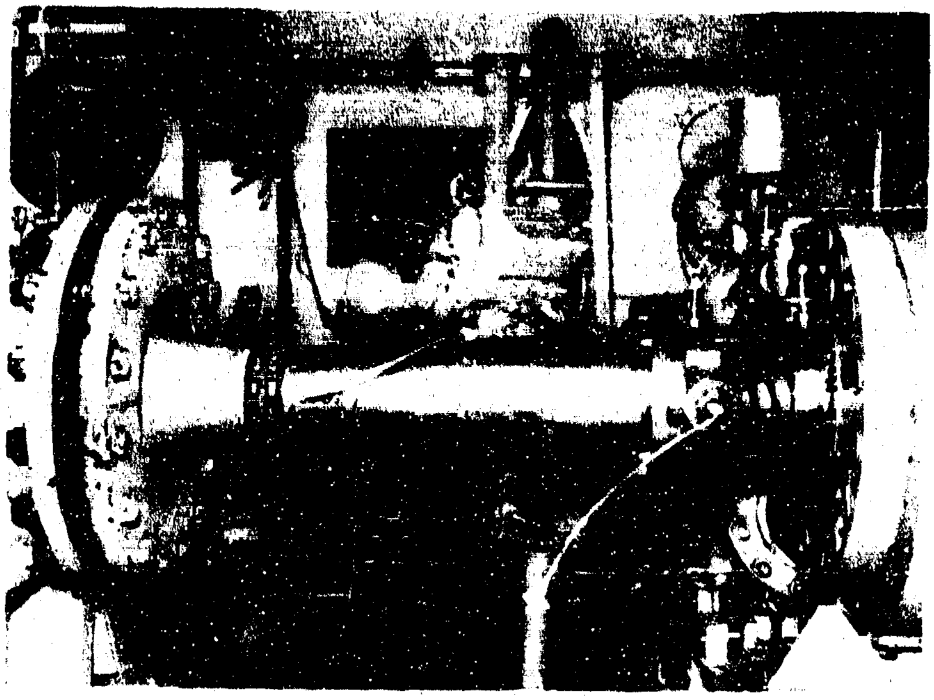

(U) Figure 137. Straight Inlet Test Installation FE 75097

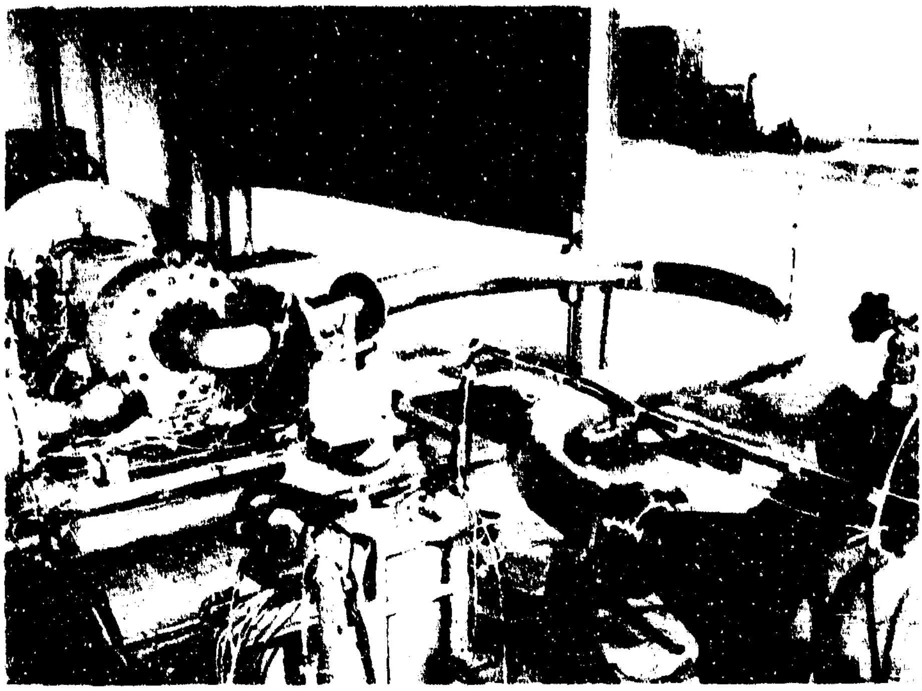

(U) Figure 138. Short Radius Elbow With Turning Vanes Inlet Test Installation FC 16029

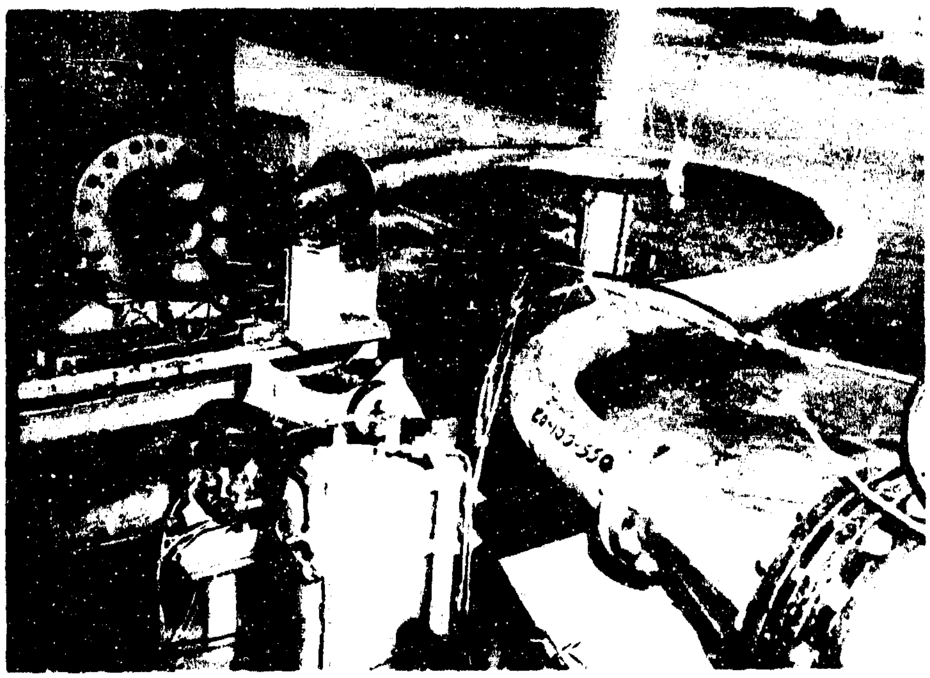

(U) Figure 139. Pancake Inlet Test Installation FE 76743

(U) Figure 140. Cavitation Damage on Lucite Viewing Section FE 75129

(C)(U) Table XVI. Cavitation Test Data

Flow (gpm)	Speed (rpm)	Q/N (gpm/rpm)	Inlet Pressure at 3% Cavitation (psia)	Suction Specific Speed $\left(\frac{(\text{rpm})(\text{gpm})^{1/2}}{\text{ft}^{3/4}}\right)$	Net Positive Suction Head (ft)
			Straight Inlet		
1450	7000	0.21	12.5	22,600	27.0
1540	8500	0.18	17.8	20,900	40.0
1260	7000	0.18	13.0	19,900	29.0
1670	7000	0.24	13.9	21,900	31.0
2025	8500	0.24	19.2	22,600	43.3
1750	8500	0.21	17.4	22,800	39.0
1035	7000	0.15	15.4	15,300	35.0
1030	7000	0.15	14.6	16,700	32.5
1260	8500	0.15	20.0	17,400	45.0
420	7000	0.06	22.0	7,800	49.0
500	6000	0.08	14.6	9,900	32.5

(C)(U) Table XVI. Cavitation Test Data (Continued)

Flow (gpm)	Speed (rpm)	Q/N (gpm/rpm)	Inlet Pressure at 3% Cavitation (psia)	Suction Specific Speed $\left(\frac{(rpm)(gpm)^{1/2}}{ft^{3/4}}\right)$	Net Positive Suction Head (ft)
			Elbow With Turning Vanes		
1910	8500	0.23	18.2	22,500	42.0
1750	8500	0.21	16.4	23,250	38.0
1455	7000	0.21	11.3	23,060	26.3
1545	7500	0.21	12.3	23,900	28.5
2015	8500	0.24	17.4	23,700	40.5
1670	7000	0.24	12.1	23,450	28.1
1565	7000	0.22	11.7	23,100	27.5
1495	8500	0.18	17.9	20,200	41.5
			Banjo Inlet		
1250	8500	0.15	20.7	17,370	44.7
1550	8500	0.18	16.3	22,830	36.0
1830	8500	0.22	16.9	23,450	38.5
2050	8500	0.24	21.3	21,400	47.2
1770	8000	0.22	17.2	22,500	37.0
600	7000	0.086	17.3	11,330	37.5
1010	7000	0.14	14.0	17,100	30.5
1220	7000	0.17	11.0	22,950	23.5
1575	7000	0.23	13.2	22,200	29.0
1695	7000	0.24	15.1	21,100	32.8

4. Analysis

a. Cavitation Performance

(U) Suction performance was based on an inlet pressure in a straight section of line upstream of each of the inlet housings. The approximate locations of the inlet pressure taps are shown in Figures 141, 142, and 143. The suction specific speed versus unit flow for the straight, elbow, and pancake inlets is presented in Figures 144, 145, and 146, respectively. These curves are based on 3% inducer noncavitating head fall-off. The percent predicted head coefficient versus net positive suction head for all cavitation points is provided in Figures 147 through 152. In some instances, the 3% head fall-off point was not reached; however, it was apparent visually and from increased noise, that the inducer was cavitating. Percent predicted head coefficient versus suction specific speed is shown in Figures 153 through 158.

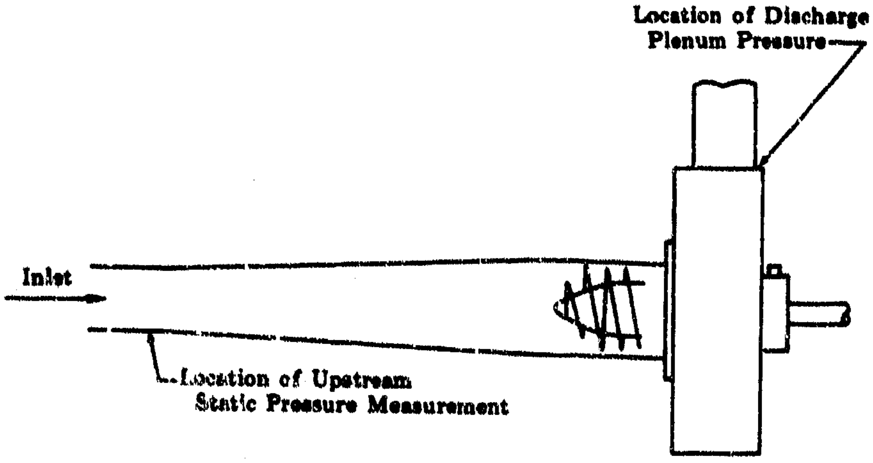

(U) Figure 141. Straight Inlet Test Section Pressure Tap Locations FD 25424

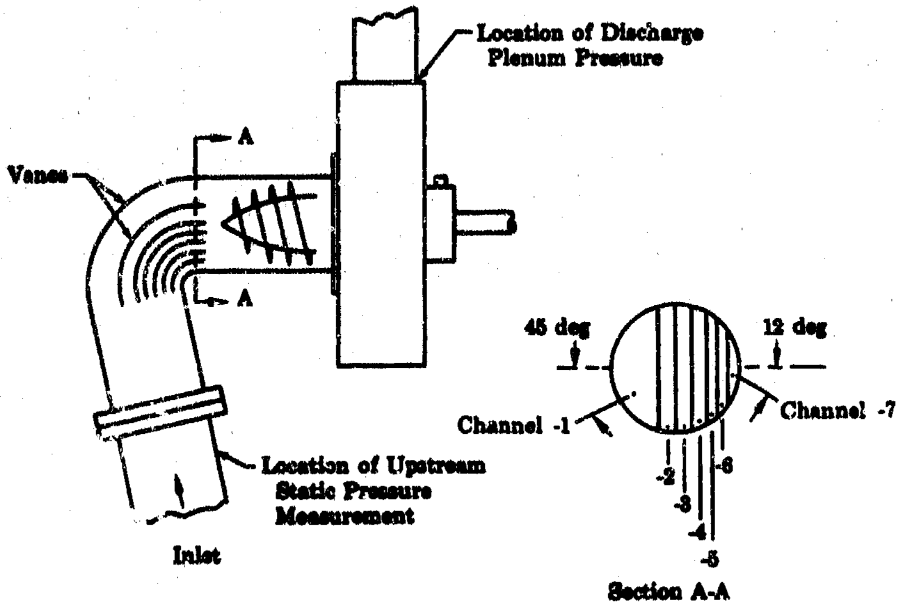

(U) Figure 142. Elbow Test Section Pressure Tap Locations FD 25425

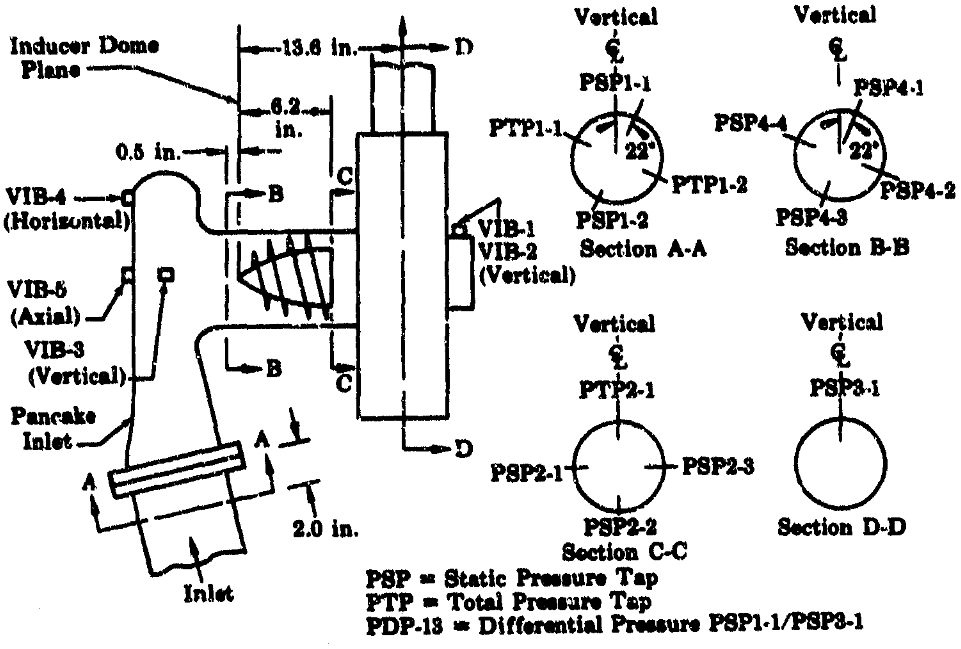

PSP = Static Pressure Tap
PTP = Total Pressure Tap
PDP-13 = Differential Pressure PSP1-1/PSP3-1

(U) Figure 143. Pancake Test Section Pressure Tap Locations FD 25426

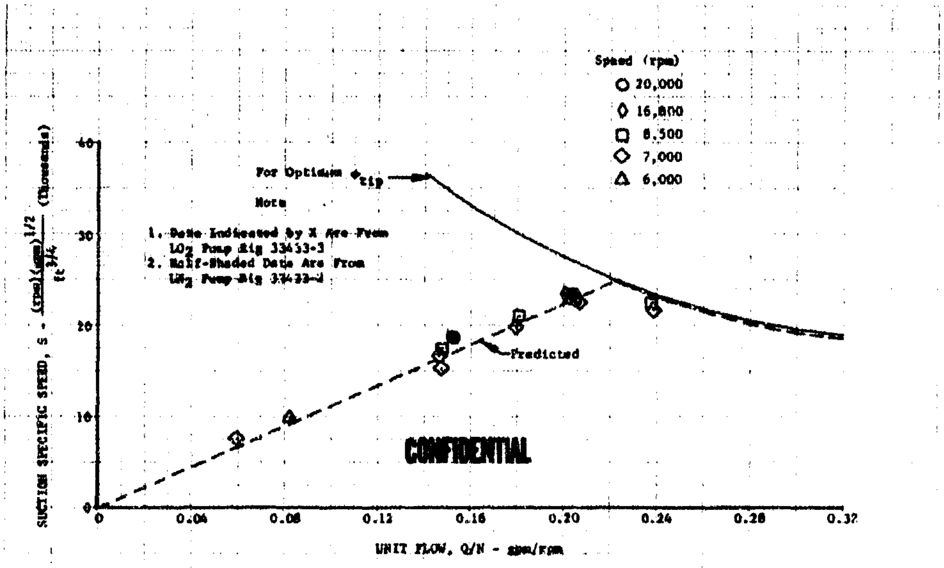

(U) Figure 144. Suction Specific Speed vs Unit Flow for Straight Inlet DFC 66833

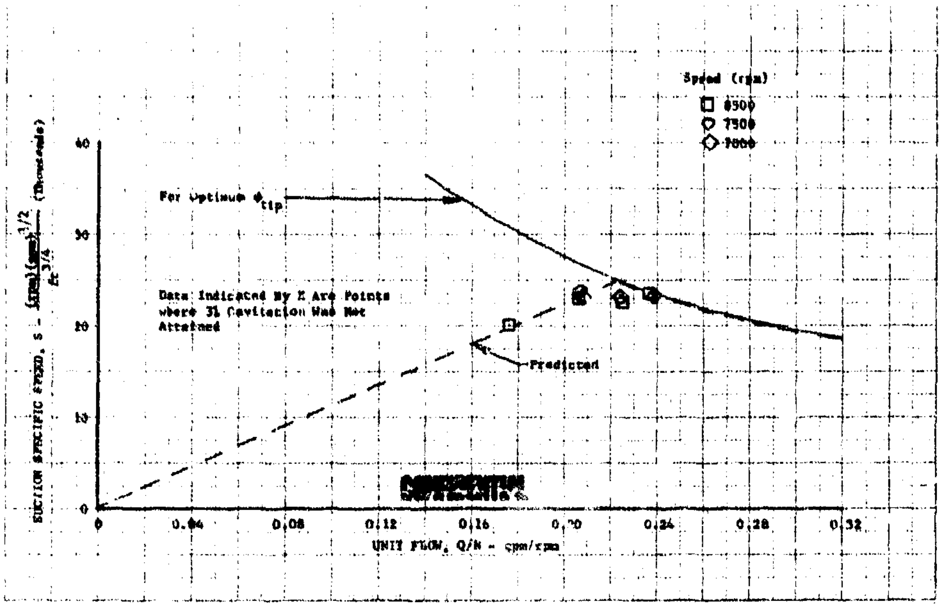

(U) Figure 145. Suction Specific Speed vs Unit Flow for Elbow Inlet DFC 66834

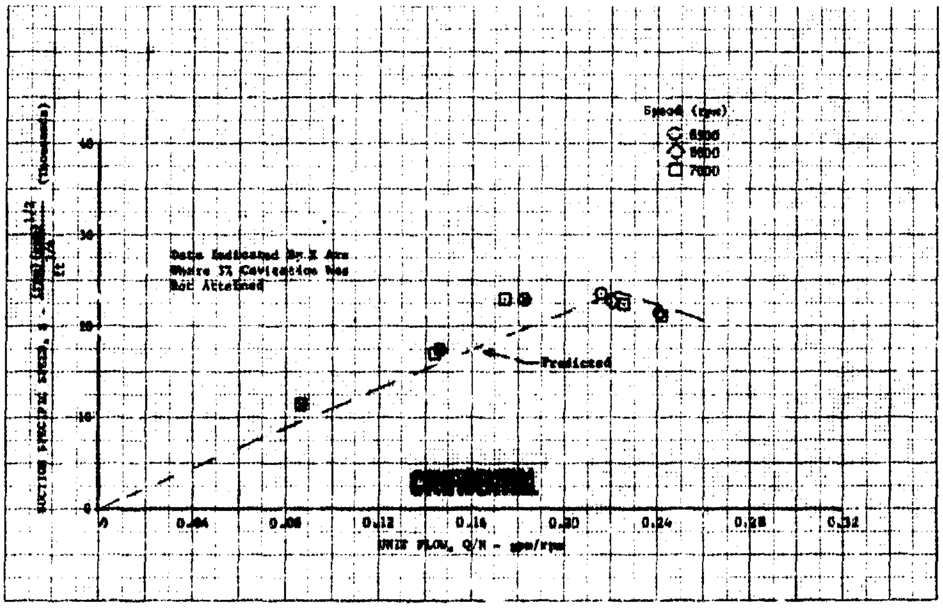

(U) Figure 146. Suction Specific Speed vs Unit Flow for Pancake Inlet DFC 66835

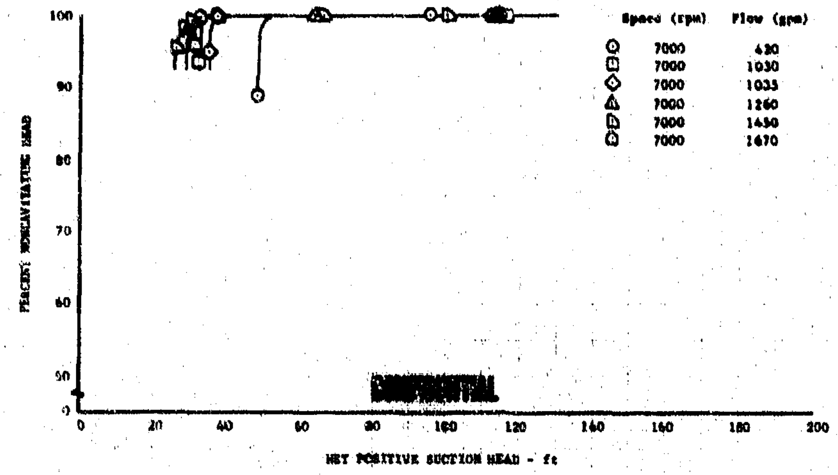

(U) Figure 147. Percent Noncavitating Head vs Net Positive Suction Head (Straight Inlet) DFC 66836

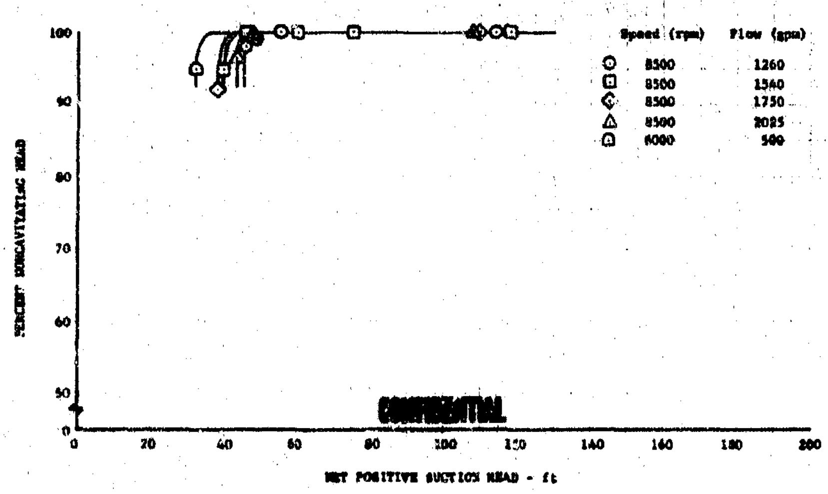

(U) Figure 148. Percent Noncavitating Head vs Net Positive Suction Head (Straight Inlet) DFC 66837

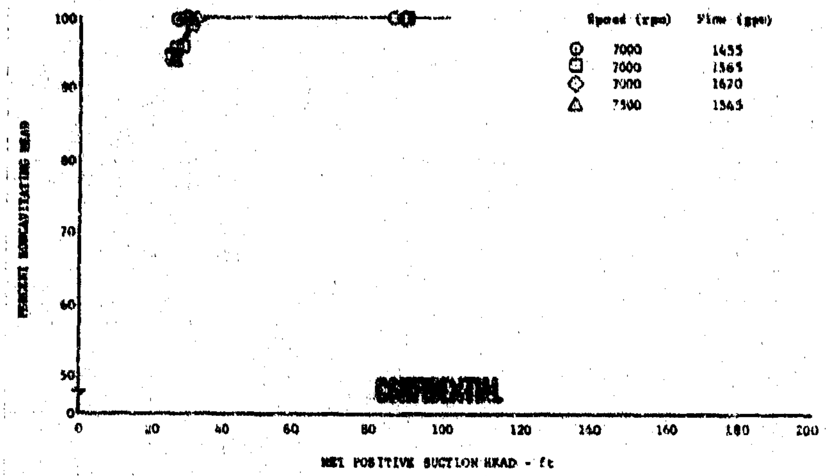

(U) Figure 149. Percent Noncavitating Head vs Net Positive Suction Head (Elbow Inlet) DFC 66838

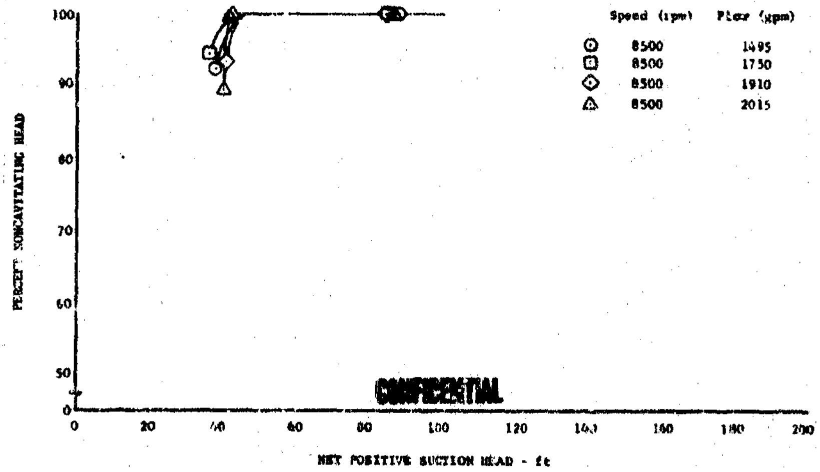

(U) Figure 150. Percent Noncavitating Head vs Net Positive Suction Head (Elbow Inlet) DFC 66839

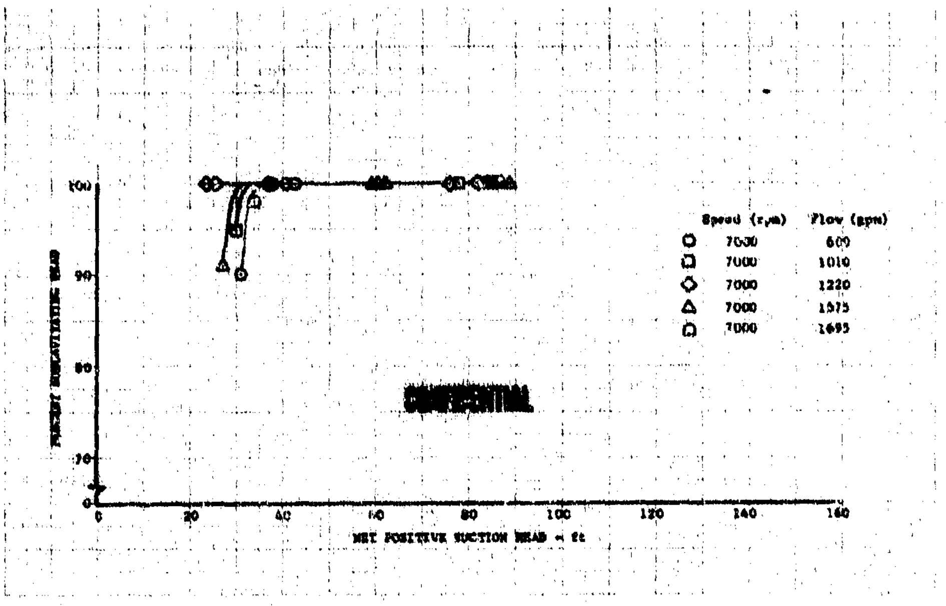

(U) Figure 151. Percent Noncavitating Head vs Net Positive Suction Head (Pancake Inlet) DFC 66840

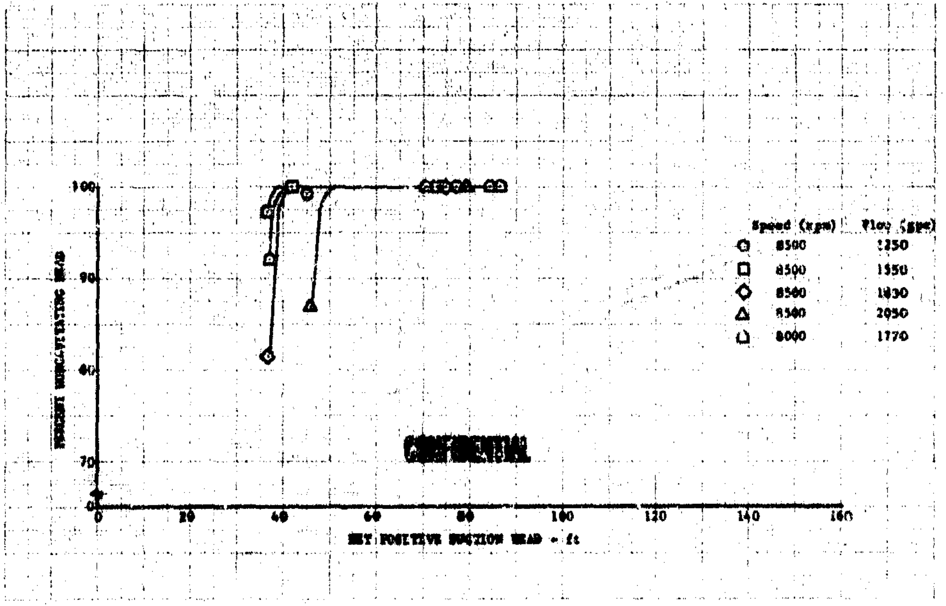

(U) Figure 152. Percent Noncavitating Head vs Net Positive Suction Head (Pancake Inlet) DFC 66841

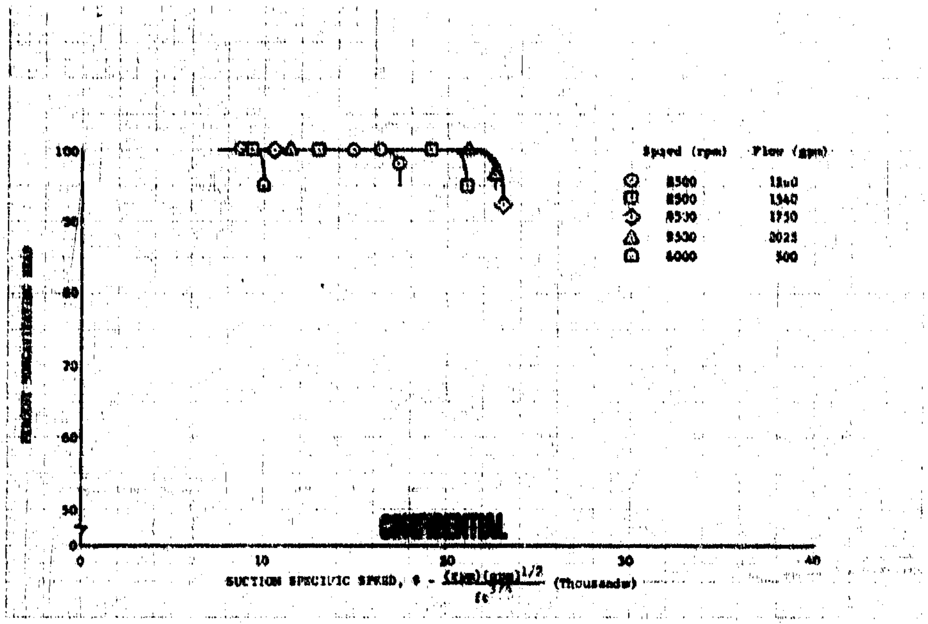

(U) Figure 153. Percent Noncavitating Head vs Suction Specific Speed (Straight Inlet) DFC 66842

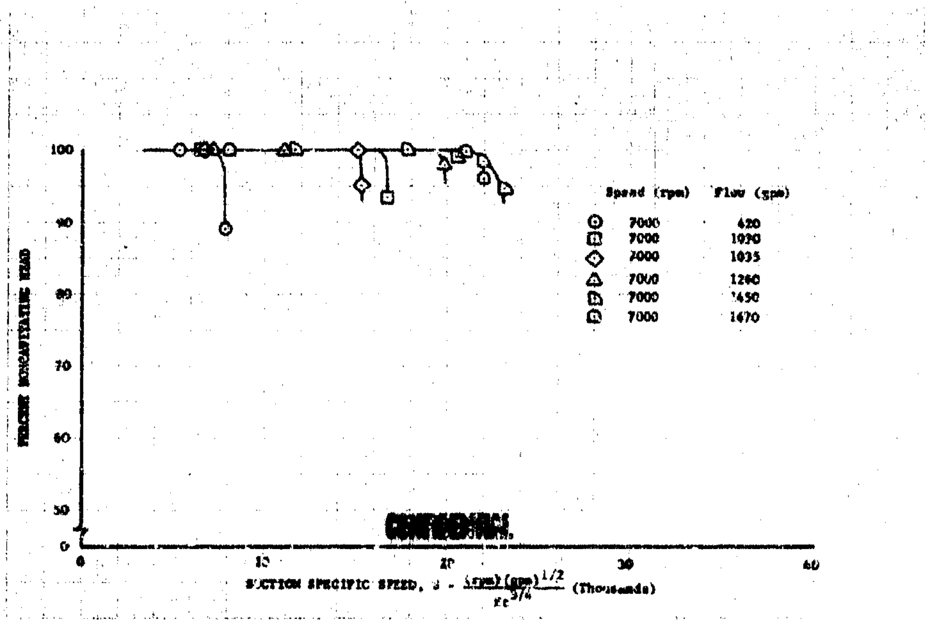

(U) Figure 154. Percent Noncavitating Head vs Suction Specific Speed (Straight Inlet) DFC 66843

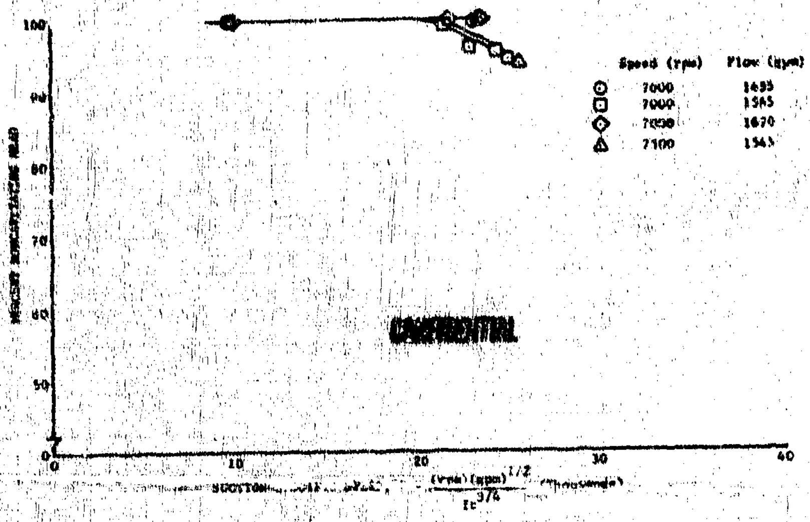

(U) Figure 155. Percent Noncavitating Head vs Suction Specific Speed (Elbow Inlet) DFC 66844

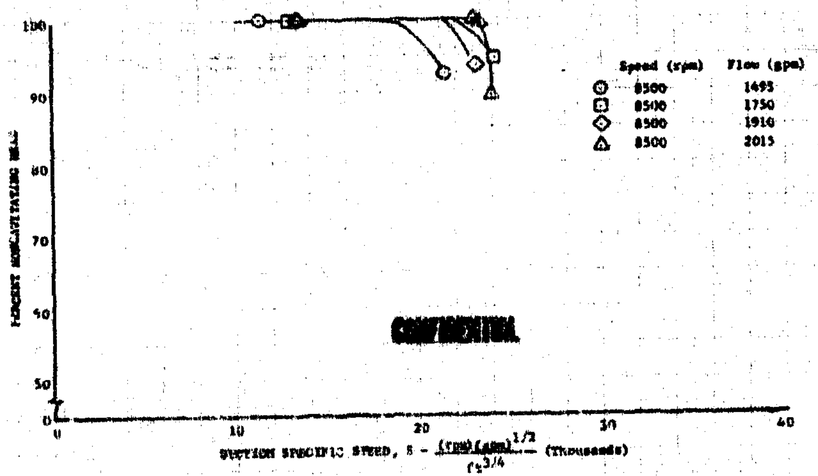

(U) Figure 156. Percent Noncavitating Head vs Suction Specific Speed (Elbow Inlet) DFC 66845

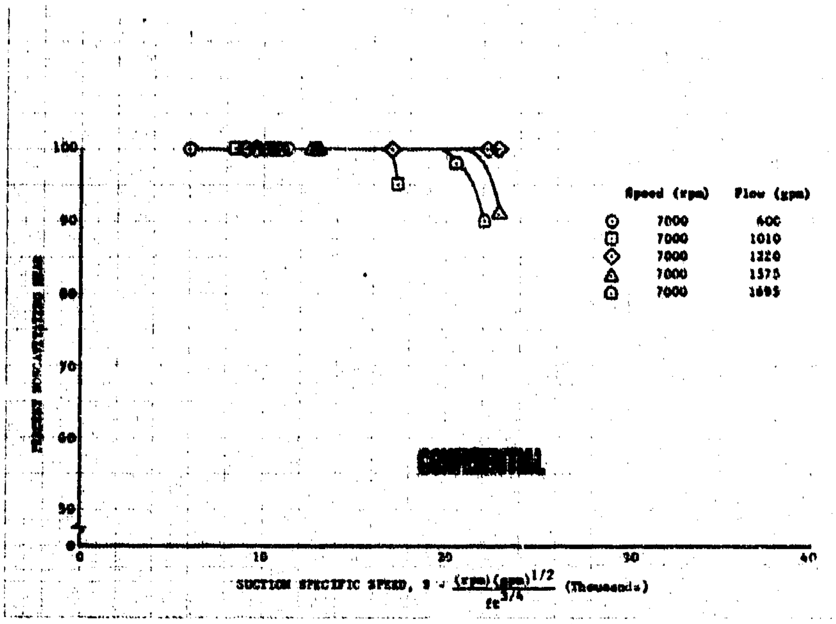

(U) Figure 157. Percent Noncavitating Head vs Suction Specific Speed (Pancake Inlet) DFC 66846

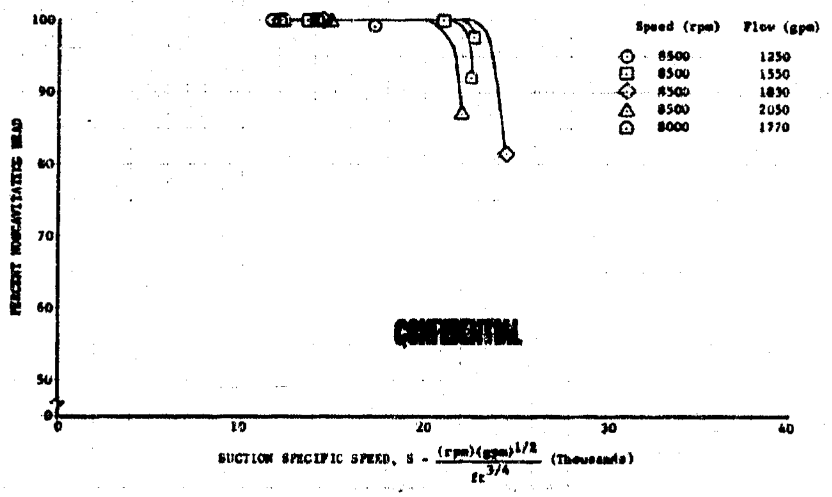

(U) Figure 158. Percent Noncavitating Head vs Suction Specific Speed (Pancake Inlet) DFC 66847

(U) Suction performance of the 350K inducer for all three inlet configurations was as predicted. The predicted levels for the elbow and pancake inlets used the baseline level for the straight inlet, corrected for the expected total pressure losses in the elbow and pancake, respectively, using the loss factors predicted by the electrical analog study shown in Figure 134. The predicted total pressure loss through the elbow inlet was small, thereby providing a suction specific speed curve that is essentially the same as the baseline straight inlet. Predicted peak suction specific speed for the pancake was 23,700 rpm $(gpm)^{1/2}/ft^{3/4}$, which represents a loss of 1300 rpm $(gpm)^{1/2}/ft^{3/4}$ from the straight inlet baseline.

(C) Data from the 350K pump rig using both LO_2 and LN_2 obtained under Contract NAS8-2540 are shown in Figure 144. Suction specific speed values for LO_2 and LN_2 data were corrected for recirculation flow and thermodynamic suppression head and are also based on 3% inducer head fall-off. Although the water tests were limited to flow rates and speed of about 40% of design because of test stand limitations, the excellent agreement between the water data and the high speed (20,000 rpm) LO_2 tests indicate that the water test results can be used to predict engine requirements.

(U) At low flow-to-speed ratios, noise and vibration levels were considerably higher than at flow-to-speed ratios near design. Large static pressure losses in the inlet section of both the elbow and pancake configurations accompanied by severe inlet pressure oscillations were also noted. During throttling operation the pump would operate in the flow-to-speed ratio range of these inlet disturbances. Several cavitation points were taken with the pancake inlet at these conditions and suction performance was as predicted. No cavitation data were obtained at low flow-to-speed ratios with the elbow inlet, however, the results of the pancake inlet did not indicate that cavitation performance was adversely affected.

b. Noncavitated Performance

(U) Noncavitated performance, which is shown in Figures 159, 160, and 161, was based on a static discharge pressure measured in the discharge plenum. Although this does not represent the true inducer characteristics because of the additional housing losses, it was used for comparison because it was believed that the plenum pressure measurement was the most repeatable.

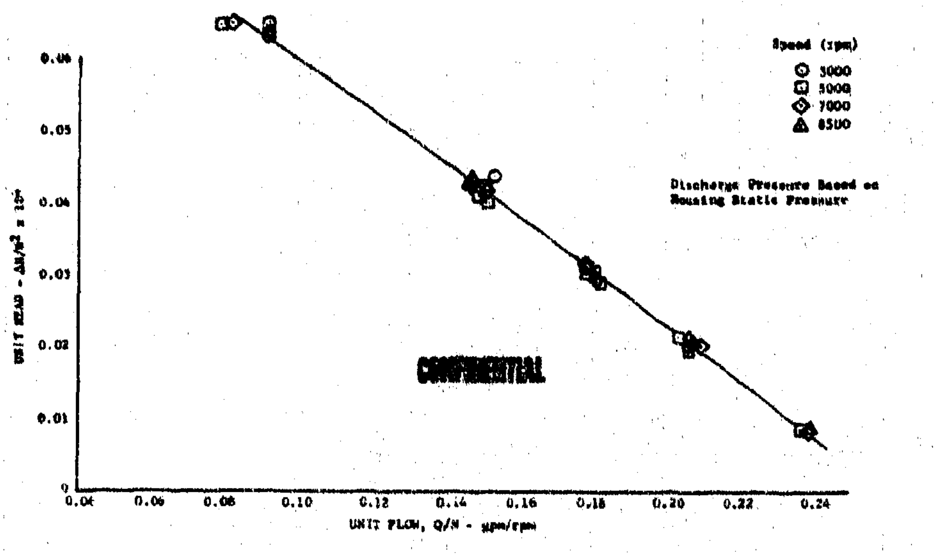

(U) Figure 159. Unit Head vs Unit Flow (Straight Inlet) DFC 66848

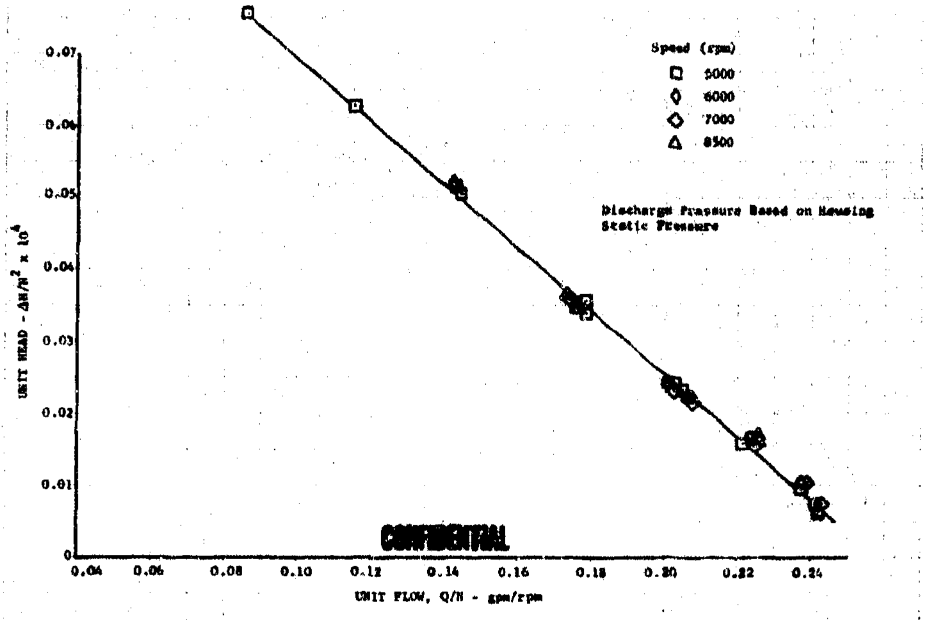

(U) Figure 160. Unit Head vs Unit Flow (Elbow Inlet) DFC 66849

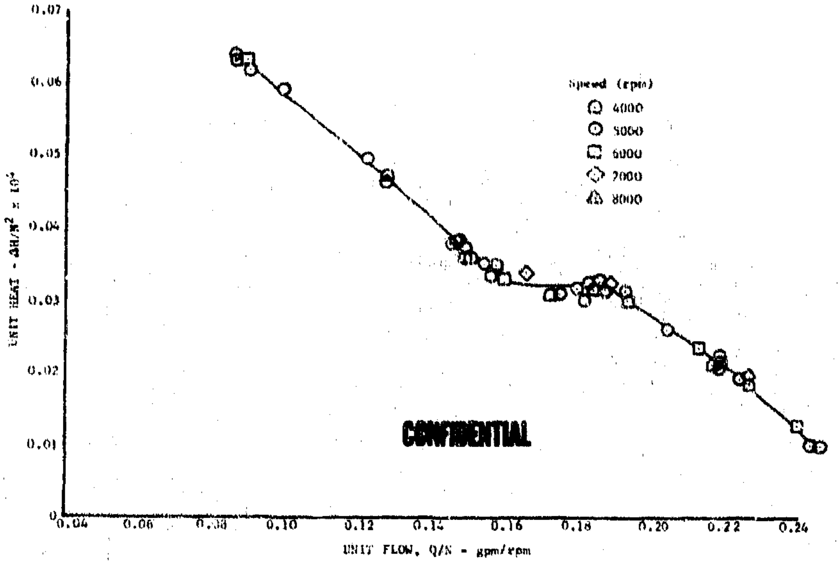

(U) Figure 161. Unit Head vs Unit Flow (Pancake Inlet) DFC 66850

(U) Noncavitated head rise based on the static pressure tap at the impeller discharge was approximately 15% lower than observed with liquid oxygen during previous testing with the discharge pressure tap in a similar location. The reduced head rise may be attributed to; (1) leakage past labyrinth seals that could affect the static inducer discharge measurement (the pressure tap location was directly upstream of the impeller front labyrinth seals and the water test rig had no seals or impeller); (2) the running blade clearance was greater for the water tests than on the liquid oxygen tests. Although both pumps had the same assembled tip clearances they operated at significantly different temperatures and the difference in thermal contraction of the inducer and housing reduced running clearance at liquid oxygen temperatures. The increased recirculation flow during the water tests with increased tip clearances would be expected to reduce head rise.

(C) The noncavitated head coefficient for the elbow inlet was higher and had a steeper slope than the straight inlet. This effect is because of the reduction of prerotation with the elbow inlet. At capacities less than design, prerotation with a straight inlet is in the direction of impeller rotation, which results in a reduction of head. It can be seen from Euler's equation for ideal head rise,

$$H_i = \frac{U_2 C_{u_2} - U_1 C_{u_1}}{g}$$

that with the tangential component of inlet fluid velocity (C_{u1}) positive (i.e., in the direction of impeller rotation) a reduction of head results. Prerotation with the straight inlet was investigated and is shown in Figure 162, presented as an inlet line wall static pressure rise. It can be seen that the pressure rise reached a minimum (no prerotation) at the design flow-to-speed ratio of 0.22.

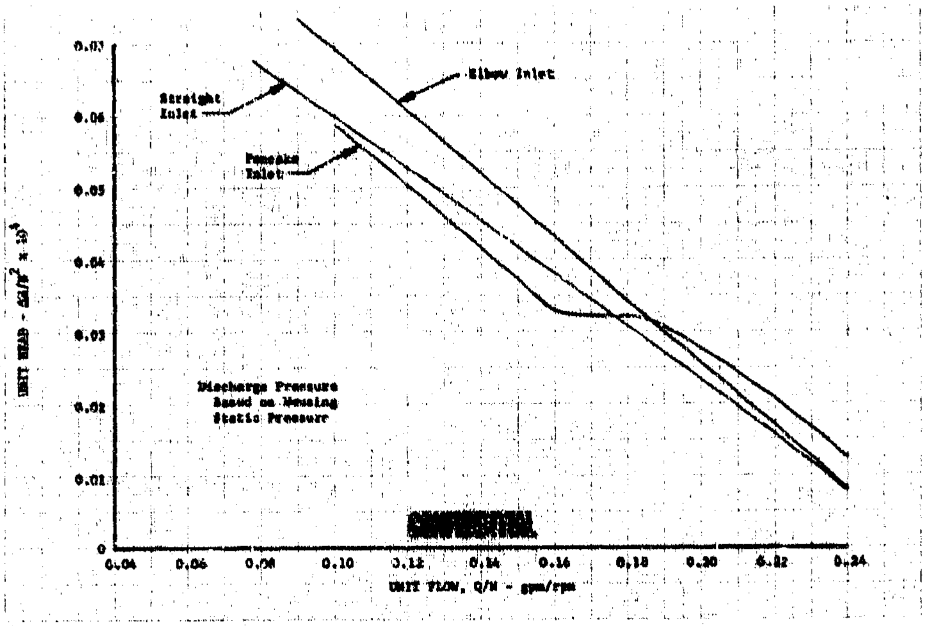

(U) Figure 162. Comparison of Unit Head vs Unit Flow for All Inlets Tested DFC 66851

(C) The head coefficient, flow coefficient characteristic with the pancake inlet was approximately the same level as with the straight inlet but had a discontinuity between flow-to-speed ratios of 0.16 and 0.18.

(U) A comparison of the head coefficient, flow coefficient characteristics for all inlets tested is provided in Figure 163. The velocity profile obtained from a traversing total pressure probe located just upstream of the inlet is provided in Figure 164. The curve indicates the effect of the upstream bend. The magnitude of the variation about a mean velocity is small and should not be a major factor in the inlet pressure disturbances.

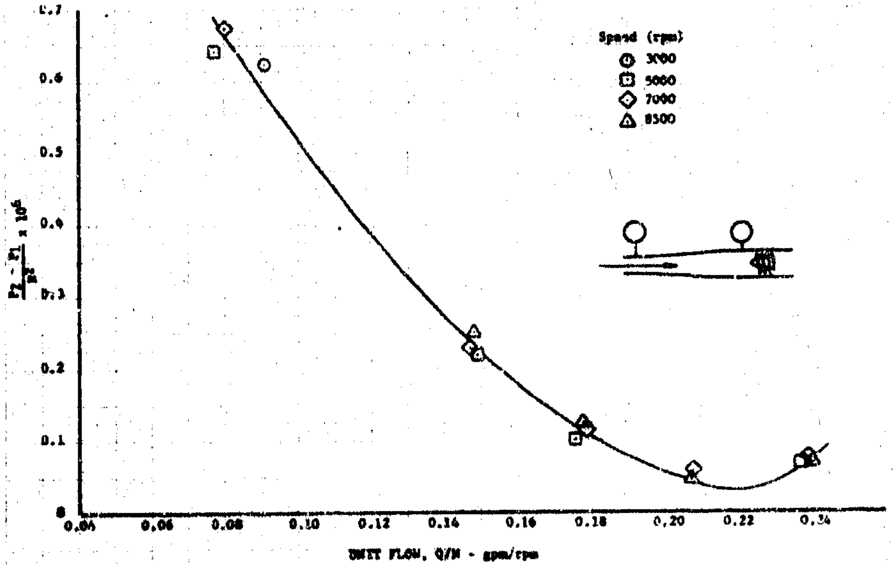

(U) Figure 163. Inlet Line Wall Static Pressure Rise Because of Prerotation (Straight Inlet) DF 68530

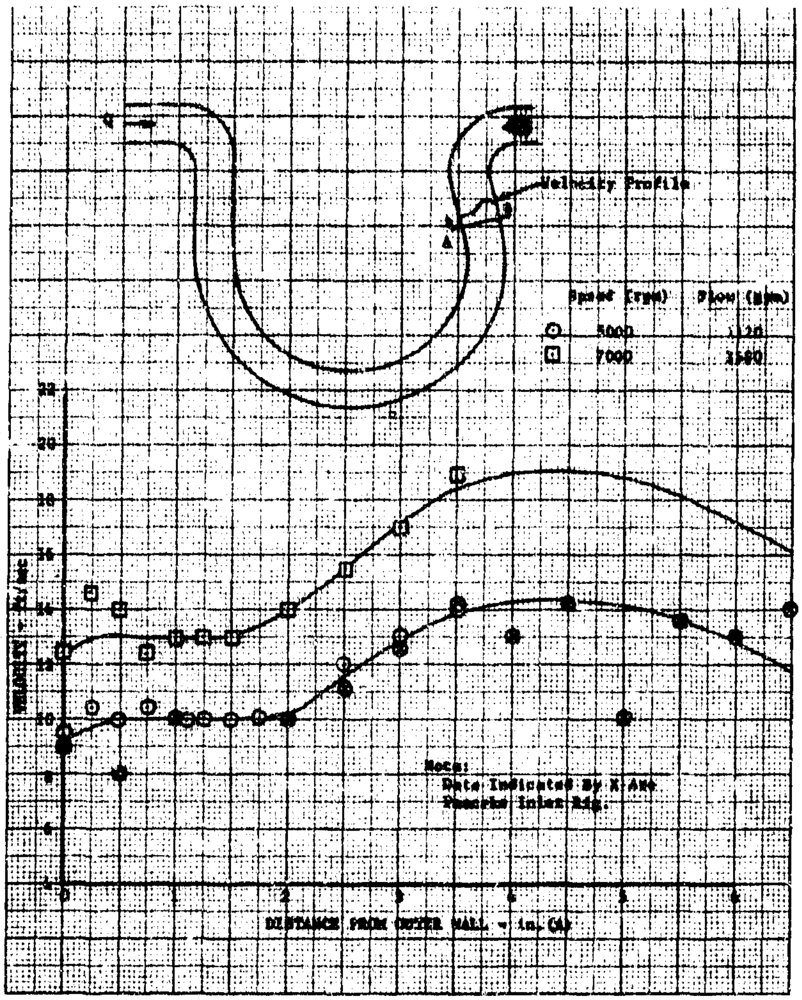

(U) Figure 164. Velocity Profile at Inlet Housing Flange DF 66852

D. NOZZLE FABRICATION INVESTIGATION

1. Introduction. 173
2. Summary, Conclusions, and
Recommendations 173
3. Analysis. 173
4. Fabrication Investigation 180
5. Test. 183

D. NOZZLE FABRICATION INVESTIGATION

1. Introduction

(U) An investigation of nozzle fabrication techniques was conducted to provide additional data and information to support the subsequent design of the two-position nozzle. Sample nozzle panels were fabricated to evaluate manufacturing techniques, and successful panels were subjected to hydraulic stress and thermal cycling tests to determine structural capability.

2. Summary, Conclusions, and Recommendations

(U) Nozzle design and fabrication optimization studies were conducted and completed. It was concluded that the material most suitable for constructing this two-position nozzle application was Inconel 625 (AMS 5599) and that the internal corrugated design was the most feasible to fabricate. An important factor in this selection was that the design allowed the use of standard stiffener bands on the smooth outer surface.

(U) It was also concluded that stiffener bands of the "dunce hat" design would be used for the optimum lightweight configuration. The progressive die forming process produced good corrugation detail with minimum elongation and was selected for final fabrication. Resistance seam welding the assembly provided the easiest and most reliable construction method and produced high quality stiffener bands, as substantiated by the samples fabricated and the hydrostatic tests performed.

(C) Twenty-one thermal fatigue tests were conducted on segments of the sample panels. The proposed panel (0.005-inch thick corrugated inner sheet with 0.010-inch thick outer sheet) could not complete the required minimum of 300 thermal cycles at the predicted nozzle temperatures; in fact, the average was 33 cycles. The nozzle hot wall temperature had to be decreased to 1760°R, which is 400° below that desired, before 300-cycle fatigue life could be achieved. Increasing the thickness of the corrugated sheet to 0.010 inch allowed the hot wall temperature to be increased to 2010°R for 300 cycles of fatigue life, while causing only a 10% increase in the total nozzle weight. Therefore, this 0.010/0.010-inch thick nozzle configuration using the internal corrugation design is recommended for the subsequent two-position nozzle design.

3. Analysis

a. Design Study

(U) To optimize the performance of an engine using a lightweight, two-position nozzle, it was necessary to design the nozzle to maintain the inner wall temperature as hot as possible. This level of temperature was controlled mainly by the material selection, material thickness, coolant flow rate, coolant velocity, and configuration geometry.

(U) It is desirable to exit the cooling gases at as high a temperature as possible, which would be as shown in Figure 165. To do this, the inner hot wall must be run at as high a temperature as physically possible for the entire length of the nozzle (i.e., constant hot wall temperature).

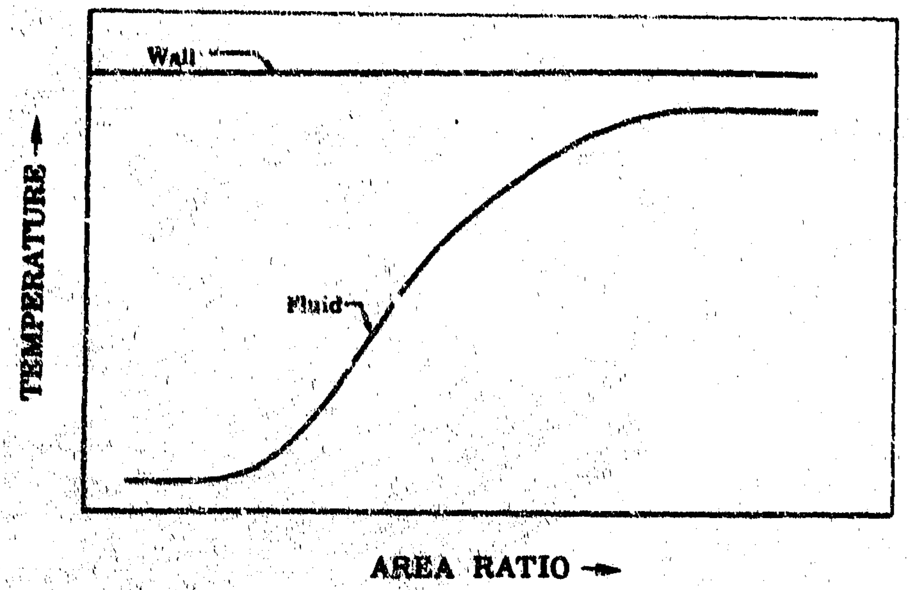

(U) Figure 165. Fluid Temperature vs Area Ratio FD 25317

(U) Because the heat flux (Q/A) decreases along the nozzle length, as shown in Figure 166, and film coefficient, h, is equal to (Q/A)ΔT, the inside film coefficient plotted against area ratio is as shown in Figure 167. Because h ≅ (1/A), the coolant passageway flow area required along the nozzle is shaped as shown in Figure 168.

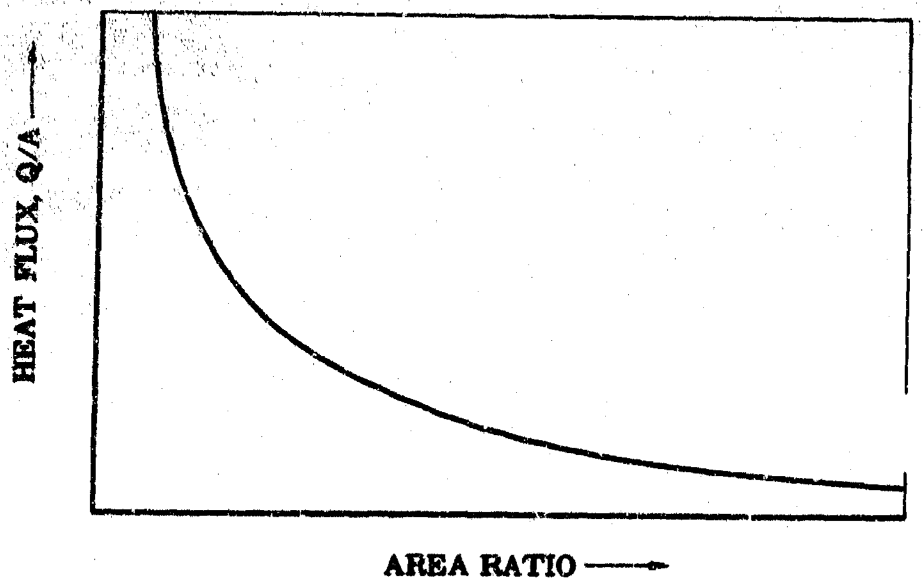

(U) Figure 166. Heat Flux vs Area Ratio FD 25318

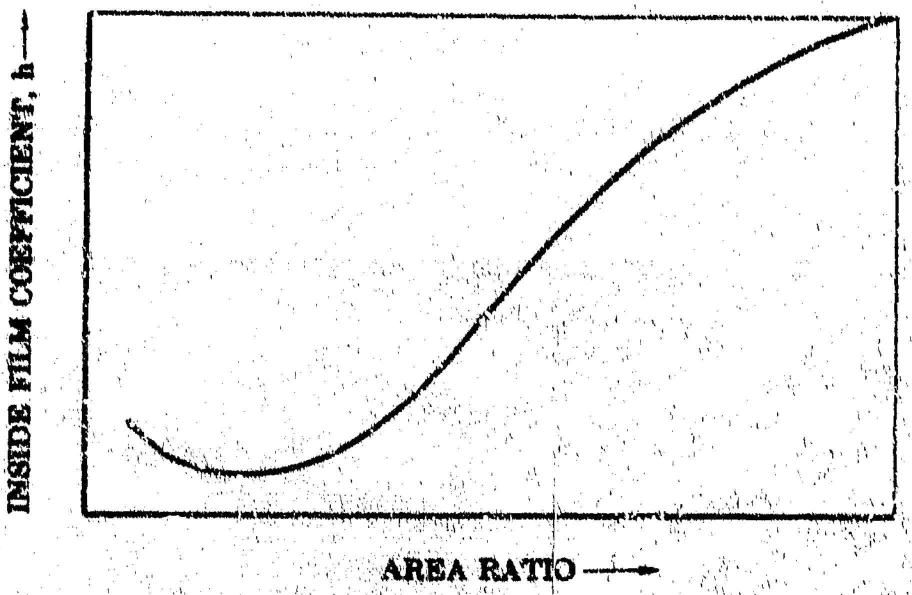

(U) Figure 167. Inside Film Coefficient vs Area Ratio FD 25319

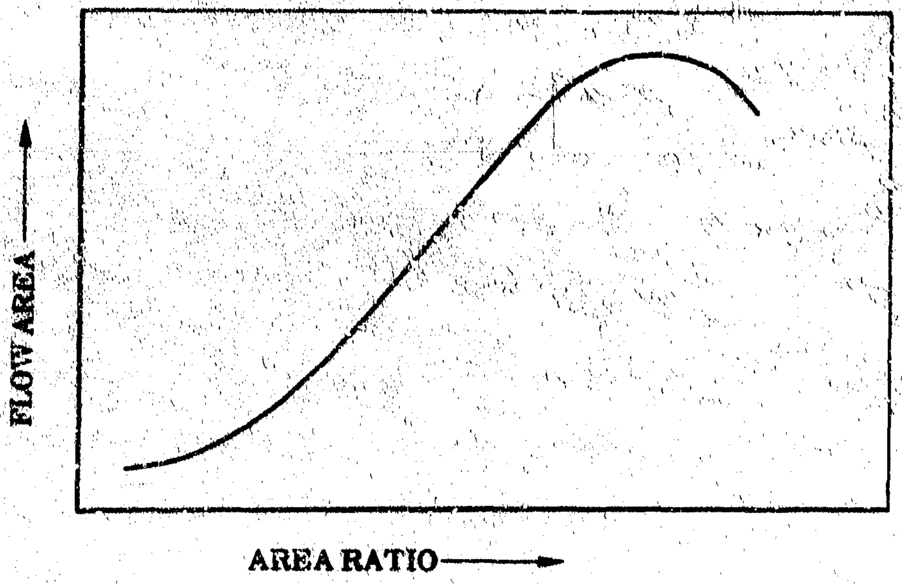

(U) Figure 168. Coolant Passageway Area vs Area Ratio FD 25320

b. Material Selection

(U) All available material candidates were studied for use in this nozzle application, comparing physical properties, mechanical properties, and ease of fabrication. The material had to have high strength at elevated temperatures and good ductility at both room temperature and elevated temperatures so it could be formed easily and would exhibit high thermal cycle fatigue strength. Table XVII provides a comparison between the final material candidates. Inconel 625 (AMS 5599) proved to be the most suitable for this application. Table XVIII lists the pertinent material properties.

(U) Table XVII. Comparison of Material Candidates

	Elongation, %			
	Room Temperature	2000°R	0.2% Yield Strength at 2000°R (psi)	Weldability
Inconel 625 (AMS 5599)	50	*105	40,000	Good
Hastelloy X (AMS 5536)	37	20	22,000	Fair
Hastelloy N (PWA 1036)	45	12	22,000	Fair
Ni 200 (AMS 5553)	50	*110	3,600	Good
TD Nickel (PWA 1035)	12	2	20,000	Poor
Stainless Steel (AMS 5646)	50	35	10,000	Good

*International Nickel Data

(U) Table XVIII. Properties of Inconel 625 (AMS 5599)

Density - 0.305 lb/in.^{3}

Ultimate Tensile Strength at Room Temperature - 147,000 psi

0.2% Yield Strength at Room Temperature - 72,300 psi

0.2% Yield Strength at 1460°R - 53,000 psi

0.2% Yield Strength at 2160°R - 32,000 psi

Elongation - 50% at Room Temperature

Brazability - Good

Formability - Good

Corrosion Resistance - Excellent

Weldability - Good

c. Configuration Study

(U) A study of different heat exchanger configurations was conducted. Table XIX summarizes the advantages and disadvantages of each configuration studied. Several configurations were eliminated during this study, with only two candidates selected for further investigation. These were the corrugated inside and outside diameter configurations.

(U) Two additional sandwich-type configurations were investigated (rectangular and triangular coolant passages) in response to an Air Force request for alternative designs and for geometries suitable for diffusion bonding. These configurations were not fabricated because of the limited time allowable for this initial investigation and the nonavailability of equipment for diffusion bonding.

d. Heat Transfer Analysis

(U) All work performed during the heat transfer analysis assumed a low-speed inducer tapoff coolant supply condition.

(1) Corrugated Geometry

(U) The design point weight flows were set using a one-dimensional "idealized" analysis. However, a two-dimensional procedure was used to set the flow area and included-angle schedules and to investigate the effects of geometry variations from the design point. The external corrugation design was evaluated first. To prevent hoop failure, it was necessary to attach a system of external bands to the nozzle outer diameter. Corrugations on the external surface made the band attachment extremely difficult; therefore, the internal corrugation design was chosen. Because this configuration increased the exposed surface area to the hot gases, a 22% coolant flow increase was required.

(2) Alternative Configuration Analysis

(U) The rectangular coolant passage configuration was investigated first. Parametric curves were developed that defined the coolant passage geometry at locations of primary interest. Using these geometries, the cross-sectional temperature distribution was established, and coolant pressure drop and temperature rise trend information was obtained. Results indicate that this scheme offers a reduction in coolant flow relative to the internal corrugation configuration with little change in weight.

(U) In analyzing the triangular coolant passage, the coolant flow requirements were assumed to be identical to the rectangular configuration. Parametric curves were developed that defined the coolant passage geometry. This configuration weighed more than the basic corrugated and rectangular passage configurations. Figure 169 illustrates the three basic designs with a weight and flow comparison.

(U) Table XIX. Configuration Study

	Advantages	Disadvantages
1. 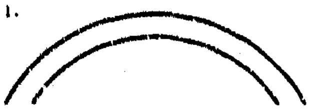 Annular	1. Simplicity of construction 2. More uniform inner sheet temperature gradient	1. Area required would dictate a 0.020-in. high gap at the inlet that would present a tolerance control problem 2. Hot inner sheet would expand approximately 0.250 in. on the radius at the inlet during operation and would close off 0.020 in. gap due to cold (not expanding) outer sheet 3. Both sheets will see entire coolant pressure as hoop pressure at the 33 in. R station, stress ≈ 240,000 psi 4. No vibration control of inner liner 5. Excessive axial growth which is only restrained at inlet and exit
2. 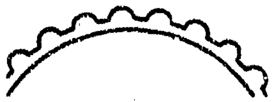 Corrugated OD	1. Smooth inner sheet <u>might</u> result in better nozzle performance 2. Lower coolant flow than corrugated ID 3. Can be gather formed and spot welded (small die required)	1. Nozzle requires stiffener bands which are cold and the inner sheet (being stronger of two sheets) expands approximately 0.250 in. on the radius and cuts off coolant passageway or buckles the inner sheet 2. Difficult to attach stiffeners to thin material 3. High bending stress because coolant is on hot low strength side ≈ 90,000 psi bending
3.  Corrugated ID	1. Hot inner sheet removes radial thermal growth in corrugations and has no tendency to close off passageways (even with stiffener bands) 2. Can be gather formed and spot welded (small die required) 3. Easier stiffener attachment 4. Might allow axial growth with folded integral bands on flat sheet, thereby increasing LCF life 5. Because flat sheet is always thicker than corrugation, this configuration has an enhanced "fin" effect at the welds	1. 25% higher coolant flow than outside corr. because of larger surface area to be cooled 2. Exit rocket nozzle fabrication difficult in order to keep discontinuities out of hot gas stream
4. 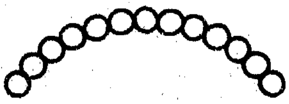 Tubular	1. Has rigid construction 2. Allows installation of stiffener bands directly to tubes without closing off passageway 3. Experience and test data are available from RL10 4. Less exposed surface area than configuration 3. Somewhat less flow requirement	1. Heavy because of 15 lb braze material and double wall thickness between passageways 2. Taper of the tubes would be complicated to maintain required area and circumference 3. Expensive to fabricate (tubes, mandrels, retort) 4. Difficult to attach stiffener rings to thin wall tube 5. Great number of tubes at inlet (2330 round tubes) 6. High temperature pushing braze limit 7. Deviations from area schedule to smooth out contour would require more coolant flow 8. More pressure drop for same coolant flow as in configuration 3.

(U) Table XIX. Configuration Study (Continued)

	Advantages	Disadvantages
5.  Waffle Plate	1. Rigid structure in all planes 2. Adaptable to bending in the flat, then hydroforming	1. Depends on elongation to form 2. Tolerance control to match weld flats would be difficult 3. Full size (entire nozzle) dies would be necessary to form contour if passageways were formed first or full size dies would be necessary 4. LCF possibility in radial as well as axial 5. Difficult to predict inside film coefficient due to uncontrolled flow path 6. Poor flow area control axially 7. Should stagger local area reductions to increase heat transfer 8. High pressure drop
6.  Double Corrugations	1. If radial growth is not allowed by attachment to the flats, thermal radial growth is taken in corrugations with little effect on area 2. Might allow hydroforming in an inside-outside die 3. Low stress from coolant pressure	1. Corrugation angles would have to be smaller to obtain a given area schedule since the area would be cut approximately in half for each corrugation. Shallow corner angles give poor heat transfer 2. Difficult to attach stiffeners and prevent buckling 3. All hoop loads must be transmitted to the stiffener bands, because corrugations cannot take loads
7.  Sandwich Design	1. Rigid construction for buckling and noise 2. Coolant flow requirement similar to 2 above because of minimum surface area 3. Radial growth would be tolerated as flat sheet deforms between supports 4. Simplified support bands 5. Minimum surface area exposed to hot gas - thus low flow requirements relative to configurations 3, 4, 5 and 6 6. Webs are easier to cool than welds of configurations 2, 3, 5 and 6	1. High bending stress on inside sheet hot side from coolant pressure - 90,000 psi 2. Struts may buckle because of thermal growth 3. Difficult to fabricate 4. Exit rocket nozzle fabrication problem similar to inside corrugations 5. Gap height very small at inlet section, therefore, heavy - relatively thick webs will be required to keep the gap height to reasonable values at the inlet region 6. Probably more pressure drop than configuration 2.

Configuration	Nozzle Weight Parameter	Nozzle Basic Weight (lb)	Support Band Weight (Sea Level) (lb)	Support Land Weight (Altitude) (lb)	Total Weight (Sea Level) (lb)	Total Weight (Altitude) (lb)	Coolant Flow Rate (lb/sec)
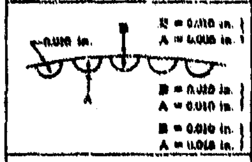	$R_T = 8.75$	50	80	40	130	90	2.36
	$R_T = 11.6$	66	70	35	136	101	
	$R_T = 16.3$	89	70	35	159	124	
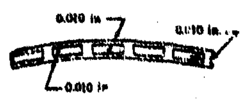	$R_T = 13.1$	75	60	30	135	105	1.88
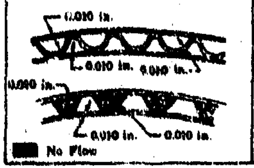	$R_T = 23.1$	130	60	30	190	160	1.38
	$R_T = 13.4$	75	60	30	135	105	

CONFIDENTIAL

(U) Figure 169. Nozzle Configuration Comparison FDC 25321A

e. Structural Band Study

(U) Several configurations of the sheet metal support bands for the ring-stiffened translating nozzle under hoop compression were studied. Of all the configurations, the integral "rib," the "hat band," and the "dunce hat" designs seemed more promising, and these were studied in detail. The "rib" band was found to have serious adverse pressure drop effects as compared to the "hat band" or "dunce hat" configurations. Of the two remaining configurations, the "dunce hat" stiffener had the best characteristics (ease of fabrication, moment of inertia, buckling, etc.) and showed a 33% weight savings in comparison to the "hat band" design. Figure 170 shows that the "dunce hat" design has the largest moment of inertia for a given material cross section of the several configurations studied. A comparison of the band weights for different applications is shown in Figure 169.

4. Fabrication Investigation

a. Method Selection

(U) The first step in this fabrication study was to select a method to form the corrugated section of the assembly. Several techniques were considered, including explosive forming, hydrostatic forming, and die forming. The explosive forming method was used previously on a small dump-cooled nozzle extension of an RL10 nozzle, but material thinning and difficulty in holding tolerances eliminated this method. From the two remaining methods, die forming was selected because it offered the highest degree of success. Figure 171 illustrates the type of gather forming die selected to form the sample panel and low cycle thermal fatigue test samples. The corrugated sheets were joined to the flat sheets by resistance welding (as was successfully demonstrated in the RL10 dump-cooled nozzle program).

(U) A die was fabricated to form corrugated panels, but with a panel size reduced to 18-inch long and 16 corrugations wide. The corrugation height was varied from 0.293 to 0.350 inch over the 18-inch sample. The samples represented the nozzle inlet configuration where maximum thermal stresses occur.

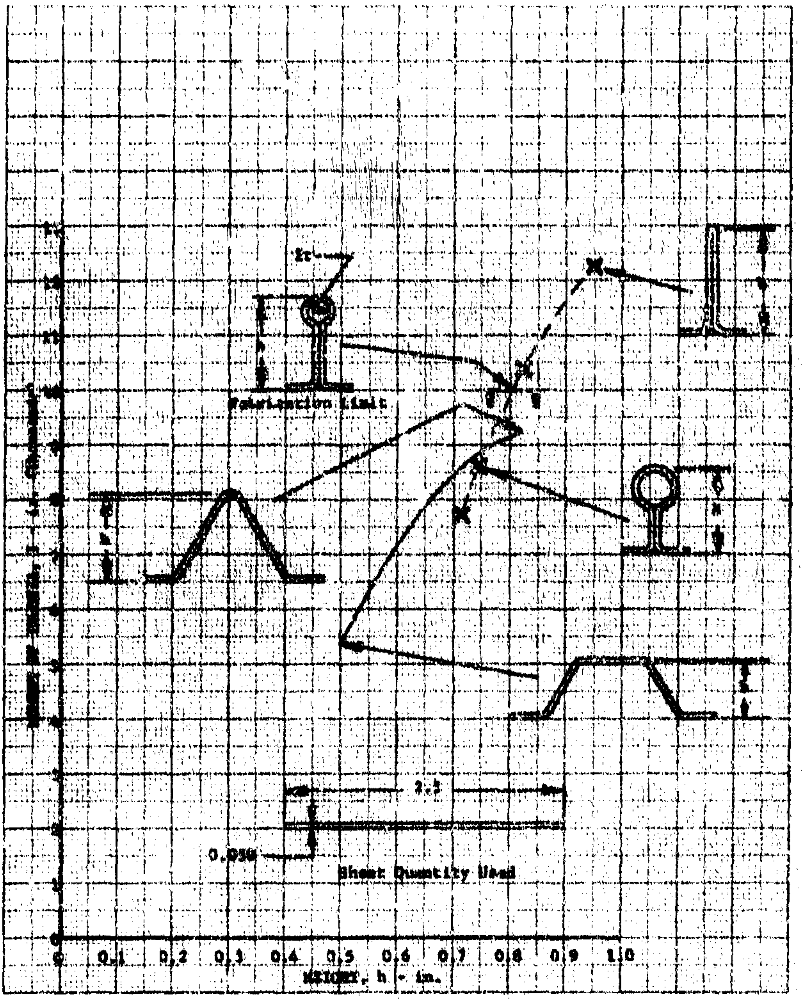

(U) Figure 170. Band Height vs Moment of Inertia for Several Configurations DF 68251

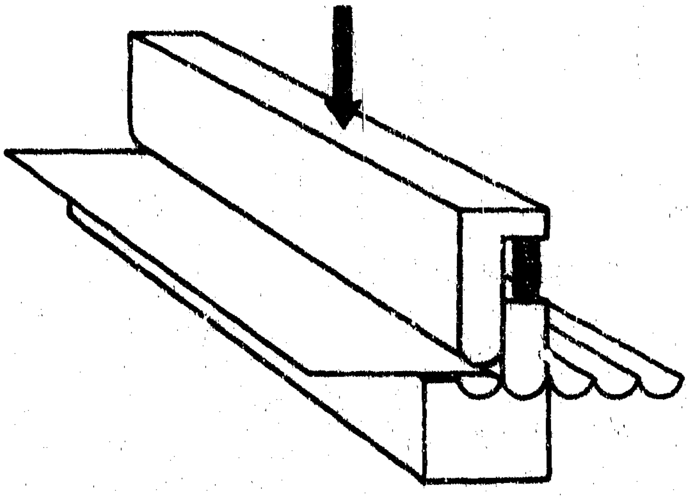

(U) Figure 171. Gather Forming Die FD 23215

b. Fabrication

(U) The first corrugated sheet formed with the die set was measured and found to have corrugation heights 16.5% below the blueprint requirements. The material spring-back after forming had caused this. The final die set for the actual nozzle will be designed to compensate for this material spring-back to obtain the blueprint limits. It was impractical to rework this die set because it was for sample panels only. To eliminate some of the spring-back, all the corrugated panels were placed in a retort, annealed at 1875°F ± 25°F for 30 minutes in hydrogen, cooled in the retort, and then restruck with the forming die. This increased the corrugation height to within 5% of the blueprint requirements.

(U) The corrugated sheets were then resistance seam welded to flat sheet stock to make sample assemblies, as shown in Figure 172.

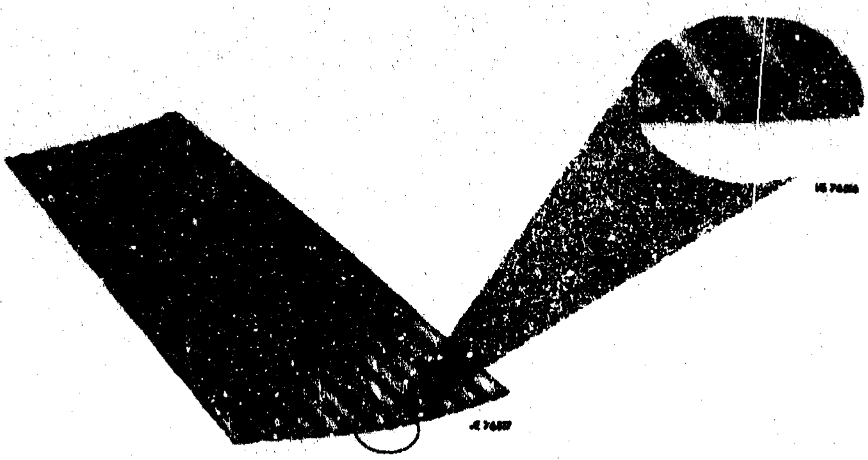

(U) Figure 172. Corrugation Sample Panel FD 23227

(U) Altitude and sea level configuration supporting bands of the "hat band" style were spun. These rings were cut into segments and tacked in place on the flat side of the sample assemblies to maintain their position during the braze cycle. Silver braze wire was then tacked in place at the joints of the stiffeners and the assembly run through the furnace braze cycle. The stiffeners would not need to be tack welded to the full-scale nozzle, as was done in the case of these small segments, but would be fixtured and held in position.

(U) Three assemblies were made that demonstrated the integral band design. The corrugated sheets were resistance welded to stacked segments of a spun ring. The ribs of the rings were then welded to form the assembly, as shown in Figure 173. The corrugated sheets were also cut into smaller segments and seam welded to special shaped flat sheets for thermal fatigue subassembly samples. The sample panels were cut into segments and used as hydrostatic pressure test specimens.

5. Test

a. Hydrostatic Pressure Test

(1) Unrestricted Specimens

(U) Three two-corrugation pressure test specimens were made per Figure 174. These specimens are sections of the sample 12-corrugation panel assemblies.

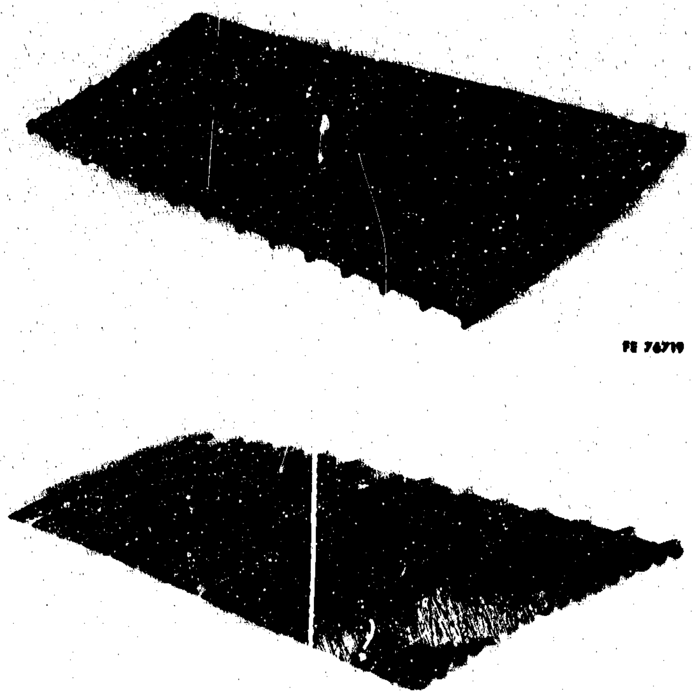

FE 76719

FE 76718

(U) Figure 173. Integral Band Design Sample Panel FD 25322

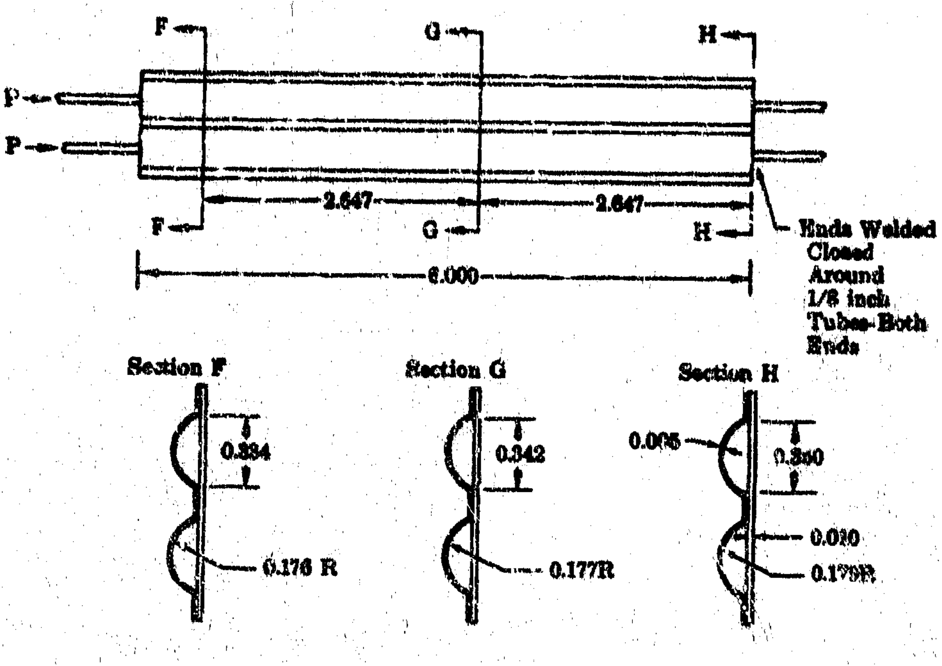

(U) Figure 174. Hydrostatic Test Samples FD 24993

(U) The first specimen pressurized failed at 275 psig. Examination revealed that the specimen failed at a spot tack weld that was outside the resistance weld width. The failure is depicted in Figure 175a. The corrugated sheets were spot tack welded to the flat back sheet prior to resistance welding of the assemblies. The resistance welds were supposed to cover the spot tacks. The test specimen failed at one tack weld that was not centered and the resistance weld had not covered it.

(U) The next two specimens were pressurized and failed at 275 psig and 400 psig, respectively. Both specimens started to roll up as shown in Figure 175b, and both failed at the edge of the resistance weld, but at random points along the specimen.

(2) Restricted Specimen

(U) All of the unrestricted specimens tended to roll up. To assure that this rolling did not cause early failures, a specimen was tack welded along the edges (four places both sides) to a 1/8-inch steel sheet. This specimen was pressurized to 380 psig, at which point one of the tack welds tore loose and caused a leak in the corrugation, as shown in Figure 175c. The other tack welds on the No. 1 corrugation side still held, so the No. 2 corrugation was pressurized. This corrugation held until the other tack welds on the No. 1 side broke loose; when the No. 1 corrugation folded up, the No. 2 corrugation failed next to the resistance weld. This again indicated that the rolling up caused premature failures.

(U) The second specimen was seam welded on both sides to the 1/8-inch thick plate, as shown in Figure 175d. This specimen had both corrugations pressurized to 1300 psig. At this pressure, one corrugation failed next to the seam weld. The other corrugation held 1300 psig with no failure.

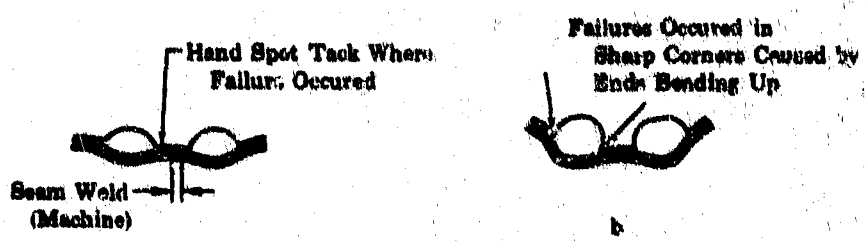

a
225 psig Failure

b
337 psig ave Failures

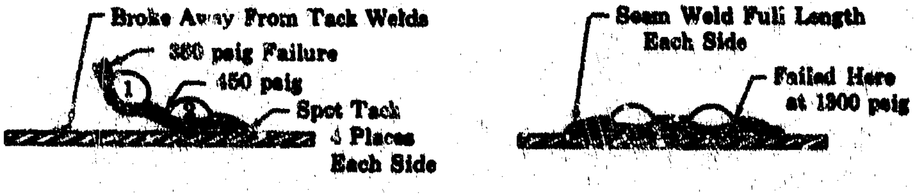

c
1. 360 psig Failure From Tear
2. 450 psig Failure When No. 1 Corrugaution Folded Up

d
1. 1300 psig Failure
2. Other Corrugation Held at 1300 psig

(U) Figure 175. Failed Hydrostatic Test Samples FD 24994

b. Resistance Weld Quality Tests

(1) Micro-Examination of Joints

(U) A section of a sample corrugated panel was taken to the Materials Development Laboratory (MDL), mounted in plastic, and examined to determine the quality of the resistance weld. The mounted specimen and a closeup of the joint are shown in Figure 176. Table XX shows the results of this examination.

(U) Surface burning and expulsion were present in the seam welds. These conditions can cause rejection and must be eliminated on the final assembly.

(U) During this examination, the thickness of the 0.005-inch thick corrugated sheet was checked to see if thinning had occurred during die forming. Microscopic and micrometer readings showed no measurable thinning had occurred.

(2) Tensile Test of Resistance Welds

(U) The tensile test specimens were constructed by cutting the sheet into 1-inch wide strips, 12-inch long. The two thicknesses to be evaluated were stacked and resistance welded 6 in. from the end, giving a 1-inch length of weld to be tested. The two ends of the same thickness material were folded back together and the load applied to these ends, as shown in Figure 177.

Mounted Nozzle Sample Panel Specimen

Closeup of Joint of Specimen

(U) Figure 176. Resistance Weld Examination Specimen FD 25323

(U) Table XX. Resistance Weld Measurements

	No. 1 (in.)	No. 2 (in.)	No. 3 (in.)
Penetration into 0.005 in.-thick material	0.001	0.001	0.001
Penetration into 0.010 in.-thick material	0.005	0.004	0.003
Weld nugget width	0.045	0.044	0.040

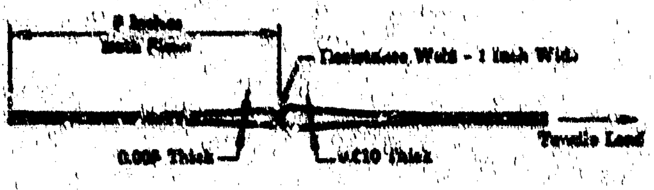

Tensile Test Specimen

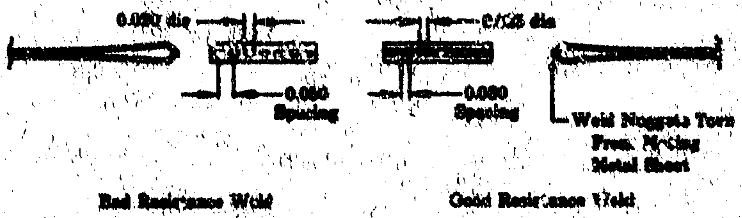

Bad Resistance Weld

Good Resistance Weld

Failed Tensile Specimens

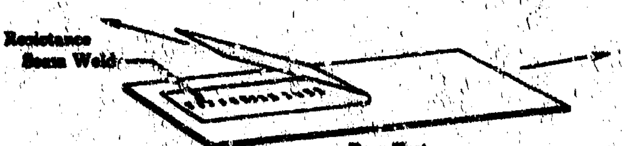

Tear Test

(U) Figure 177. Resistance Weld Test Samples FD 24995

(U) The initial tests were conducted with 0.005-inch thick Inconel 625 (AMS 5599) welded to 0.010-inch Inconel 625 (AMS 5599) with the following results:

Maximum Load, lb	
225	189 lb average
218	
125	

Examination of the welds after failure revealed the weld nuggets to be 0.050-inch apart (center-to-center) and the nugget diameter was 0.020 inch. The nuggets should overlap as illustrated in Figure 177. A second test conducted with this material combination showed the following results:

Maximum Load, lb	
435	357 lb average
302	
336	

Examination revealed the weld nugget diameter to be 0.025 inch and nuggets were overlapping with 0.030 inch center-to-center distance. Figure 178 shows the specimens from the first two tests.

(U) Figure 178. Specimens After First Two Tests FE 78030

(U) The next test was conducted with 0.010-inch thick Inconel 625 (AMS 5599) welded to 0.010-inch thick Inconel 625 (AMS 5599) with the following results:

Maximum Load, lb	
353	423 lb average
599	
343	
399	

The weld nuggets were 0.035 inch in diameter and nugget center-to-center distance was 0.030 inch, resulting in a good overlapping seam weld.

(3) Tear Test of Resistance Weld

(U) An inch wide piece of 0.005-inch thick Inconel 625 (AMS 5599) and 0.010-inch thick Inconel 625 (AMS 5599) were resistance welded along the length for 2 inches and centered 0.500 inch from the edge. The ends not welded were pulled apart, and a maximum force of 7.5 lb average was recorded, as shown in Figure 177c. All specimens tore evenly, with the original torn edge rounded with a 0.015-inch radius. The weld nugget was 0.020 inch in diameter.

c. Thermal Fatigue Investigation

(U) An attempt was made to predict the LCF life for the corrugations of the two-position nozzle. The prediction system used was the S. S. Manson technique, which uses the universal slopes equation for calculating the predicted LCF life. When using this equation, it is required that, for low cycle rates and relatively high temperatures, an additional check be made to determine if the failures might be time dependent or creep limited. A check was made and the limit case for the expected operating conditions was not creep but fatigue ruptured. Therefore, the Manson equation for selected values of total strain was used to determine cycle life, as follows:

$$\Delta\epsilon_t = \frac{3.5\sigma_u}{E} \eta_f^{-0.12} + D^{0.6} \eta_f^{-0.6}$$

where

E = Modulus of elasticity
σ_u = Ultimate tensile strength
D = Ductility
η_f = Cycle life
$\Delta\epsilon_t$ = Total strain range

(U) Because prediction of LCF becomes more of a definition of LCF range than an actual predicted number, it should be understood that when actual conditions are inserted in the equation, estimates of elevated temperature LCF behavior can be made as follows:

1. As an estimate of the lower range of life, use either 10% η_f or η_f'(Creep), whichever is the lower. For the two-position nozzle, the temperatures were such that the lower limit case was η_f or LCF, not η_f' creep rupture.
2. As an estimate of average life, use two times the lower range life.
3. As an estimate of upper range of life, use 10 times the lower range life.

(U) These limits, which the LCF test data should fall within, are shown in figure 179. The actual test data from the LCF test are also shown on this figure as being within the acceptable predicted scatter of test data It should be noted that there are no published data for reduction of area (required to determine ductility for the Manson equation) for thin sheet metal. P&WA laboratory tests indicated values around 20% to 30% and were used to establish the limits shown in Figure 179.

(C) The purpose of the thermal fatigue investigation was to develop a method to simulate in the laboratory the nozzle thermal stress that would occur during actual nozzle firings. The theoretical nozzle temperatures to be obtained with the corrugated inside diameter design were: (1) corrugation crown temperature to be 2060°R; (2) resistance weld at the valley temperature to be 1800°R to 1900°R; and (3) center of the cold side temperature to be 150°R. These conditions exist at the coolant inlet to the nozzle and produce the maximum temperature difference from cold side to crown in the nozzle.

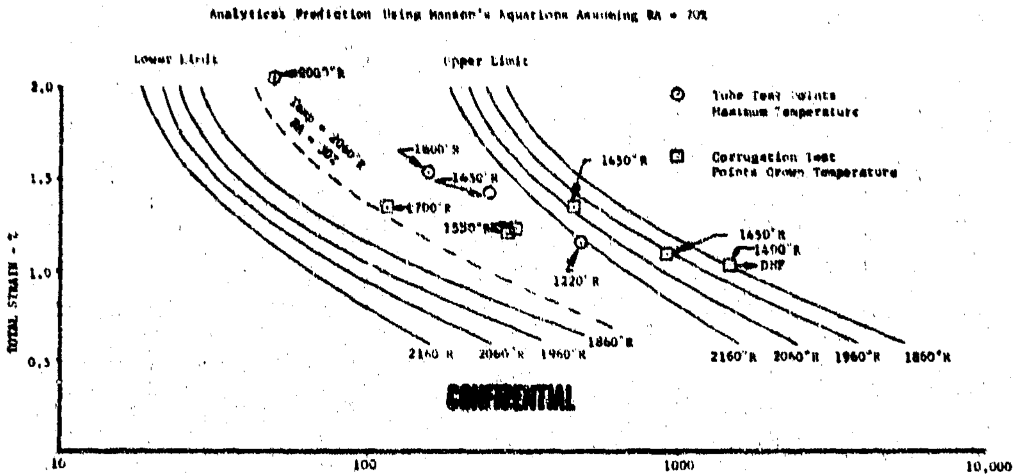

(U) Figure 179. Strain vs Cycle Life for Inconel 625 (AMS 5599) DFC 68256

(1) Flat Sample Tests

(U) Corrugated segments of the configuration shown in Figure 180 were used for the initial investigation of heating and cooling techniques. The heat was supplied with a portable quartz lamp unit producing 75 watts per square inch. The flat side of the specimen was first air-cooled and then water-cooled by suspending it in a water bath. One of the specimens had a 1/8 inch coating of Rockide applied to the flat side of the resistance weld area and the center of the cold side exposed.

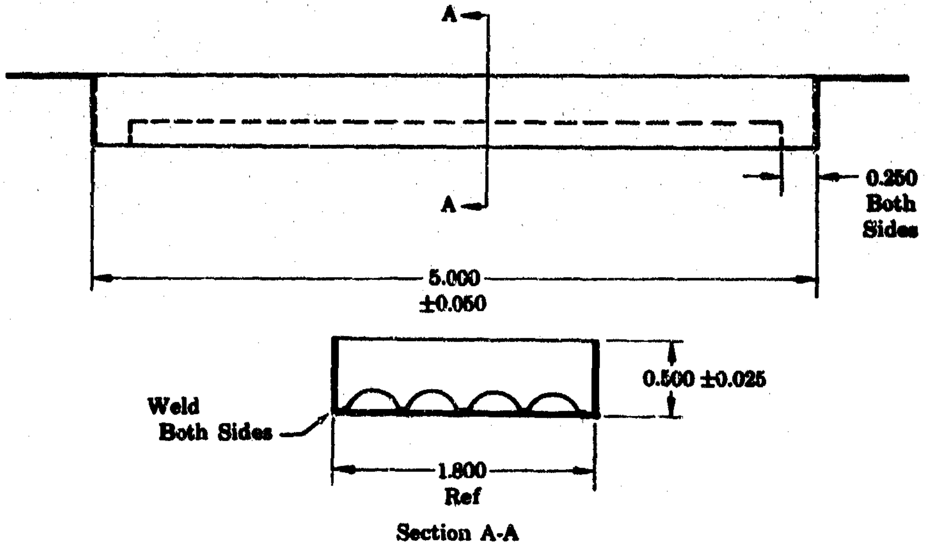

(U) Figure 180. Initial Thermal Fatigue Sample FD 25324

(U) The data from these tests, shown in Figures 181 through 184, showed that different heating and cooling methods were required to obtain the correct temperature difference.

(2) Finned Sample Tests

(U) Thermal fatigue specimens of the configuration shown in Figure 185 were constructed to evaluate cooling with copper fins (0.040-inch thick). Considerable time was spent developing an induction coil geometry that would give a broad heating pattern across the corrugated samples. Finally, the twin-coil configuration, which is shown in Figure 186, was developed and testing begun. The first tests were run with the copper fins suspended in liquid nitrogen. Additional tests were made with prechilled helium gas flowing through the corrugations, but no liquid nitrogen on the fins. The final tests were run with prechilled helium and the cooling fins in liquid nitrogen. The best results were obtained with the cooling fins in liquid nitrogen and no helium coolant (1625° ΔT). The test results are shown in Figure 187.

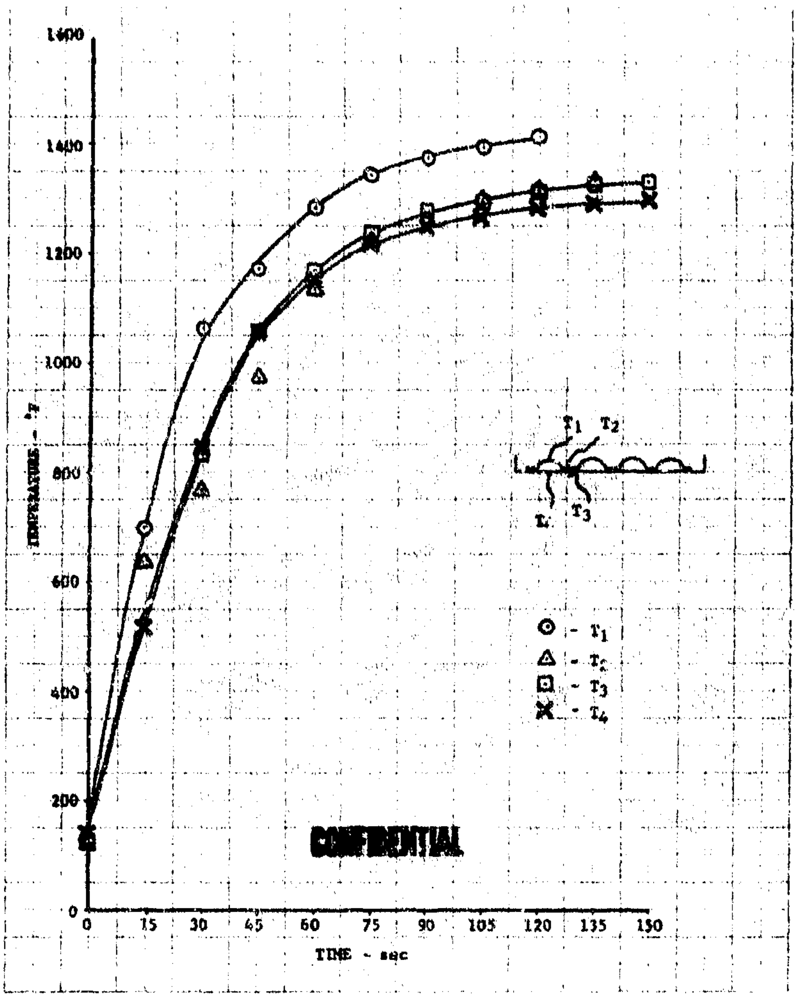

(U) Figure 181. ΔT Investigation With Air-Cooled Back DFC 63252

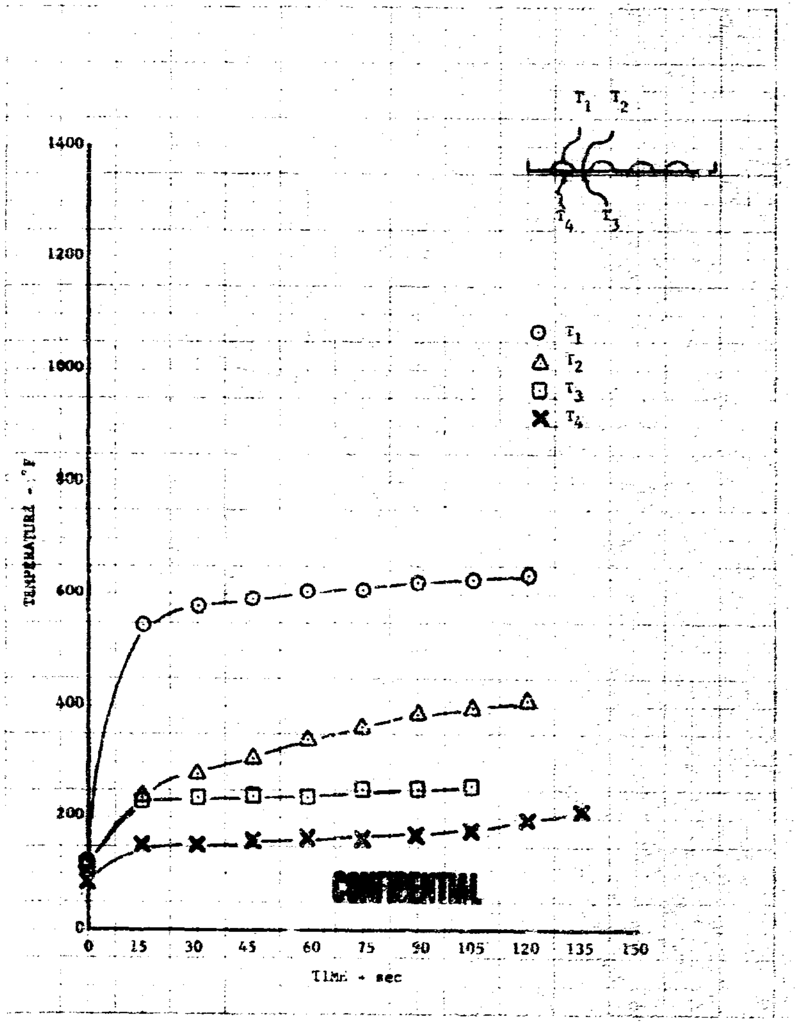

(U) Figure 182. ΔT Investigation With Water-Cooled Back DFC 68253

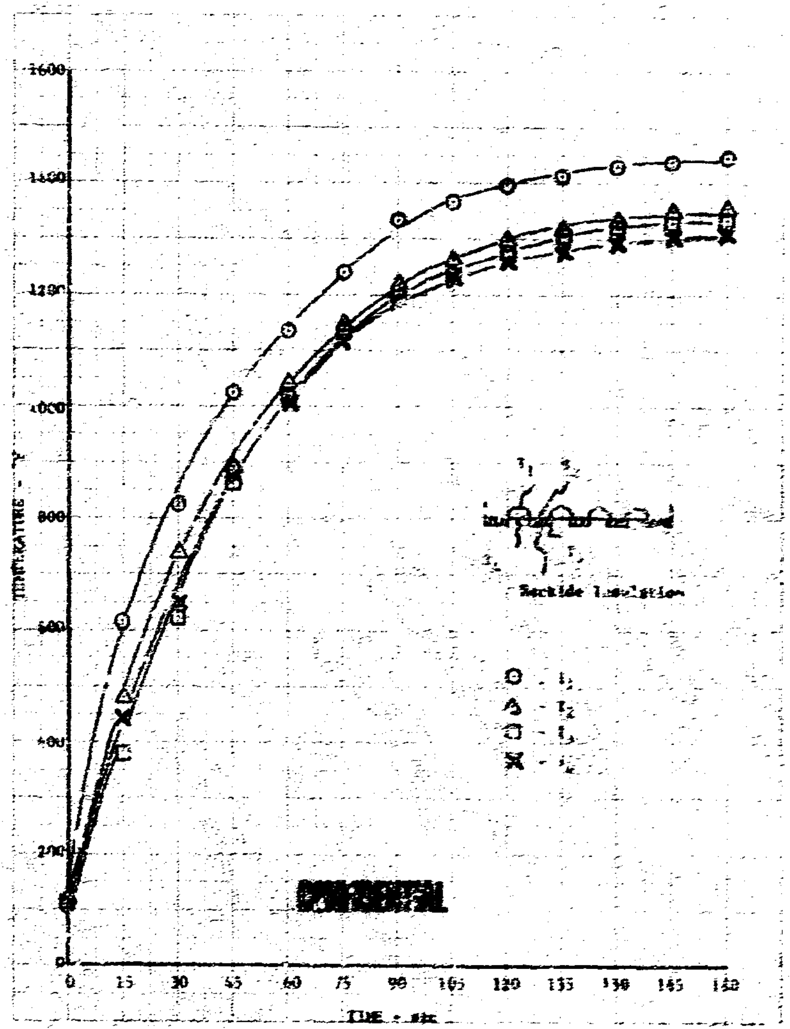

(U) Figure 183. ΔT Investigation With Air-Cooled Back and Insulated Weld Joint DFC 68254

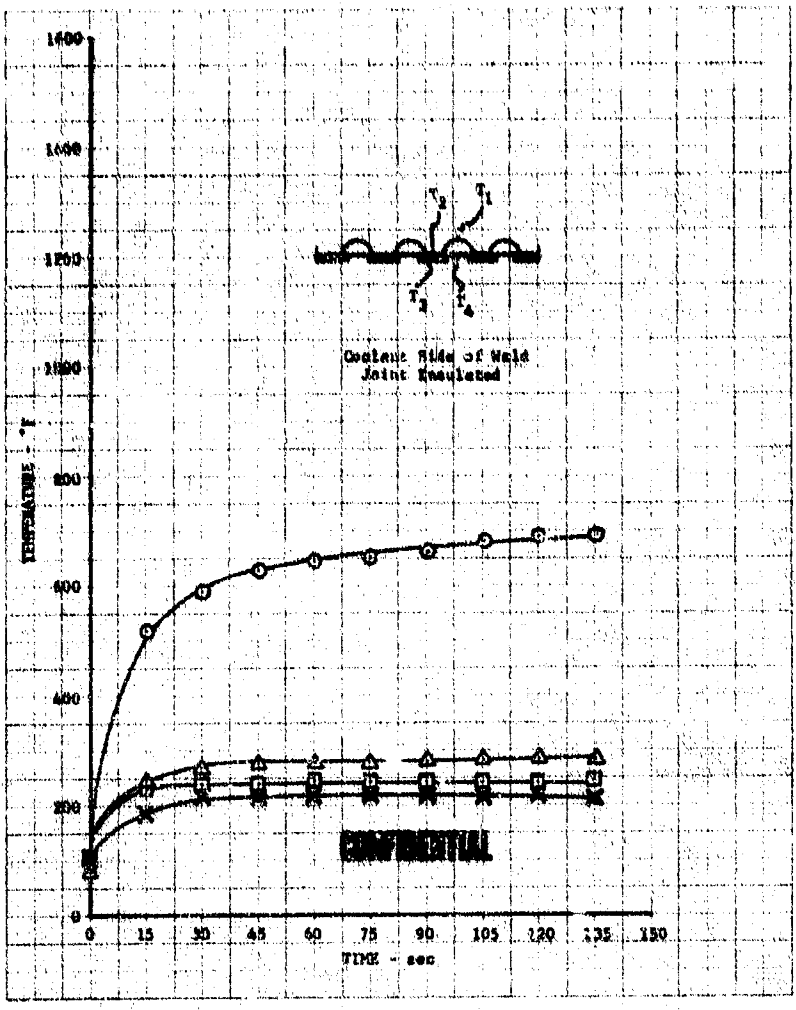

(U) Figure 184. ΔT Investigation With Water-Cooled Back and Insulated Weld Joint DFC 68255

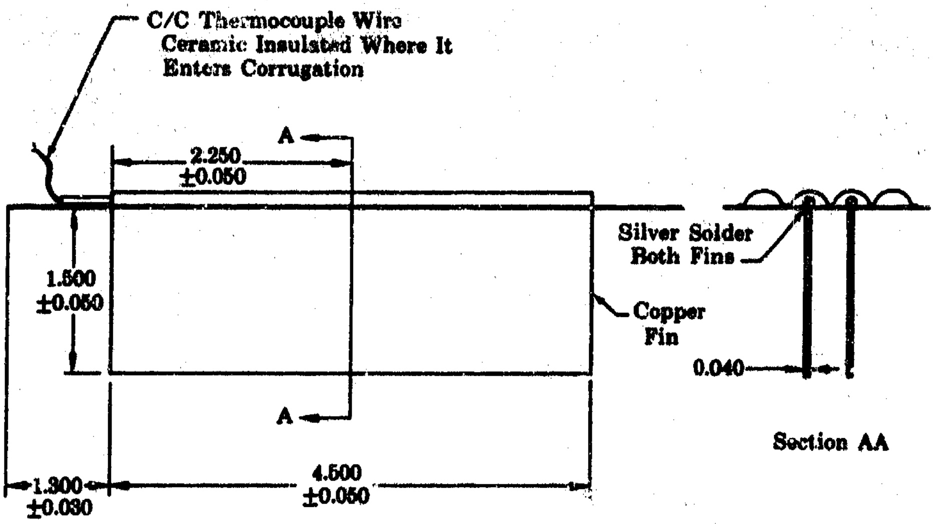

(U) Figure 185. Thermal Fatigue Sample With Cooling Fins FD 25325

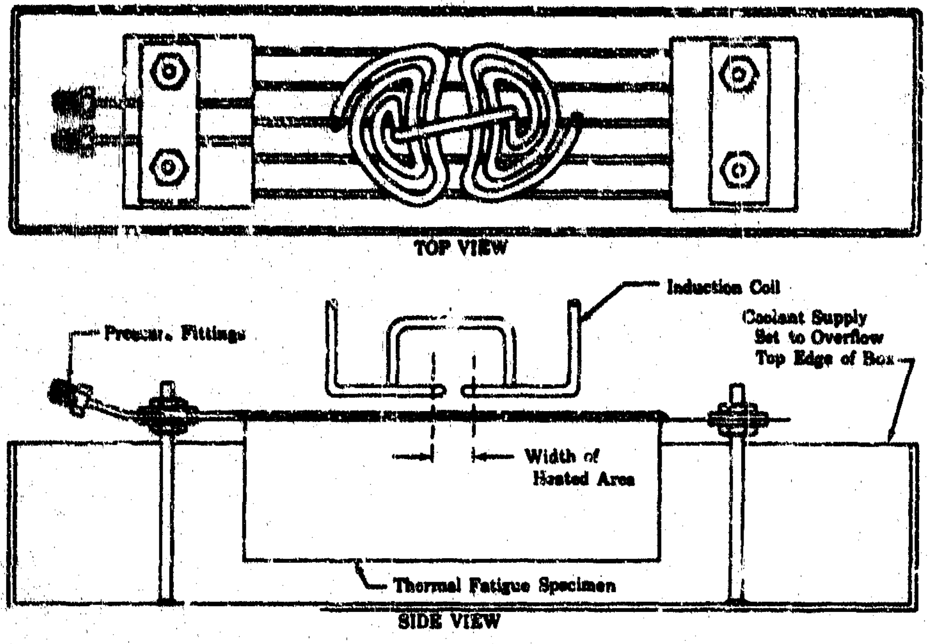

(U) Figure 186. Thermal Fatigue Cycling Setup FD 24996

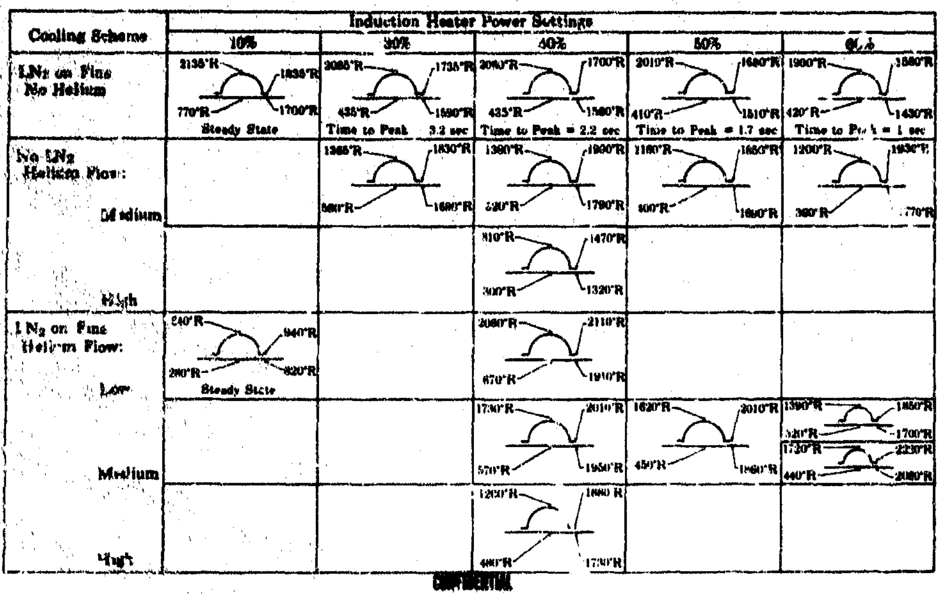

Cooling Scheme	Induction Heater Power Settings				
	10%	30%	40%	50%	60%
LN₂ on Fins No Helium	2135°R 1835°R 770°R 1700°R Steady State	2065°R 1735°R 435°R 1590°R Time to Peak 3.2 sec	2090°R 1700°R 435°R 1580°R Time to Peak = 2.2 sec	2010°R 1680°R 410°R 1510°R Time to Peak = 1.7 sec	1900°R 1580°R 420°R 1430°R Time to Peak = 1 sec
No LN₂ Helium Flow: Medium		1365°R 1830°R 580°R 1690°R	1380°R 1900°R 520°R 1790°R	1180°R 1650°R 400°R 1690°R	1200°R 1930°R 380°R 770°R
High			810°R 1470°R 300°R 1320°R		
LN₂ on Fins Helium Flow: Low	240°R 940°R 280°R 820°R Steady State		2060°R 2110°R 670°R 1910°R		
Medium			1730°R 2010°R 570°R 1950°R	1620°R 2010°R 450°R 1960°R	1390°R 1850°R 520°R 1700°R 1720°R 2230°R 440°R 2080°R
High			1200°R 1880°R 480°R 1730°R		

CONFIDENTIAL

(U) Figure 187. Test Results of Flat Sample With Corrugations and Copper Fins FDC 25326

(3) Evaluation of Cooling Fin Thickness

(U) When it was determined that a corrugated sample with copper cooling fins would best simulate engine conditions, the next step was to optimize the thickness of cooling fins. Rather than waste corrugated specimens, flat sheets of 0.0165-inch thick Inconel 625 (AMS 5599) the same size as the specimen were used and different thickness copper fins were brazed on the plate. The thickness ranged from 0.040 to 0.125 inch. The results of these tests are shown in Figure 188.

(U) A 0.250-inch thick cooling fin was brazed on a corrugated sample and compared to a 0.060-inch thick finned sample. These results are also shown in Figure 188. The results shown the optimum cooling fin thickness to be 0.065 inch.

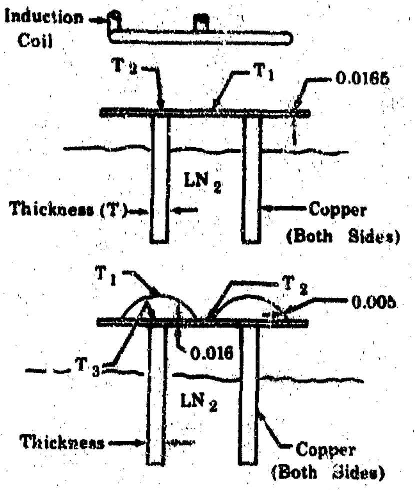

Thickness	T_1 (°R)	T_2 (°R)	ΔT
0.040	2088	796	1292
0.065	2110	410	1700 ←
0.125	2090	436	1654

Thickness	T_1(°R)	T_2(°R)	T_3(°R)	$\Delta T (T_1 - T_3)$
0.065	2150	1600	320	1830 ←
0.250	2105	1696	392	1713

CONFIDENTIAL

(U) Figure 188. Cooling Fin Thickness Test Results FDC 25327

(4) Corrugated Can Configuration

(U) A corrugated can configuration was tested in an attempt to obtain the required temperature difference. A 4-inch diameter can, with corrugations on the outside diameter and a manifold for flowing a coolant in the corrugations, was constructed. A standard circular induction coil was placed around the can and prechilled helium gas used for the coolant. The can was heated, then coolant flow was started. The results are shown in Figure 189.

(U) The third test run with the oxyacetylene torch proved that the cold side was being induction heated, and that this test method could not be used. To keep induction heating from occurring in the corrugation, and to assure heating with radiant heat, a metal shield was used on the fourth test. The cooldown time was too long (4 minutes) to make this test realistic, and good temperature gradients were not achieved.

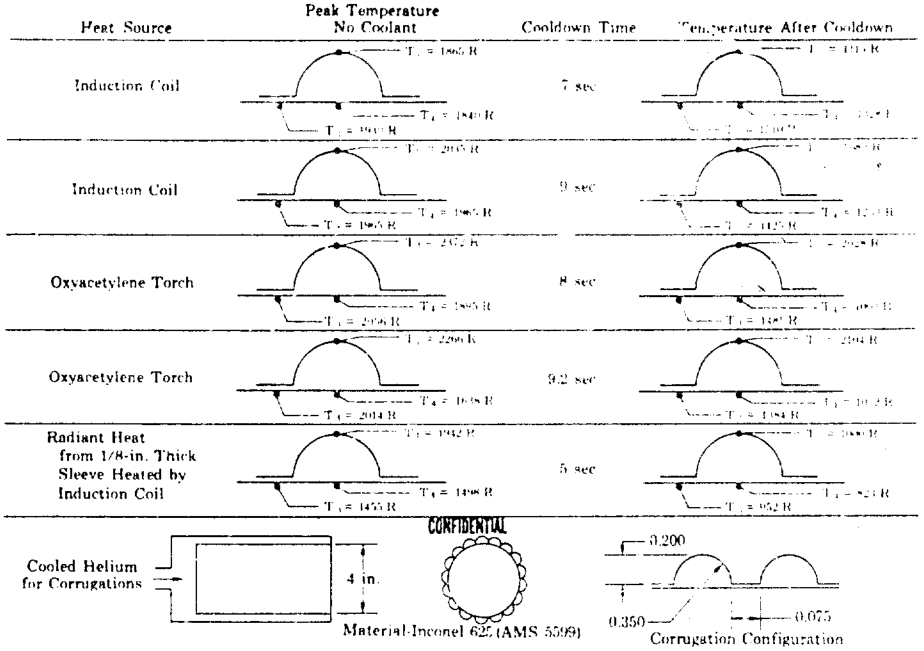

(U) Figure 189. Test Results of 4-inch Diameter Corrugated Can FDC 25328A

(5) Line Resistance Heating Using the Proximity Effect

(U) Induction heating or flame heating in the laboratory appeared to heat the crown of the corrugation higher than the valley. For this reason, high frequency resistance heating, using the proximity effect, was investigated as a means of localizing the heat where required.

(U) This type of heating is a form of resistance heating (where the current is passed through the material, causing the material to heat). To control the path of the current in the specimen and, therefore, control the heated areas, the proximity effect principle was used. This principle states that if the high frequency alternating current being delivered to resistance heat the piece of metal is passed through a lead that is run parallel and very close to the metal surface, the return current in the specimen will follow a path directly under the lead. The concentration of the current under the lead is dependent upon the height of the lead above the surface. This phenomenon is illustrated in Figure 190.

(U) The first test was run as illustrated in Figure 190. A flat sheet 0.016-inch thick and 10-inch long was heated. The distance, d, between loops was varied to determine how close the loops could be spaced and still have effective line heating under 100% of the lead-in. At d = 0.500 inch, the system line heated, but at d = 0.400 inch, the current took a straight line between the inlet and discharge post.

(U) The second test was run with another thermal fatigue specimen and the line heater set up as shown in figure 191. The copper lead-in was insulated from the specimen by coating the copper with Rockide. With the cooling fins in liquid nitrogen, the test was run and results obtained as shown in Figure 192. The temperature difference between resistance weld and cooling fins was less than 1000°, and the welds were hotter than the crown of the corrugations. In an effort to increase the temperature difference, the lead-in coil was raised by placing 1/16 inch ceramic spacers between coil and specimen. This decreased the temperature difference even more, as shown in Figure 192. This type of heating was discontinued because of temperature difference limitations and also the difficulty in attaching and spacing the coil from the specimen.

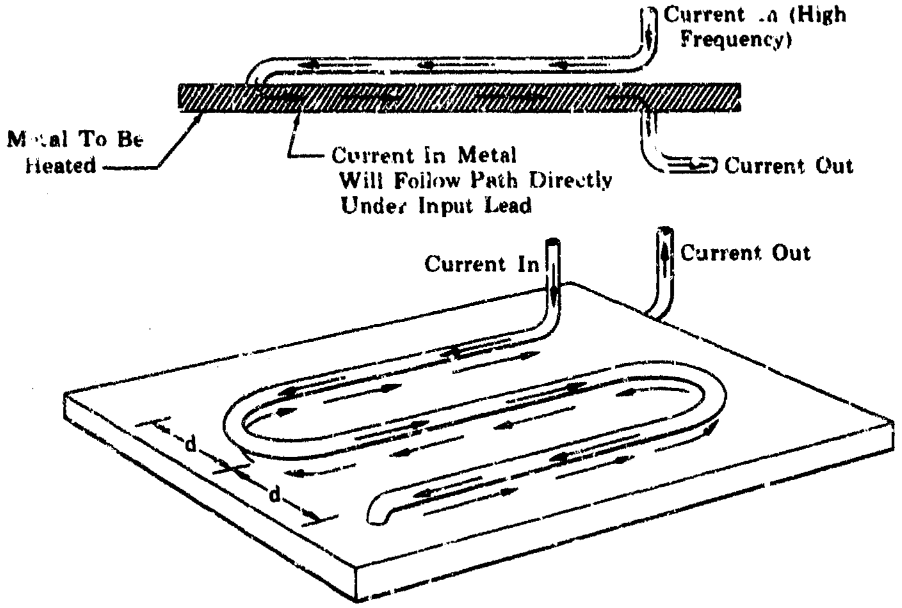

(U) Figure 190. Line Resistance Heating Using Proximity Effect FD 25329

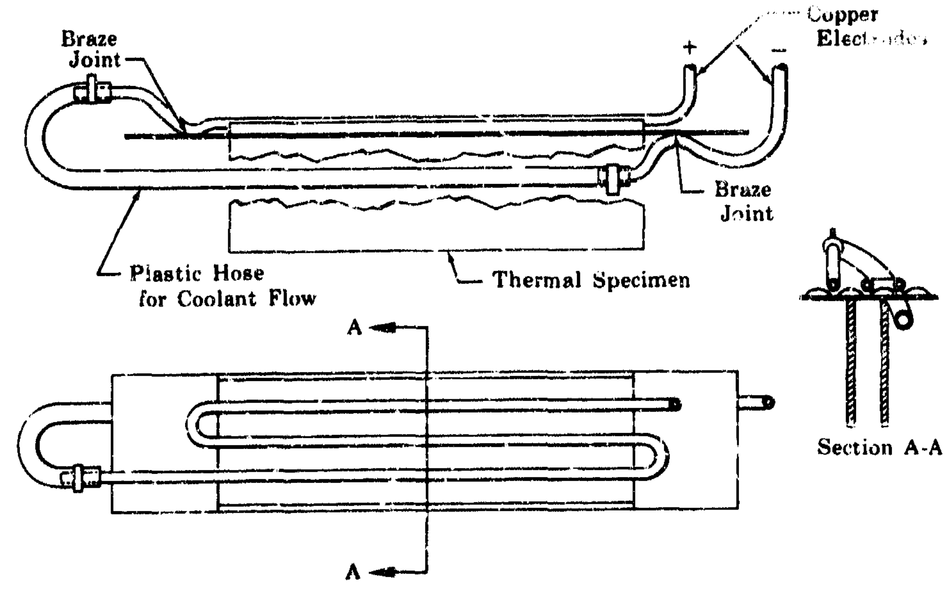

(U) Figure 191. Line Heater Assembly FD 25330

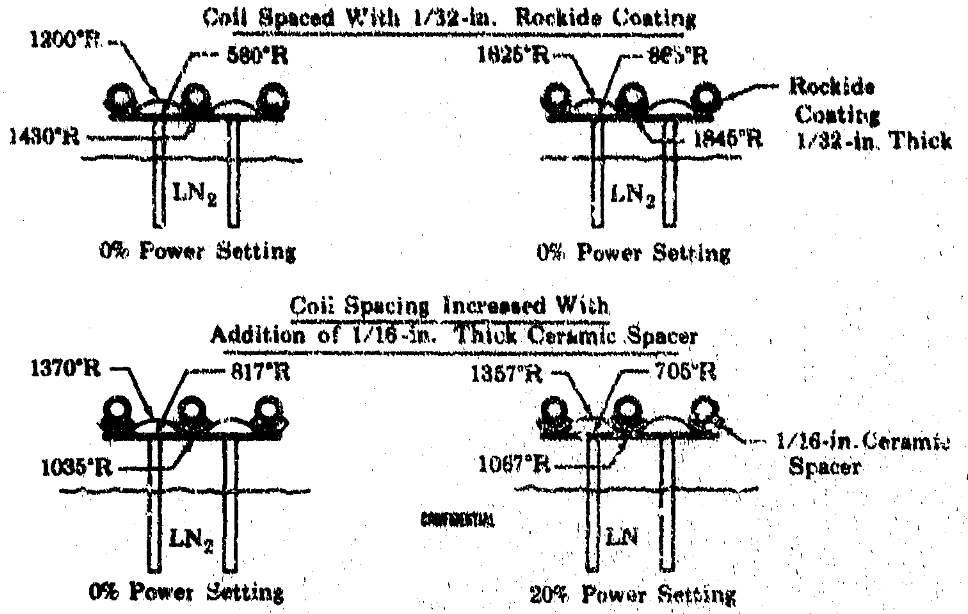

(U) Figure 192. Line Heating Test Results FDC 25331A

d. Evaluation of Final Design Thermal Fatigue Specimen

(U) Using the data previously obtained, five thermal fatigue specimens, as shown in Figure 193, were designed and procured. These specimens were used to determine the final conditions for low cycle fatigue tests.

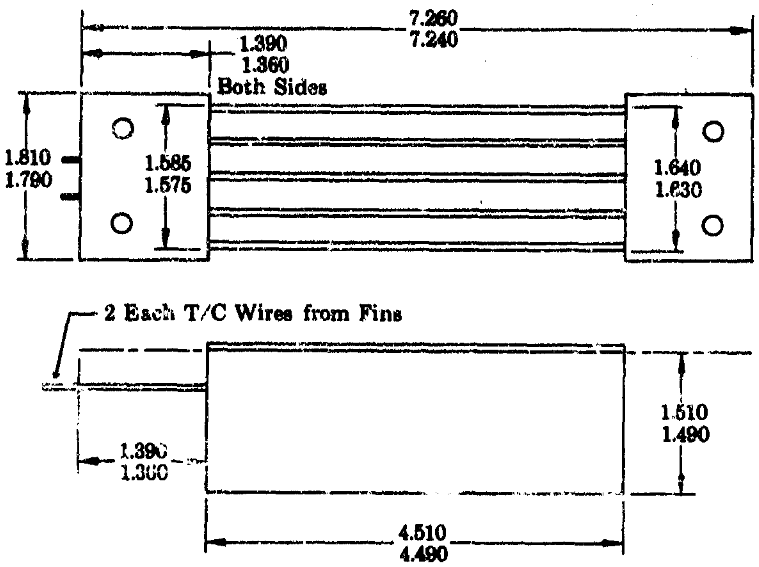

(U) Figure 193. Thermal Fatigue Sample FD 25332

(U) The corrugations of the first specimen could not be pressurized. The cooling fins were immersed in liquid nitrogen and the induction heater pattern set. The induction coil was set 0.160 to 0.180 inch above the crown of the corrugation and the induction heat power setting placed at 10% to 12%. The desired temperatures and those obtained on the first test are shown in Figure 194.

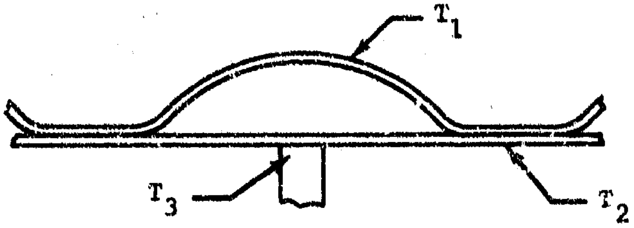

CONFIDENTIAL

	T_1 (°R)	T_2 (°R)	T_3 (°R)
Desired	2060	1800 to 1900	160
Actual	2060	1820	300

(U) Figure 194. Initial Test Temperatures

(U) The crown temperature (T_1) was read from a thermocouple attached at that point and from an optical pyrometer. The thermocouple wires were attached to the crown for these first tests so that optical pyrometer emmisivity settings could be checked and calibrated.

(U) The automatic timer was set to produce a 20-second heating cycle and a 21-second cooldown cycle. The heating cycle is shown in Figure 195, which is a reproduction of the visicorder tape on these first tests. These times were sufficient to let all temperatures reach steady-state before the next cycle began.

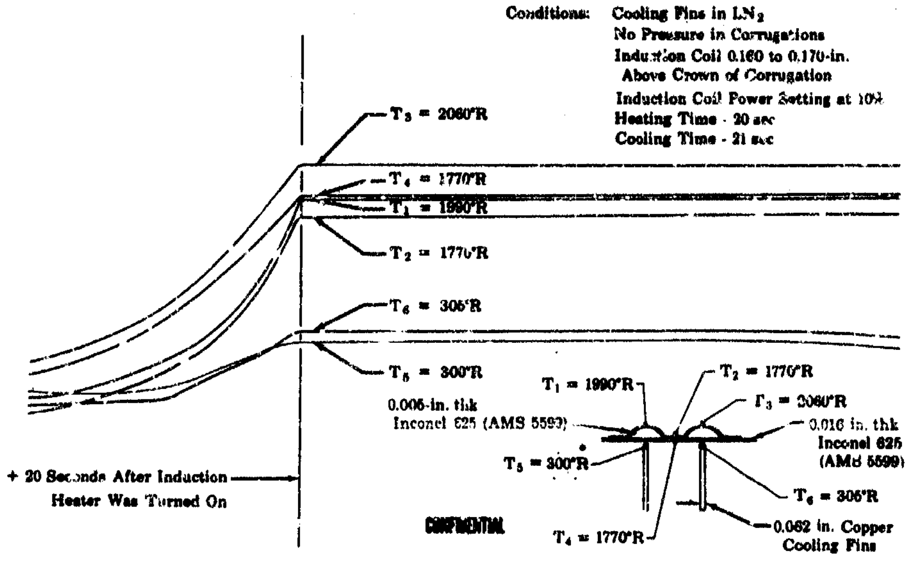
Conditions: Cooling Fins in LN_2
No Pressure in Corrugations
Induction Coil 0.160 to 0.170-in. Above Crown of Corrugation
Induction Coil Power Setting at 10%
Heating Time - 20 sec
Cooling Time - 21 sec

(U) Figure 195. Visicorder Tape of Heating Cycle Tests FDC 25333A

(C) The first specimen completed 100 cycles and was then examined. Thermal fatigue cracks were visible in all four corrugations, as shown in Figure 196, and appeared to have occurred early in the 100 cycles. Because this specimen was not pressurized, the exact number of cycles at times of failure could not be determined. The failed area was sectioned and photographs were taken. Figure 197 shows one side of the crack in the 0.005-inch thick Inconel 625 (AMS 5599) prior to etching. It clearly shows the large number of fatigue cracks in the area around the failure. Figure 198 shows the same failed area after etching, with the oxide buildup on the surface and in the cracks. Contamination of the grain boundaries is also visible. The oxidation is more severe in this instance because the specimen was cycled many times after the failure had occurred.

(C) The second specimen was assembled to allow pressurization of the passages as shown in Figure 186. The 2060°R crown temperature point with the cooling fins in liquid nitrogen was repeated with this specimen with the corrugations pressurized to 80 psig. One corrugation failed after 24 cycles; another failed at 45 cycles.

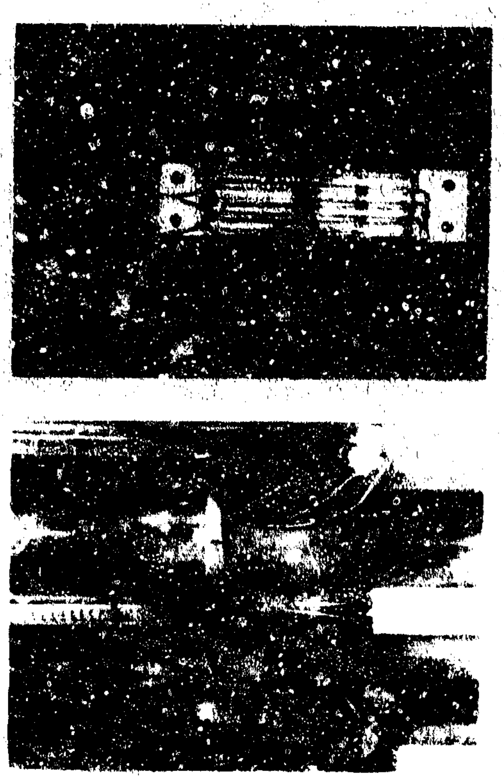

(U) Figure 196. Initial Thermal Fatigue Specimen and Enlarged View Showing Thermal Fatigue Fractures

FM 25767

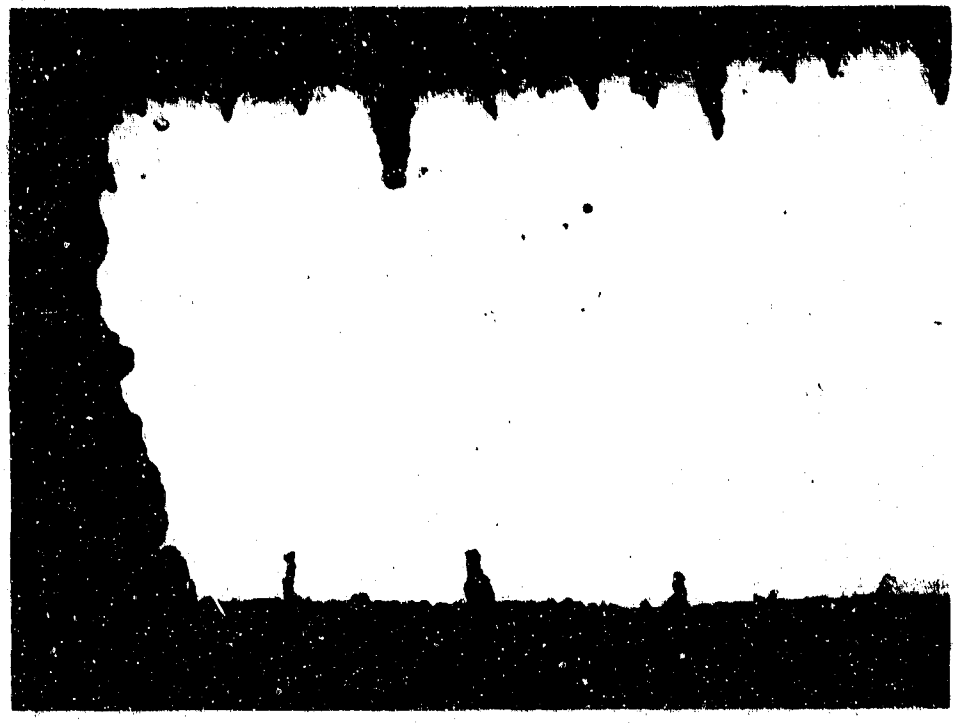

(U) Figure 197. Crack in 0.005-inch Thick Inconel 625 (AMS 5599) Before Etching (500X Magnification) FM 24964

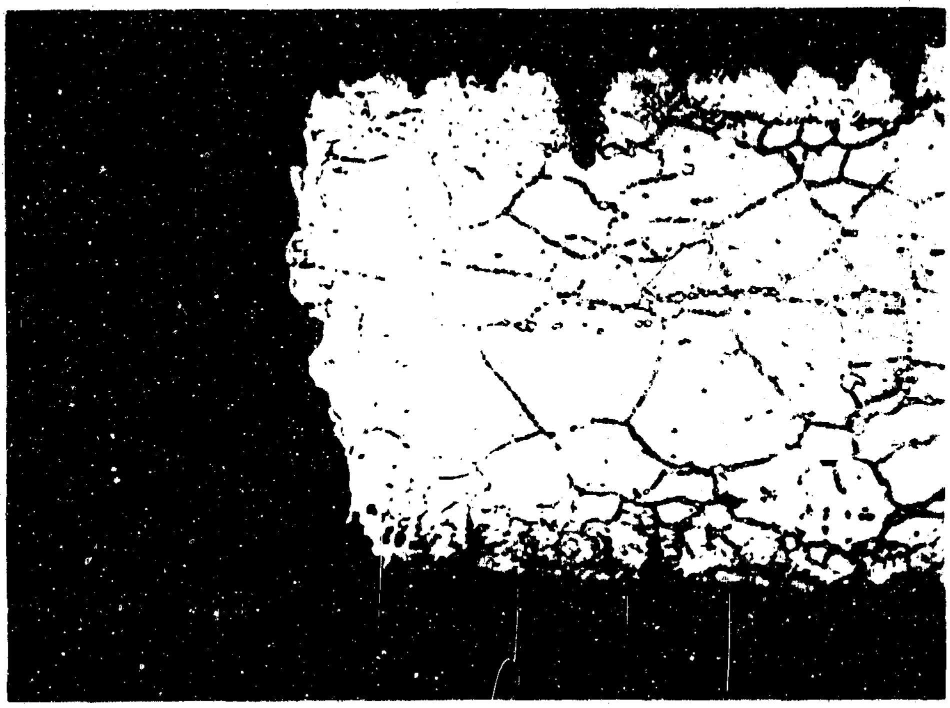

(U) Figure 198. Crack in 0.005-inch Thick Inconel 625 (AMS 5599) After Etching (500X Magnification) FM 24964

(C) Up to this point, the temperatures strived for were the predicted engine conditions. The test samples were then investigated to determine how the addition of the copper fin to the cold side affected the strain simulation. The increase in strength and stiffness from adding the large copper fin cross-sectional area allowed only a negligible strain on the cold side caused by the mismatch force. Therefore, a smaller temperature differential could be used to produce the expected hot side strain. Although the nozzle would have a 2060°R hot side and a 150°R cold side, the finned specimens only need a 2060°R hot side and 560°R cold side to produce the same hot side strain.

(C) Three more specimens were run, setting temperatures as close to the desired level as possible. The results of these tests are shown in Table XXI. With the crown temperature 2060°R, the cold side became 100° hotter than desired. Therefore, to produce the required hot side strain, the crown temperature was raised 100°R on the final series of tests. A photograph of the specimen being run at these final conditions is shown in Figure 199.

e. Thermal Fatigue Testing

(1) Specimen Configuration

(U) The final specimens were assembled as shown in Figure 200. The 0.005 in. thick corrugations were cut from the corrugated panels. These panels were struck on the new die set, annealed in a hydrogen atmosphere at 1875°F ± 25° for 30 minutes, and restruck to bring them to within 10% of the designed configuration. The base sheet was 0.010 inch thick. The copper fins were furnace-brazed at a temperature of 1475°F to 1500°F. This temperature was required because the copper forms an eutectic with the silver braze and lowers the melting point of the silver. The first two assemblies through the furnace braze cycle lost their fins when run in the thermal fatigue rig. The copper used for these assemblies was found to be not oxygen-free, which caused voids in the braze when the oxygen combined with the purge hydrogen to form a water vapor at the interface of the copper and the Inconel 625 (AMS 5599). New oxygen-free copper fins were made and used on later assemblies. The final assemblies are shown in Figure 201, 202, and 203.

(2) Instrumentation

(U) A 1/16 in. diameter shielded copper/constantan thermocouple wire with a closed end was attached to the two center cooling fins. The tip of the wire was brazed into the silver braze joint at the same time the fin joint was being furnace-brazed. The chromel/alumel thermocouple wires for reading valley temperature were attached in the Materials Development Laboratory. The crown temperature was read using the optical pyrometer.

(C)(U) Table XXI. Preliminary Thermal Fatigue Cycling Test Results

Test No.	Crown Temperature, (°R)	Valley Temperature, (°R)	Fin Temperature (°R)	Number of Cycles Before Failure	Date		Comments
					Started	Completed	
1	2060	1820	(LN_2) 300	approx 40 to 50	3-5-68	3-7-68	The corrugation configuration was not correctly shaped and was not pressurized; therefore, the No. of cycles is approximate.
2	2060	1720	(LN_2) 400	$\frac{24}{45}$	3-10-68	3-10-68	Pressurized to 80 psig; one corrugation failed at 24 cycles and the other at 45 cycles.
3	2160	1960	(H_2O) 660	42	3-14-68	3-14-68	The speciman was highly overheated on the first heating cycle.
4	2060	2020	(H_2O) 649	--	3-15-68	3-15-68	Not cycled because corrugations were damaged. (Used to check heat pattern.)
5	2060	1900	(H_2O) 660	42	3-18-68	3-19-68	First furnace braze sample (good braze).

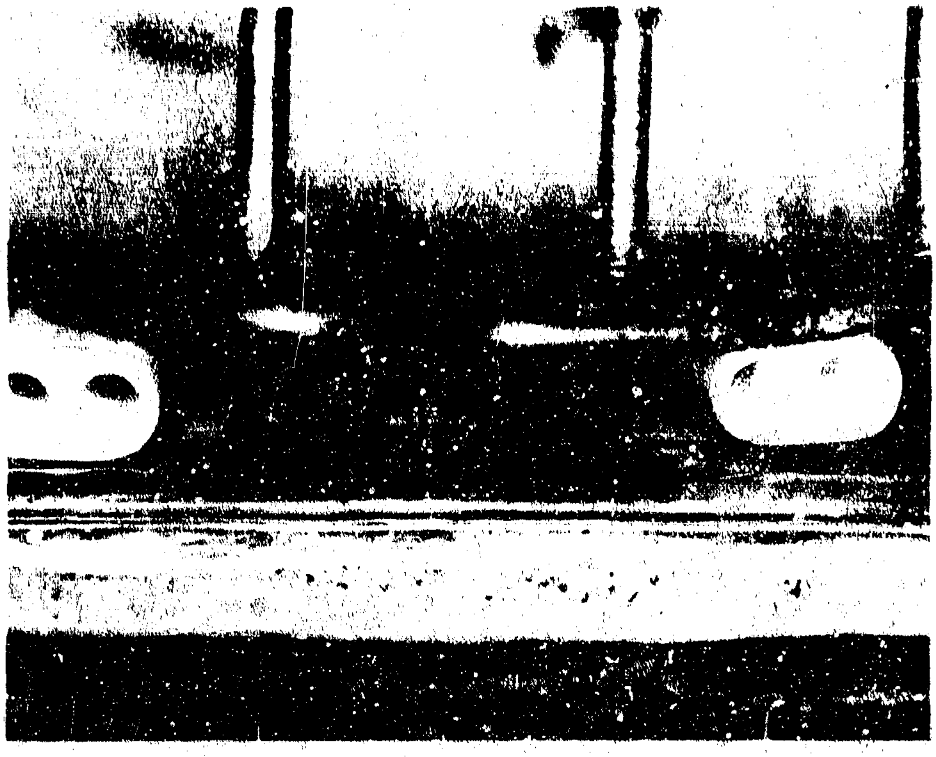

(U) Figure 199. Specimen Being Tested at Final Conditions FE 76618

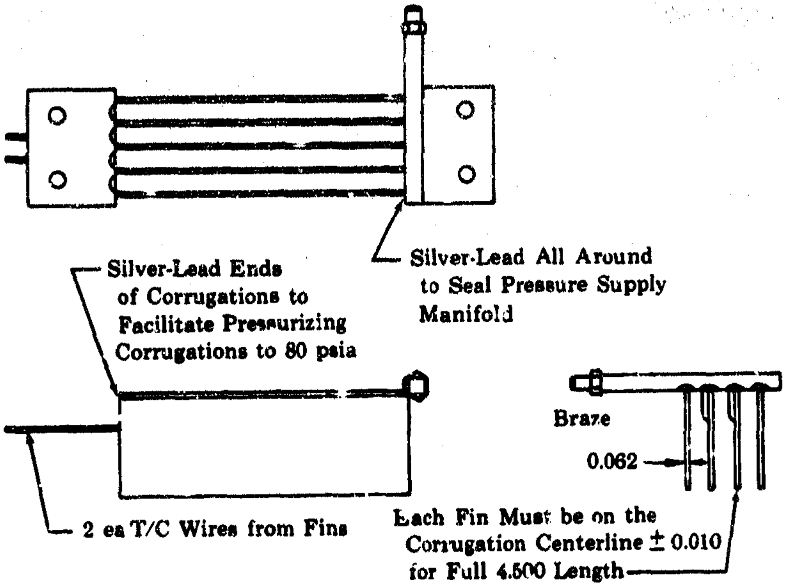

(U) Figure 200. Final Thermal Fatigue Specimen Configuration FD 25334

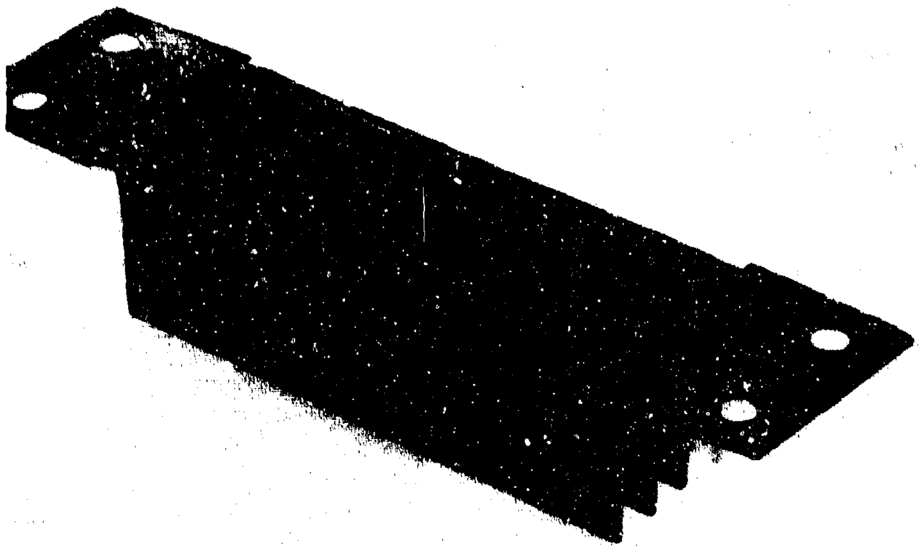

(U) Figure 201. Thermal Fatigue Specimen Final Assembly (Top View) FE 76594

(U) Figure 202. Thermal Fatigue Specimen Final Assembly (Side View) FE 76592

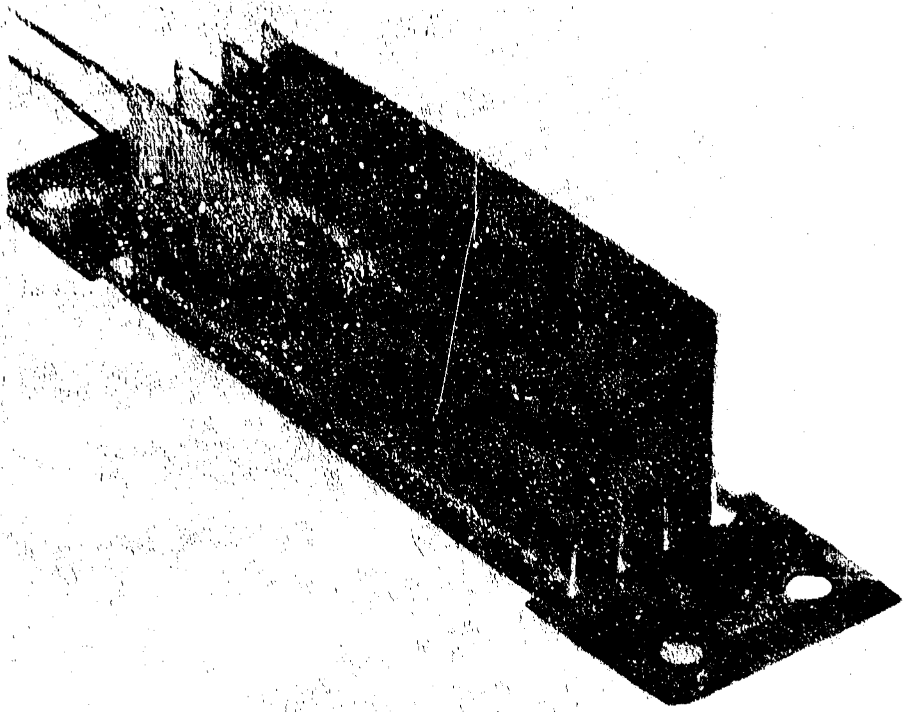

(U) Figure 203. Thermal Fatigue Specimen Final Assembly (Bottom View) FE 76593

(3) Fatigue Testing

(a) Peak Engine Condition Tests

(C) The following are the adjusted temperatures necessary to simulate the predicted hot side strain at peak engine conditions:

Crown temperature - 2160°R

Valley temperature - 2160°R

Fin Joint Temperature - 660°R

300 thermal cycles required

(U) Specimens No. 1 and 2 were set to run at these temperature conditions, but voids in the braze weakened the joints so that the joints failed when a small strain was applied and the cooling fins broke off before the conditions could be set.

(C) Specimen No. 3 had one fin break loose, but continued until the corrugation failed at 36 cycles. Number 4 ran 25 cycles at these conditions and then all the fins separated at the braze joint. Specimens No. 4 and 5 completed 30 cycles before corrugation thermal fatigue failure occurred.

(b) Determination of Crown Temperature for Required Life

(C) The No. 6 specimen was run at 1660°R crown temperature and 650°R cold side. The specimen ran 1300 cycles without failing. The test was stopped because the specimen far exceeded the required life.

(C) The crown temperature was raised to 1860°R, and three specimens were cycled at this level. They ran 136 cycles, 189 cycles, and 137 cycles, respectively, before failing (154 cycle average). The test was repeated at 1860°R in an argon atmosphere. This test was to determine if excessive oxidation of the surface was causing early failures. The specimen was cycled 200 times prior to failure. This increase of 11 cycles over the prior maximum was not considered sufficient to continue testing in argon.

(C) The crown temperature was lowered to 1760°R with a cold side temperature of 660°R and three tests were performed. The first specimen completed 350 cycles and failed in the thermocouple tack weld. The tack was made too close to the corrugation and had missed the resistance weld bead. The last two tested completed 680 and 441 cycles with failures occurring in the resistance welds in both cases and a small leak occurring next to the cooling fin in the cold side of the 680-cycle specimen.

(C) All the results of the thermal fatigue tests of the configuration shown in Figure 200 are plotted in Figure 204. Figure 204 indicates that for a sample with 0.005-inch thick corrugation and 0.010-inch thick flat sheet, 1580°R is the maximum ΔT for a fatigue life of 300 cycles. The cold side temperatures on all of these tests stayed within the range of 660°R ± 10°

(4) Configurations Change and Associated Cycle Life

(a) 0.010 in. Thick Corrugation

(U) Six specimens were fabricated with 0.010 inch thick corrugated sheet. The specimens were identical to the assembly illustrated in Figure 200, except for the corrugation thickness.

(C) The first specimen was run at 1860°R crown temperature and 660°R cold side temperature. The test was stopped at 1100 cycles without a failure. The crown temperature was increased to 2160°R on the second specimen and the cold side temperature set at 674°R. The specimen failed after 115 cycles, and a photograph of the failed corrugation is shown in Figure 205. These two tests bracketed the required 300 cycles.

(C) Two specimens were run at 2010°R crown temperature and 670°R cold side. The cycle life was 295 and 281 cycles. The temperature was dropped to 1910°R on the next specimen and cycle life increased to 960 cycles. A photograph of this failure is shown in Figure 206.

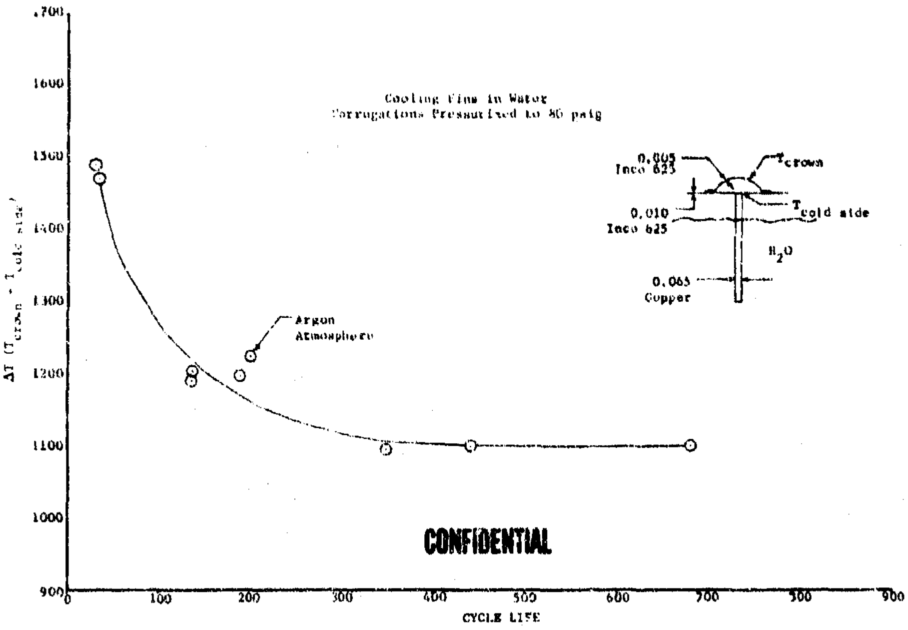

(U) Figure 204. ΔT vs Cycle Life for 0.005-inch Thick Corrugations DFC 65303

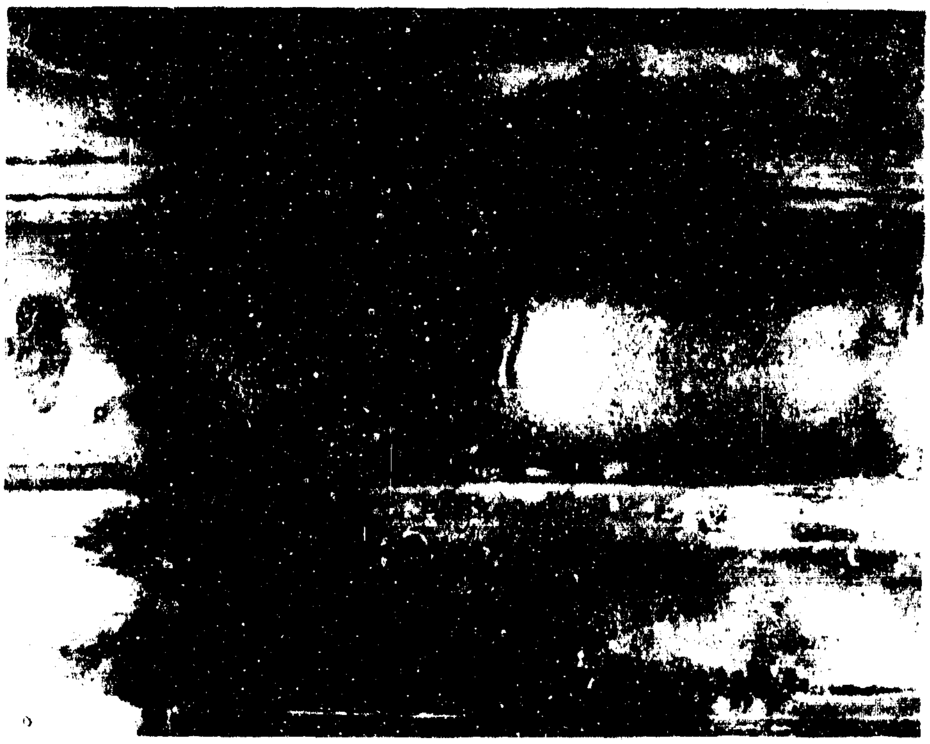

(C) Figure 205. Photograph of Failed Corrugation With Crown Temperature at 2160°R FE 77547

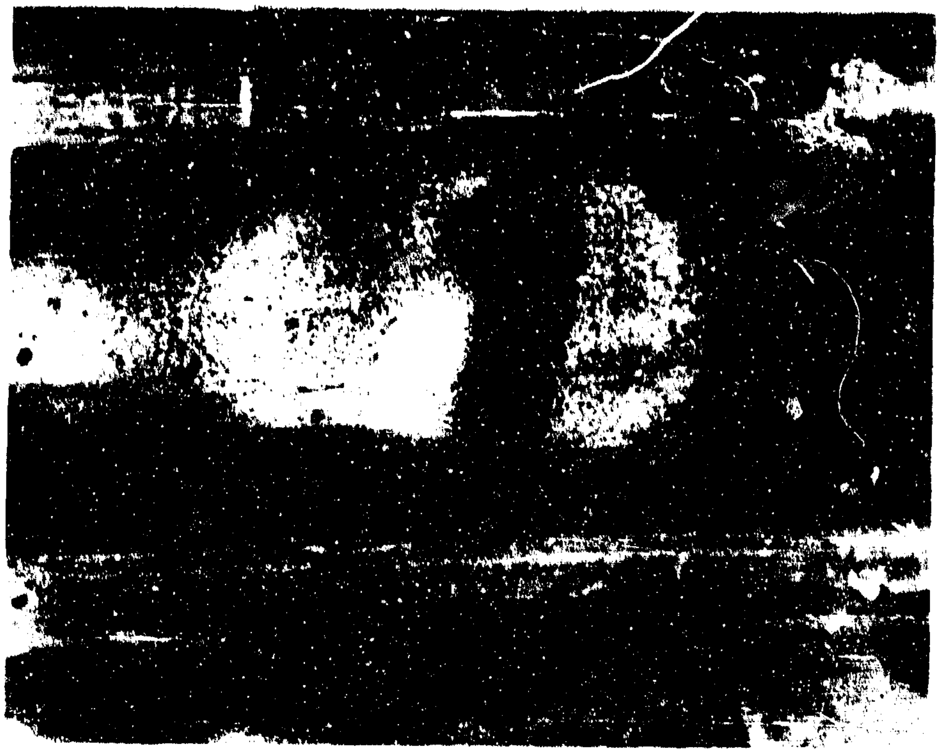

(C) Figure 206. Photograph of Failed Corrugation With Crown Temperature at 1910°R FE 77524

(C) These five tests proved that by increasing the thickness of the corrugated sheet from 0.005 to 0.010 in., the maximum allowable crown temperature for a 300-cycle thermal fatigue life could be increased from 1780°R to approximately 2000°R.

(C) The last specimen was cycled at 1910°R, but with the cooling fins in liquid nitrogen. The cold side temperature stabilized at 219°R, giving a ΔT of 1691 Rankine degrees. These conditions were set to determine what effect an increase in strain at a constant hot wall temperature would have on cycle life. The specimen failed at 441 cycles. Therefore, a 34% increase in strain caused a 52% loss of thermal fatigue cycle life.

(U) It should be noted that the strain obtained with the fins in liquid nitrogen is greater than a predicted nozzle strain, and, therefore, the test was more severe than required.

(b) Inconel 625 (AMS 5599) Cooling Fins

(U) Two thermal fatigue specimens were constructed with the cooling fins made of Inconel 625 (AMS 5599). The rest of the assembly was identical to the configuration in Figure 200, with the corrugation and flat side 0.005-inch and 0.010-inch thick, respectively.

(U) The purpose of these specimen tests was to determine if assembling and furnace-brazing corrugated sheets, flat back sheets, and cooling fins (all of the same material), would reduce the stresses built into the specimen prior to fatigue testing and, therefore, increase fatigue life.

(U) The corrugation crown started to ripple as soon as heat was applied to the first specimen. While the crown heating pattern was being adjusted, the specimen failed. The crown had rippled so severely that it had torn the 0.005-inch material next to the resistance weld.

(U) The second specimen was mounted and heat applied. The heating pattern was being adjusted when it was noticed that the outside cooling fin was beginning to separate from the 0.010-inch thick sheet at the braze joint. Before the heating pattern could be adjusted, all the fins had broken loose halfway across, thus relieving the crown stresses and causing the part to overheat. Eutectic braze joints were formed on these two samples. Using pure silver joints would probably eliminate joint problems. These were the only specimens available of this configuration, and production of more samples would have delayed the completion of thermal testing. Therefore, it was decided to eliminate further studies of this design.

(5) Thermal Fatigue Summary

(C) The following data summarize the thermal fatigue testing of nozzle design specimens:

1. Fatigue life at design conditions (T_{crown} = 2160°R with 660°R cold side):
    - a. 0.005-inch thick corrugation - 30 cycles
    - b. 0.010-inch thick corrugation - 110 cycles
    - c. Required nozzle life - 300 cycles
2. Corrugation hot side temperatures that gave 300 cycles:
    - a. 0.005-inch thick corrugation - 1780°R
    - b. 0.010-inch thick corrugation - 2000°R
    - c. Designed nozzle temperature - 2160°R with 660°R cold side temperature

All the test data are summarized in Table XXII. The total strain for each of these tests has been plotted against cycle life and is shown in Figure 207. The strain was calculated using the following formula:

$$\epsilon_{total} = \alpha_{hot} (T_{hot} - 70) + \alpha_{cold} (70 - T_{cold})$$

where:

ϵ_{total} = Total strain (in./in.)

α_{hot} = Coefficient of thermal expansion in in./°R

α_{cold} = Coefficient of thermal expansion in in./°R

T_{hot} = Corrugation crown temperature in °R

T_{cold} = Cooling fin temperature in °R

These test data are compared with the total strain data from the RL10 nozzle tube fatigue tests and are also plotted on the strain vs life curve. An operating hot wall temperature of 1910°R has been selected for the design of the demonstrator engine two-position nozzle.

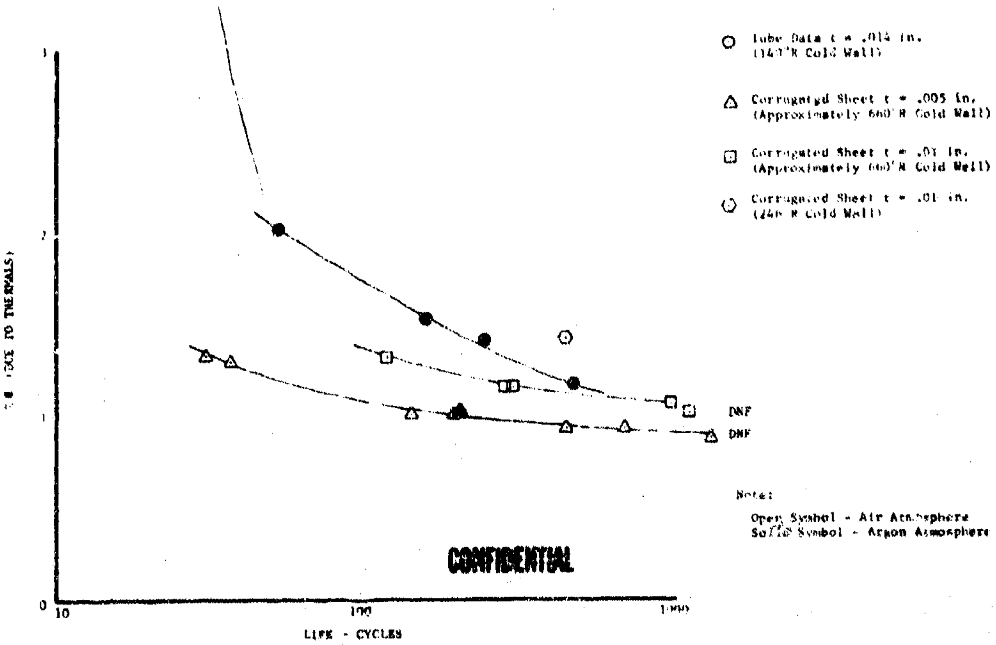

(U) Figure 207. Thermal Fatigue of Inconel 625 (AMS 5599) Tube vs Corrugated Sheet DFC 65305

(C) (U) Table XXII. Thermal Fatigue Cycling Test Results

Test No.	Crown Temperature (°R)	Valley Temperature (°R)	Fin Temperature (°R)	Number of Cycles to Failure	Date		Comments
					Started	Completed	
1					3-27-68		Cooling fins broke off due to insufficient braze coverage; not cycled.
2					3-27-68		Cooling fins broke off due to insufficient braze coverage; not cycled.
3	2130	2166	660	36	4-4-68	4-4-68	One copper fin separated from sample causing poor heat pattern - poor furnace braze.
4	2160	2157	665	No Test	4-5-68	4-5-68	Cooling fins separated from sample after 25 cycles - test was stopped.
5	2150	2140	660	30	4-5-68	4-5-68	
6	1660	1650	650	Did Not Fail	4-8-68	4-10-68	Stopped test at 1300 cycles.
7	1860	1830	670	136	4-15-68	4-15-68	
8	1760	1755	665	350	4-17-68	4-17-68	Failed in valley where thermocouple was tack welded to skin outside resistance weld.
9	1760	1718	660	680	4-18-68	4-19-68	Failed in resistance weld out of heat zone and on bottom side next to cooling fin.
10	1860	1847	663	189	4-23-68	4-23-68	
11	1860	1809	657	137	4-24-68	4-24-68	
12	1860	1801	637	200	4-29-68	4-29-68	Test run in argon atmosphere.

(C)(U) Table XXII. Thermal Fatigue Cycling Test Results (Continued)

Test No.	Crown Temperature (°R)	Valley Temperature (°R)	Fin Temperature (°R)	Number of Cycles to Failure	Date		Comments
					Started	Completed	
13	1760	1759	661	441	4-30-68	5-1-68	Failed in resistance weld.
14	1860	1759	659	Did Not Fail	5-3-68	5-7-68	(0.010 in. thick corrugation) Stopped test at 1100 cycles.
15	2160	1981	674	115	5-7-68	5-7-68	(0.010 in. thick corrugation)
16	1860	1760	700	-	5-8-68	5-8-68	(Inconel 625 fins) Corrugations rippled during heat adjustment and tore hole in material next to resistance weld.
17	1860	1760	700	-	5-9-68	5-9-68	(Inconel 625 fins) Cooling fins broke off during heat adjustment.
18	2010	1840	669	295	5-9-68	5-10-68	(0.010 in. thick corrugation)
19	2010	1840	670	281	5-13-68	5-13-68	(0.010 in. thick corrugation)
20	1910	1597	656	960	5-15-68	5-17-68	(0.010 in. thick corrugation)
21	1910	1560	(LN_2) 219	441	5-20-68	5-23-68	(0.010 in. thick corrugation) Run to check which had most effect on life crown temperature or ΔT.

E. CONTROLS COMPONENT TESTS

1. Main Chamber Oxidizer Valve 215
2. Preburner Oxidizer Valve. 243
3. Translating Seal Rig F-33435. 268
4. Static Seals. 299

E. CONTROLS COMPONENT TESTS

1. Main Chamber Oxidizer Valve

a. Introduction

(U) The main chamber oxidizer valve was tested during Phase 1 (Contract AF04(611)-11401). Eight builds of valve F-33466 and five builds of valve F-35106 were tested. This testing indicated that the disk seal required redesign to attain the 10 sccs shutoff leakage goal established for this valve. In addition, rotary shaft lip seals were developed that required valve design revisions to optimize the seal application to the valve.

b. Summary, Conclusions, and Recommendations

(1) Summary

(U) During this report period, design, procurement, and endurance testing of four main chamber oxidizer valve shutoff seal candidate configurations were completed. The shutoff seal candidates were; (1) the looseleaf Kapton F-FEP Teflon seal; (2) the silver-plated hoop seal; (3) the strap-actuated seal, and (4) the cam-actuated seal. All seals were tested at cryogenic conditions. None of the seals met the leakage requirements throughout the cryogenic tests; however, the silver-plated hoop seal and the cam-actuated seal test results indicated that additional development potential existed for both. (See Section V-J for additional tests.) Attempts to replate the hoop seal indicated a need for improved access to the inside of the seal for cleaning purposes, and improved plating procedures. The cam-actuated seal element failed during the test, indicating a need for improved support and a more flexible seal material. The shaft lip seal support housing designs were revised and two seal thicknesses were tested. A seal laminate of three layers of 0.005 inch Kapton F and one layer of 0.005 inch FEP Teflon bearing on the shaft gave satisfactory results.

(2) Conclusions

(U) 1. The silver-plated hoop seal and the cam-actuated seal designs were considered to be acceptable shutoff seals for continued development for the canted shaft butterfly valve.

(U) 2. The strap-actuated and looseleaf shutoff seals did not appear to warrant further effort.

(U) 3. Laminated Kapton-Teflon lip seals met the leakage and durability goals and were recommended for this application.

(3) Recommendations

(U) 1. Continue development of the hoop seal to improve manufacturing methods and cleaning capability.

(U) 2. Continue development of the cam-actuated seal to improve durability.

c. Hardware Description

(U) The main chamber oxidizer valve was designed and fabricated during Phase 1 (Contract AF04(611)-11401). It was designed to control the overall engine oxidizer-to-fuel weight ratio by regulating the flow of oxidizer to the main burner injector. The valve is positioned by a rotary servoactuator as a function of the engine thrust level and the scheduled mixture ratio.

(U) The main chamber oxidizer valve is located upstream of the main burner injector. The valve is a butterfly type and incorporates a shutoff seal for the oxidizer flow to the main burner injector. To accomodate this shutoff feature, a canted shaft with integral disk was selected so that an uninterrupted disk sealing surface would be provided. Incorporation of the shutoff seal in this valve eliminates the need for a separate shutoff valve between the main chamber oxidizer valve and the main burner injector.

(U) The canted shaft arrangement requires a split main housing for assembling the valve. Widely spaced double roller bearings are incorporated to take the loads produced by the maximum valve pressure drop. Shaft thrust bearings are required to restrain the shaft against the flow-pressure thrust loads resulting from the canted shaft. These flow loads are minimized by partially pressure balancing the shaft to oppose them. The valve configuration at the end of Phase I (Contract AF04(611)-11401) is shown in Figure 208.

d. Facilities

(C) Testing was conducted in the B-22 test stand shown in Figure 209. For environmental endurance tests, the valves were mounted in the stand and instrumented as shown schematically in Figure 210. The tests were performed by submerging the valve in liquid nitrogen or liquid argon and pressurizing with nitrogen to internal pressures of 50 to 6000 psig. The valves were cycled at these conditions and valve seal leakages were measured periodically. For the later tests, liquid argon was selected for the cryogenic bath to ensure that all of the nitrogen leakage vaporized at the valve external ambient pressure. This allows satisfactory steady-state leakage measurement accuracy for all data points. Leakages of 0.14 to 5200 sccs were measured by a series of gaseous nitrogen flowrates. Lower leakages were measured by positive displacement leak detectors.

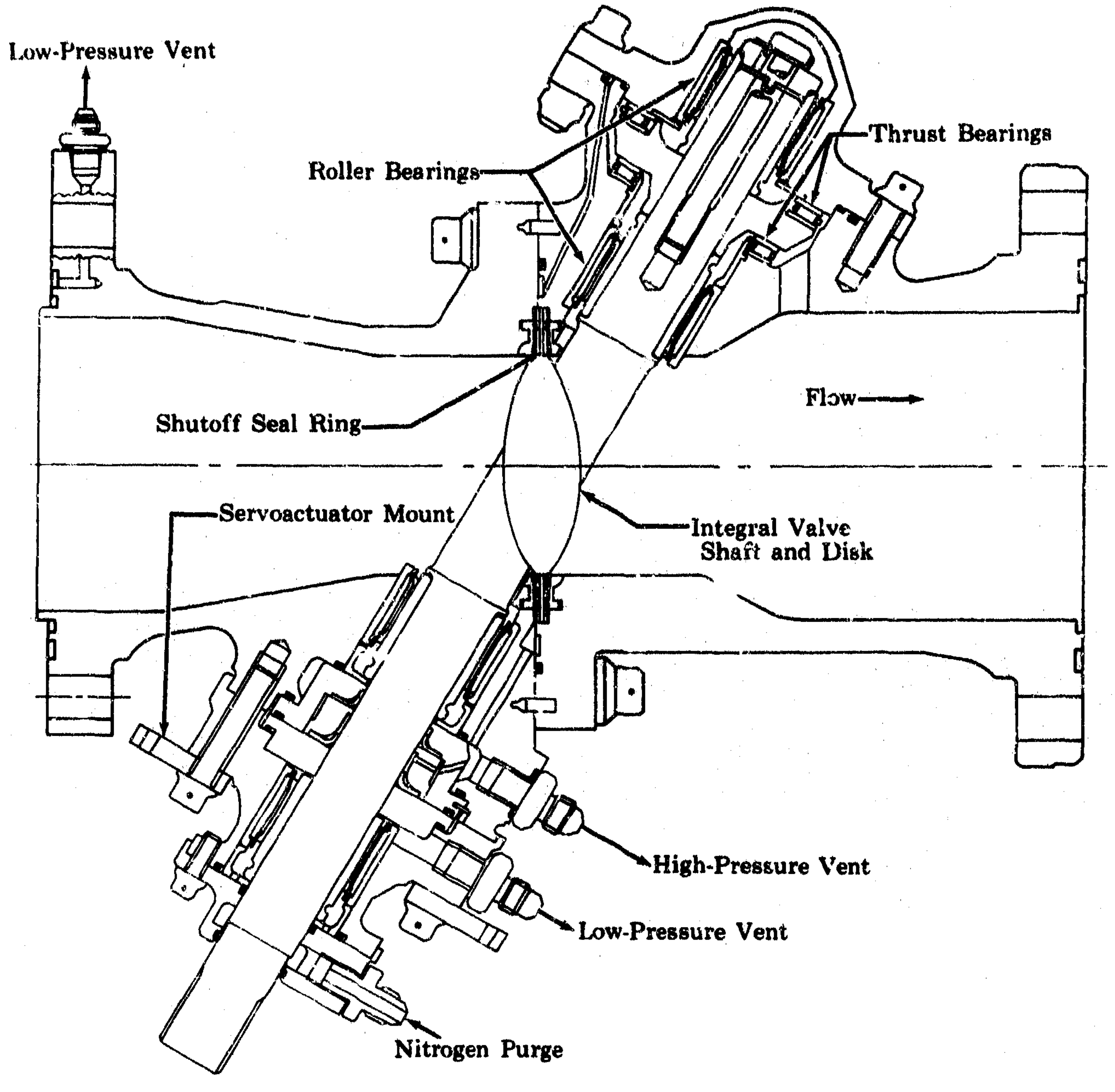

(U) Figure 208. Main Chamber Oxidizer Valve FD 18938A

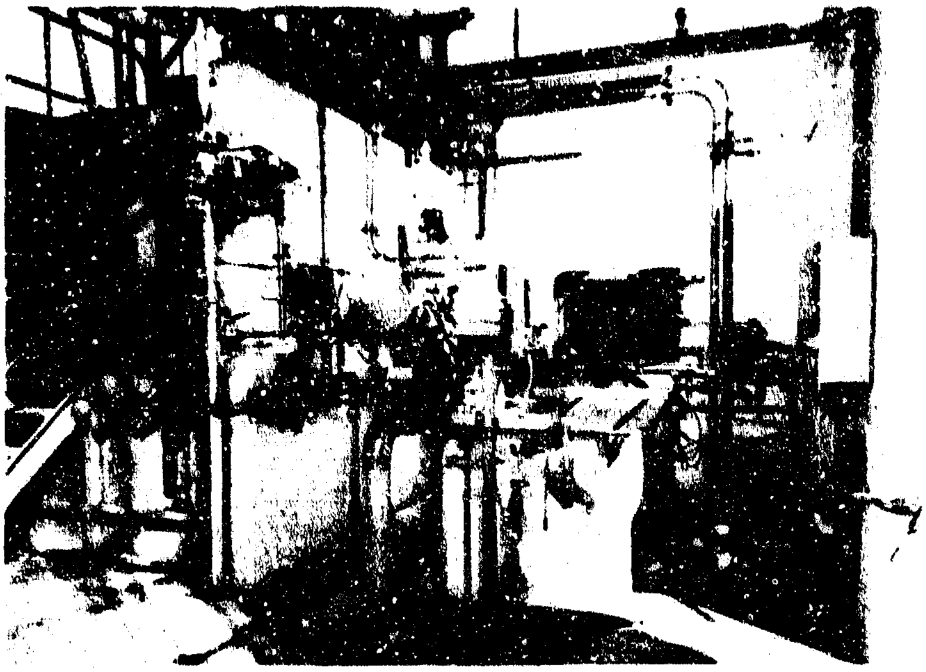

(U) Figure 209. B-22 Cryogenic Static Cycle Test Stand FC 13799

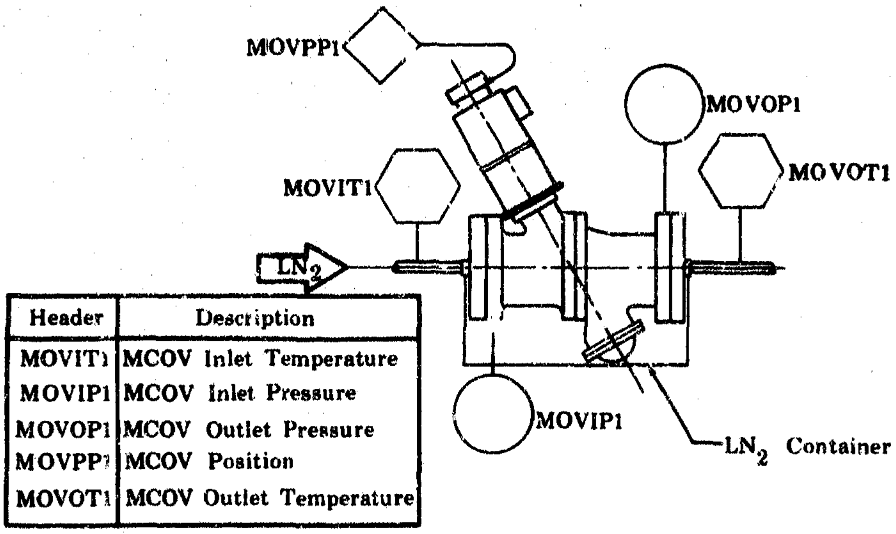

Header	Description
MOVIT1	MCOV Inlet Temperature
MOVIP1	MCOV Inlet Pressure
MOVOP1	MCOV Outlet Pressure
MOVPP1	MCOV Position
MOVOT1	MCOV Outlet Temperature

(U) Figure 210. Main Chamber Oxidizer Valve Instrumentation Schematic (B-22 Stand) FD 23066A

e. Testing

(1) Valve F-33466-Build No. 9

(U) Main chamber oxidizer valve F-33466-9 incorporated the following sealing configurations:

1. A Looseleaf (OD bonded) Kapton F-FEP Teflon disk seal was used (0.005-inch thick sheets in alternate layers). An Inconel ring loaded each outside Kapton F layer against the housing faces to prevent leakage around the seal. Figure 211 shows the shutoff seal configuration.
2. A primary lip seal of laminated Kapton F (two layers) and FEP Teflon (one layer next to shaft) of 0.015-in. total thickness was used. The lip seal retainer was modified to mate with the thinner lip seal.
3. An inverted U-ring center flange static seal assembly that loaded the 0.015-inch thick laminated Kapton F static seals was used.
4. The primary shaft seal housing was modified to isolate static seal leakage from the primary lip seal leakage. A vent passage was added to the valve inlet housing to conduct this leakage overboard.

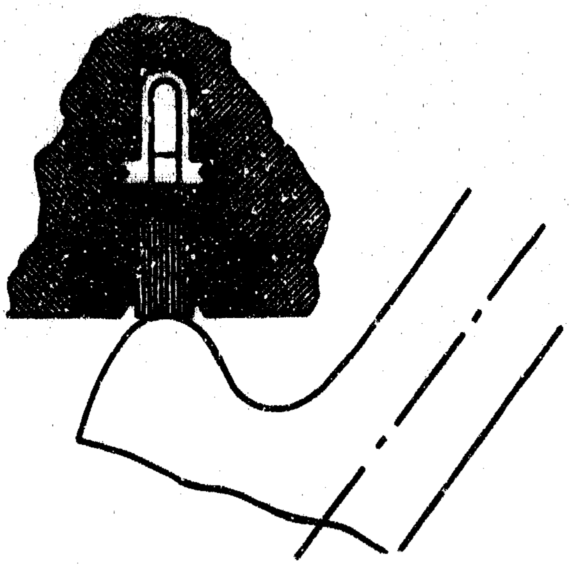

(U) Figure 211. Laminated Kapton Shutoff Seal FD 25481

(C) The disk seal leakage at 50 psid was 3 sccs GN_2 with the valve at ambient temperature, and the torque required to rotate the valve shaft was as follows:

Rotation out of disk seal	125 in.-lb
Clockwise and counterclockwise rotation	15 to 20 in.-lb
Rotation into disk seal	200 in.-lb

(C) The valve was mounted in the B-22 test stand for an environmental endurance and leakage test; 5000 partial stroke actuation cycles, 250 shutoff cycles, and 153 pressure cycles were performed. Leakages from the primary lip seal, disk seal, primary shaft seal housing, and the main housing center flange primary static seal are shown in Figure 212. The maximum bearing cover primary static seal leakage was 75.5 sccs and the maximum inlet flange trapped Teflon primary static seal leakage was 1.9 sccs. The outlet flange primary O-ring static seal vent was capped after 2500 actuation cycles and 125 shutoff cycles due to excessive leakage. The secondary and vent shaft seal leakages remained less than 1.4 sccs throughout the test.

(U) The valve was removed from the B-22 test stand when the outlet flange static seal leakage exceeded the stand limit. The torque required to rotate the valve shaft at ambient temperature was as follows:

Rotation out of disk seal	85 in.-lb
Clockwise and counterclockwise rotation	10 in.-lb
Rotation into the disk seal	90 in.-lb

(U) Disassembly of the valve revealed the following:

1. The primary lip seal was in good condition with negligible wear.
2. A section of the disk seal had failed as shown in Figure 213 and was found in the outlet housing. One disk seal axial support ring was bent as shown in Figure 214.
3. The shaft disk outside diameter was scored where it contacted the bent support ring.
4. Contamination particles were imbedded in the Teflon coating of the outlet flange primary O-ring static seal.

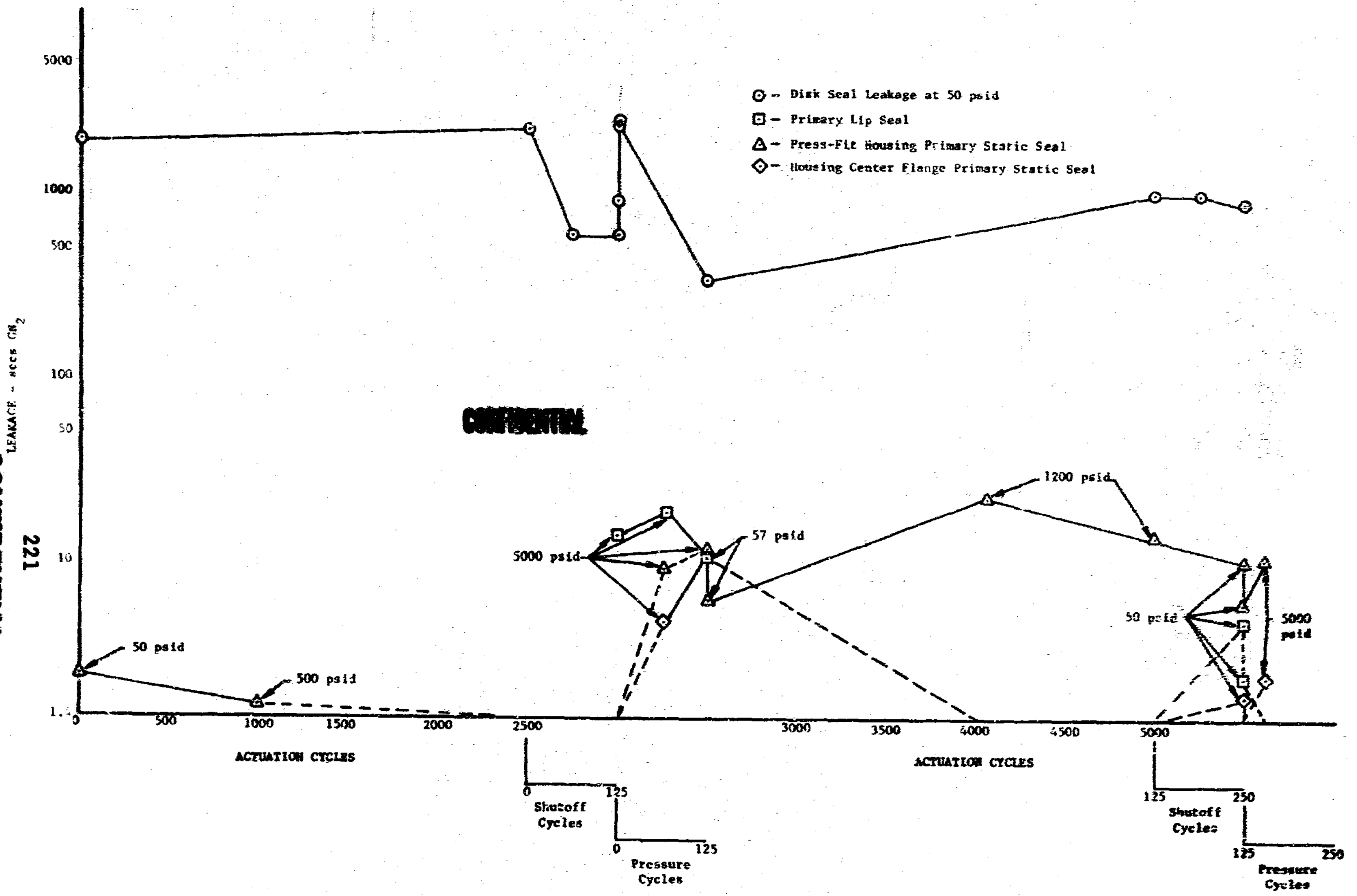

(U) Figure 212. Laminated Kapton F-FEP Teflon Seal Leakage vs Actuation, Shutoff, and Pressure Cycles, Rig F-33466-9

DFC 62170

(U) Figure 213. Failed Portion of Disk Seal After Test FE 74152

(U) Figure 214. Disk Seal Axial Supporting Ring After Test FE 74153

(2) Valve F-35106-Build No. 6

(U) Main chamber oxidizer valve F-35106-6 incorporated the following sealing configurations:

1. A silver-plated hoop disk seal with a 0.011-inch tight fit on the disk. (See Figure 215.) The disk seal was installed on the shaft disk in the closed position by heating the seal to approximately 250°F and cooling the disk in liquid nitrogen.

2. The Inconel 718 (AMS 5663) disk sealing surface was 0.090-inch wide with a 5 microfinish.

3. The revised shaft lip seal design as shown in Figure 216.

4. 0.019-inch thick laminated Kapton F (3 layers) and FEP Teflon (1 layer next to shaft, primary and secondary shaft lip seals.

5. A trapped 0.010-inch thick laminated Kapton F primary inlet flange static seal.

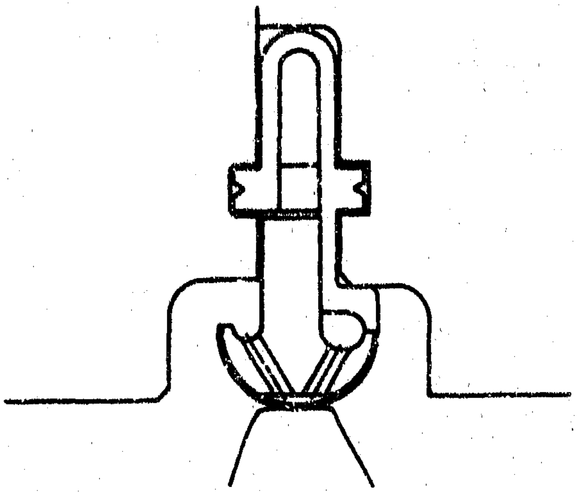

(U) Figure 215. Hoop Shutoff Seal FD 24949A

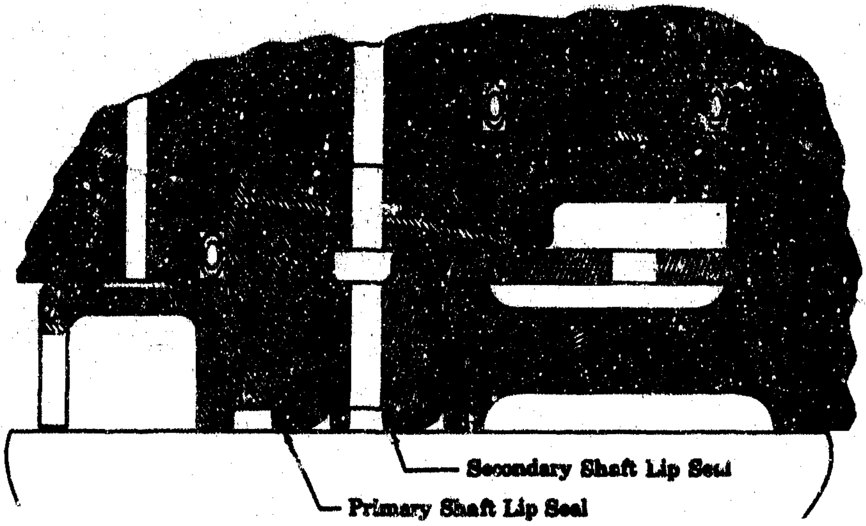

(U) Figure 216. Lip Seal Package FD 24852

(C) The valve was mounted in the B-22 test stand for an environmental endurance and leakage test; 10,000 partial stroke actuation cycles, 600 shutoff cycles, and 500 pressure cycles were completed. This endurance test was conducted with the valve submerged in liquid nitrogen.

(U) Indicated disk seal leakage was somewhat unstable and varied with time as shown in Figure 217. The measurements were apparently affected by variations in vent line vaporization rates due to both variable flow rates and cooling bath levels. The values shown on Figure 218 are the final readings taken at each point. After the endurance test was completed, an additional 100 shutoff cycles were performed using helium as the pressurizing and leakage test fluid to improve stability. During these tests, the valve position for minimum leakage was found to be 3.2 degrees from the full closed position. The test results using helium as the pressurizing medium and with the valve at 3.2 degrees open are shown in Figure 219.

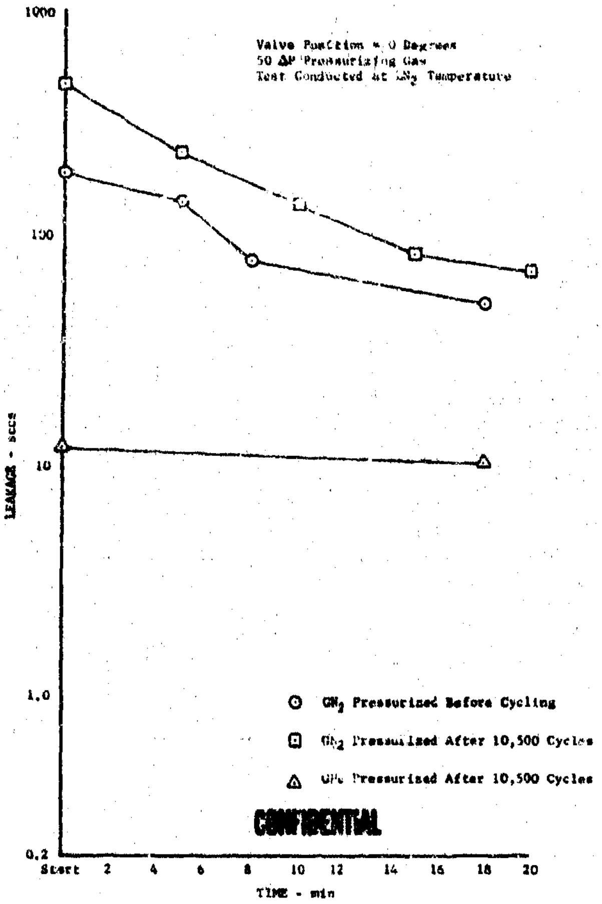

(U) Figure 217. Hoop-Type Disk Seal Leakage vs Time, Rig F-35106-6 DFC 65061

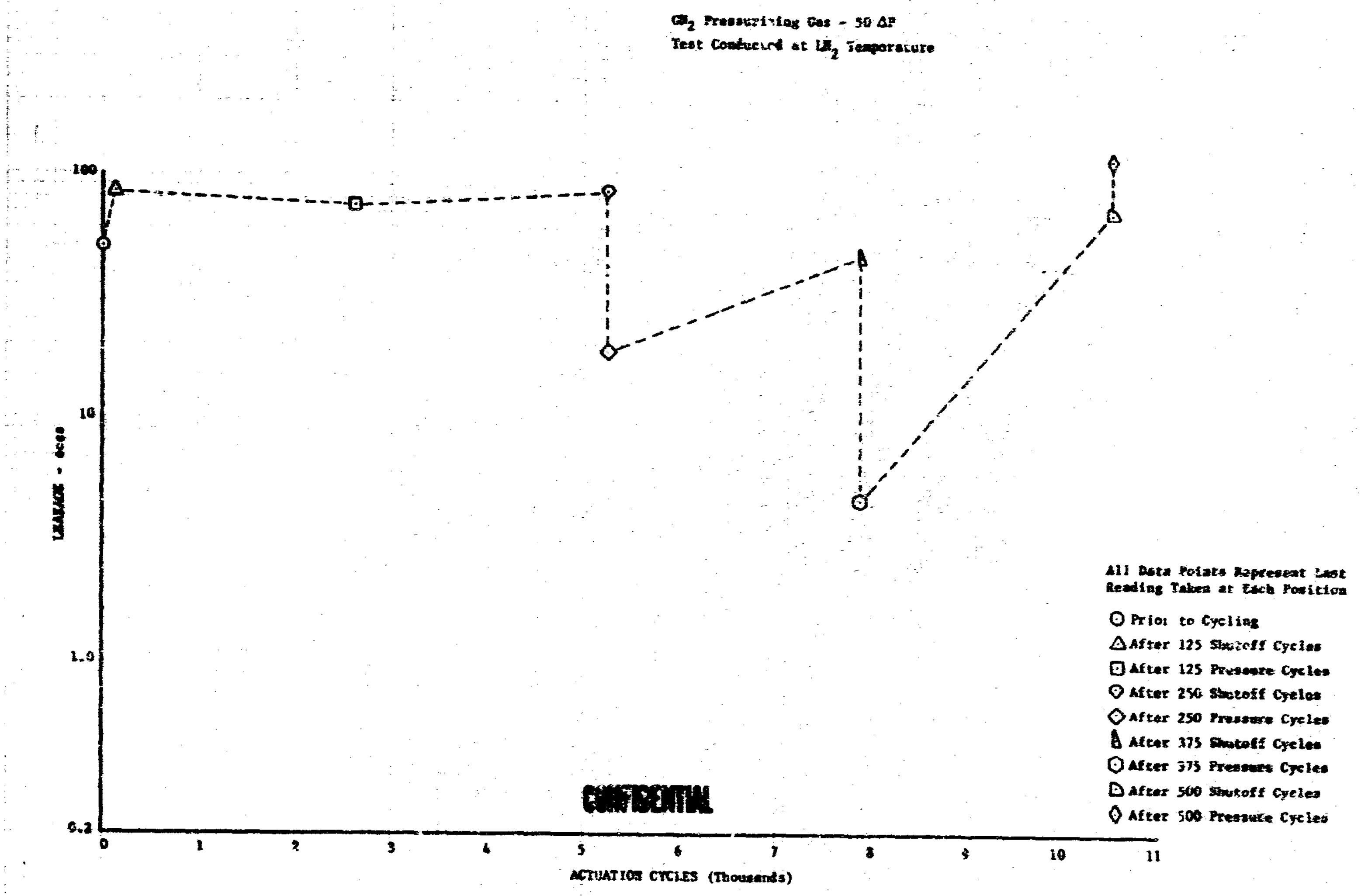

(U) Figure 218. Hoop-Type Disk Seal Leakage vs Actuation Cycles, Rig F-35106-6

DFC 65062

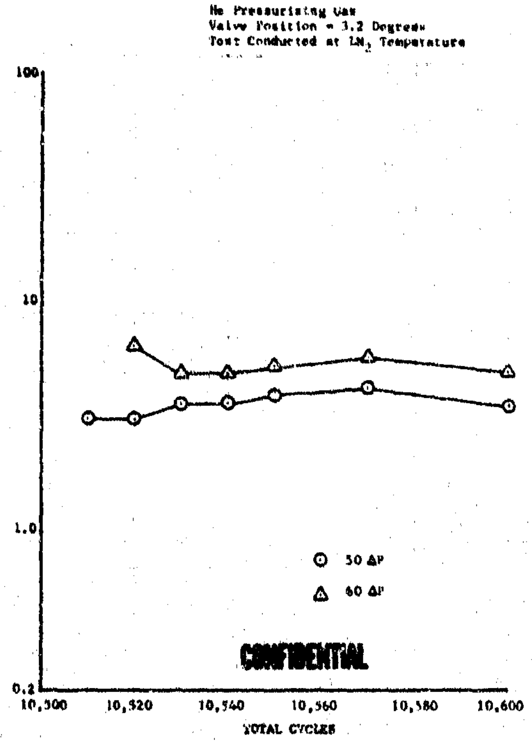

(U) Figure 219. Hoop-Type Disk Seal Leakage vs Total Cycles, Rig F-35106-6 DFC 65063

(C) No mechanical malfunctions were observed during the test. The thrust bearing cap primary static seal leaked excessively at pressures above 2000 psig. The vent was capped after 2625 actuation cycles. The primary and secondary shaft seal and static seal leakages during the test are shown in Figure 220.

(U) Prior to disassembly, the ambient temperature disk seal leakage at 50 psid GN_2 was 1.33 sccs with the disk positioned at 3.2 degrees from the closed position. At the closed position the leakage was 4.5 sccs. No other seal leakage was evident.

(U) Disassembly of the valve revealed no significant parts deterioration The disk seal showed some wear on the silver-plated hoop seal surface as shown in Figure 221. The shaft disk sealing surface is shown in Figure 222. Seal-to-disk fit was 0.0035 tight. All other parts were in excellent condition.

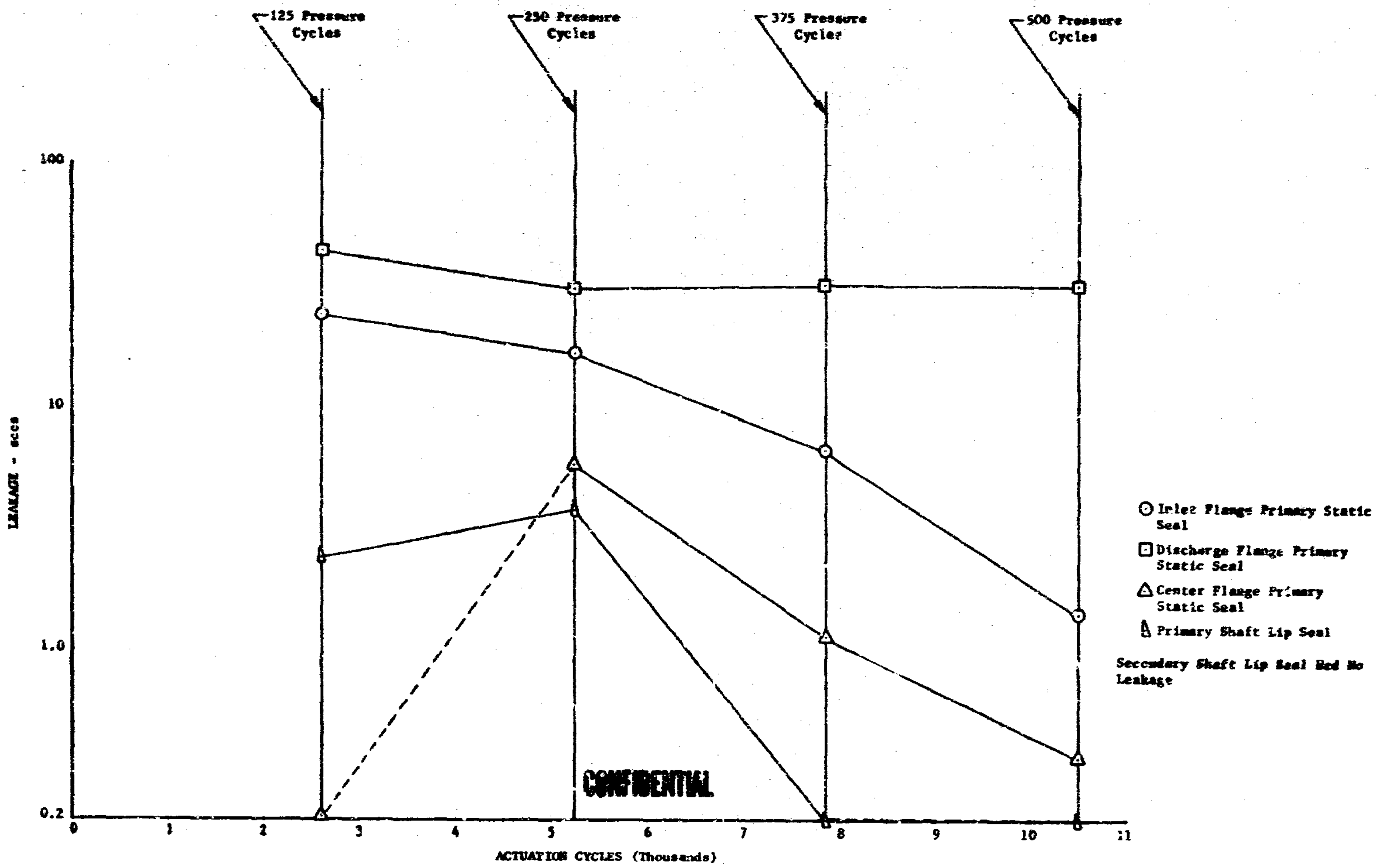

(U) Figure 220. Primary and Secondary Shaft Lip Seals and Static Seals Leakage vs Actuation Cycles, Rig F-35106-6

DFC 65064

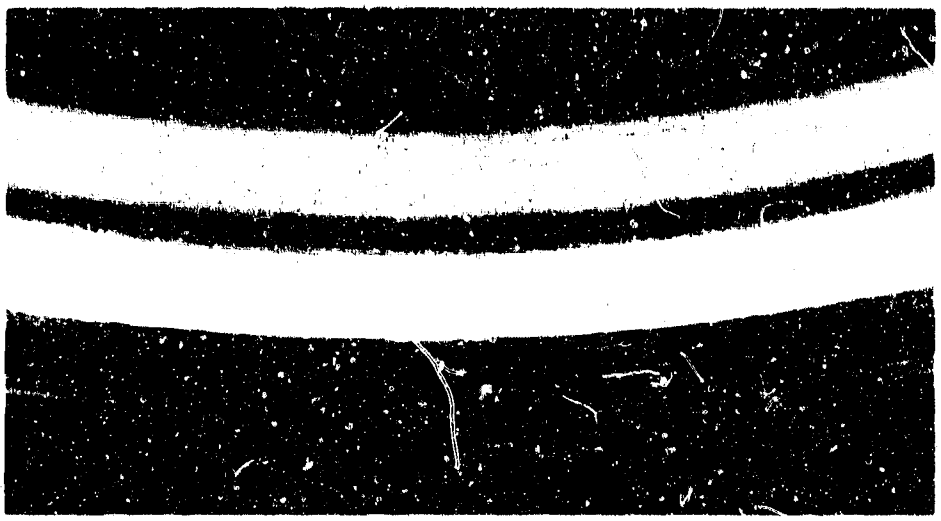

(U) Figure 221. Hoop Seal Surface After Test, Rig F-35106-6 FE 77114

(U) Figure 222. Shaft Disk Surface After Test, Rig F-35106-6 FE 77111

(3) Valve F-33466-Build No. 10

(U) Main chamber oxidizer valve F-33466-10 incorporated the following modifications from the previous build.

1. A silver-plated and Teflon primer coated 0.005-inch thick Inconel X (AMS 5598) seal element, as shown in Figure 223, was used for the disk seal. The seal element was contracted against the disk surface by a shaft lug and circumferential strap. A 0.012-inch shim was used to adjust the seal load. Ambient seal leakage was 1 sccs at 50 psid of GN_2 prior to cryogenic test. Figure 224 shows the shutoff seal configuration.

2. A seal actuating lug was welded to the shaft. The disk had a flat (cylindrical) sealing surface 0.090 inch wide with an 11 micro inch surface finish.

3. The revised shaft lip seal package design used is shown in Figure 216.

4. A laminated seal of Kapton-F (3 layers) and FEP Teflon (1 layer next to shaft) was used for the primary shaft lip seal. The total thickness of this lip seal was 0.019 inch.

5. A trapped 0.020-inch thick laminated Kapton-F seal was used for the inlet flange static seal.

6. An Inconel X (AMS 5667) inverted U-ring center flange static seal assembly was used for the center flange static seal. It loaded two 0.015-inch thick laminated Kapton-F seals.

7. A Teflon-coated Omega-shape design, which incorporated an assembly preload spacer and was pressure energized to follow flange deflection during operation, was used for the discharge flange static seal.

8. A rotary hydraulic servoactuator was used.

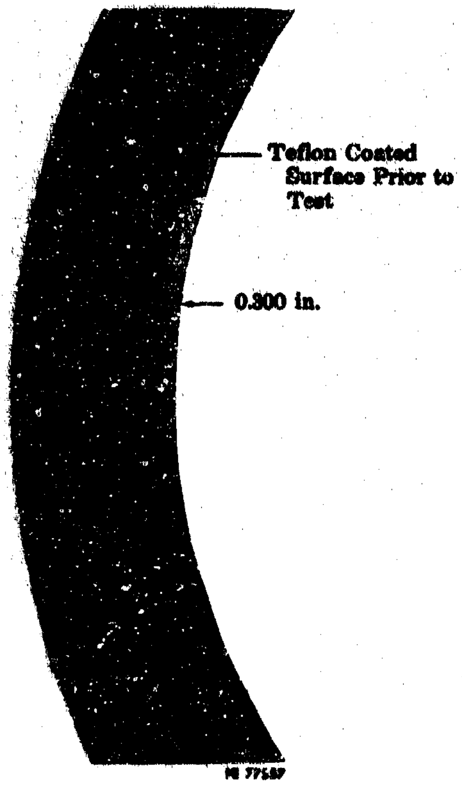

(U) Figure 223. Shutoff Seal Prior to Test, Rig F-33466-10 FD 24858

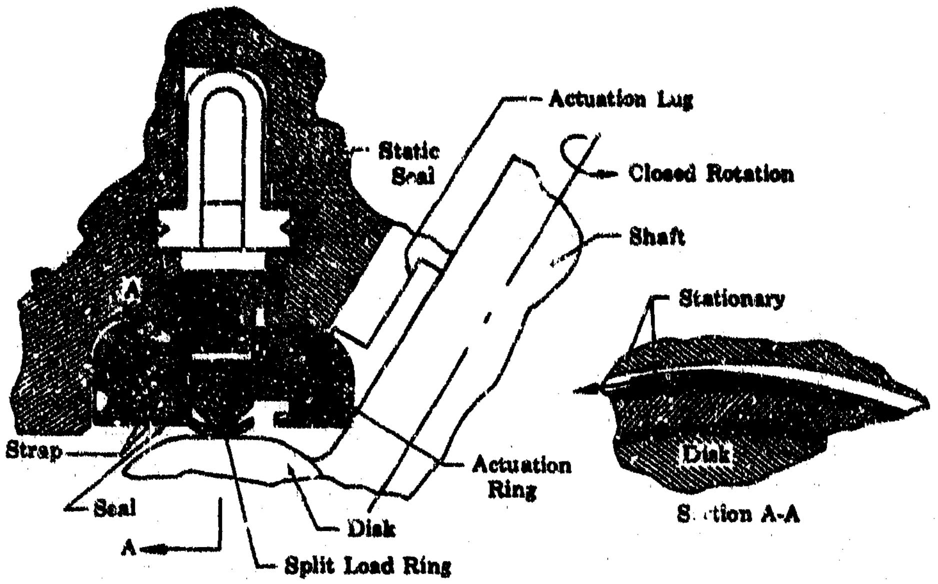

(U) Figure 224. Strap-Actuated Shutoff Seal FD 24851A

(C) The valve was mounted in the B-22 test stand for an environmental leakage and endurance test; 10,000 partial stroke actuation cycles, 500 shutoff cycles and 500 pressure cycles were completed. This endurance test was conducted with the valve submerged in liquid Argon.

(U) Liquid nitrogen boiloff at the start of each measurement point resulted in indicated disk seal leakage variation with time as shown in Figure 225. The values shown in Figure 226 are the final readings taken at each set point. An ambient temperature GN_2 purge to the discharge housing prior to each disk seal leakage measurement point was apparently only partially effective in removing the liquid nitrogen that had accumulated in the housing.

(C) No mechanical malfunctions were observed during the test. The thrust bearing cap and shaft seal housing static seals leaked excessively at pressures above 1200 psid. The vents were capped after 2625 actuation cycles. The primary and secondary shaft seal leakage is shown in Figure 227. The static seal leakages are shown in Figure 228.

(U) Prior to disassembly, the following ambient temperature seal leakages were measured at 50 psid GN_2:

Disk Seal	0.80	sccs
Shaft Primary Static Seal	0.0059	sccs
Discharge Static Seal	0.0182	sccs

No leakage was detected at the other seals.

(U) Disassembly of the valve revealed the following:

1. A glycol base oil was found on the inlet surface of the disk. (See Figure 229.) The same type oil was subsequently found in a line used for the valve pressure check just prior to teardown.

2. The disk seal was in good condition. The Teflon primer was worn through in two local areas of the seal surface. These conditions are shown in Figures 230 and 231.

3. The shaft disk had minor seal surface scratches, and Figure 232 shows a typical disk seal surface condition.

4. All other parts were in excellent condition as shown in Figure 233.

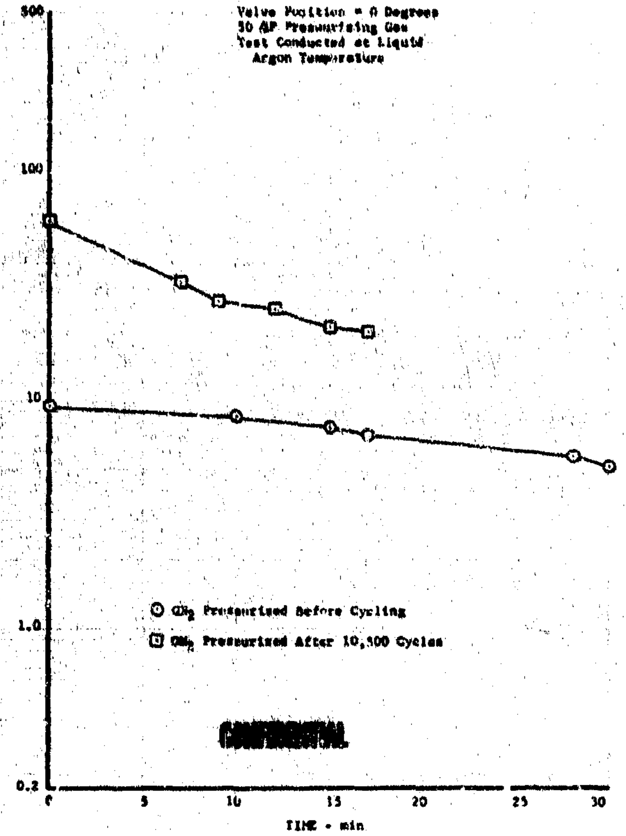

(U) Figure 225. Strap-Actuated Disk Seal Leakage vs Time, Rig F-33466-10

DFC 64959

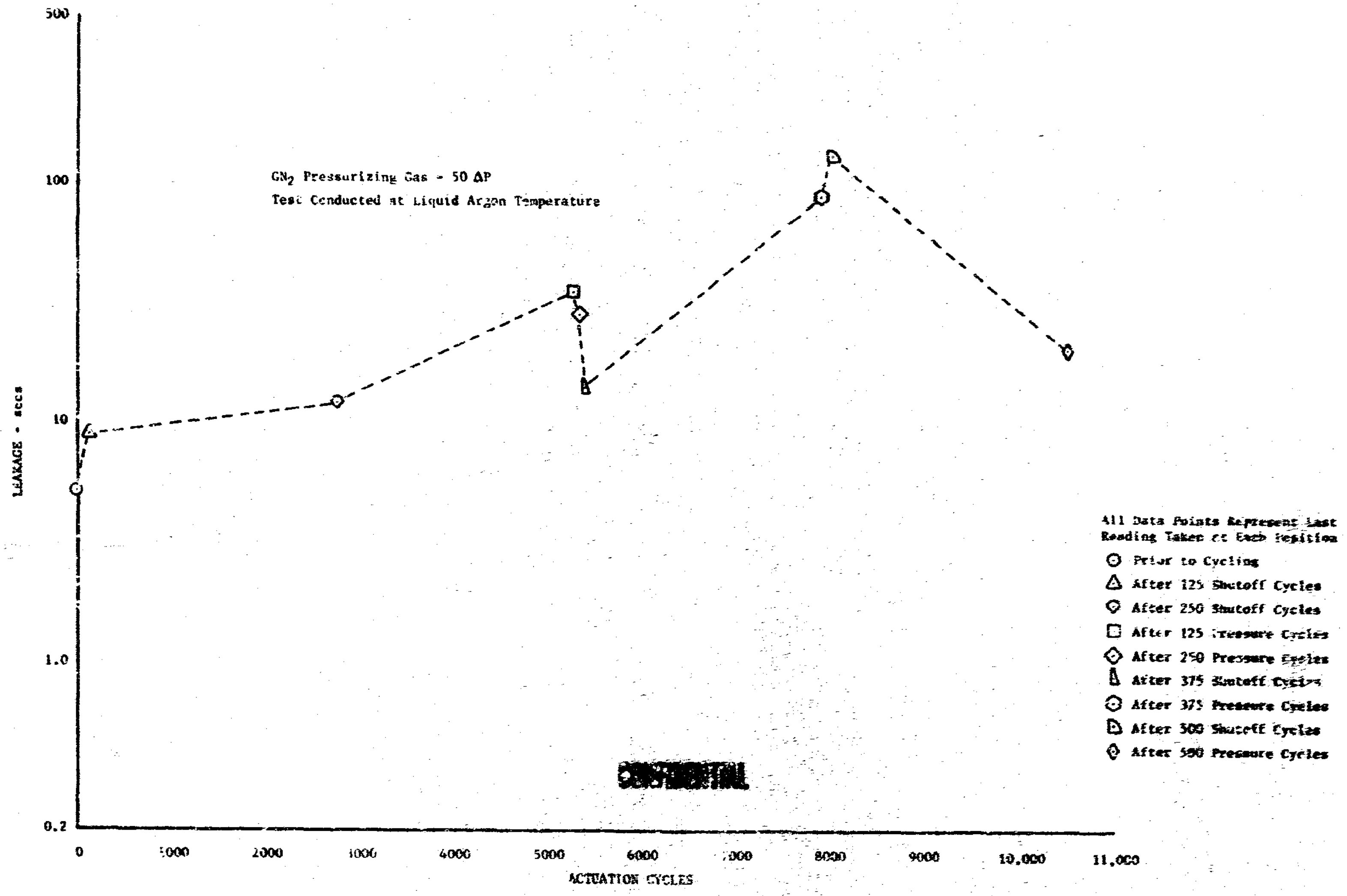

(U) Figure 226. Strap-Actuated Disk Seal Leakage vs Actuation Cycles, Rig F-33466-10

DFC 64960

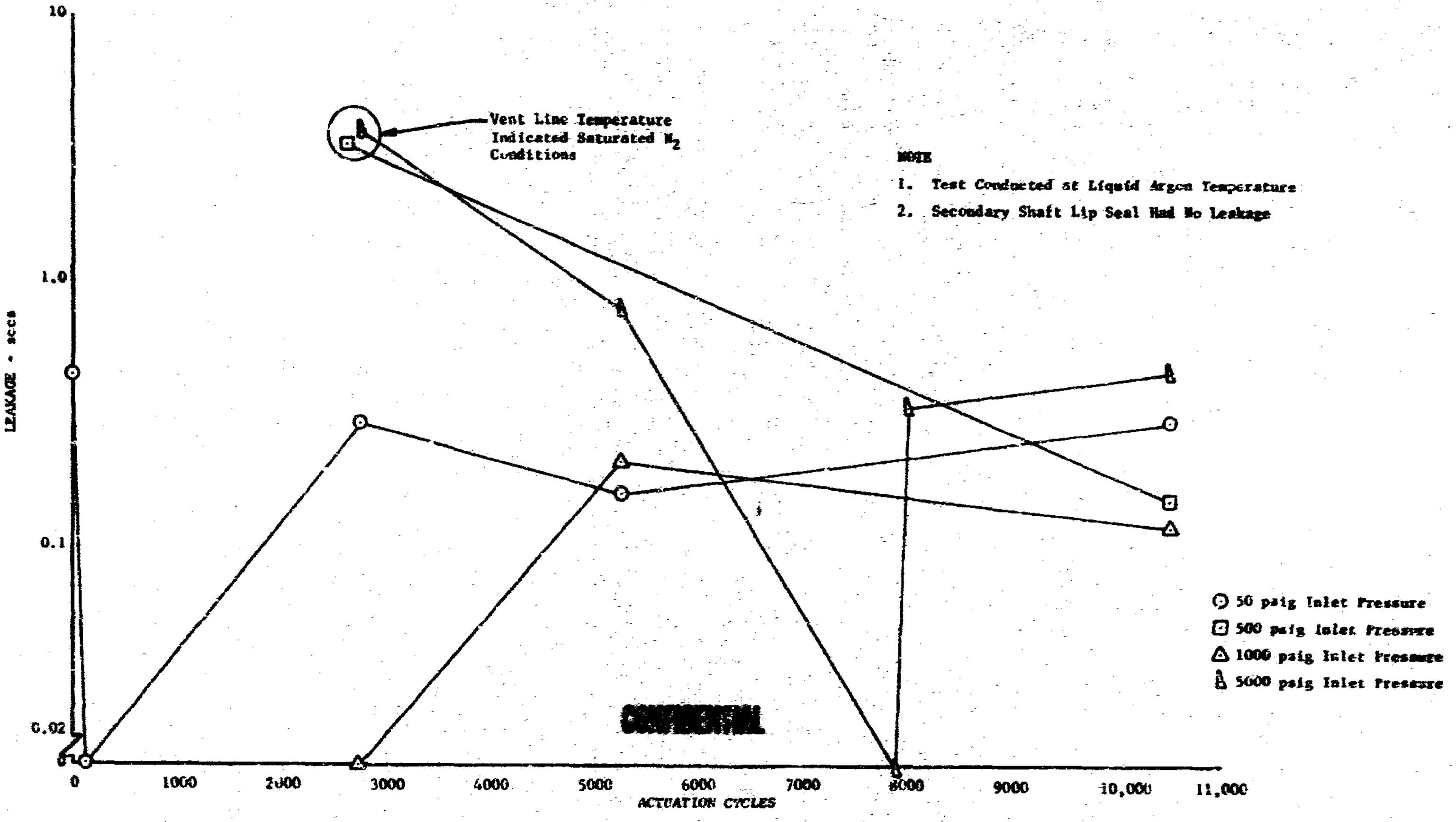

(U) Figure 227. Primary Shaft Lip Seal Leakage vs Actuation Cycles, Rig F-33466-10

DFC 64961

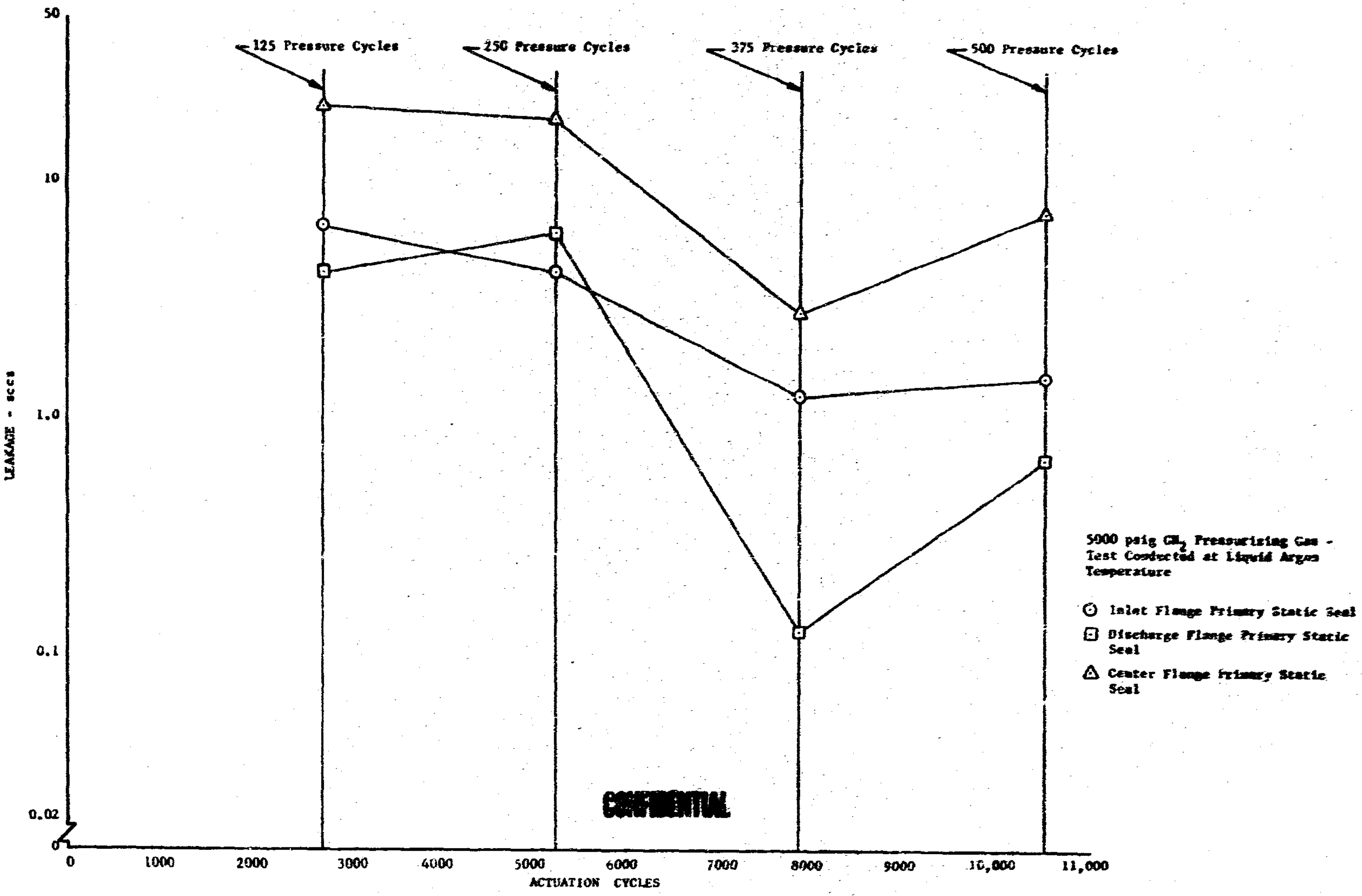

(U) Figure 228. Static Seal Leakages vs Actuation Cycles, Rig F-33466-10

DFC 64962

(U) Figure 229. Glycol Contamination on Inlet Side of Disk, Rig F-33466-10 (Disk is 2.990 inches in Diameter) FE 77843

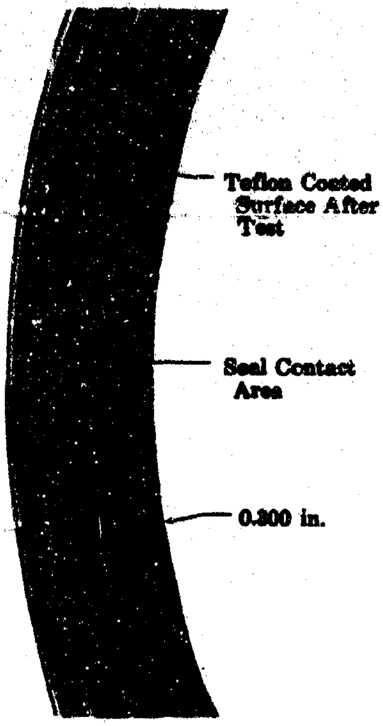

(U) Figure 230. Shutoff Seal After Endurance Test, Rig F-33466-10 FD 24853

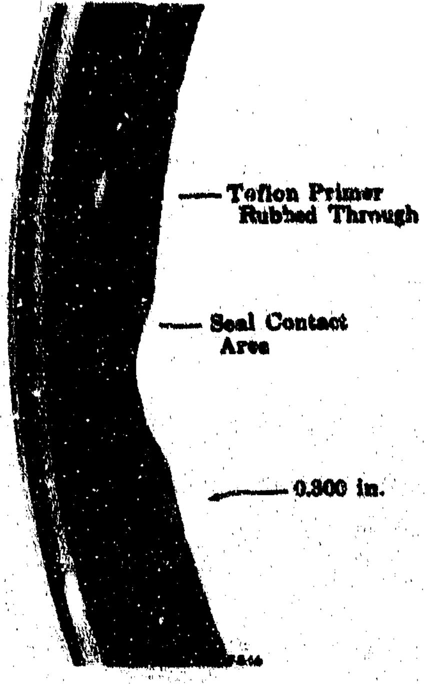

(U) Figure 231. Shutoff Seal After Endurance Test, Rig F-33466-10 FD 24854

(U) Figure 232. Disk Seal Surface After Endurance Test, Rig F-33466-10 FD 24856

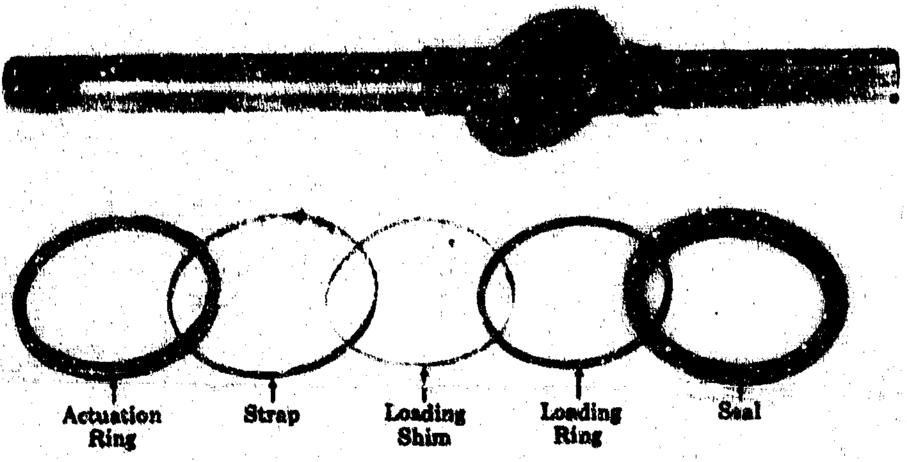

(U) Figure 233. Strap Actuated Disk Seal, Rig F-33466-10 FD 24855

(4) Valve F-35106 - Build No. 7

(U) Main chamber oxidizer valve F-35106-7 incorporated the following sealing configurations:

1. A Kel-F disk seal element contracted against the disk surface by a cam-actuated tapered slip ring. (See Figure 234.)
2. A spherical chrome plated Inconel 718 (AMS 5663) disk seal surface with a 9.5 microfinish. The cam actuation lug was electron beam welded to the shaft.
3. A trapped 0.020-inch thick laminated Kapton F primary inlet flange static seal.
4. The center flange static seal was an Inconel X (AMS 5667) inverted U-ring static seal assembly that loaded a portion of the Kel-F seal element against the inlet housing and a 0.020-inch laminated Kapton-F seal against the discharge housing.
5. The discharge flange static seal was a Teflon-coated omega-shaped design that incorporated an assembly preload spacer and is pressure energized to follow flange deflections during operation.
6. The bearing cap static seal was 0.010-inch thick laminated Kapton-F formed around the outside diameter of a ring.

(C) The valve was mounted in the B-22 test stand for an environmental endurance and leakage test, 10,000 partial stroke actuation cycles, 500 shutoff cycles, and 260 pressure cycles were completed. The test was conducted with the valve submerged in liquid Argon.

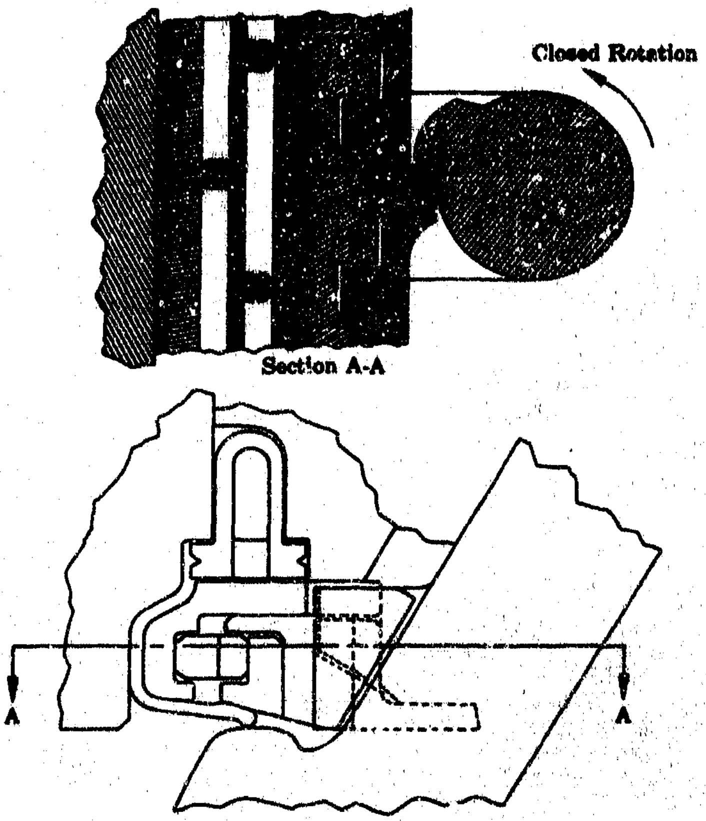

(U) Figure 234. Cam-Actuated Shutoff Seal, Rig F-35106-7 FD 24991

(U) The Disk seal leakage measurements varied with time as shown in Figure 235. The values shown in Figure 236 are the final readings taken at each set point. The disk seal leakage prior to pressure cycling was less than 0.025 sccs. The seal failed during either pressure or actuation cycling after 125 shutoff cycles and 2500 actuation cycles had been completed satisfactorily.

(C) The test stand supply valve actuator failed after 250 pressure cycles so the remainder of the programmed 500 pressure cycles was not performed. The discharge flange primary static seal leaked excessively above 1000 psig. Primary shaft seal leakage is shown in Figure 237 and static seal leakages are shown in Figure 238.

(U) Visual inspection of the disk seal prior to disassembly revealed failure of the Kel-F seal element. Pieces of the seal were found in both the inlet and the discharge housings. The seal condition after the test is shown in Figure 239. Failure of the seal element at the edge of the shaft cutout, as shown in Figure 240, appears to have been caused by either a reverse differential pressure across the seal or seal drag during valve opening after the pressure cycles. The possibility of excessive reverse pressurization during pressure cycling existed because of valve inlet and discharge cavity pressurizing line volume differences. The shaft disk sealing surface is shown in Figure 241.

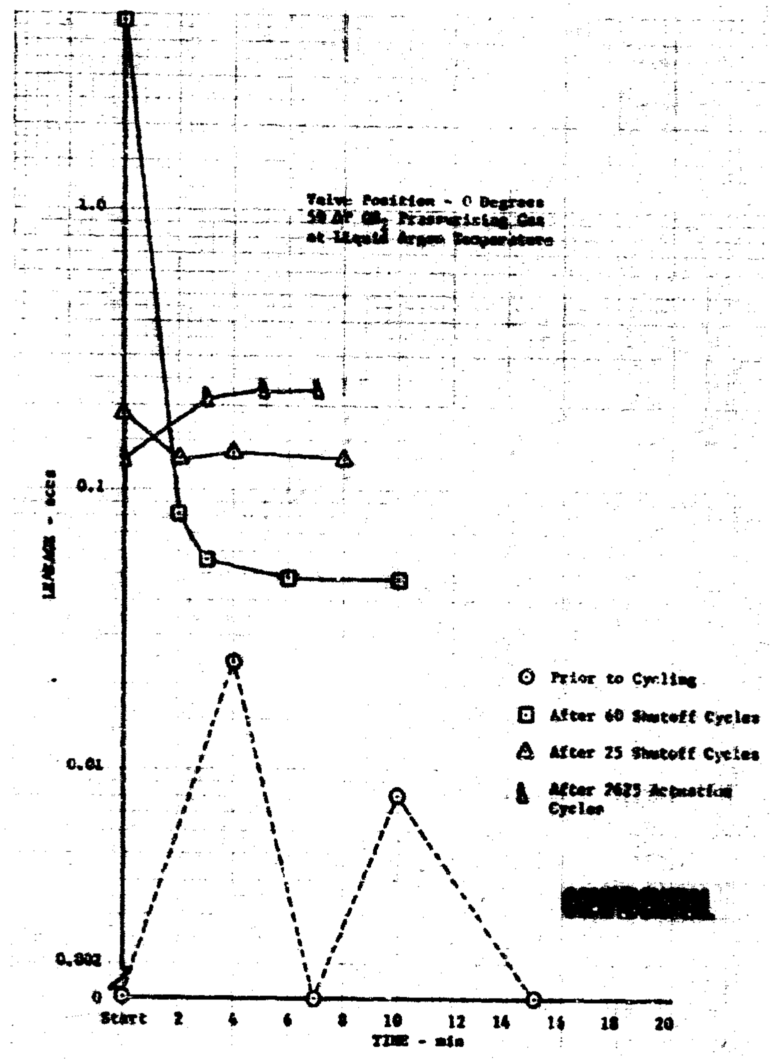

(U) Figure 235. Cam-Actuated Disk Seal Leakage vs Time, Rig F-35106-7 DFC 65226

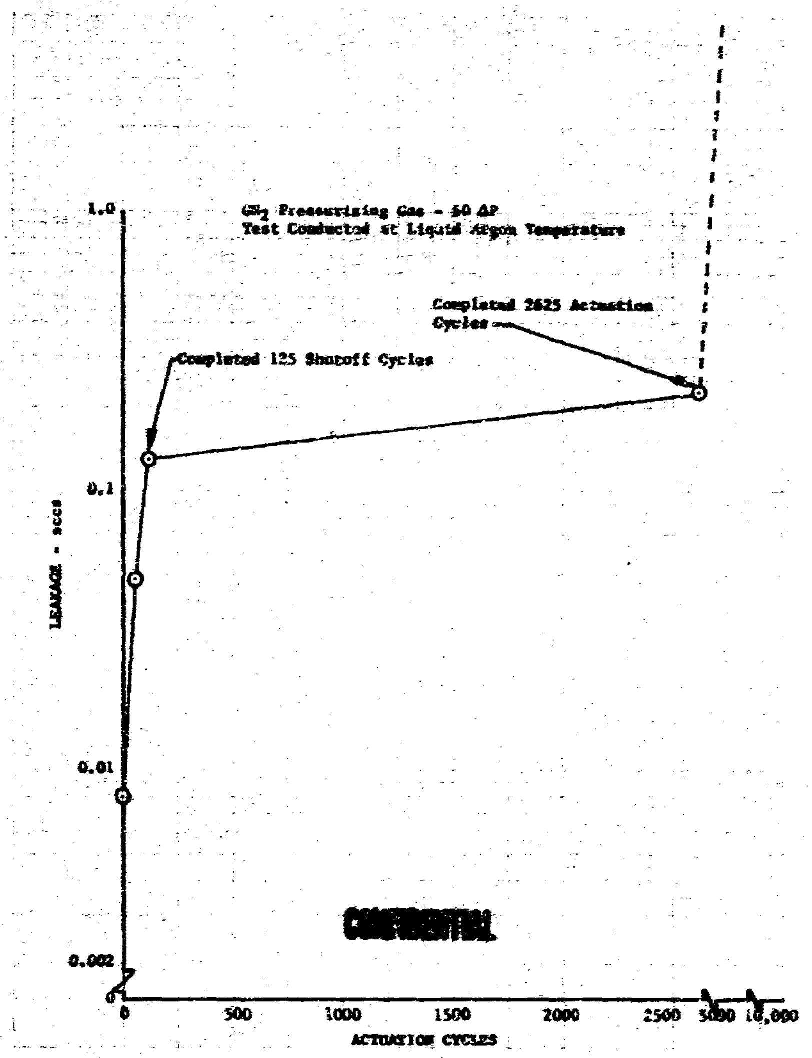

(U) Figure 236. Cam-Actuated Disk Seal Leakage vs Time, Rig F-35106-7 DFC 65227

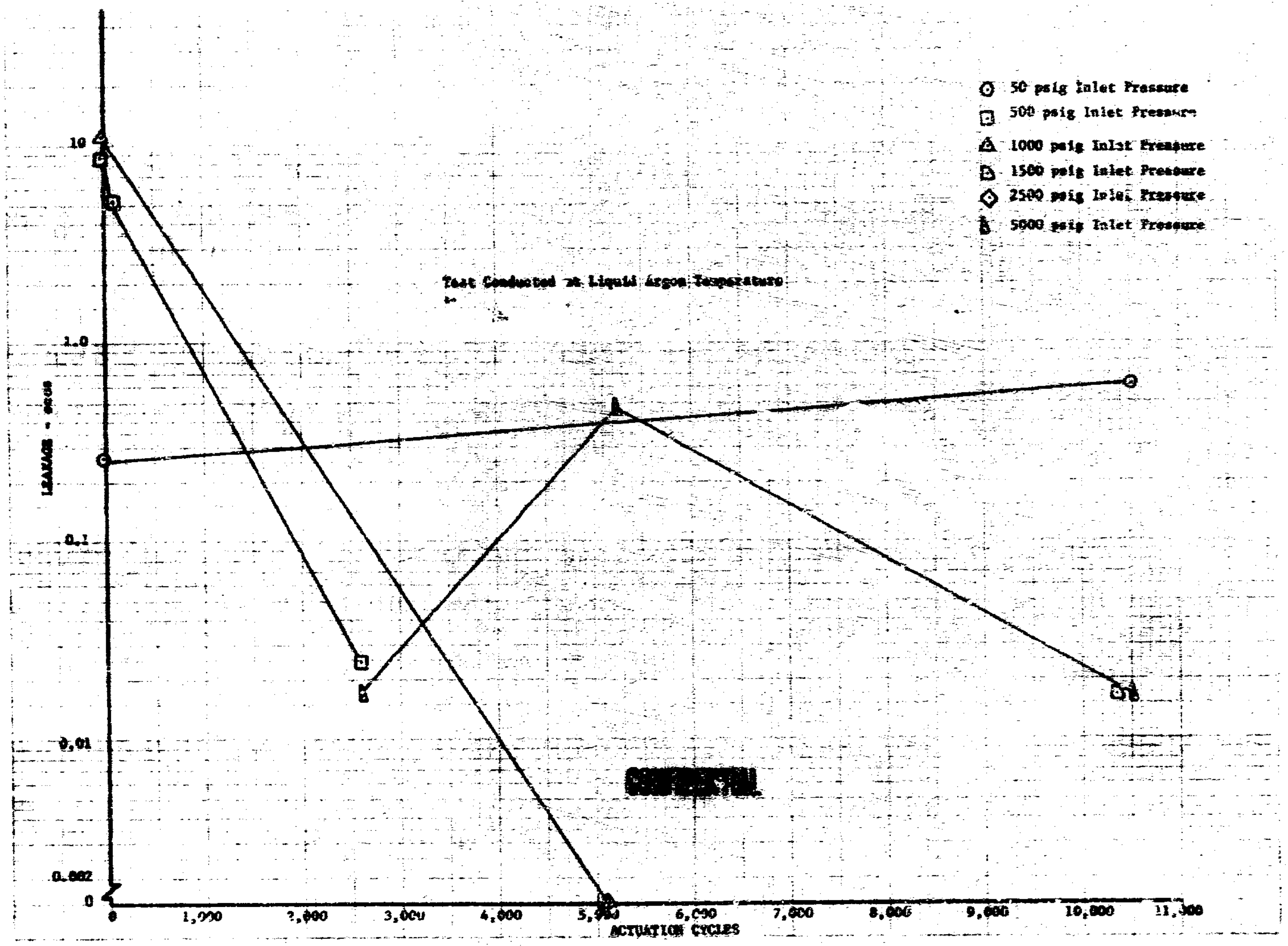

(U) Figure 237. Primary Shaft Lip Seal Leakage vs Actuation Cycles, Rig F-35106-7

DFC 65228

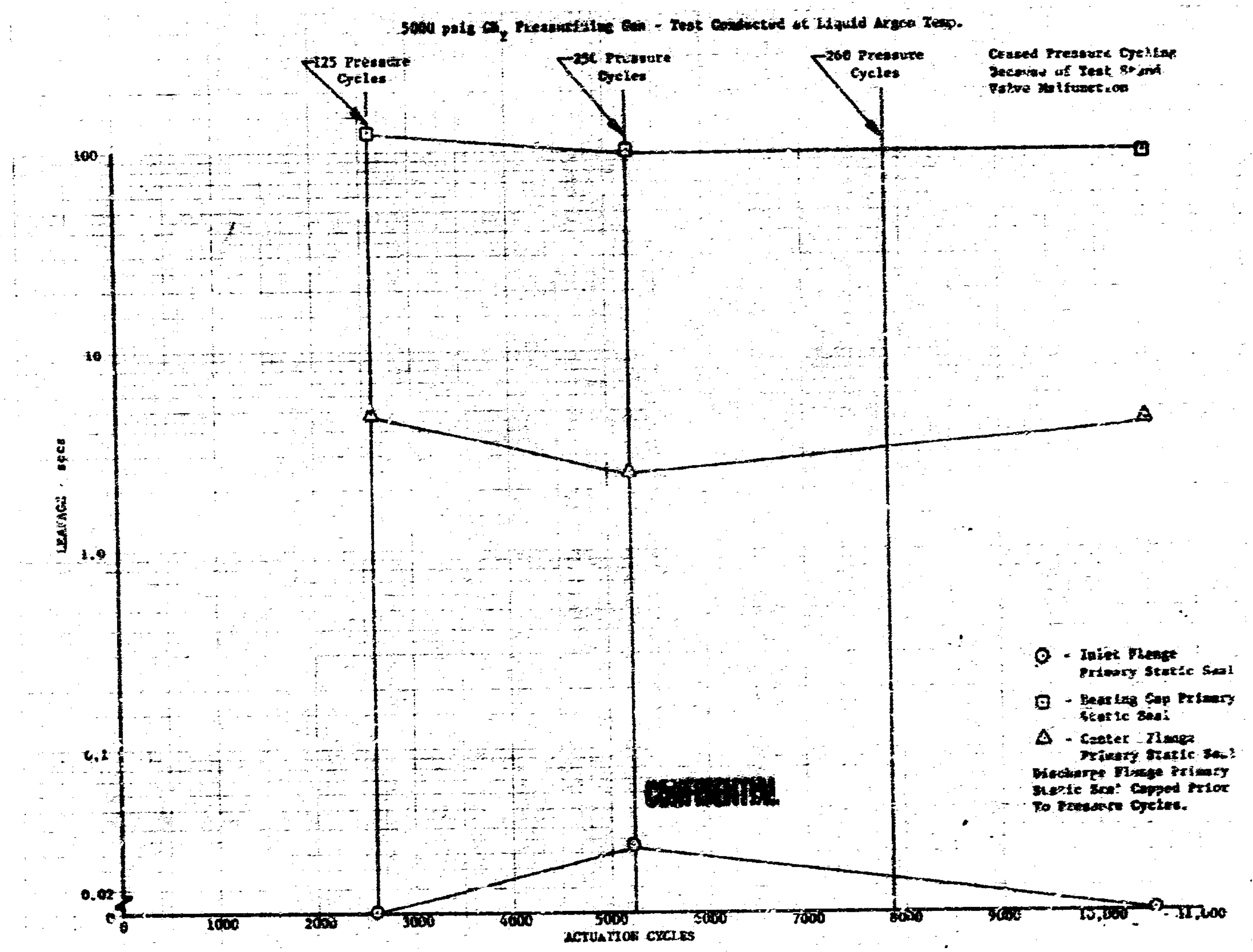

(U) Figure 238. Static Seal Leakage vs Actuation Cycles, Rig F-35196-7

DFC 65229

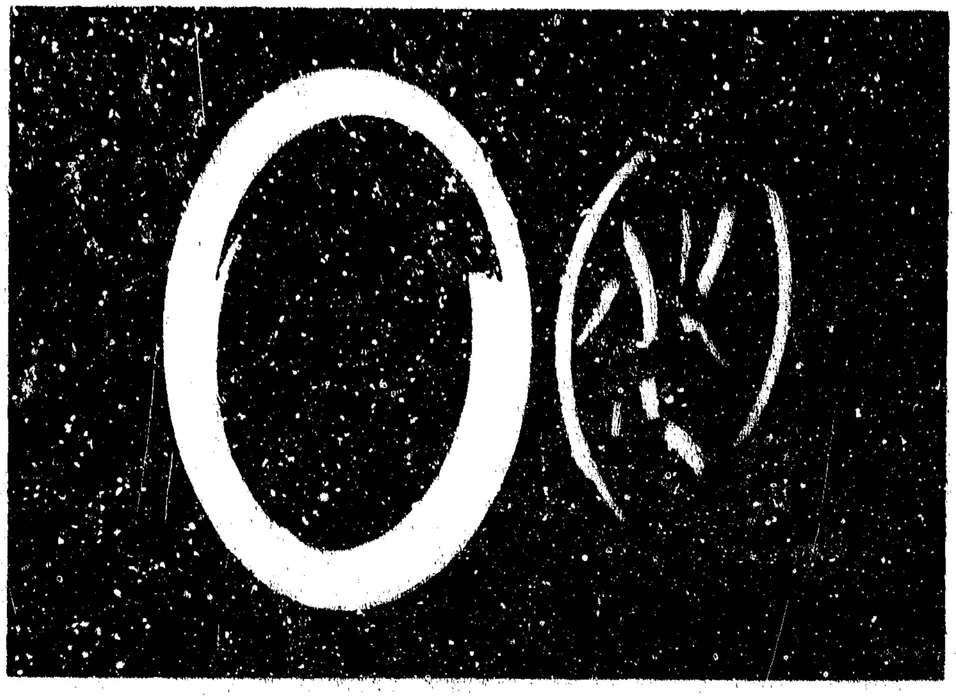

(U) Figure 239. Disk Seal After Test, Rig F-35106-7 FE 78243

(U) Figure 240. Area of Seal Element Failure FE 78241

(U) Figure 241. Shaft Disk Sealing Surface After Test, Rig F-35106-7 FE 78242

(U) The discharge static seal, which had been used in several test series without recoating the seal surface prior to this build, had insufficient contact load. All other parts were in excellent condition.

2. Preburner Oxidizer Valve

a. Introduction

(U) During testing of the sleeve-type preburner oxidizer valve during Phase I (Contract AF04(611)-11401), it was found that the wear characteristics of the BeCu piston rings on the chrome-coated main housing were not acceptable. The objective, therefore, of this subtask was to investigate improved surface coatings and a pressure balanced piston ring design.

(U) A series of tests was conducted to obtain an improved surface coating and a piston ring pressure balance study was made.

(U) Four cyclic endurance tests were made to evaluate the design changes on the wear characteristics of the piston rings operating at high differential pressures.

b. Summary, Conclusions, and Recommendations

(U) The wear results on all four configurations tested demonstrated acceptable wear characteristics. The piston ring leakage on all four tests was also acceptable. A variation in leakage observed between the tests was primarily because of variations in the fit between the piston ring and housing. Strain gages were installed on the secondary sleeve and actuator shaft on Rigs F-33458-7 and -8 to determine actuator loads for balanced and unbalanced piston rings.

(U) As a result of the test program the following conclusions and recommendations have been made:

1. Precision chrome coating has been selected for the preburner oxidizer valve application because the plating techniques are sufficiently developed. The application of molybdenum-chromium will require further coordination with an outside vendor or in-house plating shop to produce consistent results. Further development of molybdenum-chromium is recommended for extremely high load applications where the wear characteristics of precision chrome is not acceptable.
2. The balanced piston rings provided acceptable wear characteristics and a reduction in actuation force as compared to the unbalanced rings; however, further force reduction is desirable to minimize actuator power requirements.

c. Electrolytic Coating Investigation

(U) After it was discovered that the wear characteristics of the BeCu piston rings on the chrome-coated main housing were not acceptable, a program was initiated to develop and evaluate a wear resistant electrolytic coating that would be superior under high loading stress at cryogenic temperatures. A chromium-molybdenum alloy was considered the chief candidate because reports had been made that small amounts of molybdenum in chromium produce improvements in wear resistance. Several preliminary tests were conducted to compare adhesion quality, abrasive wear, surface characteristics, and corrosion resistance of normal chrome plate to a chromium-molybdenum alloy. When these tests were completed, force-wear tests were conducted on all candidates to determine the best wear resistant coating. The following paragraphs generally outline the test procedures that were followed.

(1) Preliminary Tests

(U) Several stainless steel (AMS 5646) panels (about 3 in. x 3 in. x 0.25 in.) were plated on one side with chromium or chromium-molybdenum alloy. The chromium-molybdenum alloy was electrolytically deposited from a chromic acid bath into which about 3 ounces of molybdenum per gallon of solution had been anodically dissolved. The composition of each panel was analyzed to determine the percentage of molybdenum in each deposit. It was found that the amount of molybdenum in the deposits varied with plating conditions. Plating at 1.5 amperes per square inch and 110 to 130°F yielded deposits containing about 1% molybdenum.

(U) Adhesion tests were then made. Holes (0.27-inch diameter) were drilled from the unplated side to within 0.06 inch of the plated surface. A steel rod (0.25-inch diameter) was then inserted in the hole and pressure was applied until the rod was forced through the plating. An examination was made of the break area to find indications of adhesion quality. Comparing the results (Figure 242) revealed that the chromium-molybdenum alloy plate has the same adhesion to stainless steel (AMS 5646) as regular chrome plate. Examination of low power magnifications of the pressed out portions revealed that the crack pattern on the alloy plated surface was finer and not as severe as on the regular chromium plated surface indicating that the alloy plate was softer than the chromium plate.

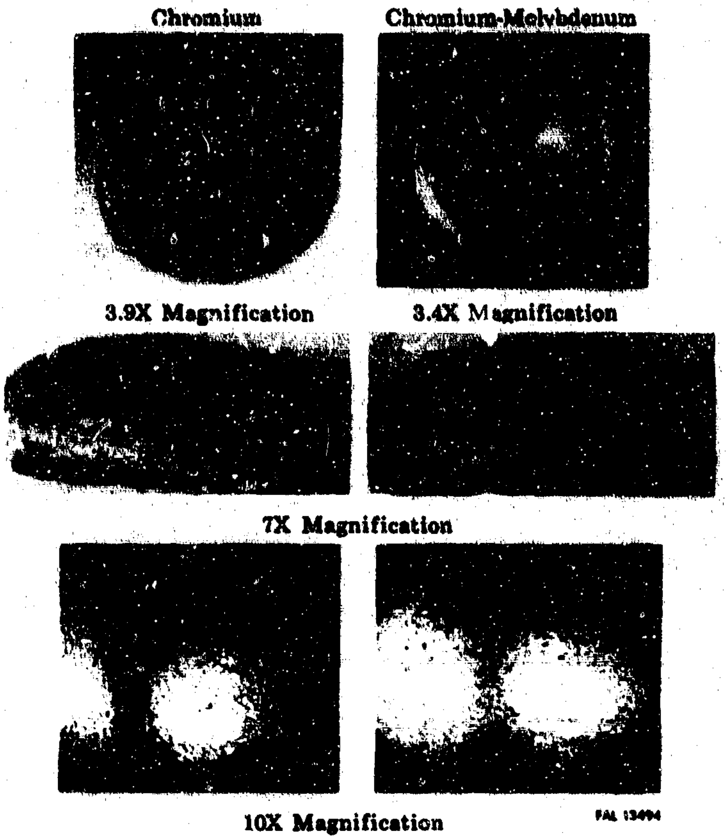

(U) Figure 242. Adhesion Tests of Chromium and Chromium-Molybdenum Plating on Stainless Steel (AMS 5646) FD 25271A

(U) Abrasive wear tests were then made of chromium and chromium-molybdenum alloy deposits. A Taber Abraser Model 174 with a CS-10 Calibrase Wheel was used to make these tests. The test results, which indicate the alloy has about six times the abrasive wear resistance of chromium, are shown in Table XXIII. Previous tests of the alloy in an amsler machine showed an improvement of six to eight times over chromium plate.

(U) Table XXIII. Taber Abraser Wear Testing of Chromium and Chromium-Molybdenum Alloy Electroplate

Cycles to First Indication of Failure	
Chromium	Chromium-Molybdenum
4000	23,000
3000	19,000
4000	31,000

(U) Surface characteristics of both the chromium plate and the chromium-molybdenum plate were then compared. Figure 243 shows magnified views of stainless steel (AMS 5646) surfaces after plating with both materials. The characteristic heavy crack pattern noted on conventional chrome is reduced substantially on the alloy.

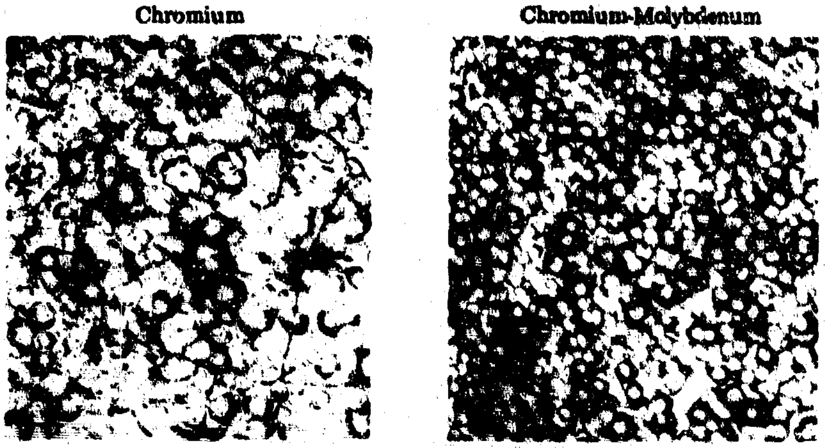

280X Magnification

(U) Figure 243. Surface Characteristics of Chromium and Chromium-Molybdenum Plating on Stainless Steel (AMS 5646) FD 25272A

(U) When the plating is conducted in a bath using ultrasonic energy, the differences are more pronounced. By comparing the regular chromium and chromium-molybdenum plates shown in Figure 243 with their counterparts from a bath using ultrasonic energy shown in Figure 244, ultrasonic plating results in: (1) a reduction in number and size of surface cracks on the chromium plate, (2) elemination of cracks on the alloy plate, and (3) a finer texture, expecially for the alloy. These results suggest that plating in a bath using ultrasonic energy will result in denser deposits with corresponding better wear and corrosion characteristics.

(U) Corrosion resistance tests were then made with stainless steel (AMS 5646) panels plated with 0.001 inch of either chromium or chromium-molybdenum alloy. These samples were placed in a salt-spray test chamber for 250 hours. As shown in Figure 245, rust spots were evident on the surface of the chromium plate but no indications of corrosion were noted on the alloy.

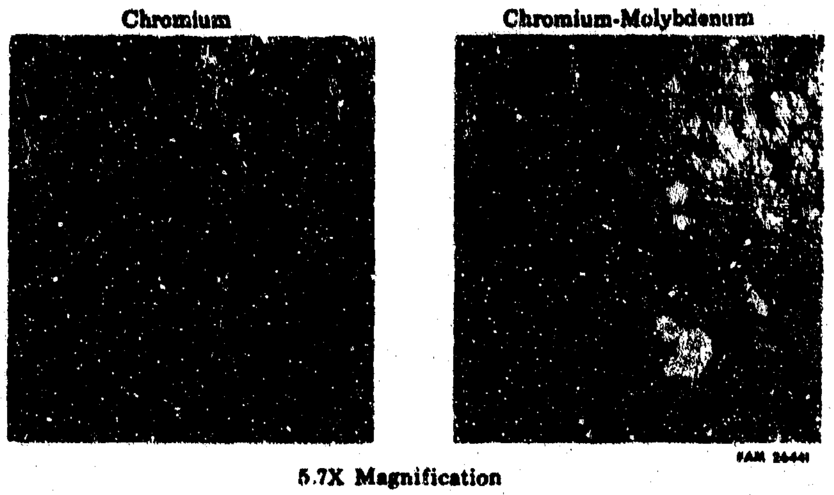

Chromium

Chromium-Molybdenum

5.7X Magnification

(U) Figure 244. Surface Characteristic of Chromium and Chromium-Molybdenum Ultrasonic Plating on Stainless Steel (AMS 5646) FD 25273A

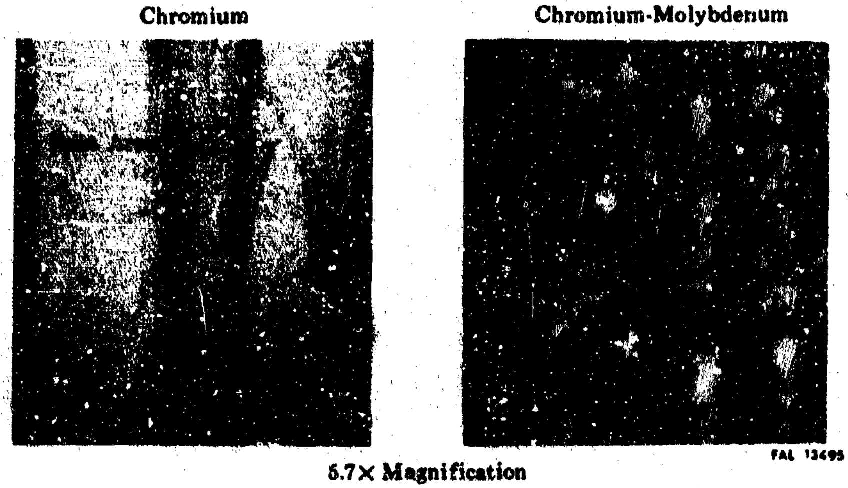

Chromium

Chromium-Molybdenum

5.7X Magnification

(U) Figure 245. Chromium and Chromium-Molybdenum Plated Surfaces After 250 Hours of Salt Spray Testing FD 25274A

(U) The results of these preliminary tests clearly indicate that a chromium-molybdenum alloy electrodeposit is generally superior to a conventional chromium electrodeposit. Ultrasonic agitation used with the chromium-molybdenum alloy plating appears to have merit in that the deposits appear to be free of cracks, denser, and more wear resistant.

(2) Force-Wear Tests

(U) Force-wear tests were required to screen the candidates for the pre-burner oxidizer valve. The Materials Development Laboratory (MDL) coefficient of friction machine, shown in Figure 246, was adapted to enable the disk and rider specimens to be immersed in liquid nitrogen.

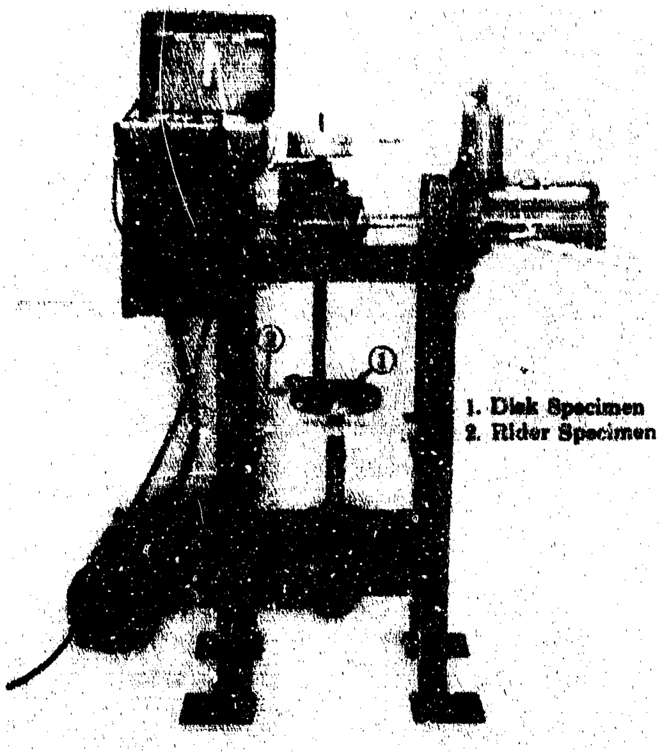

FAC 9305

(U) Figure 246. Coefficient of Friction Machine FD 25275

(U) The disk and rider specimens were secured to the power shaft and transfer shaft, respectively, of the friction machine and were immersed in liquid nitrogen. The start of each test was delayed until nitrogen boil-off was minimal. A normal load of 97 lb was then applied to the rider specimen and the disk was rotated at a surface speed of 6 in./sec as adjusted with the variable speed drive. Dynamic friction force curves were obtained for each rider-disk combination at various points during the 250 cycle test runs. Friction force curves were used to obtain sliding friction coefficient data. Coefficients of friction were calculated by dividing the friction force (lb) by the dead weight normal load (lb).

(U) From the test program, summarized in Table XXIV, the following conclusions were drawn.

1. Both the chrome (0.001-inch thick) and the molychrome (0.0015-inch thick) plated disks running against uncoated Berylco 25 (AMS 4650) rider specimens produced acceptable wear characteristics.

2. The wear of the chrome plated surface was characterized by light scratches while the wear of the molychrome surface was characterized by a slight depression in the plated surface.

3. No appreciable benefit in wear characteristics or reduction in coefficient of friction was noted during testing of the various lubrication coatings. A comparison of the wear characteristics of the baseline configuration (0.0001-inch thick chrome) as compared to the 0.001-inch thick chrome and the 0.0015-inch thick molychrome surfaces is shown in Figures 247, 248, and 249.

d. Piston Ring Pressure Balance Study

(1) General

(U) During Phase I (Contract AF04(611)-11401) cryogenic endurance testing of the preburner oxidizer valve, it was found that the lower piston ring wore through the chrome coating of the main housing. An analysis of the pressure loading effects of piston rings was made to determine if a piston ring redesign to balance the loading would improve the wear characteristics. The analysis was based on a procedure outlined in Engineers Piston Ring Handbook, Koppers Co., Inc., which states that for a unit cross section of the ring, the axial force per circumferential inch (F_A) and the radial force (F_R) can be determined from the pressure distribution around the sealing surfaces. An illustration of this is shown in Figure 250. The determination of F_R includes the static friction effects from the axial sealing surface. A coefficient of friction for Berylco 25 (AMS 4650) on either steel alloy (AMS 5735) or chrome plate in the presence of liquid oxygen was assumed to be 0.25. A ratio of F_A/F_R of less than 3.0 is desirable to ensure that the piston ring will not bind on the axial sealing surface.

(2) Analysis Summary

(a) As Designed Upper Piston Ring

(U) For a given pressure differential ($P_H - P_L$), the upper seal is loaded radially at the following rate:

$$F_R = 0.065\ (P_H - P_L)\ \text{lb/in. circumference.}$$

At a pressure differential of 1000 psi, the radial loading of the upper seal is:

$$F_R = 0.065\ (1000)\ \text{lb/in. circumference,}$$

$$F_R = 65\ \text{lb/in. circumference,}$$

or, unit pressure, UP = 620 psi.

(U) The upper piston ring demonstrated acceptable wear characteristics during previous testing at a pressure differential of up to 1000 psi. Therefore, a radial unit pressure of 620 psi and F_R = 65 lb/in. circumference, were used as design criteria. This seal to housing loading was assumed to be satisfactory providing the valve housing is chrome plated to 0.001 inch maximum thickness to approach the hardness of the valve sleeve.

(U) Table XXIV. Force Wear Tests

Test No.	Disk Material	Disk Plating and Thickness	Rider Material	Rider Coating	Dynamic Friction Coefficient	Wear Track Description	Material Combination Rating
1	Stainless Steel (AMS 5646)	PWA 48 chrome (0.0001-in. thick)	Berylco 25 (AMS 4650)	No coating	0.23-0.45	Scratches, light BeCu deposits	Fair
2	Stainless Steel (AMS 5646)	PWA 48 chrome (0.0010-in. thick)	Berylco 25 (AMS 4650)	No coating	0.23-0.44	Slight scratches	Good
3	Stainless Steel (AMS 5735)	PWA 48 chrome (0.0010-in. thick)	Berylco 25 (AMS 4650)	No coating	0.26-0.48	BeCu deposits	Fair
4	Stainless Steel (AMS 5646)	Molychrome (0.0015-in. thick)	Berylco 25 (AMS 4650)	No coating	0.20-0.34	Slight surface depression	Good
5	Stainless Steel (AMS 5646)	Nickel-Tin (0.0015-in. thick)	Berylco 25 (AMS 4650)	No coating	0.26-0.52	Heavy wear	Poor
6	Stainless Steel (AMS 5646)	PWA 48 chrome (0.0010-in. thick)	Berylco 25 (AMS 4650)	Microseal 100-1 Graphite	0.34-0.52	Scratches, Heavy BeCu deposits	Poor
7	Stainless Steel (AMS 5646)	PWA 48 chrome (0.0010-in. thick)	Berylco 25 (AMS 4650)	Microseal 200-1 Molydisulphide	0.34-0.46	Light scratches, light BeCu deposits	Good
8	Stainless Steel (AMS 5646)	PWA 48 chrome (0.0010-in. thick)	Berylco 25 (AMS 4650)	(PWA 566) (0.0010 in.- 0.0012-in. thick)	0.25-0.43	Scratches, light BeCu deposits	Fair
9	Stainless Steel (AMS 5646)	PWA 48 chrome (0.0010-in. thick)	Berylco 25 (AMS 4650)	Alpha Molykote Molydisulphide	0.29-0.52	Scratches, BeCu deposits	Poor
10	Stainless Steel (AMS 5646)	Molychrome (0.0015-in. thick)	Berylco 25 (AMS 4650)	Microseal 100-1 graphite	0.22-0.40	Slight depression - light BeCu deposits	Fair
11	Stainless Steel (AMS 5646)	Molychrome (0.0015-in. thick)	Berylco 25 (AMS 4650)	Microseal 200-1 Molydisulphide	0.31-0.52	Slight depression - heavy BeCu deposits	Poor
12	Stainless Steel (AMS 5646)	Molychrome (0.0015-in. thick)	Berylco 25 (AMS 4650)	(PWA 566) (0.0010-in. - 0.0012-in. thick)	0.20-0.34	Slight depression	Good
13	Stainless Steel (AMS 5646)	Molychrome (0.0015-in. thick)	Berylco 25 (AMS 4650)	Alpha Molykote Molydisulphide	0.23-0.46	Slight depression - heavy BeCu deposits	Poor

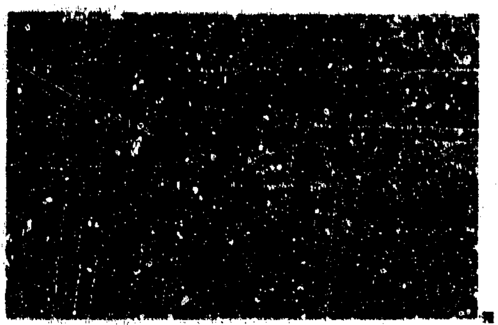

Stainless Steel (AMS 5646) Disk With 0.0001-Inch Thick Chrome Plate (PWA 48)

Berylco 25 (AMS 4650) Rider

(U) Figure 247. Wear Characteristics of 0.0001-Inch Thick Chrome Plate (PWA 48) FD 25590A

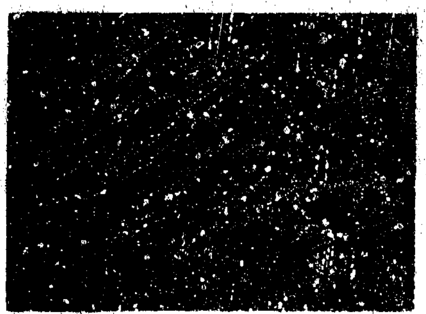

Stainless Steel (AMS 5646) Disk With 0.001-Inch Thick Chrome Plate (PWA 43)

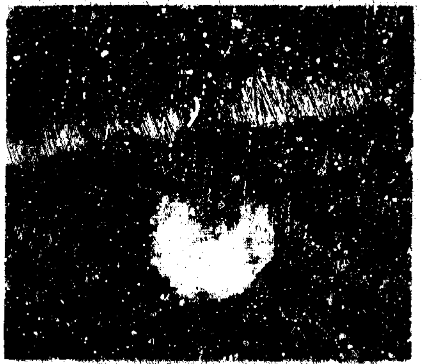

Berylco 25 (AMS 4650) Rider

(U) Figure 248. Wear Characteristics of 0.001-Inch Thick Chrome Plate (PWA 48) FD 25591A

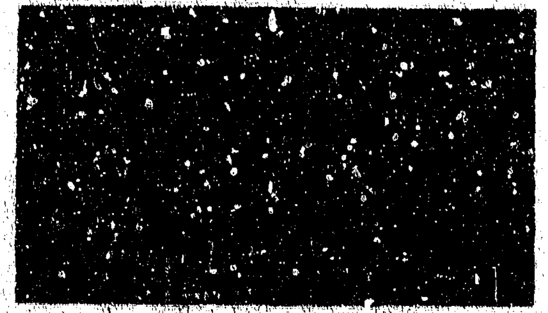

Stainless Steel (AMS 5646) Disk With 0.001-Inch Thick Chromium-Molybdenum Plate FE 75559

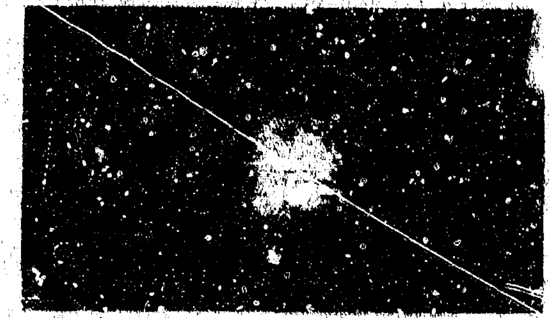

Berylco 25 (AMS 4650) Rider FE 75598

(U) Figure 249. Wear Characteristics of 0.001-Inch Thick Chromium-Molybdenum FD 25532A

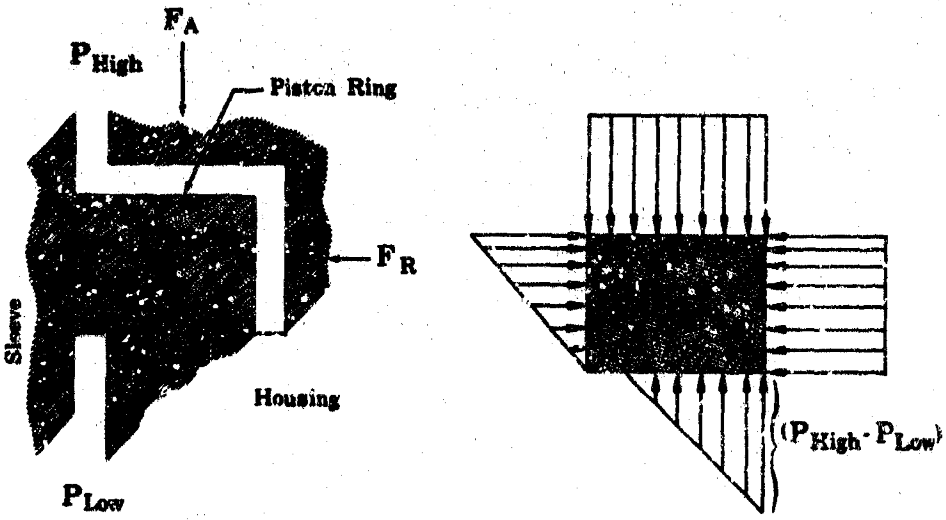

Installation Configuration

Piston Ring Pressure Distribution

(U) Figure 250. Piston Ring Installation Configuration and Pressure Distribution FD 25267

(b) Reworked Upper Piston Ring

(U) The rework configuration of the upper seal recommended for the wear rig tests at pressure differentials of up to 2000 psi is shown in Figure 251. The radial and axial loading conditions of the design are:

$$F_R = 0.032\ (P_H - P_L)$$

$$F_A = 0.077\ (P_H - P_L)$$

$$F_A/F_R = 2.4$$

$$UP = \frac{0.32\ (P_H - P_L)}{0.87}$$

Therefore, for a pressure differential of 2000 psi:

$$F_R = 64\ \text{lb/in.}$$

$$UP = 736\ \text{psi}$$

This unit pressure exceeds the maximum design criteria of 620 psi, but represents the minimum value obtainable using existing hardware, without reducing the sealing land below a minimum of 0.035 inch.

(c) Reworked Lower Piston Ring

(U) The rework configuration of the lower seal recommended for the wear rig tests at pressure differentials of up to 2000 psi is represented by Figure 251. The radial and axial loading conditions of this design for complete seal to housing contact are:

$$F_R = 0.039\ (P_H - P_L)$$

$$F_A = 0.090\ (P_H - P_L)$$

$$F_A/F_R = 2.3$$

$$UP = \frac{0.039\ (P_H - P_L)}{0.147}$$

Therefore, for a pressure differential at 2000 psi:

$$F_R = 78\ \text{lb/in.}$$

$$UP = 530\ \text{psi}$$

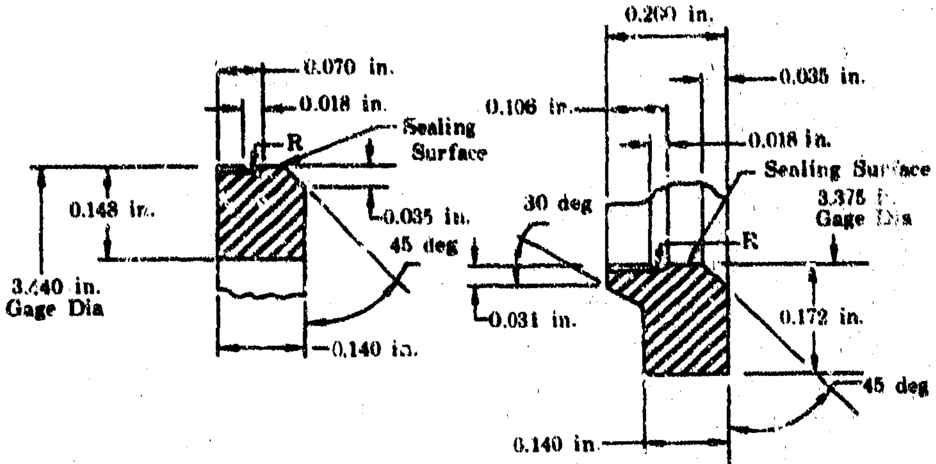

Upper Secondary Piston Ring   Lower Secondary Piston Ring

(U) Figure 251. Pressure Balance Piston Ring   FD 24097

e. Cryogenic Testing

(1) Test Procedures

(U) The preburner oxidizer valve rig illustrated in Figure 252 was used to evaluate the housing coatings and redesigned piston rings. Tests were conducted on the B-22 test stand, which is shown in Figure 253. The test procedures were similar for all four tests except that for Rigs F-33458-7 and -8 additional procedures were required to determine actuation force from the specially installed strain gages.

(U) Piston ring leakage was measured from the secondary discharge valve through the heat exchanger with the primary discharge valve closed. The rig was cold soaked with LN_2 until the dome temperature was less than 180°R. With the rig cold, the primary discharge valve closed, and the secondary discharge valve opened, the rig was cycled with a sine wave input of 3 to 6 cps. The cooldown procedures were repeated before each cycle set. The cycles per set, stroke range, secondary differential pressure and valve position for repeating piston ring leakage were recorded as shown in Table XXV.

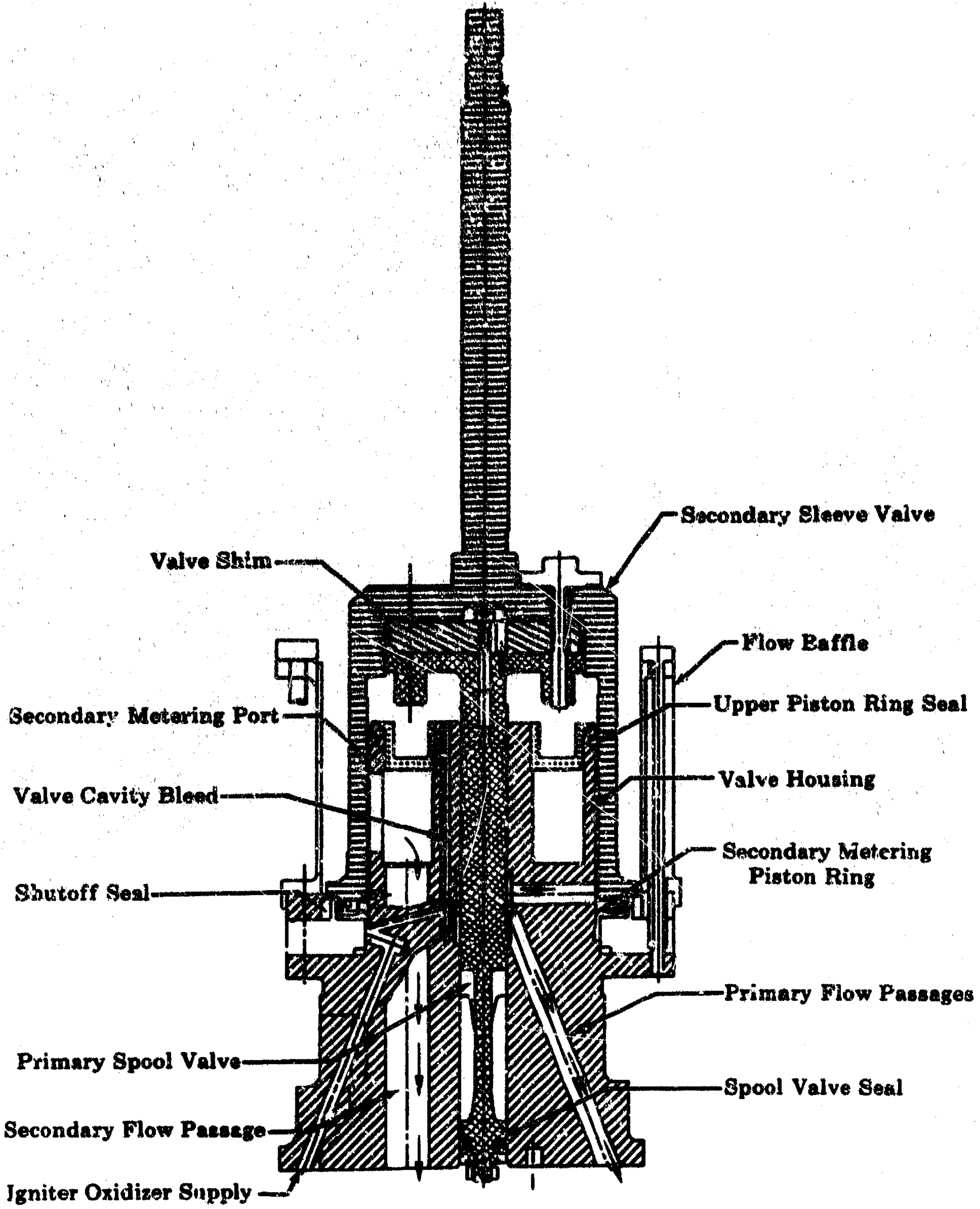

(U) Figure 252. Preburner Oxidizer Valve Rig FD 18909D

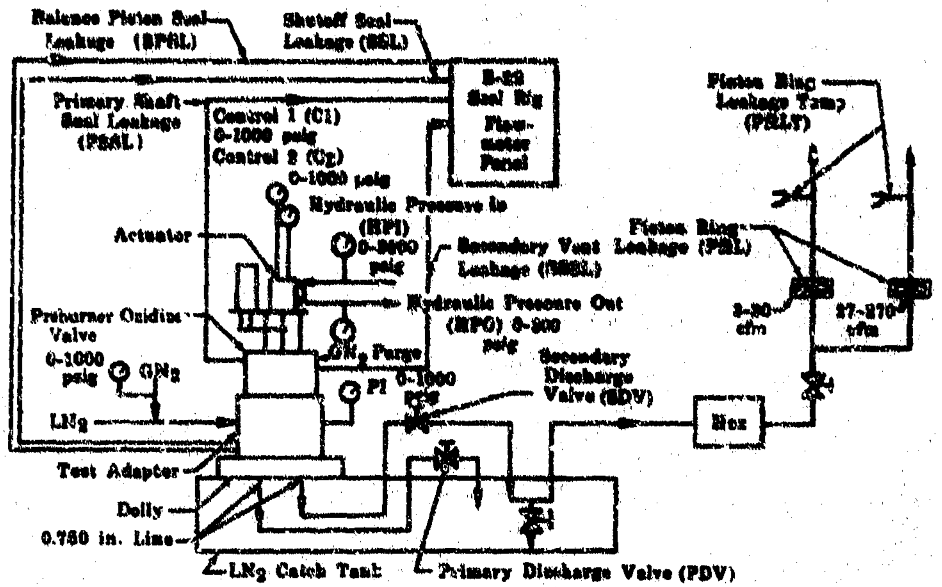

(U) Figure 253. Schematic of Preburner Oxidizer Valve Rig Test Stand Installation FD 22151B

(C)(U) Table XXV. Data Recorded During Tests

Cycle Set	Cycles	Stroke Range (in.)	Secondary ΔP	Valve* Position
A	3334	0.470 ± 0.050	1000	0.470
B	3334	0.580 ± 0.050	1500	0.580
C	3334	0.690 ± 0.050	2000	0.690

*The valve positions for Rig F-33469-7B were 0.450 with ΔP of 1000 psig, 0.600 with ΔP of 2000 psig, and 0.750 with ΔP of 1500 psig. These points were set because the primary port location did not allow a position below approximately 0.400-inch valve stroke and because the secondary port gave a maximum approximate valve position of 0.750 inch where the ports were uncovered thus providing a leakage path and the required piston ring ΔP was unattainable.

(2) Cyclic Endurance Tests

(a) Rig F-33469-7B

(C) Rig F-33469-7B had chrome coatings applied to the valve housing and the sleeve, and had the lower and upper piston ring pressure balanced. The valve housing had a 0.001-inch thick precision chrome coating that did not require subsequent machining. The sleeve had a 0.001- to 0.0015-inch thick chrome coating (per AMS 2406) that required machining to the final dimensions. The lower piston ring was pressure balanced to provide a unit bearing load of 500 psi at 2000 psid. The upper piston ring was pressure balanced to provide a unit bearing load of 736 psi at 2000 psid. Figure 251 shows both piston rings as they were after balancing. The valve was cycled a total of 10,000 cycles and the piston ring leakages are shown in Figure 254.

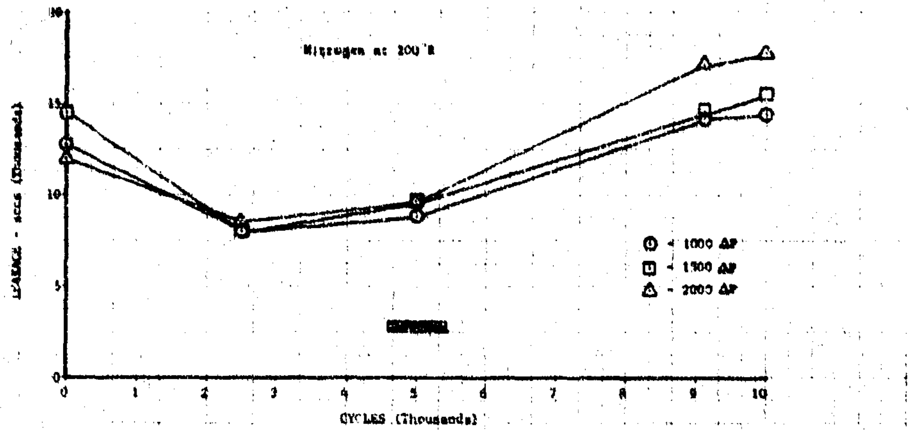

(U) Figure 254. Piston Ring Leakage on Rig F-33469-7B DFC 62512

(U) Pretest and post-test views of the housing are shown in Figure 255. The post-test view shows a light BeCu plate as a result of the cyclic wear of the lower secondary piston rings. Figure 256 provides pretest and post-test closeup views of the housing area where piston ring wear occurred.

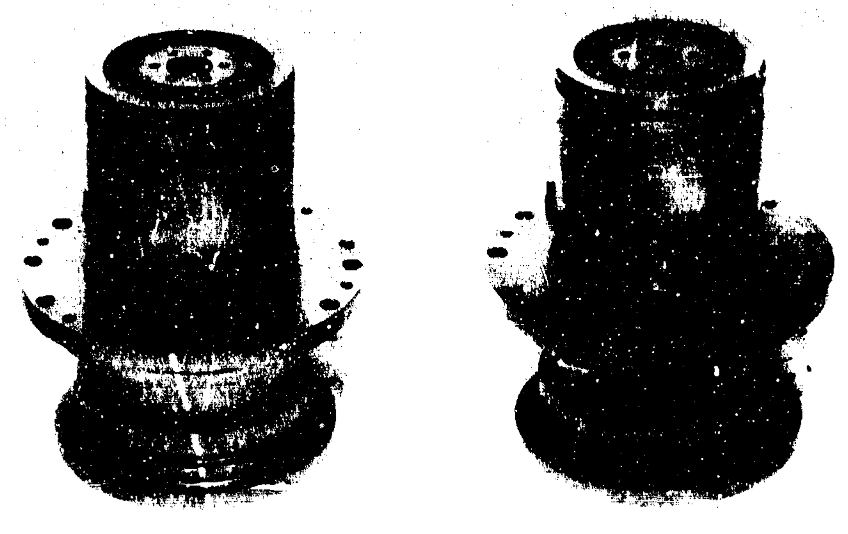
Pretest Condition **Post-Test Condition**

(U) Figure 255. Pretest and Post-Test Condition of the Housing FD 24098

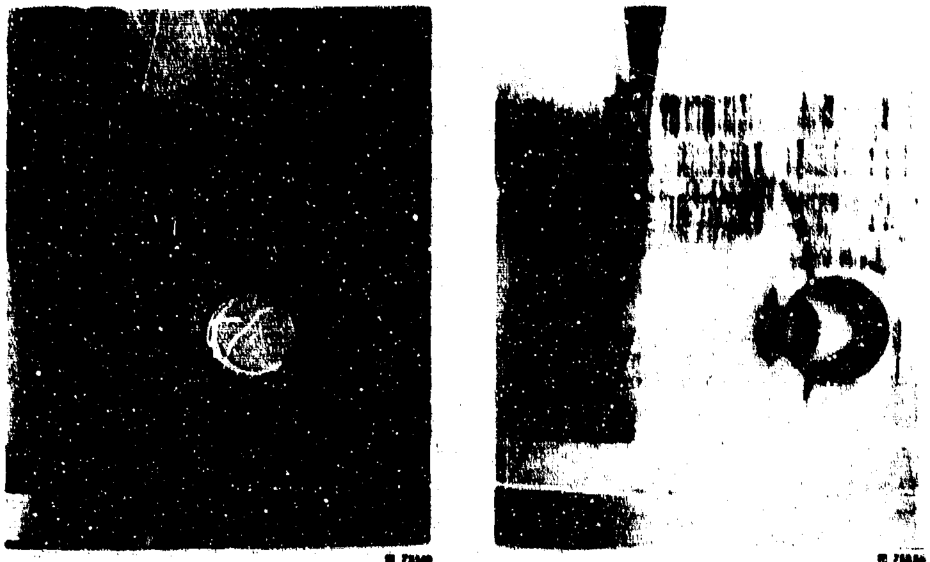

Pretest Condition **Post-Test Condition**

(U) Figure 256. Pretest and Post-Test Views of Housing Showing Piston Ring Wear Area FD 24099

(U) The upper secondary piston rings wear area is shown in Figure 257. The wear pattern is characterized by a light deposit of BeCu. The wear on the upper and the lower BeCu piston rings is illustrated by comparing the pretest and post-test conditions in Figures 258 and 259.

Pretest Condition **Post-Test Condition**

(U) Figure 257. Pretest and Post-Test Condition of Sleeve Showing Wear from Upper Secondary Piston Ring FD 24077

Pretest Condition

Post-Test Condition

(U) Figure 258. Pretest and Post-Test Condition of Upper Piston Ring FD 24100

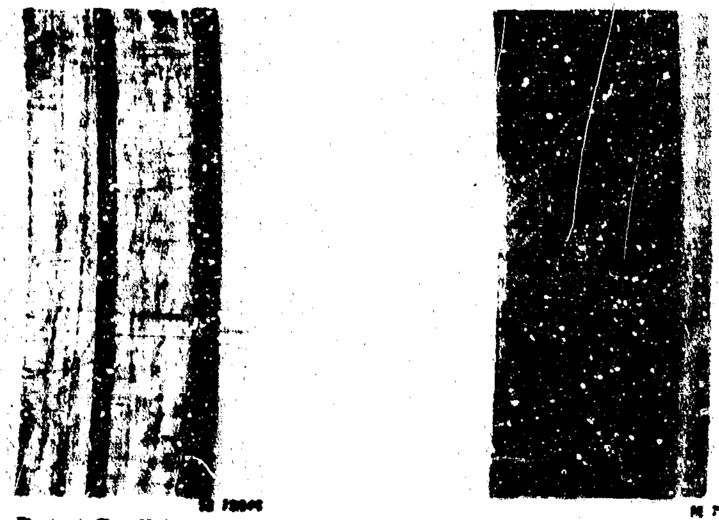

Pretest Condition

Post-Test Condition

(U) Figure 259. Pretest and Post-Test Condition of Lower Piston Ring FD 24101

(U) A comparison enlargement of the housing in the pretest condition and the three sets of wear patterns caused by the lower secondary ring is shown in Figure 260. The Beryllium copper deposits from the cyclic endurance test were removed from the valve and secondary sleeve by light-polishing with aluminum oxide.

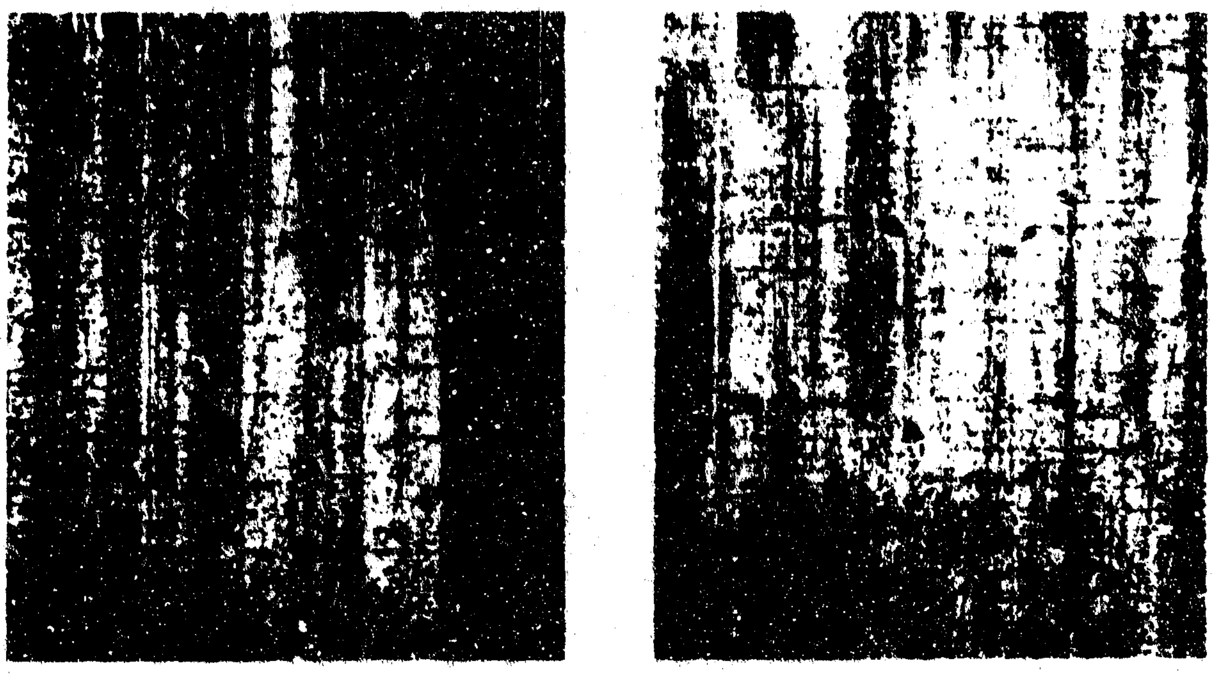

1000 psi ΔP FL 13033

1500 psi ΔP FL 13035

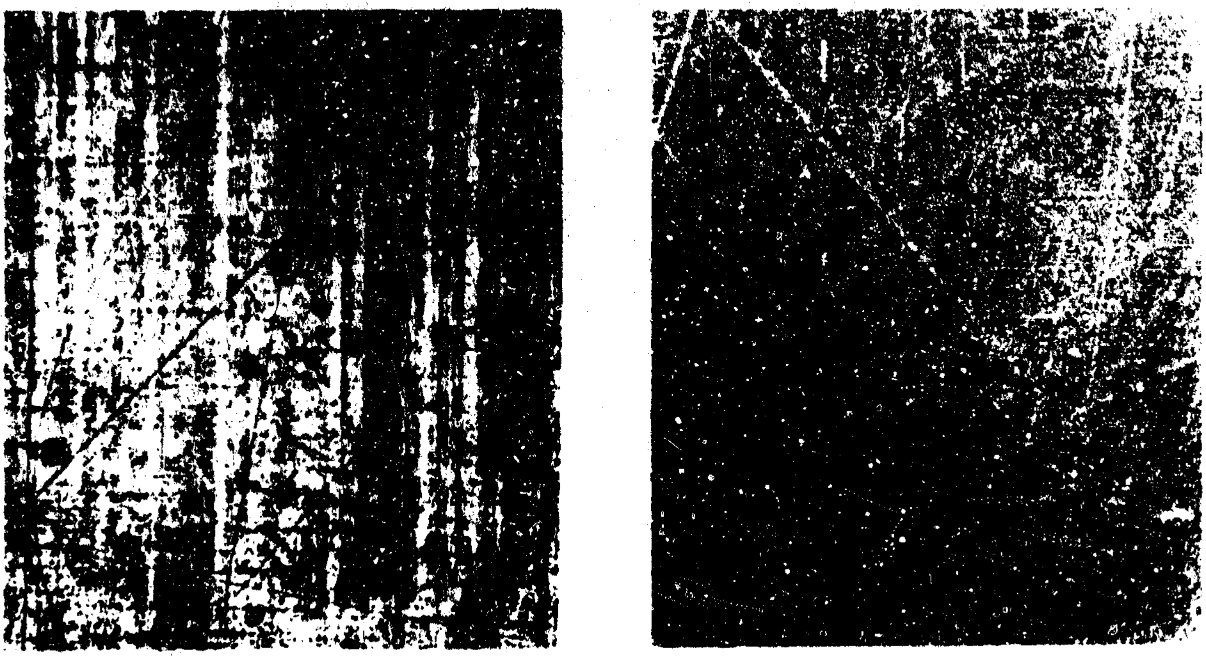

2000 psi ΔP FL 13034

Pretest FL 13037

65X Magnification

(U) Figure 260. Closeup Views of Main Housing Wear FD 24102A

(b) Rig F-33469-8

(C) The valve housing and sleeve for Rig F-33469-8 had chrome coatings applied in the same manner as Rig F-33469-7B. The unbalanced upper and lower piston rings, shown in Figure 261, provided unit bearing loads of 1240 psi and 990 psi, respectively at 2000 psid.

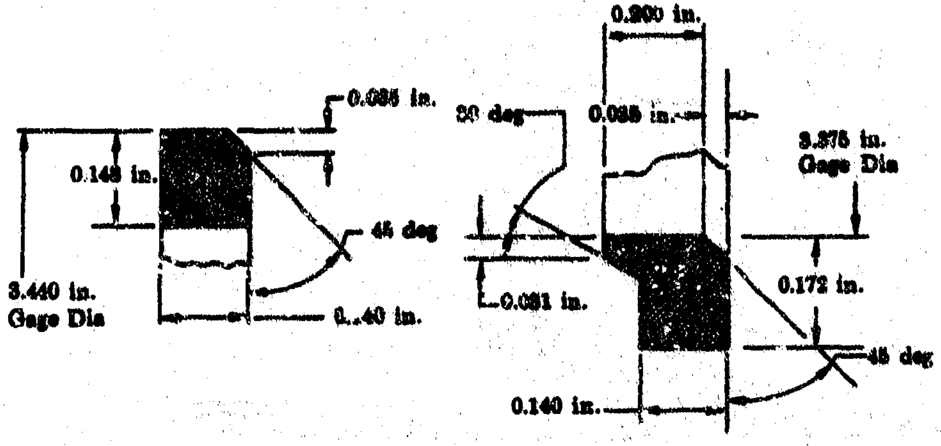

Upper Secondary Piston Ring **Lower Secondary Piston Ring**

(U) Figure 261. Unbalanced Piston Rings FD 24973

(C) The rig was subjected to a 6666-cycle endurance test at LN_2 temperatures. The test was terminated after 6666 cycles because of insufficient actuation force at the 2000-psi ΔP level. Piston ring leakages were measured with GN_2 at the various valve positions and are shown in Figure 262.

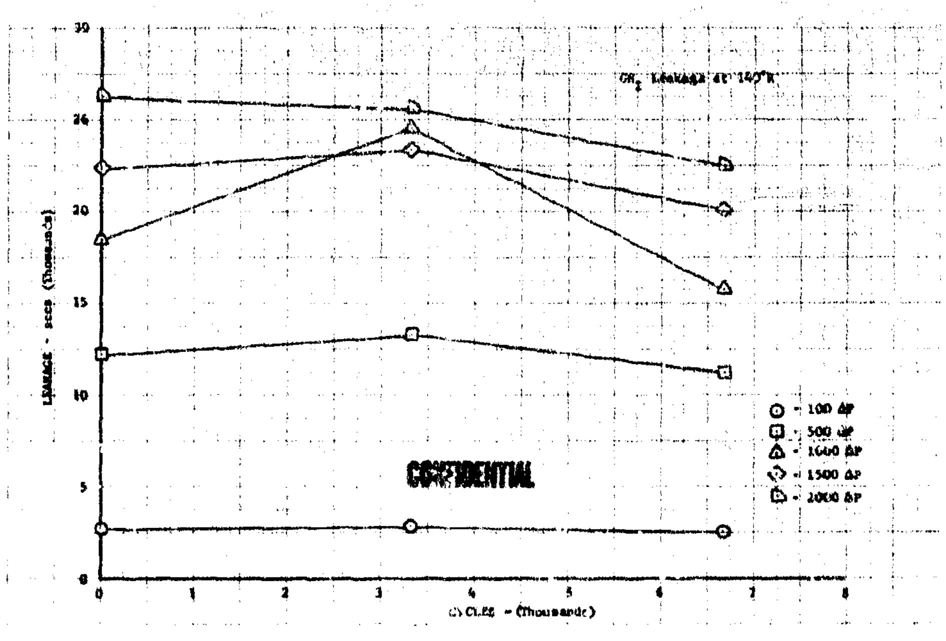

(U) Figure 262. Piston Ring Leakage on Rig F-33469-8 DFC 65289

(U) The overall pretest and post-test views of the housing shown in Figure 263 shows a light BeCu plate resulting from wear of the lower secondary piston ring. Figure 264 shows a pretest and post-test closeup of this wear area.

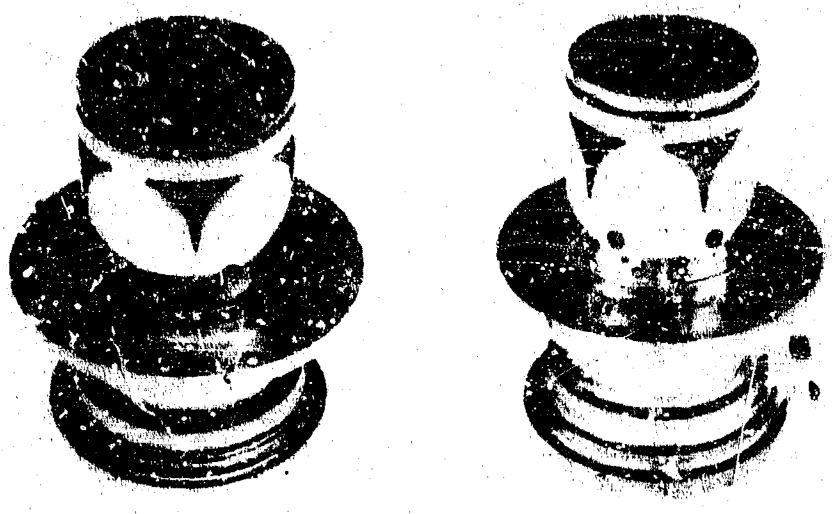

FE 76249

Pretest Condition

FE 76503

Post-Test Condition

(U) Figure 263. Pretest and Post-Test Condition of Housing, Rig F-33469-8 FD 24975

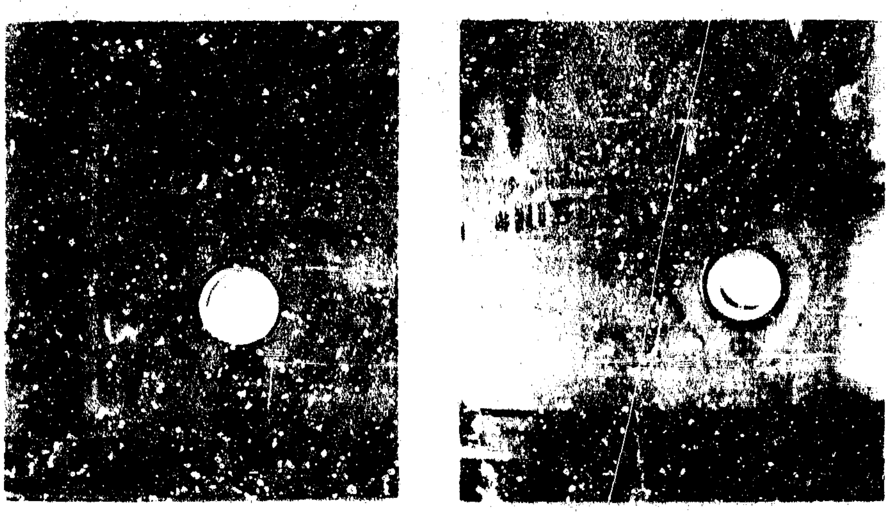

FE 76250

Pretest Condition

FE 76504

Post-Test Condition

(U) Figure 264. Pretest and Post-Test Views of Housing Showing Piston Ring Wear Area, Rig F-33469-8 FD 24

(U) The pretest and post-test upper secondary piston ring wear area is shown in Figure 265. The wear pattern is characterized by a light deposit of BeCu. The wear on the upper and lower BeCu piston rings can be seen by comparing the pretest and post-test condition in Figures 266 and 267, respectively.

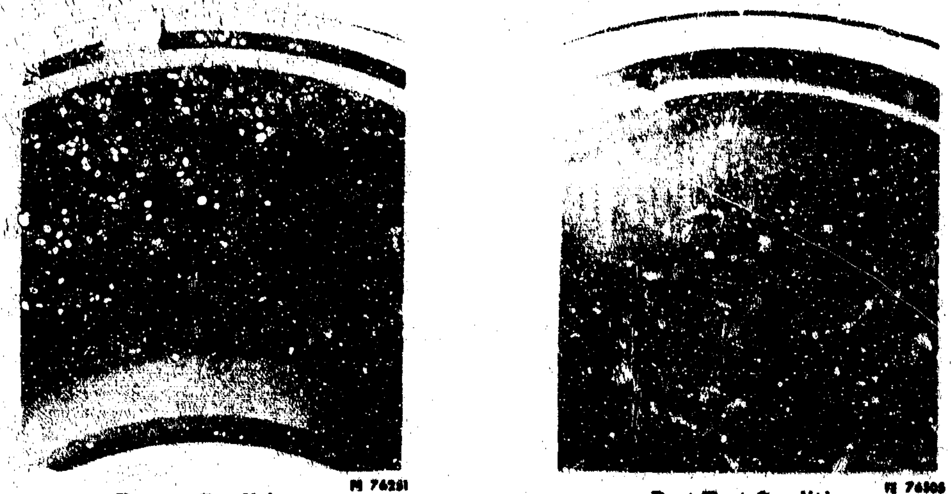

Pretest Condition **Post-Test Condition**

(U) Figure 265. Pretest and Post-Test Condition of Sleeve Showing Wear from Upper Secondary Piston Ring, Rig F-33469-8 FD 24974

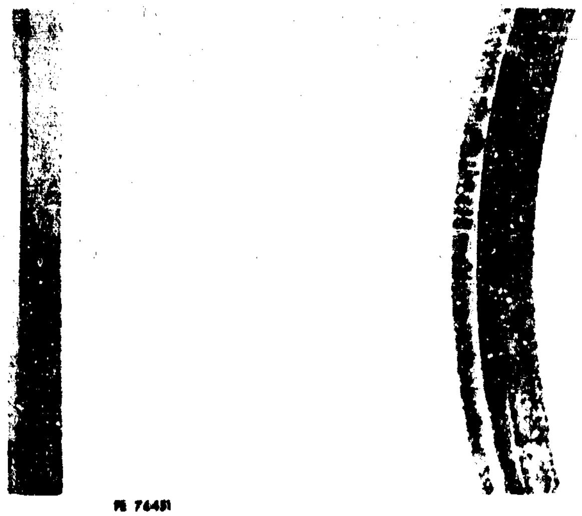

Pretest Condition **Post-Test Condition**

(U) Figure 266. Pretest and Post-Test Condition of Upper Piston Ring, Rig F-33469-8 FD 24977

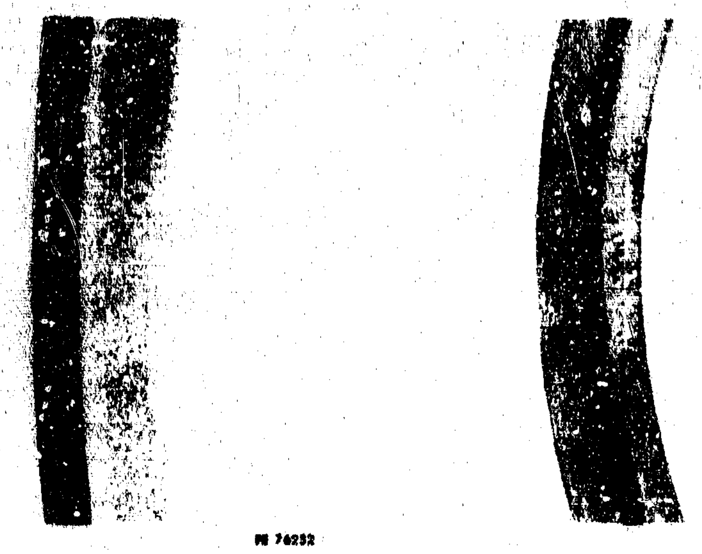

Pretest Condition

Post-Test Condition

(U) Figure 267. Pretest and Post-Test Condition of Lower Piston Ring, Rig F-33469-8 FD 24978

(c) Rig F-33458-7

(C) The Rig F-33458-7 valve housing had 0.001-inch thick molychromic coating applied without subsequent machining. The sleeve was chrome plated 0.001- to 0.0015-inch thick (per AMS 2406) and ground to the final dimensions. The unbalanced upper and lower piston rings, shown in Figure 261, provided unit bearing loads of 1240 psi and 990 psi, respectively, at 2000 psi. The valve was cycled a total of 10,000 cycles and the piston ring leakages are shown in Figure 268.

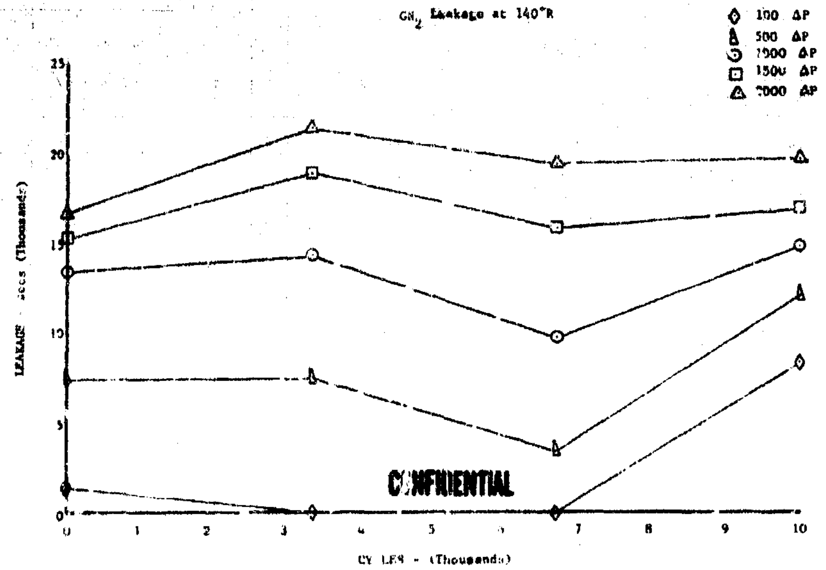

(U) Figure 268. Piston Ring Leakages on Rig F-33458-7 DFC 65291

(U) The overall pretest and post-test views of the housing, shown in Figure 269, show a light BeCu plate resulting from wear of the lower secondary piston ring. Figure 270 shows a pretest and post-test closeup of this wear area. The wear pattern of the lower piston ring on the valve housing indicates a surface waviness condition that compounded the apparent piston ring wear by increasing the unit loading.

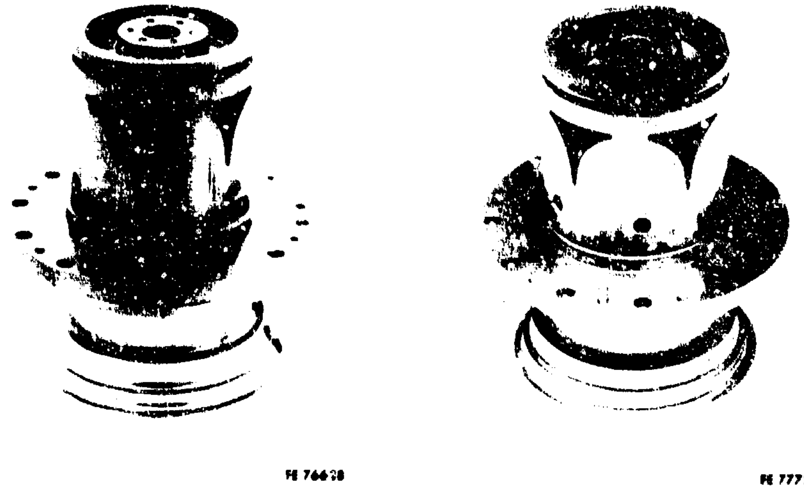

Pretest Condition

Post-Test Condition

(U) Figure 269. Pretest and Post-Test Condition of Housing, Rig F-33458-7 FD 24979

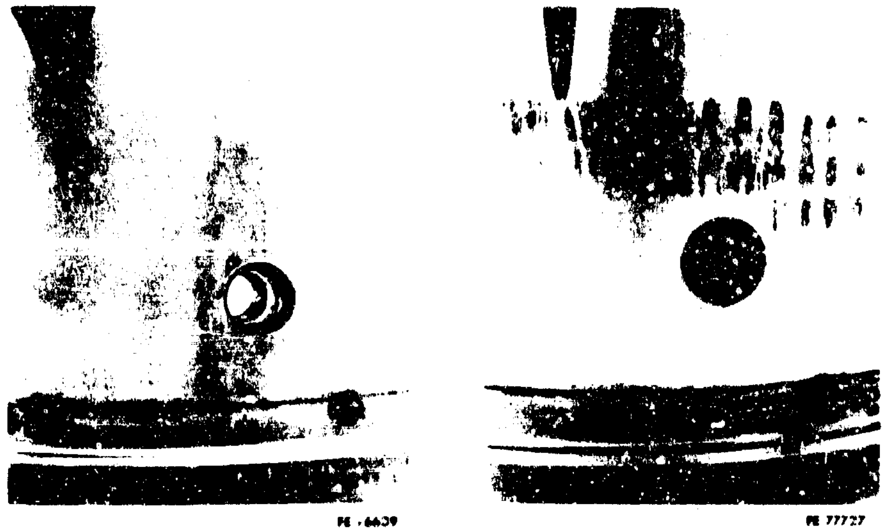

Pretest Condition

Post-Test Condition

(U) Figure 270. Pretest and Post-Test Views of Housing Showing Piston Ring Wear Area, Rig F-33458-7 FD 24980

(U) The pretest and post-test upper secondary piston ring wear area is shown in Figure 271. The wear pattern is characterized by a light deposit of BeCu. The wear on the upper and lower BeCu piston rings can be seen by comparing to the pretest and post-test condition in Figures 272 and 273, respectively.

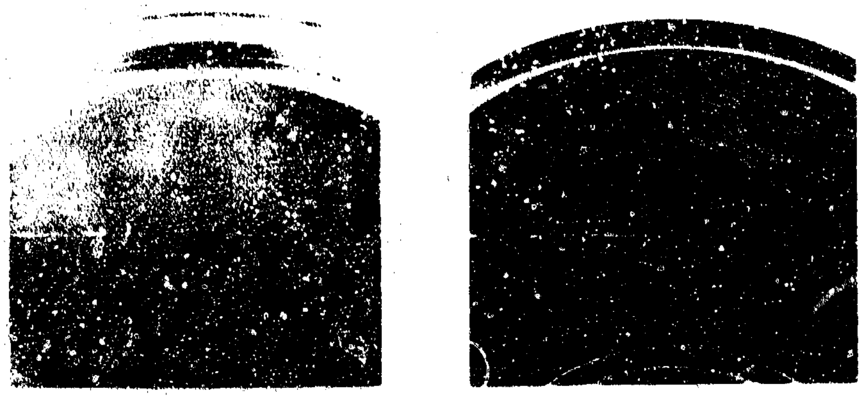

Pretest Condition **Post-Test Condition**

(U) Figure 271. Pretest and Post-Test Condition of Sleeve Showing Wear from Upper Secondary Piston Ring, Rig F-33458-7 FD 24981

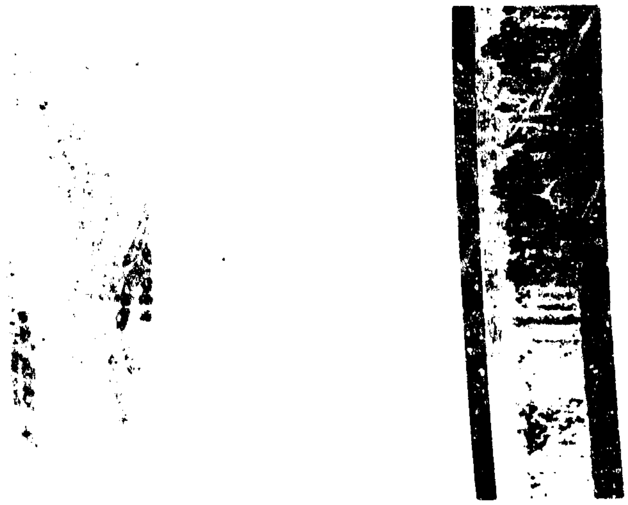

Pretest Condition **Post-Test Condition**

(U) Figure 272. Pretest and Post-Test Condition of Upper Piston Ring, Rig F-33458-7 FD 24982

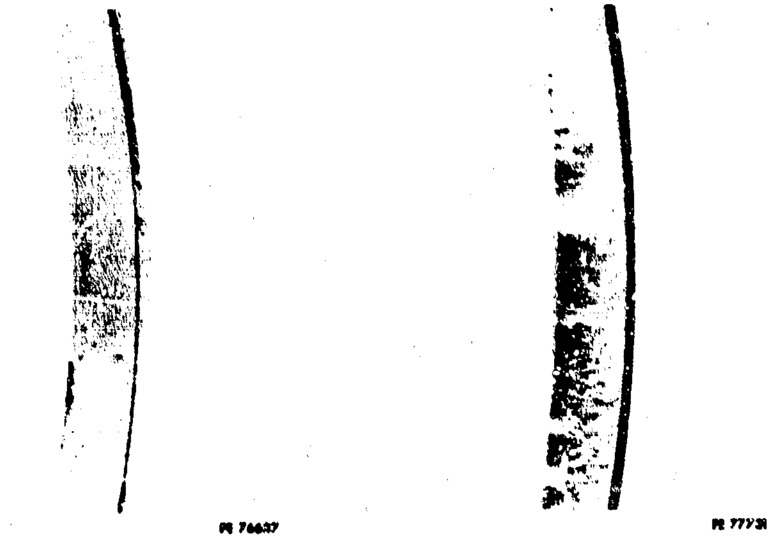

Pretest Condition **Post-Test Condition**

(U) Figure 273. Pretest and Post-Test Condition of Lower Piston Ring, Rig F-33458-7 FD 24983

(U) The actuator shaft and the secondary sleeve shaft were strain gaged by the Material Development Laboratory of FRDC to determine force requirements of the valve. The results are shown in Figure 274.

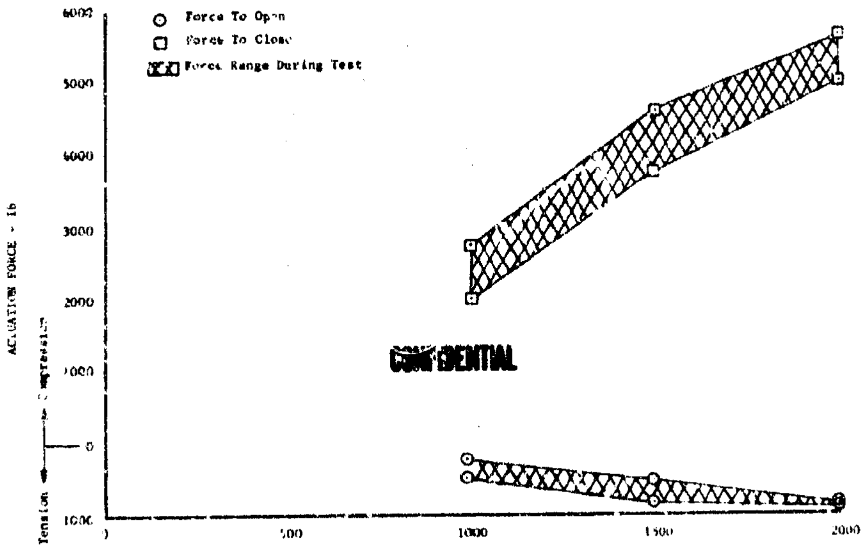

(U) Figure 274. Rig F-33458-7 Actuation Force Requirements During Cycle Endurance DFC 65290

(d) Rig F-33458-8

(C) The valve housing and sleeve for Rig F-33458-8 had coatings applied in the same manner as Rig F-33458-7. The balanced upper and lower piston rings, shown in Figure 251, provided unit bearing loads of 736 psi and 500 psi, respectively, at 2000 psid. The valve was cycled a total of 10,000 cycles and the piston ring leakages are shown in Figure 275.

(U) The overall post-test view of the housing shown in Figure 275 shows a light BeCu plate due to wear of the lower secondary piston ring. Figure 277 shows a post-test closeup of this wear area.

(U) The post-test upper secondary piston ring wear area is shown in Figure 278. The wear pattern is characterized by a light deposit of BeCu. The wear on the upper and lower BeCu piston rings is shown in Figures 279 and 280 respectively.

(U) The actuator shaft and the secondary sleeve shaft were strain gaged by the Materials Development Laboratory of FRDC to determine force requirements of the valve. The results are shown in Figure 281.

3. Translating Seal Rig F-33435

a. Introduction

(C) It was desired to reduce the seal package size of the preburner oxidizer valve by eliminating one shaft seal and changing the seal configuration to a Kapton-Teflon lip seal. To determine the best laminate for sealing translating shafts, five 10,000-cycle endurance tests were conducted.

b. Summary, Conclusions, and Recommendations

(U) The KTTTK (a five layer laminate of Kapton and Teflon with the outer layers being Kapton) laminate used in Build 10B did not exceed the vent shaft seal limit of 10 sccs as shown in Figure 282; however, the same laminate tested on Build 14 had wear of the Teflon inner layer. An additional laminate of Kapton on the shaft should eliminate wear of the Teflon inner layer. The test results obtained from Build 12, which was conducted with a KKTTK laminate, were doubtful because of a one day delay that may have resulted in rig icing and a boil-off problem. A laminate configuration of KKTTK is recommended for application at the primary and vent shaft seal locations. The primary shaft seal leakages are shown in Figure 283.

(U) A secondary test was conducted as Build 13B to determine the effect of inlet pressure on leakages. As shown in Figures 284 and 285 the inlet pressure effect will be negligible.

(U) Because of the high leakage shown in Figure 286, a lip seal is not recommended for the balance piston. The Omni seal (glass-filled Teflon) tested during Phase I (Contract AF04(611)-11401) had better wear characteristics and lower leakage.

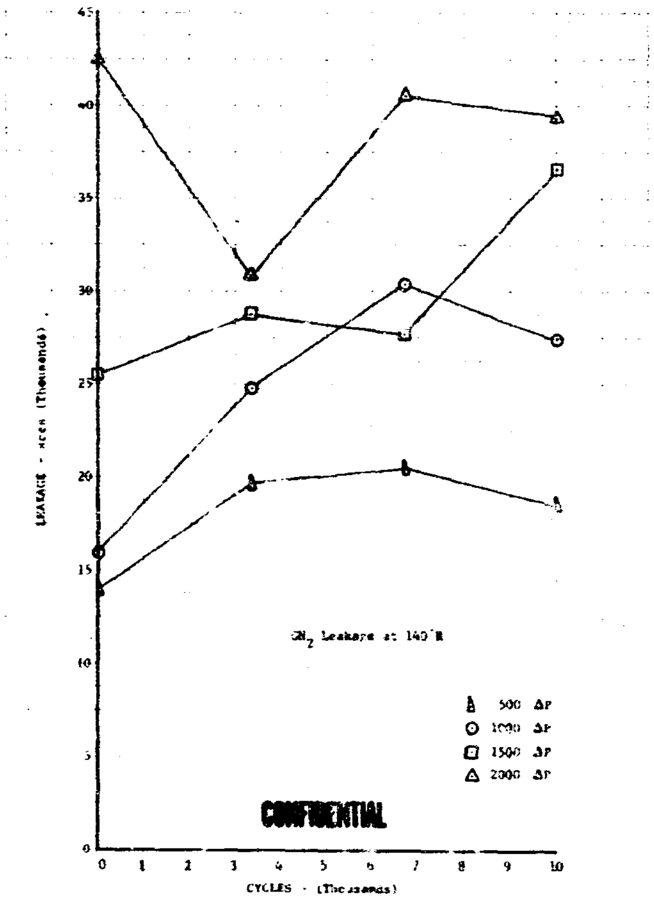

(U) Figure 275. Piston Ring Leakage on Rig F-33458-8

DFC 65292

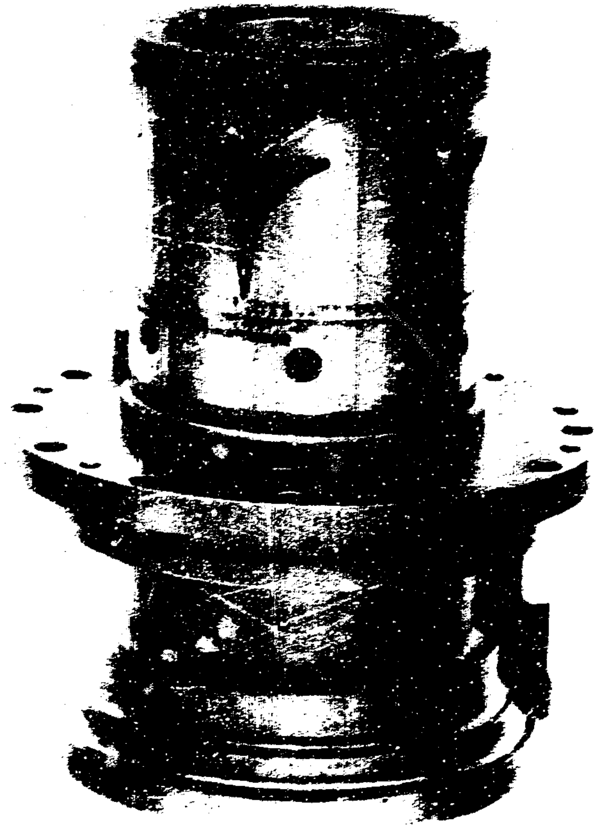

(U) Figure 276. Post-Test Condition of Housing, Rig F-33458-8

FE 78259

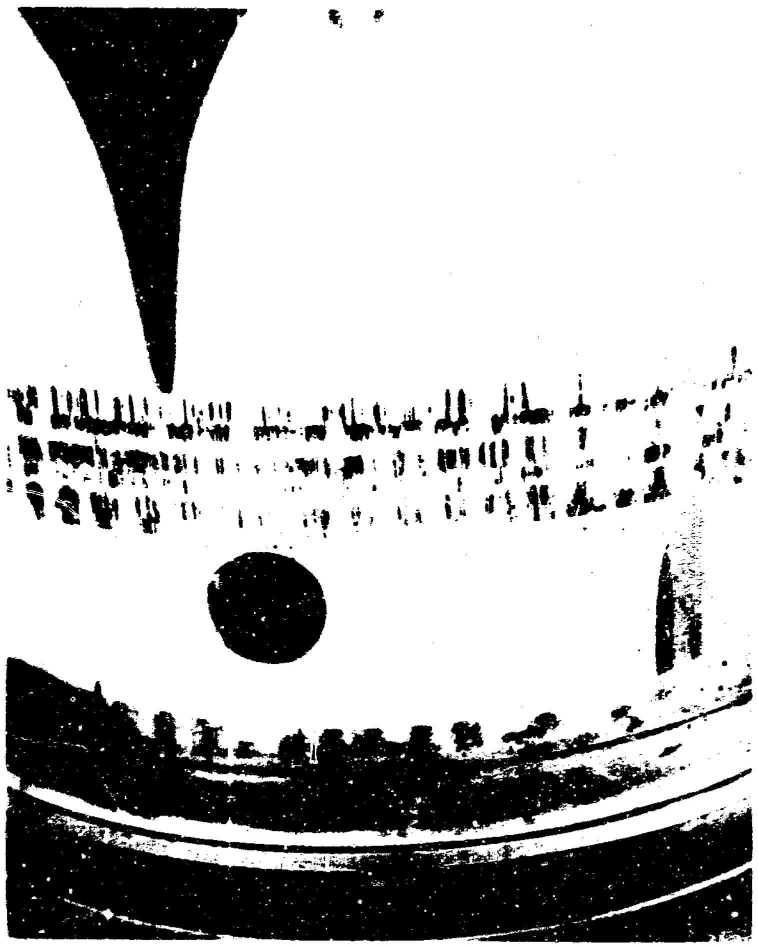

(U) Figure 277. Post-Test View of Housing Showing Piston Ring Wear Area, Rig F-33458-8 FE 78258

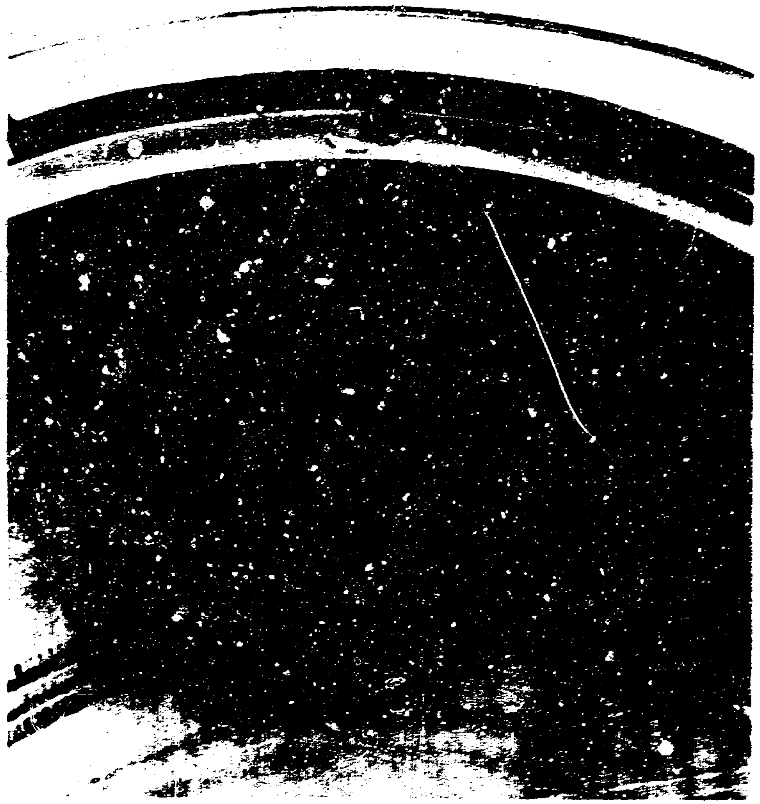

(U) Figure 278. Post-Test Condition of Sleeve Showing Wear from Upper Secondary Piston Ring, Rig F-33458-8 FE 78257

(U) Figure 279. Post-Test Condition of Upper Piston Ring, Rig F-33458-8

FE 78261

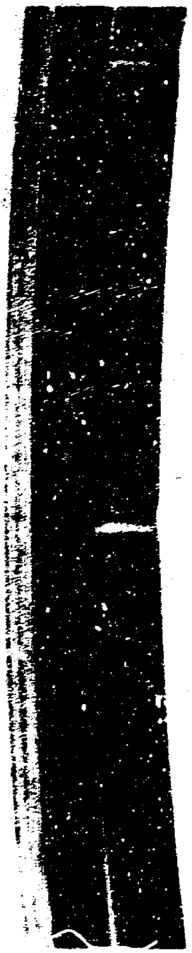

(U) Figure 280. Post-Test Condition of Lower Piston Ring, Rig F-33458-8

FE 78260

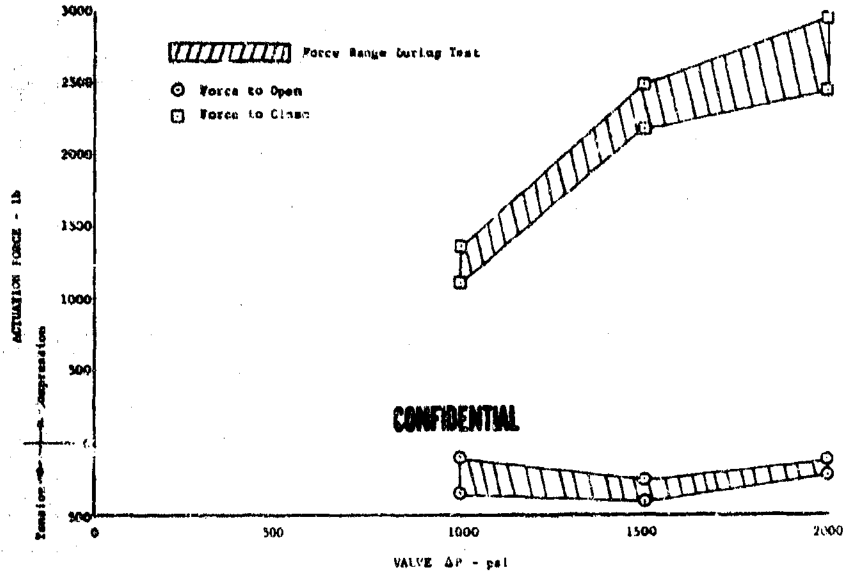

(U) Figure 281. Rig F-33458-8 Actuation Force Requirements During Cycle Endurance

DFC 65294

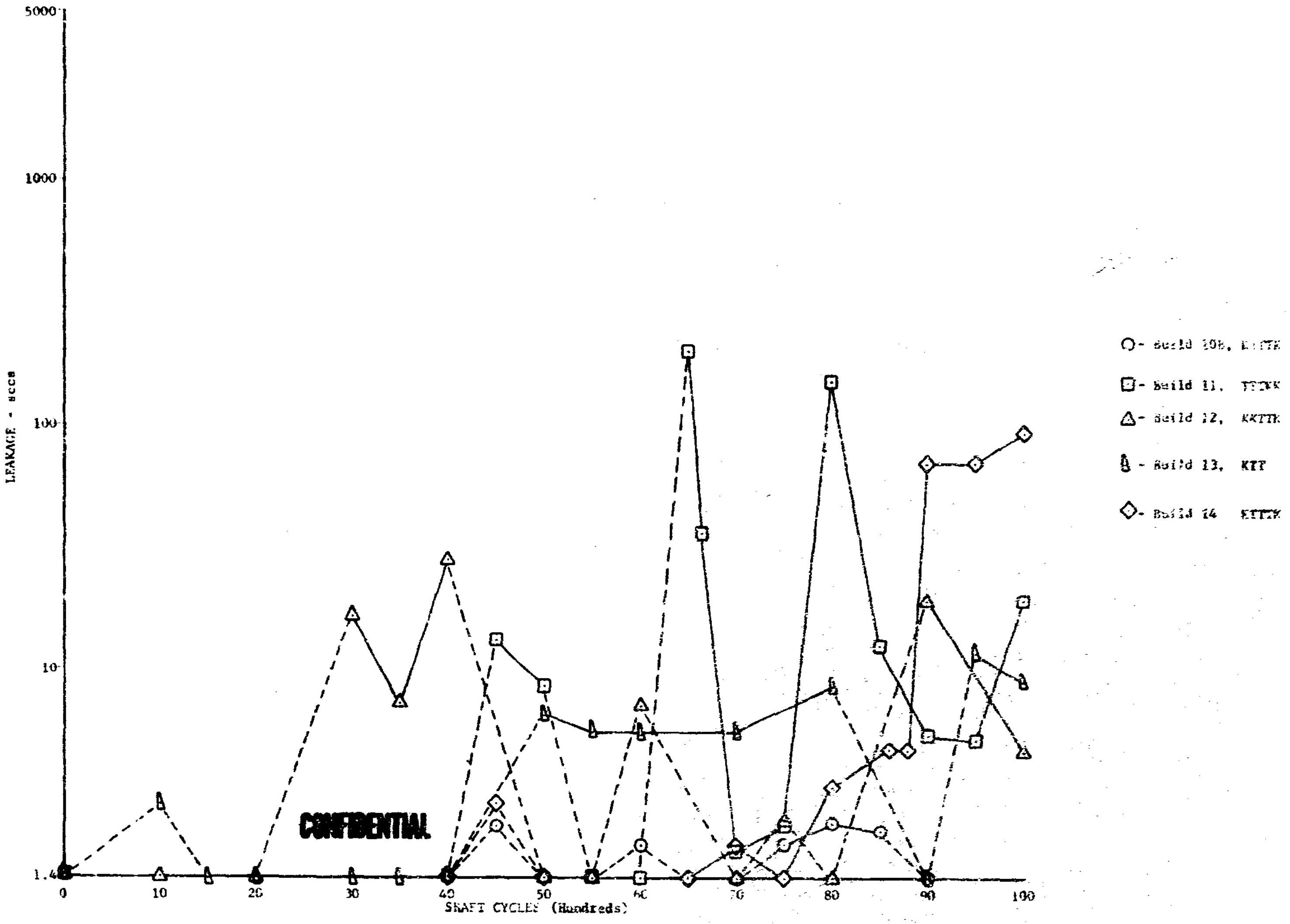

(U) Figure 282. Translating Seal Test Rig Vent Shaft Seal Leakage vs Cycles

DFC 68278

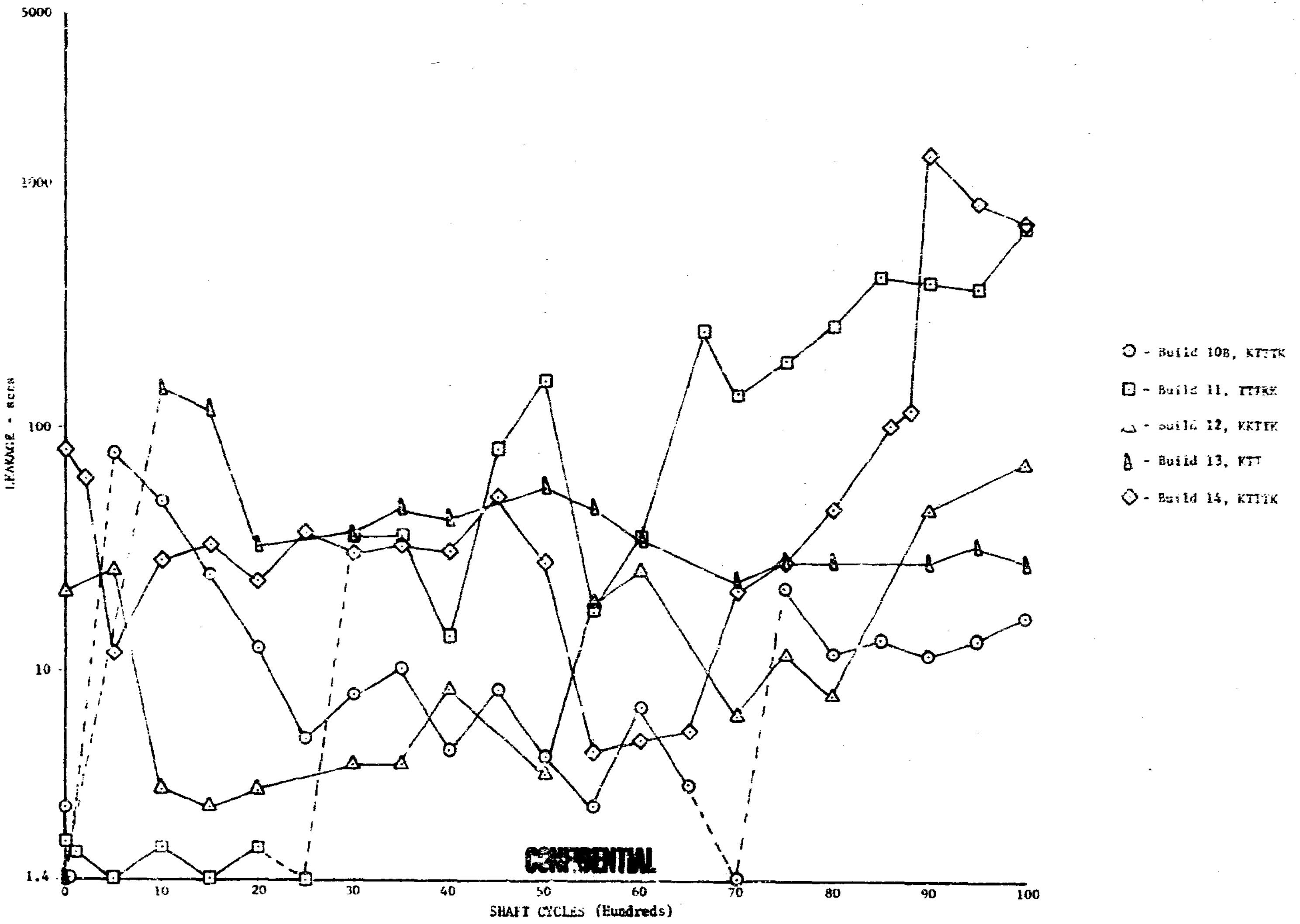

(U) Figure 283. Translating Seal Test Rig Primary Shaft Seal Leakage vs Cycles

DFC 68279

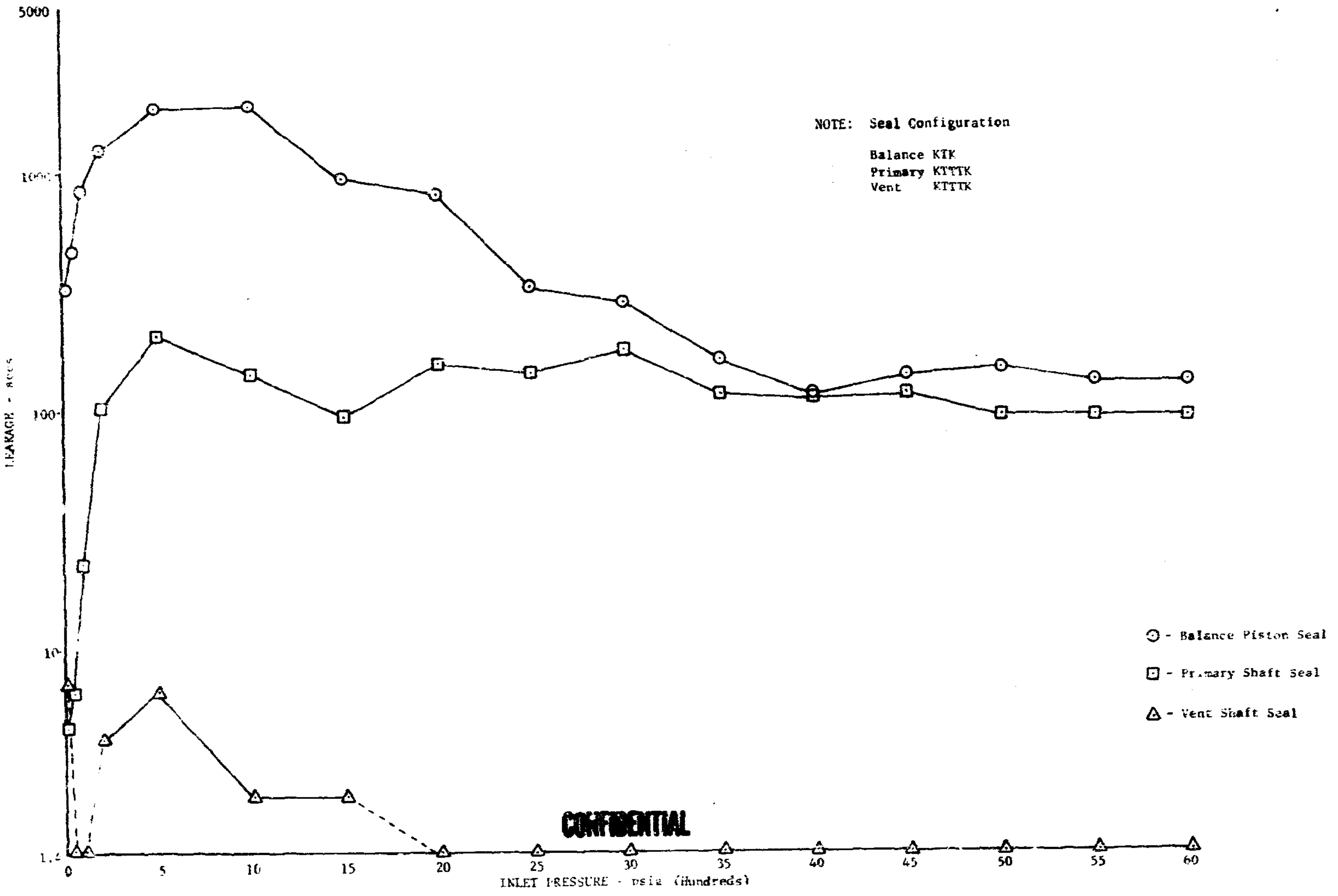

(U) Figure 284. Translating Seal Test Rig Leakage vs Inlet Pressure (Stationary Shaft) DFC 68280

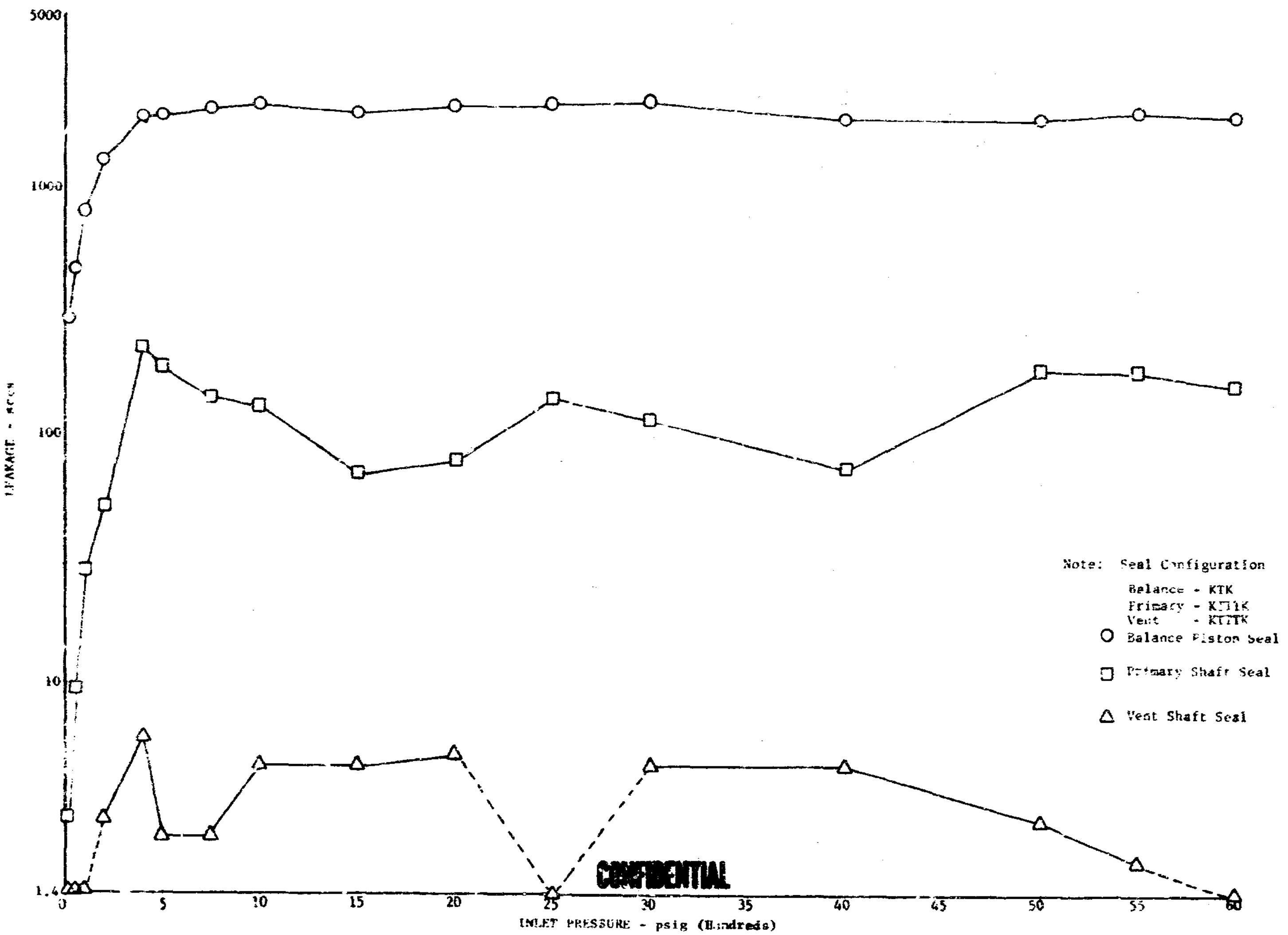

(U) Figure 285. Translating Seal Test Rig Leakage vs Inlet Pressure (Translating Shaft)

DFC 68281

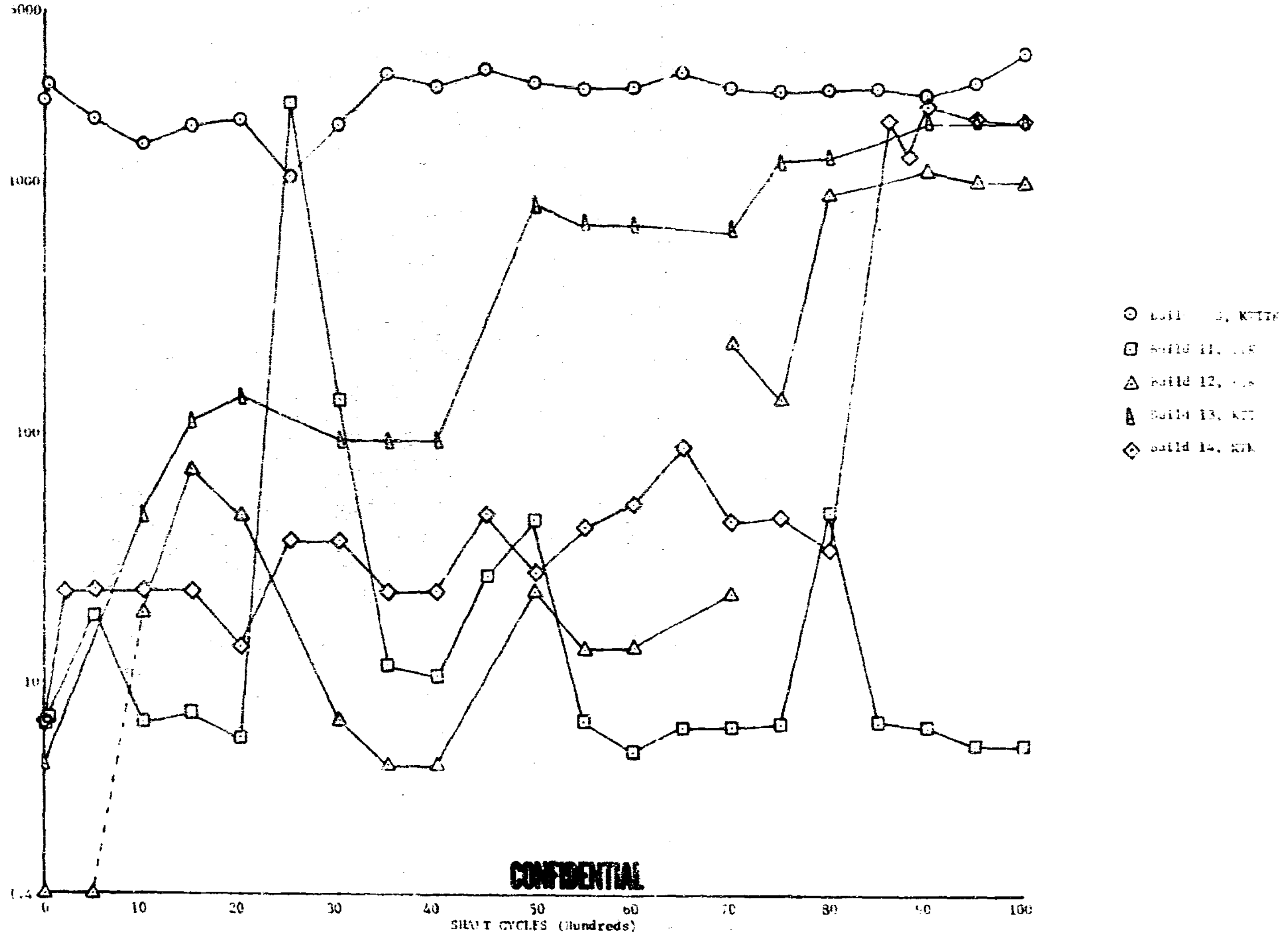

(U) Figure 286. Translating Seal Test Rig Balance Piston Seal Leakage vs Cycles

DFC 68282

(U) Because of the high leakage shown in Figure 286, an OD sealing lip seal is not recommended for the balance piston. The ID sealing lip seal is designed so it will seal around a shaft that translates through it. This application provides a uniform radial stretch about the surface where sealing is desired. In the opposite application where the OD of a lip seal is used for the sealing surface, the seal is held by the translating shaft and sealing is obtained on the housing bore. The OD of the lip seal tends to gather and provide a scalloped sealing surface. Therefore, ID sealing lip seals should be used for the balance piston as well as the actuator shaft.

c. Hardware Description

(1) Translating Seal Rig

(U) The translating seal rig was designed to evaluate lip seals for application to high pressure, cryogenic translating shaft and piston applications. The rig duplicates the preburner oxidizer valve shaft and housing configuration designed during Phase I (Contract AF04(611)-11401). An exploded view of the rig is shown in Figure 287. The test rig is translated a total stroke of 1,375 inches at a rate of 1 cps by a pneumatically actuated piston.

(2) Shaft Lip Seals

(C) Tests of this type seal in a rotary, 1.000-inch shaft seal rig at LN_2 temperature and 6000 psig GN_2 pressure during Phase I (Contract AF04(611)-11401) showed maximum primary and vent shaft (axial) leakages of 0.37 sccs and less than 0.008 sccs, respectively, after 10,000 shaft cycles. Static (radial) leakages were less than 1.4 sccs. This sealing effectiveness allows a reduction in the number of seals required for shaft sealing and eliminates separate static seals in the seal package because the lip seal seals radially as well as axially.

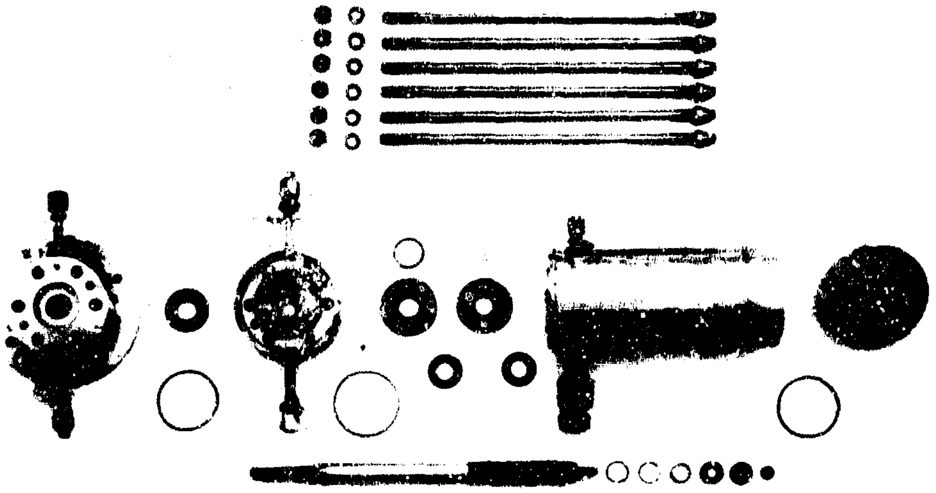

(U) Figure 287. Translating Seal Test Rig FE 76099

(U) Scaling down the rotary lip seals resulted in a 1.098-inch OD, 0.600-inch ID, 0.025-inch thick seal of laminated layers of 0.005-inch FEP Teflon and 0.005-inch Kapton. The stacking of these materials was varied during testing to determine the best combination.

(U) The shaft seal package is illustrated in Figure 288. The primary seal antiextrusion backup leaves 0.001-inch clearance between the seal gland and the shaft. The secondary seal is forced against the shaft by the primary gland configuration, thus, acting as a bearing for the floating seal package. This prevents metal-to-metal contact between the primary gland and rig shaft.

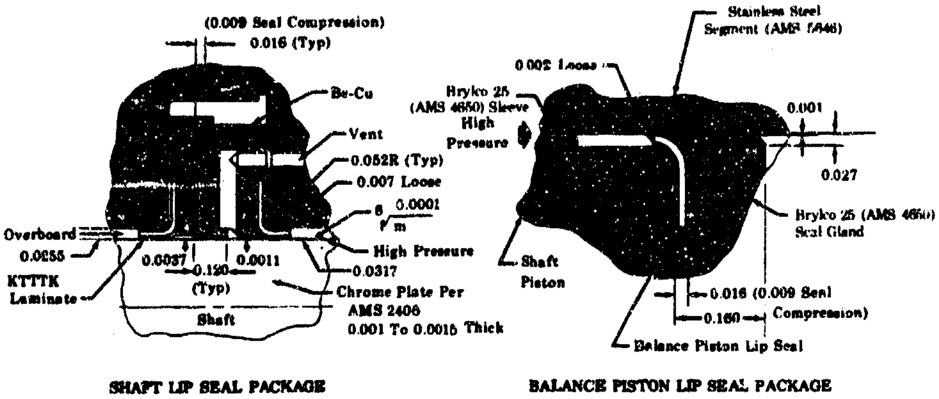

SHAFT LIP SEAL PACKAGE

BALANCE PISTON LIP SEAL PACKAGE

(U) Figure 288. Shaft Seal Package FD 24331C

(3) Piston Seal Package

(U) The initial design dimensions of the piston lip seal were 0.715-inch OD, 0.353-inch ID, and 0.025-inch thick. Material was laminated FEP Teflon-Kapton. The piston seal package is illustrated in Figure 288. The sleeve shown in Figure 288 was added to give the seal a backup during forming and force the seal against the segment bore so that it acts as a bearing and prevents the seal gland and shaft piston from making metal-to-metal contact with the segment bore.

d. Seal Laminate Fabrication

(U) The lip seals are fabricated from FEP Teflon and 500F-131 Kapton 0.005-inch thick sheet stock. The 500F-131 Kapton consists of a 0.003-inch sheet of type F Kapton with 0.001-inch thickness of FEP Teflon on each side. The following procedure outlines the fabrication process:

1. Individual seal laminates are cut with a 2.5-inch diameter cutting tool.

2. The laminates and molding tools are sonic cleaned in trichlorethylene at 170°F.

3. The desired laminate stackup is placed in a mold housing as shown in Figure 289. TFE Teflon sheet stock 0.005-inch thick is placed between the individual seals and the mold housing to prevent bonding.

4. A weight is placed on the mold plunger to provide 10 psi unit loading, and the seals are baked at 525°F ± 10°F for 1 hour.

5. The seal blanks are removed and separated by peeling off the TFE Teflon separators. Individual seals are then cut by dies.

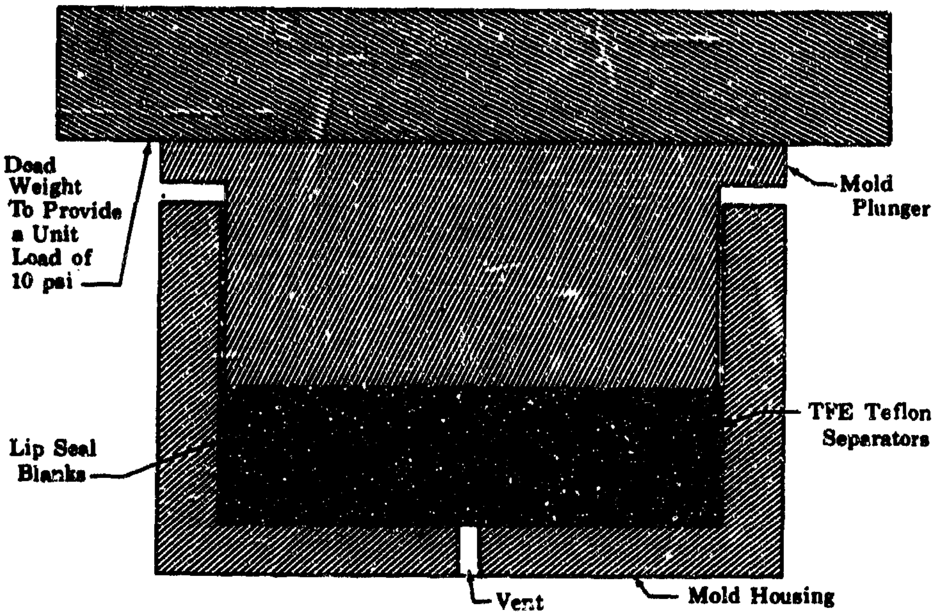

(U) Figure 289. Lip Seal Mold FD 24092

c. Endurance Tests

(C) Five 10,000 cycle endurance tests were conducted to evaluate the laminated lip seals. The test results are summarized in Table XXVI. A coding is used to identify the seal configuration. A KTTTK laminate is two 0.005-inch thick sheets of Kapton and three 0.005-inch thick sheets of Teflon. The material next to the dynamic sealing surface is identified first.

(1) Build 10B

(U) This build incorporated the same seal construction and laminate used in Build 10A; however, the balance piston seal had an increased seal lip.

(C)(U) Table XXVI. Summary of Test Results

Test Number	Seal Configuration			Maximum Leakage Recorded During Test (sccs)			Seal Wear After Test (grams)			Number of Cycles
	Balance	Primary	Vent	Balance	Primary	Vent	Balance	Primary	Vent	
33435-10A	KTTTK	KTTTK	KTTTK	Terminated Test			Terminated Test			
33435-10B	KTTTK	KTTTK	KTTTK	3400	78	2.4	0.00127	0.002715	0.000701	10,000
33435-11	TTK	TTTKK	TTTKK	2100	660	200	0.001648	0.00029	0.000751	10,000
33435-12	KTK	KKTTK	KKTTK	1080	70	28	0.011065	0.007348	0.000941	10,000
33435-13	KTT	KTT	KTT	1800	140	11.5	0.007721	0.001625	no wear	10,000
33435-14	KTK	KTTTK	KTTTK	2100	1350	94	0.007877	0.009078	0.002012	10,000

The maximum allowable vent seal leakage is 10 sccs. Balance piston and primary seal leakages are vented to controlled areas.

(C) A total of 10,000 shaft cycles and 500 pressure cycles with the rig at LN_2 temperatures was completed. The rig inlet pressure was maintained at 5900 to 6000 psig GN_2 except during pressure cycling. The leakages from the test are corrected to a nominal 6000 psig inlet pressure and are shown in Figure 290.

(U) Teardown inspection revealed the following:

1. The primary shaft lip seal had fatigue cracks and slight wear on the lip, as shown in Figure 291.
2. The vent shaft lip seal exhibited little wear, as shown in Figure 292.
3. The balance piston lip seal exhibited little wear, as shown in Figure 293.

(2) Build 11

(U) The primary and vent seals tested were TTTKK and the balance piston seal was TTK. The balance piston seal incorporated a thinner seal laminate and an increased seal lip as compared to the configuration tested in Build 10B.

(C) A total of 10,000 shaft cycles and 500 pressure cycles with the rig at LN_2 temperatures was completed. The rig inlet pressure was maintained at 5900 to 6000 psig GN_2 except during pressure cycling. The leakage from the test are corrected to a nominal 6000 psig inlet pressure and are shown in Figure 294.

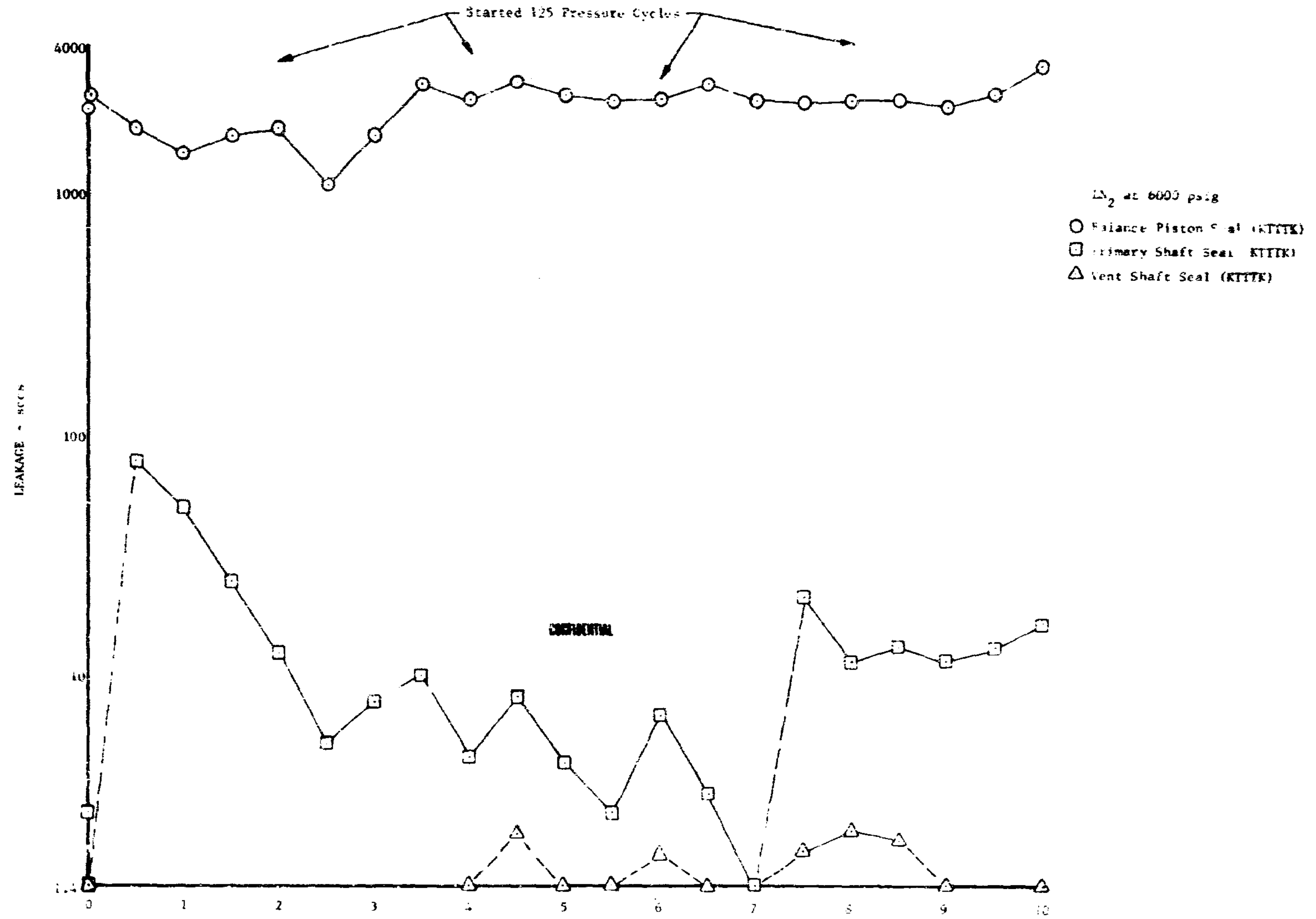

(U) Figure 290. Translating Seal Test Rig Leakage vs Cycles for Build 10B

DFC 62450

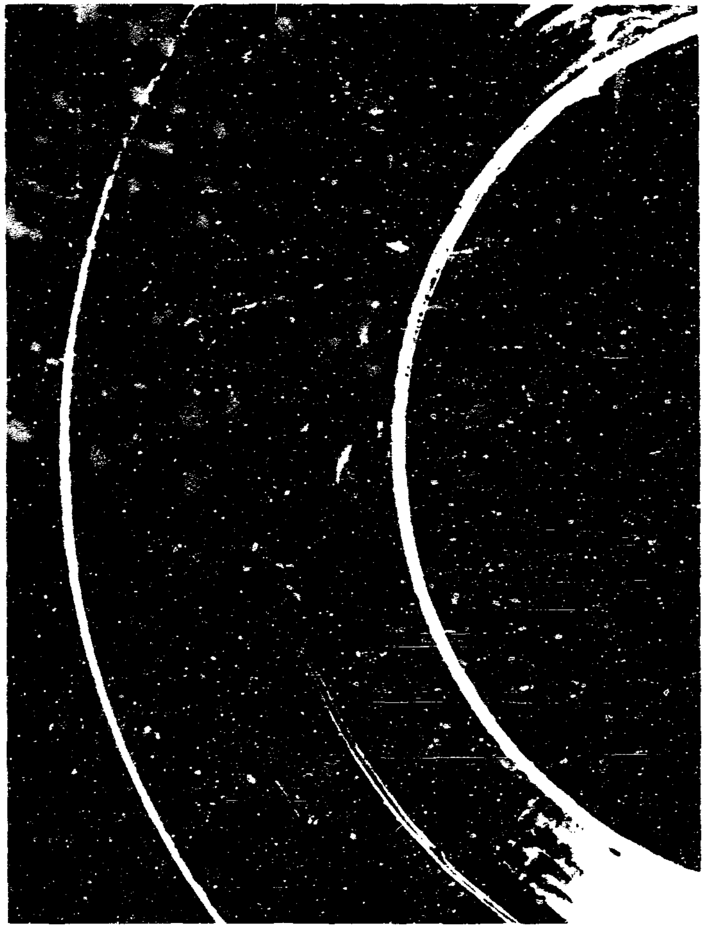

(U) Figure 291. Primary Shaft Lip Seal After Test of Build 10B FE 76263

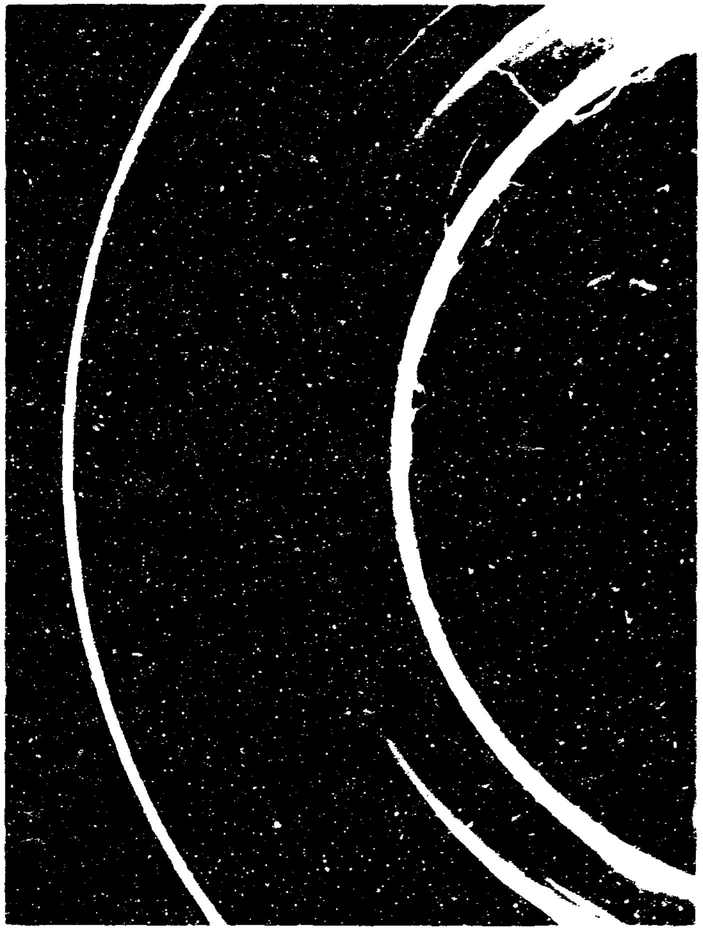

(U) Figure 292. Vent Shaft Lip Seal After Test of Build 10B FE 76264

(U) Figure 293. Balance Piston Lip Seal After Test of Build 10B FE 75832

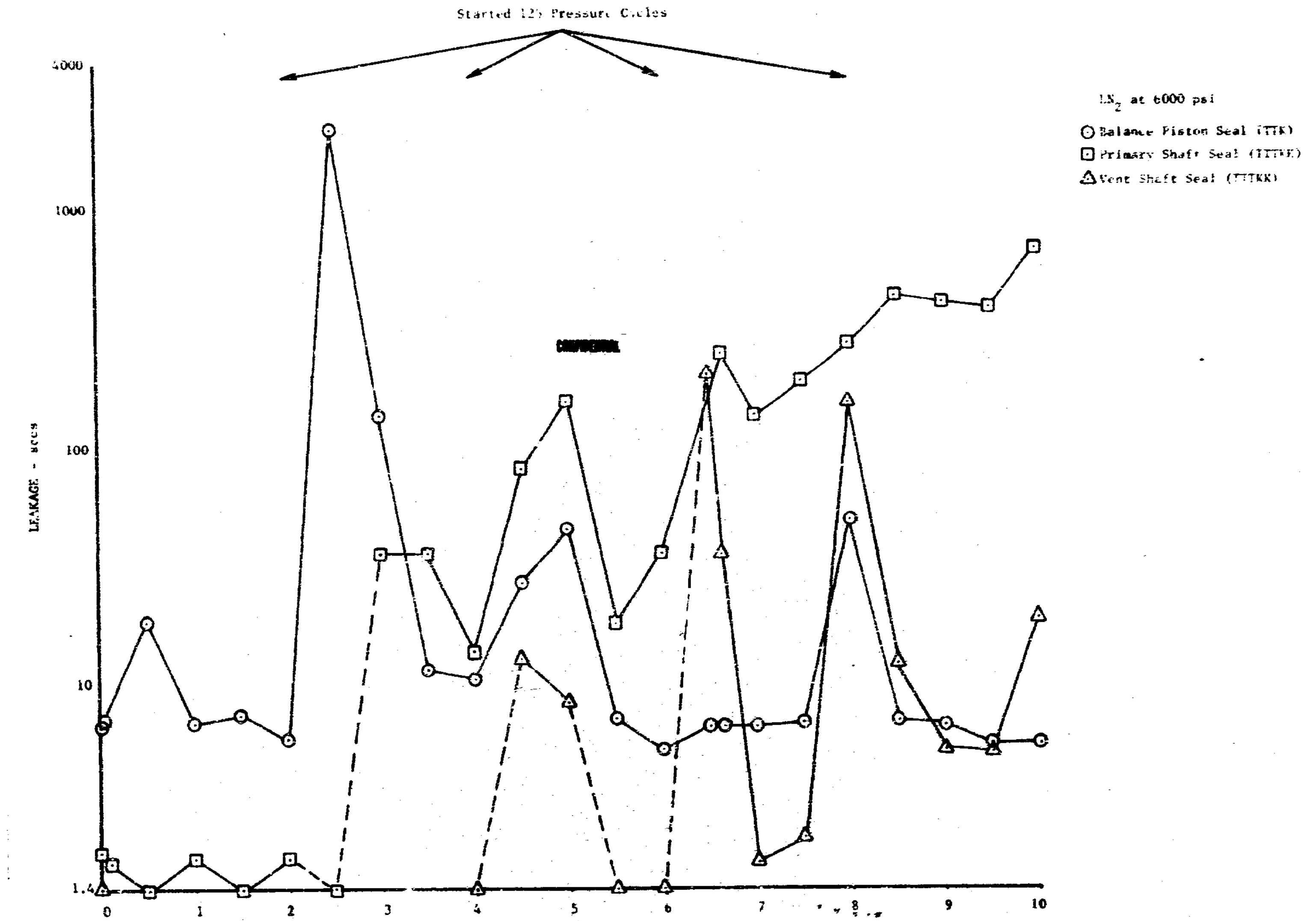

(U) Figure 294. Translating Seal Test Rig Leakage vs Cycles for Build 11

DFC 62451

(U) Teardown inspection revealed the following:

1. The primary shaft lip seal showed moderate wear. (See Figure 295.)
2. The vent shaft lip seal showed slight wear. (See Figure 296.)
3. The balance piston lip seal showed very little wear. (See Figure 297.)

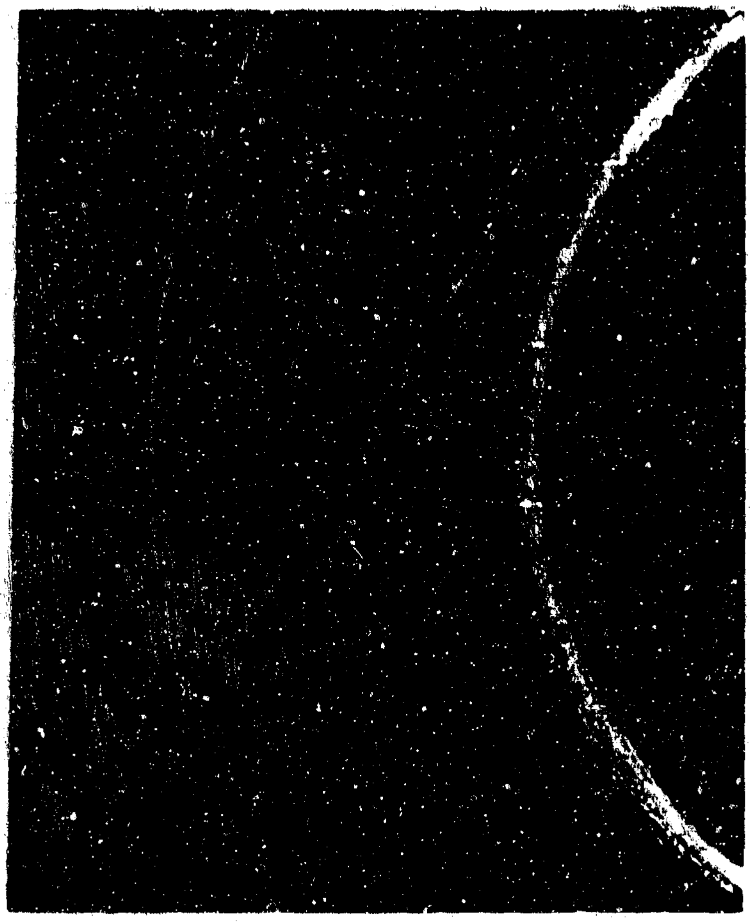

(U) Figure 295. Primary Shaft Lip Seal After Test of Build 11 FE 75904

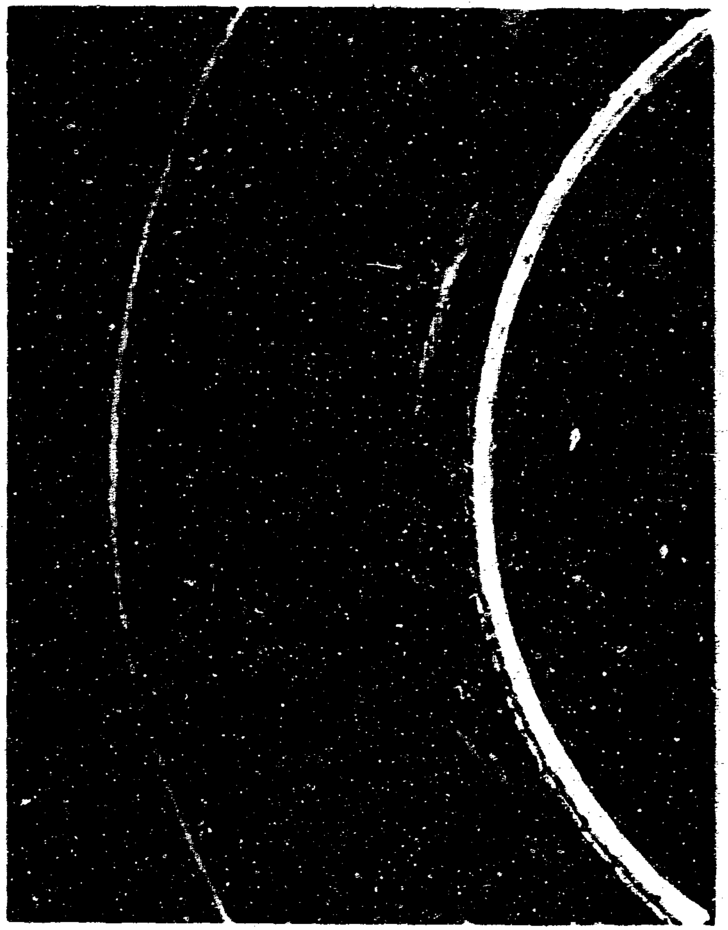

(U) Figure 296. Vent Shaft Lip Seal After Test of Build 11 FE 75905

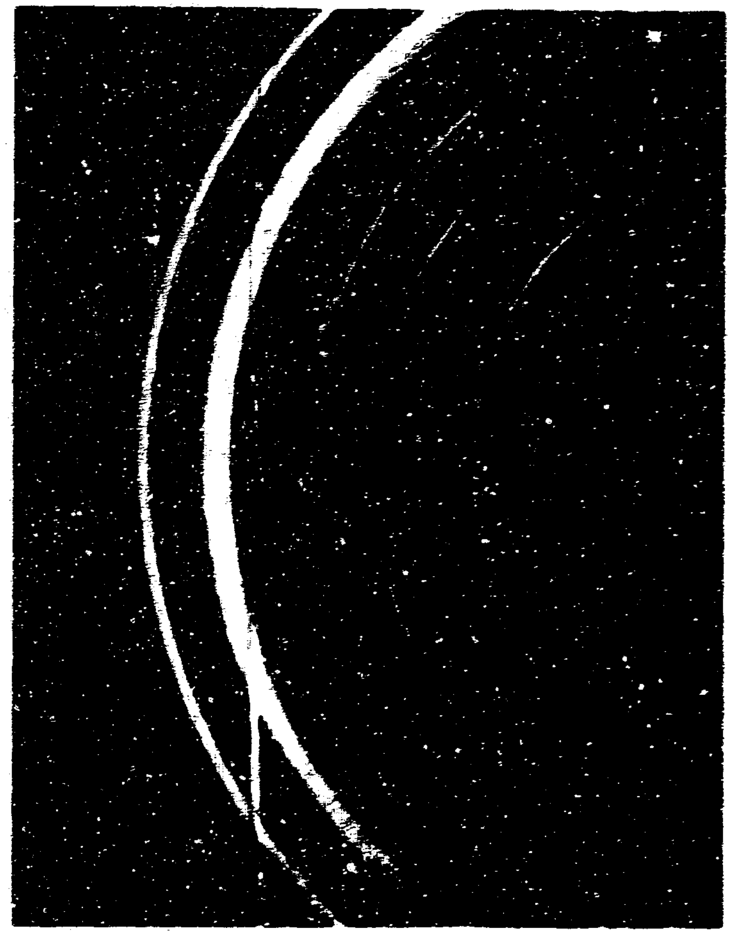

(U) Figure 297. Balance Piston Lip Seal After Test of Build 11 FE 75906

(3) Build 12

(U) The primary and vent seals tested were KKTTK and balance piston seal was KTK.

(C) A total of 10,000 shaft cycles and 500 pressure cycles with the rig at LN_2 temperatures was completed. The rig inlet pressure was maintained at 5900 to 6000 psig GN_2 except during pressure cycling. The leakages from the test are shown in Figure 298. At 7000 cycles the test was stopped and the rig allowed to warm to ambient. When the test was resumed, a step increase in the balance piston leakage was observed, which may have been caused by icing in the rig. At some points the vent leakage was above primary leakage indicating boiloff in the vent lines.

(U) A teardown inspection revealed the following:

1. The primary shaft lip seal showed moderate wear. (See Figure 299.)
2. The vent shaft lip seal showed slight wear. (See Figure 300.)
3. The balance piston lip seal showed moderate wear. (See Figure 301.)

(4) Build 13

(U) All seals tested were KTT laminate.

(C) A total of 10,000 shaft cycles and 500 pressure cycles with the rig at LN_2 temperatures was completed. The rig inlet pressure was maintained at 5900 to 6000 psig GN_2 except during pressure cycling. The leakages from the test are shown in Figure 302. Balance piston seal leakage shows a degradation as a function of cycles indicating the affects of wear. Vent seal leakage exceeded the 10 sccs limit at only one data point during the test.

(U) A teardown inspection revealed the following:

1. The primary shaft lip seal showed moderate wear. (See Figure 303.)
2. The vent shaft lip seal showed slight wear. (See Figure 304.)
3. The balance piston lip seal showed heavy wear. (See Figure 305.)

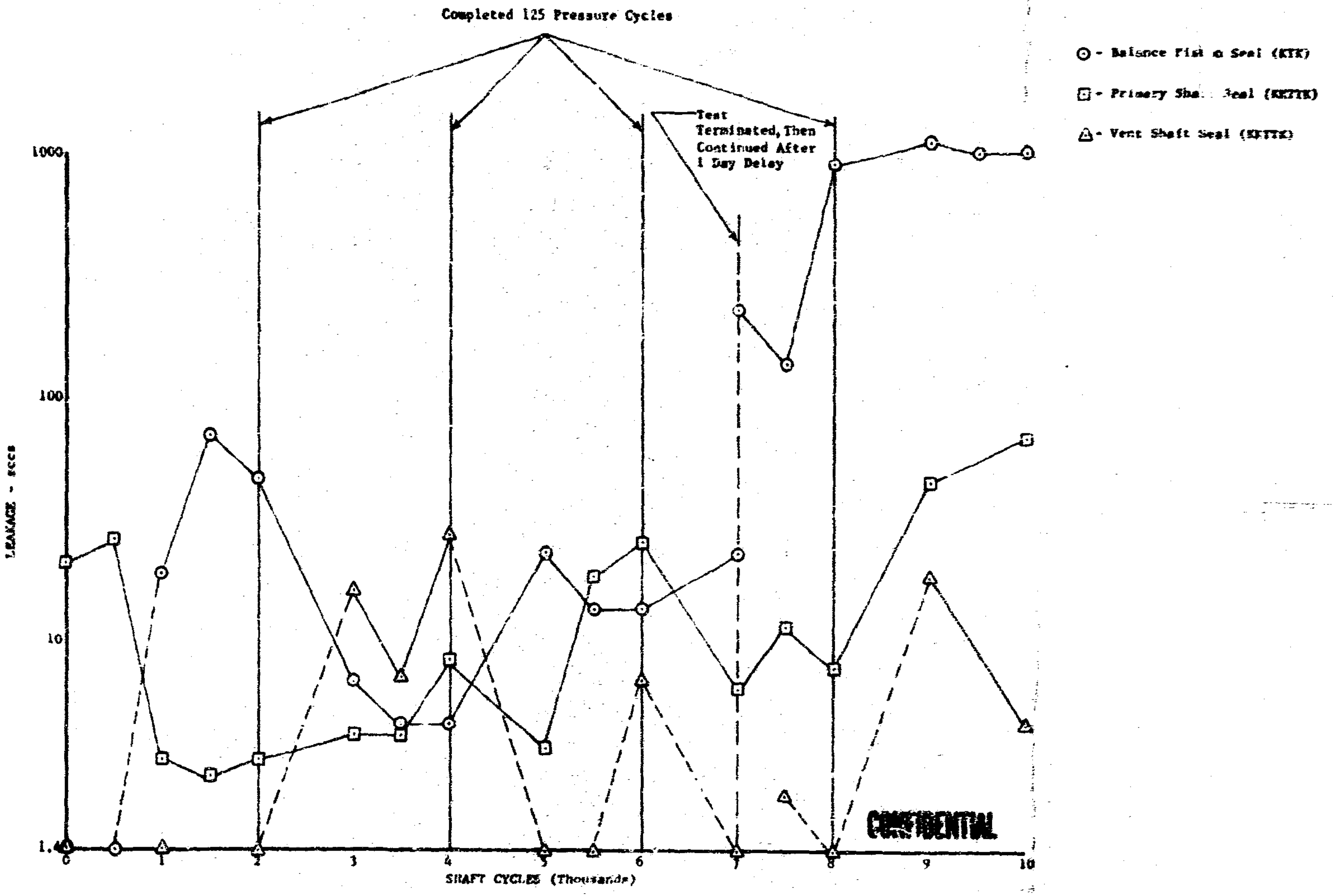

(U) Figure 298. Translating Seal Test Rig Leakage vs Cycles for Build 12

DFC 65295

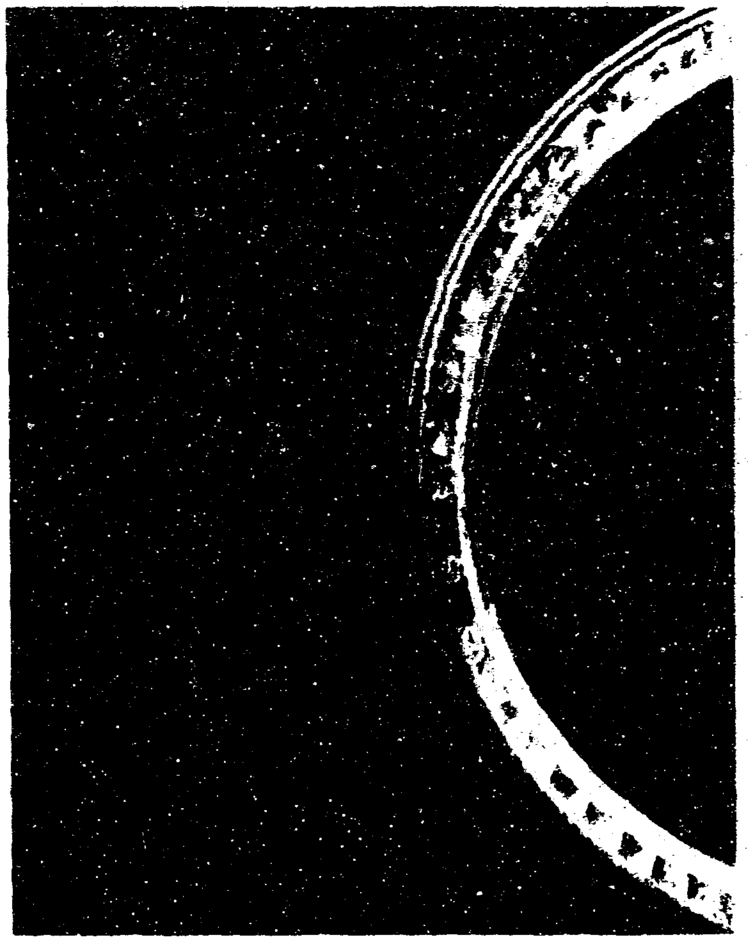

(U) Figure 299. Primary Shaft Lip Seal After Test of Build 12 FE 76475

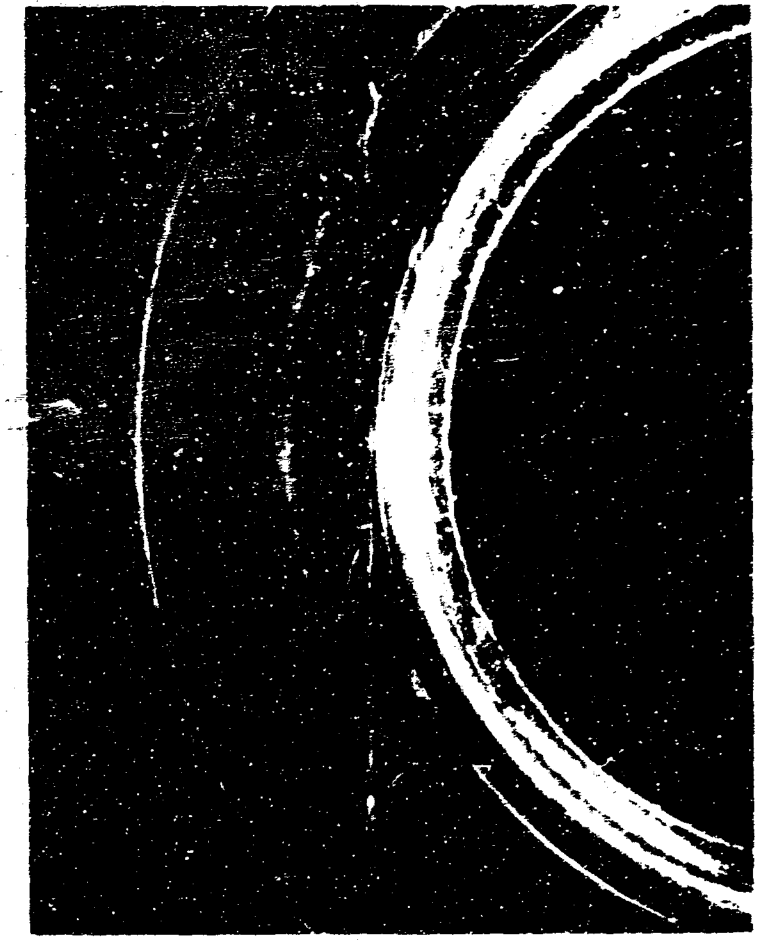

(U) Figure 300. Vent Shaft Lip Seal After Test of Build 12 FE 76476

(U) Figure 301. Balance Piston Lip Seal After Test of Build 12 FE 76477

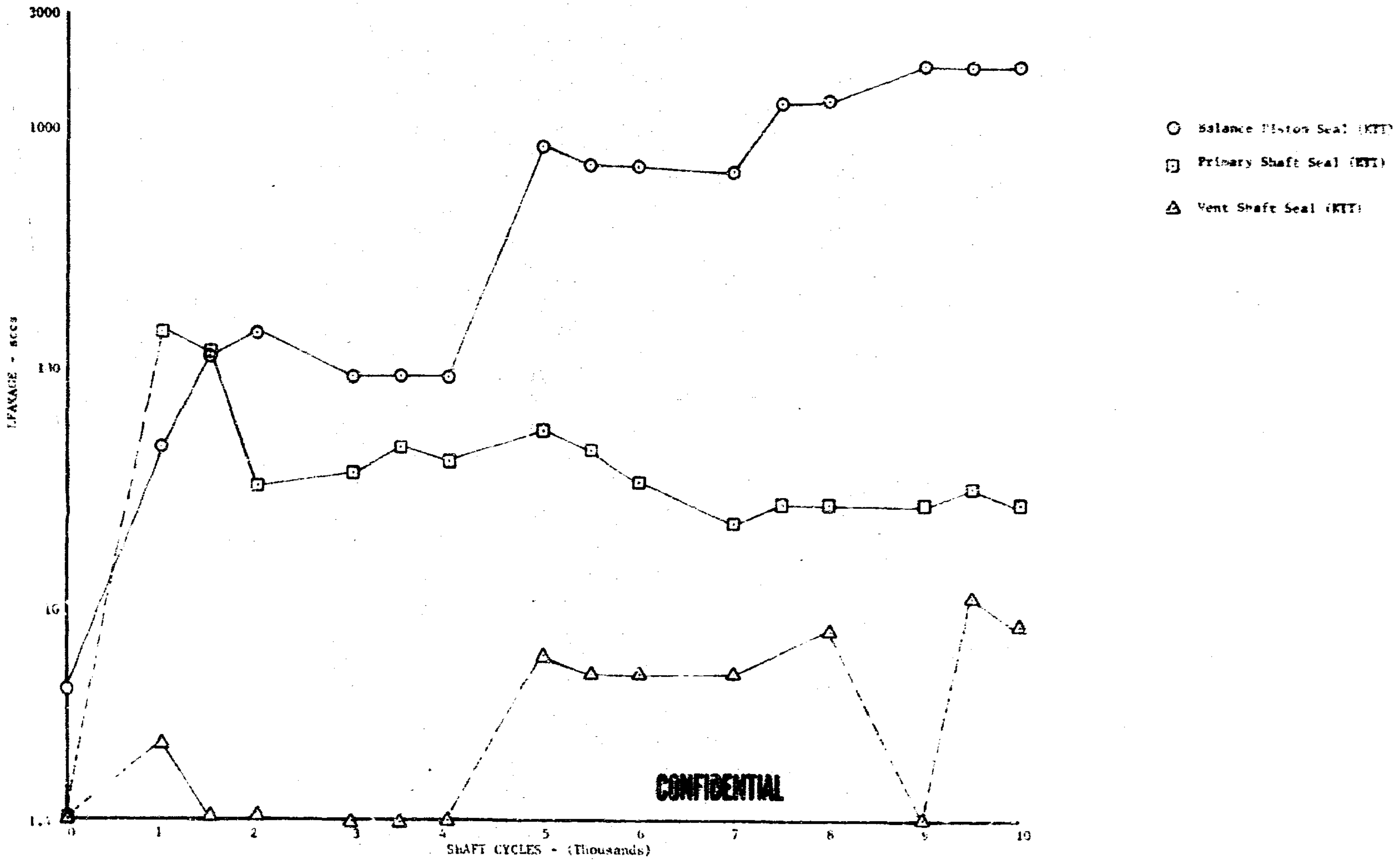

(U) Figure 302. Translating Seal Test Rig Leakage vs Cycles for Build 13

DFC 65296

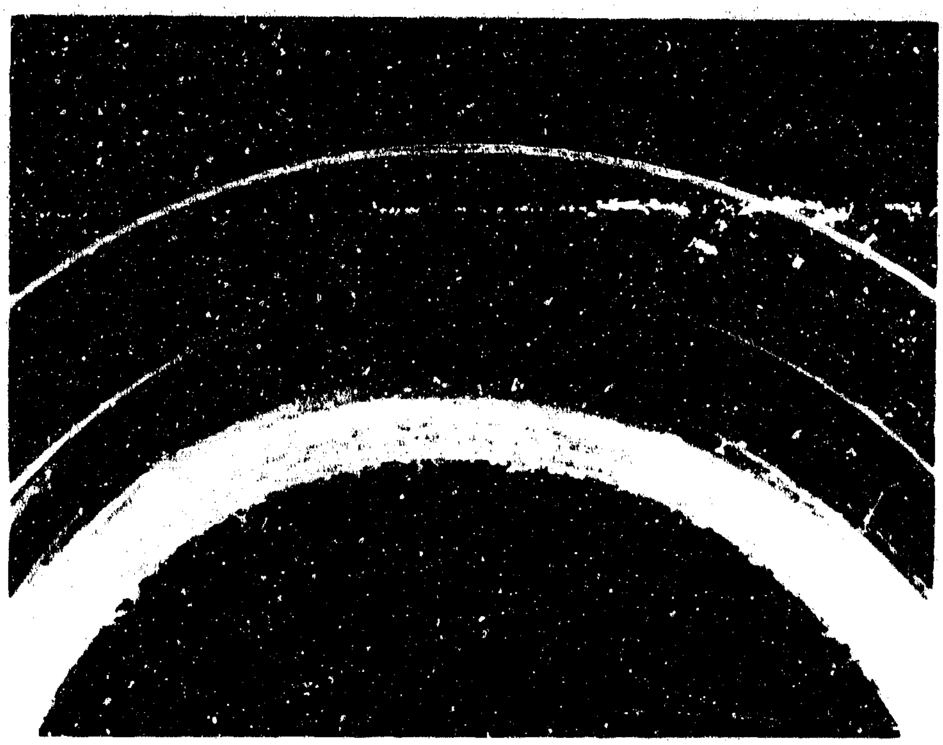

(U) Figure 303. Primary Shaft Lip Seal After Test of Build 13 FE 77097

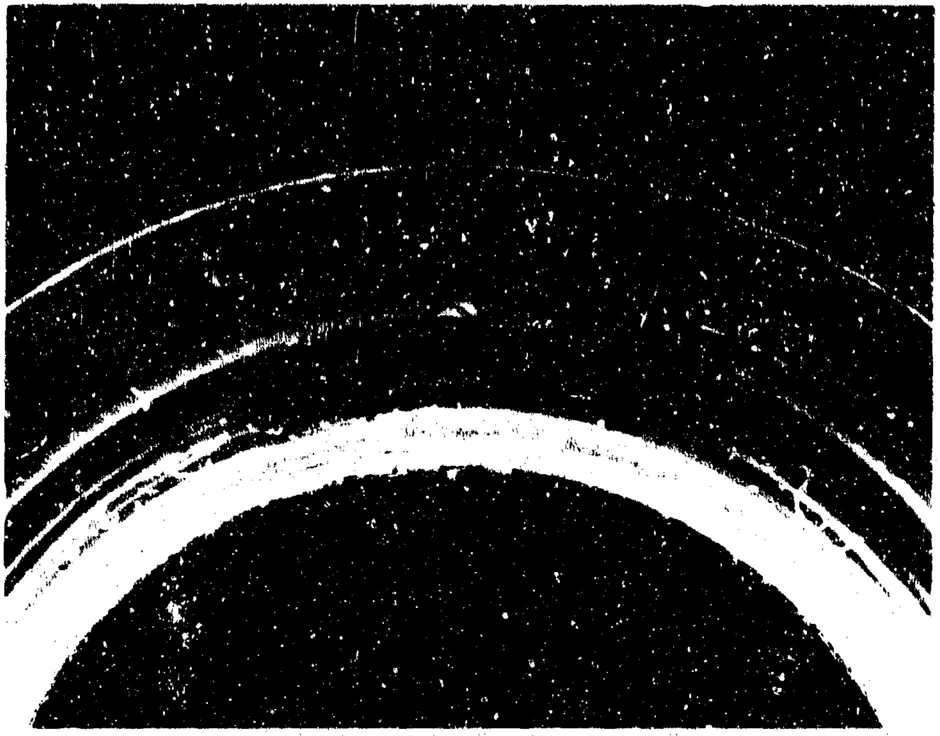

(U) Figure 304. Vent Shaft Lip Seal After Test of Build 13 FE 77096

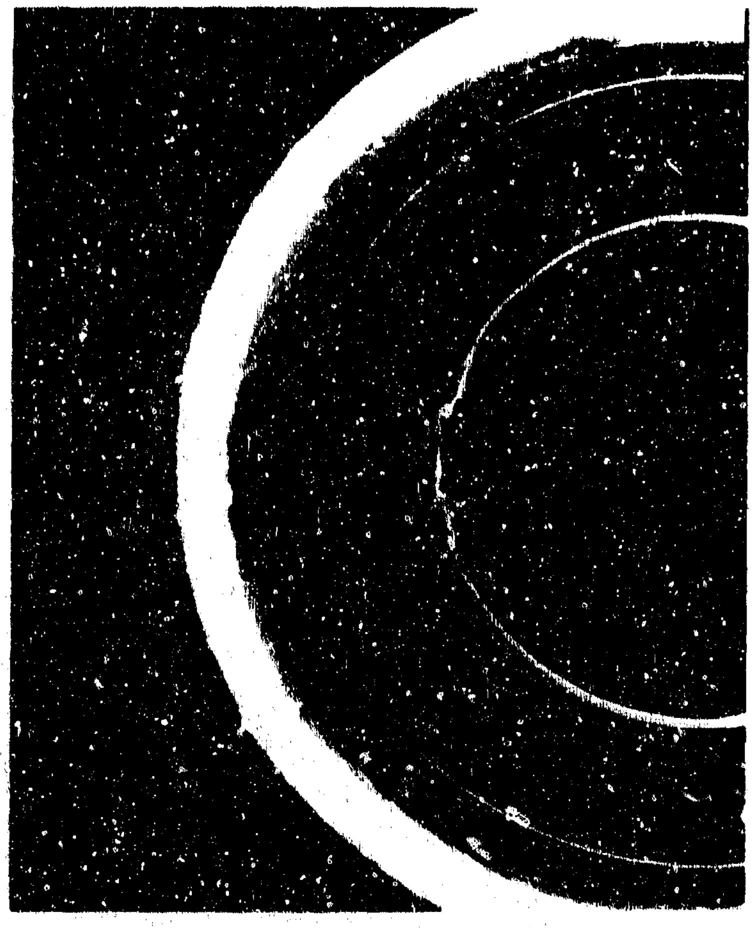

(U) Figure 305. Balance Piston Lip Seal After Test of Build 13 FE 77098

(5) Build 14

(U) The primary and vent shaft seals tested were KTTTK and the balance piston was KTK. This test was conducted with the stand configuration as shown in Figure 306. The test procedure prevents a buildup of liquid in the seal vent lines by maintaining a vacuum on the lines at all times.

f. Test Summary

(C) A total of 10,000 shaft cycles and 375 pressure cycles with the rig at LN_2 temperatures was completed. The rig inlet pressure was maintained at 5900 to 6000 psig GN_2 except during pressure cycling. The pressure cycles at the 8000 cycle point were omitted because primary lip seal leakage was excessive (above 5000 sccs) during pressured cycles. Seal wear produced some shredded material that lodged between the sealing surface and shaft during pressure cycling. The leakages are shown in Figure 307.

(U) A teardown inspection revealed the following:

1. The primary shaft lip seal showed heavy wear. (See Figure 308.)
2. The vent shaft lip seal showed slight wear. (See Figure 309.)
3. The balance piston lip seal showed heavy wear. (See Figure 310.)

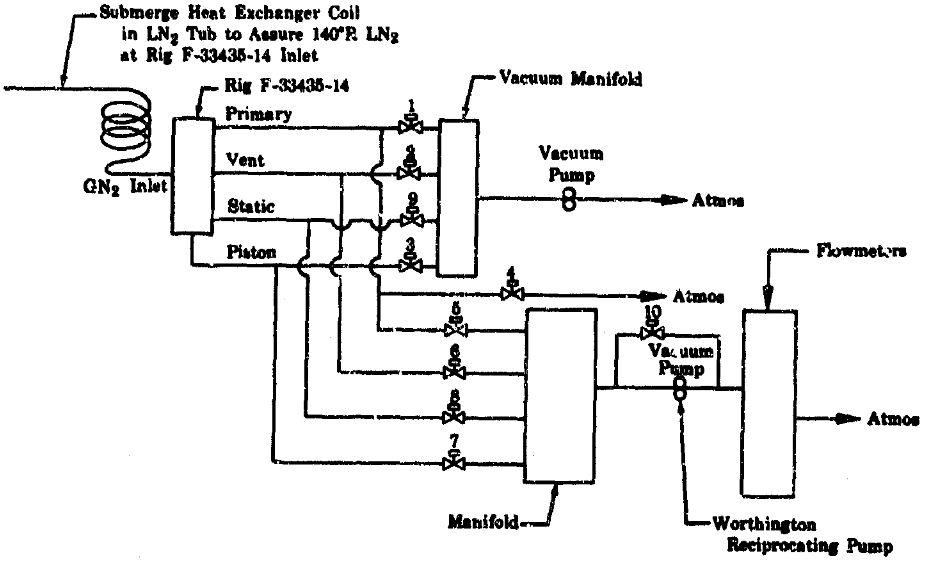

(U) Figure 306. Plumbing Schematic for Testing Build 14 FD 24986A

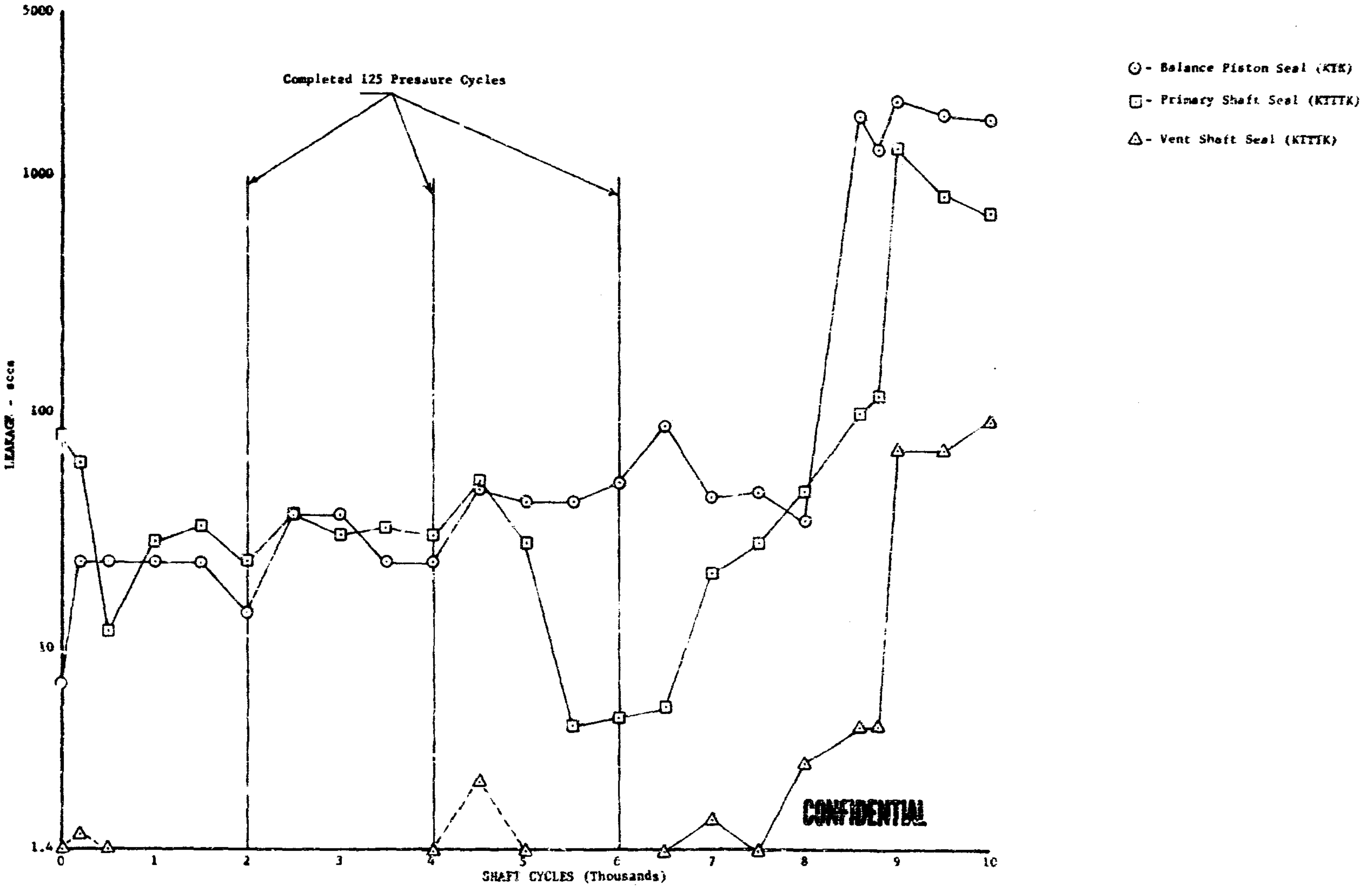

(U) Figure 307. Translating Seal Test Rig Leakage vs Cycles for Build 14

DFC 65297

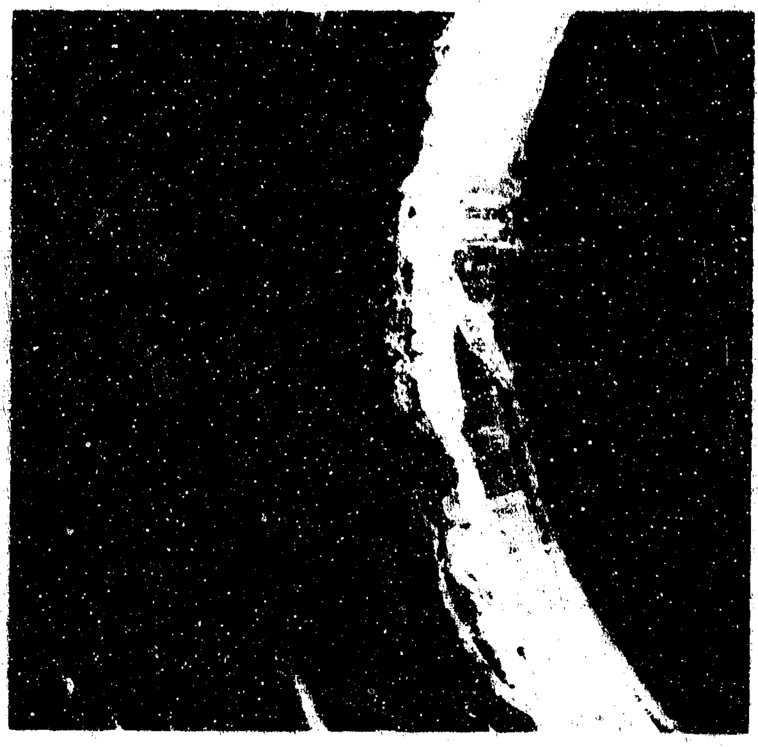

(U) Figure 308. Primary Shaft Lip Seal After Test of Build 14 FE 78381

(U) Figure 309. Vent Shaft Lip Seal After Test of Build 14 FE 78204

(U) Figure 310. Balance Piston Lip Seal After Test of Build 14 FE 78205

4. Static Seals

a. Introduction

(U) During seal rig, component, and staged combustion rig testing conducted during Phase I (Contract AF04(611)-11401), excessive overboard static seal leakage was experienced. The measured overboard primary seal leakage at maximum thrust during the staged combustion rig test firings was equivalent to an impulse loss of approximately 2 seconds, and some additional uncontrolled overboard leakage was visible. Static pressure tests on the main chamber oxidizer valve indicated that the leakage problem was aggravated by excessive flange separation and inadequate static seals.

(C) During this report period, under the current demonstrator engine design program, hydrostatic test rigs with high-pressure joints were designed and tested. These rigs did not incorporate double seals with interseal vents because of the attendant weight penalty. The design goal for the rigs was for zero axial deflection at the seal diameter with 7500 psig internal pressures at liquid nitrogen temperature. Neither of the hydrostatic test rigs met the deflection criteria, but agreement with finite element computer program predictions was satisfactory. The computer program model was improved to provide a good stress and deflection analysis capability for the seal rigs to be designed under the component development phase of this program.

b. Summary, Conclusions, and Recommendations

(U) Supporting data for satisfactory seal rig design was accomplished during this phase. The finite element computer program, as adapted to coupling analysis, will be satisfactory for optimizing coupling flanges.

(U) It is recommended that static seal test rigs be designed for the minimum deflection consistent with the demonstrator engine weight goals. The finite element computer program should be used to analyze all demonstrator engine flanges to limit deflection to the values selected for the static seal test rigs. Both axial and radial type static seals should be procured and tested in the rigs designed under the component development phase of this program.

c. Design Analysis

(U) During this report period, the primary effort was expended on obtaining information for a high pressure static seal rig design. Several initial configurations were sketched for specialized flange and seal combinations before calculation difficulties indicated that design effort should be concentrated on basic coupling configurations with analysis directed toward minimum weight and deflection with demonstrator engine materials.

(U) A 6-inch diameter aluminum (AMS 4127) pipe coupling was chosen for analysis because of its relatively poor deflection characteristics when compared to those of the same diameter steel or smaller diameter aluminum or steel couplings. A high-pressure coupling design analysis of five basic coupling types was completed. The configurations that were considered are shown as sketches A through E, in Figure 311. Basic ground rules for the analyses were as follows:

1. Standard design criteria for the engine with regard to allowable stresses, weight, etc., were to be followed.
2. Pipe and coupling designs were based on stress limits for axial (blowoff) and hoop loads only. No vibration or mechanical bending load factors were added.
3. All couplings were assumed to have a perfect seal (not deflection limited) at the coupling inside diameter.

(C) The results of the coupling spring rate deflection calculations, as shown in Figure 312, indicated that increasing the number of bolts had a minor effect on bolted coupling overall spring rate, whereas weight increase was significant. Calculations to determine the initial clamping load required for each of the couplings to provide and maintain a minimum of 460 lb/in. seal load at 7500 psi resulted in the clamping load to blowoff load ratio (F_C/F_A) values shown in Figure 311 (sketches A through E). Aside from the impracticality of attempting to obtain such high clamping loads, the numbers indicated that some method of improving the clamping load transfer to the seal area was required.

(U) Sketches F through I in Figure 311 show some methods of providing this seal force, while sketch J shows a pressure-assisted coupling intended to maintain seal load when flange deflection is present. Another method, not shown, of providing more effective seal loading would be to move the seal closer to the clamping load circle. In this case, part of the improved load transfer advantage would be lost because of the increased blowoff load. No detailed analyses of these or other variations from standard flat flange couplings have been completed, so no clear choice of coupling type for high pressure test was possible. The apparently obvious advantages and disadvantages of each coupling type for engine application were considered, and the small bolt flanged coupling was selected for detailed analysis and initial seal rig design. Analysis required for optimizing the flange configuration or seal location to provide satisfactory seal load characteristics over the full pressure range was undertaken as primary effort.

(U) A study computer program was developed to analyze proposed coupling rig designs for stress and deflection characteristics. Initial rig designs were found to be unsuitable for the intended application. A 6-inch aluminum hydrostatic coupling stress and deflection test rig was then designed to evaluate the computer program predictions. Concurrently, a finite element computer program developed for disk analysis was modified for coupling analysis.

(U) A reanalysis of the hydrostatic aluminum coupling layout using this deck on the IBM 360 computer resulted in lower predicted maximum flange stresses and higher deflections than the previous program.

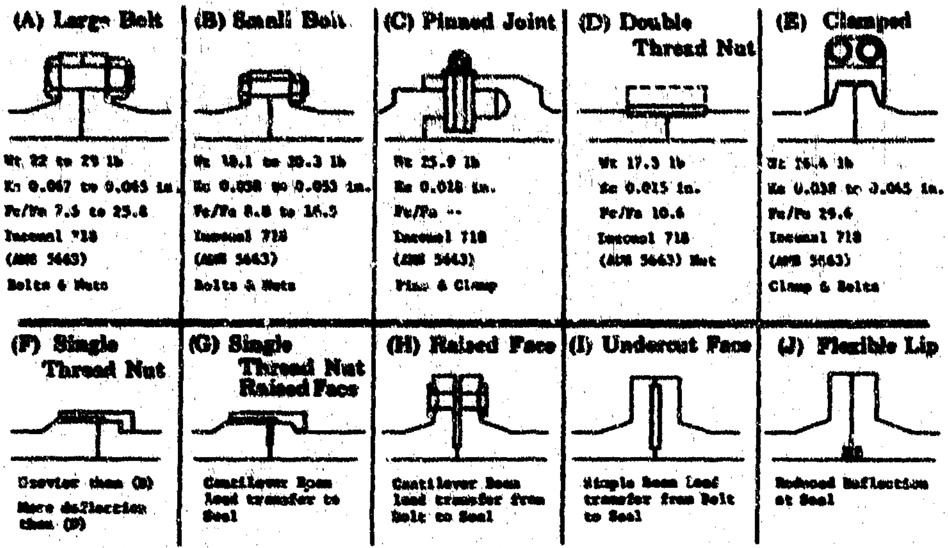

All calculations for 6-in. ID, 6 inch long span and aluminum (AMS 4130) pipe coupling.

(U) Figure 311. Coupling Configurations FD 25605A

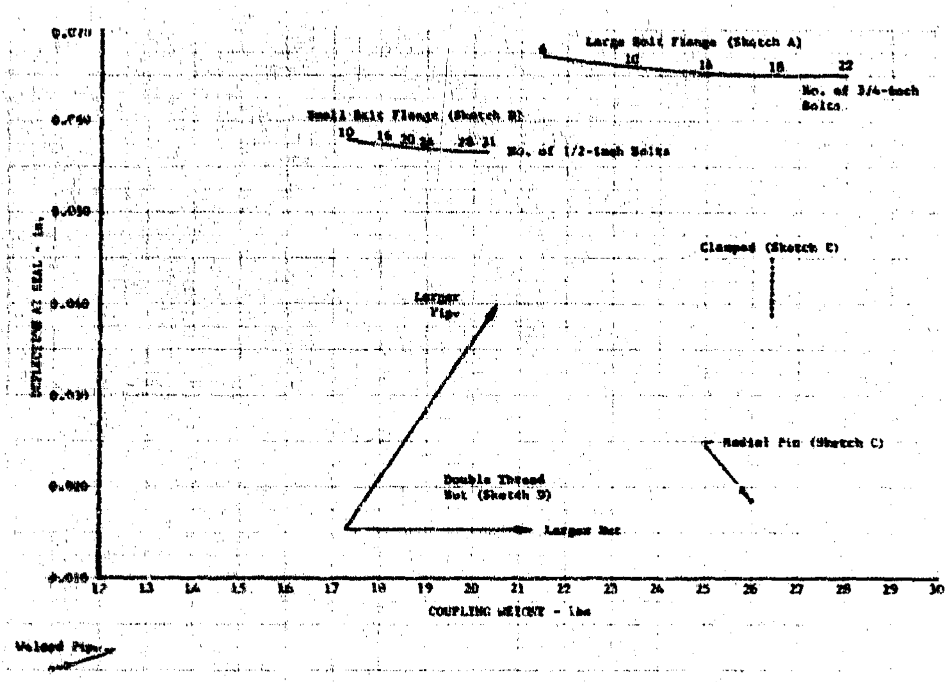

(U) Figure 312. Predicted Coupling Deflection at Seal vs Weight DF 68872

(U) Cantilever and simple beam flange seal loading schemes were then analyzed using the computer programs. This analysis indicated that the cantilever design would be lighter than the simple beam designs for the same deflection limit. A cantilever flange rework of the initial flat faced flange test rig was designed and added to the test rig layout.

(U) As testing of the hydrostatic rig progressed, the computer programs were revised to improve agreement with the test results.

(U) An additional flange design analysis based on shear center theory was completed. The application of this theory is that the load must pass through the shear center, or center of flexure to prevent twisting. Preliminary calculations indicated that the shear center design would improve flange stiffness but would probably be more bulky than a conventional flange design. Further analysis of the shear center flange design calculations indicated that effective coupling weight reduction by removing flange material that is not highly stressed may be possible without significantly affecting flange stiffness.

d. Testing

(1) Flange Tests

(U) Hydrostatic flange test rig housings and bolts were procured and delivered to the Materials Development Laboratory for assembly and testing. Rig 35120, Build 2 (Build 1 was used to test main chamber oxidizer valve inlet and outlet flange seals) was assembled as shown in Figure 313. Stresscoat was used to determine strain gage locations. Sixteen bi-axial strain gage rosettes were installed on the interior and exterior of the test rig according to the stresscoat patterns (Figure 314). Preliminary Materials Development Laboratory tests indicated that X-ray inspection would be feasible to determine flange separation during the hydrostatic tests. A review of the X-ray techniques revealed that separation at various radii could be measured if actual separation was known at one or more points. Consequently, magnetic proximity probes (Figure 315) were used to determine housing deflections at two points. The hydrostatic test rig was then assembled for testing. Six of the coupling bolts were strain gaged and calibrated for strain at the required load. All other bolts were then torqued sufficiently to obtain the average stretch obtained for the instrumented bolts. Assembly torque variation was too great to be useful for specific load application. During the test, readouts from all internal strain gages were lost due to potting material creep. The external strain gages and the proximity probes operated satisfactorily.

(C) Maximum axial tensile stress of 58,200 psi (0.9% strain) occurred in the flange radius at strain gage rosette location 11 (Figure 314) under 5300 psig internal pressure. Maximum axial tensile stress of 31,700 psi (elastic) occurred in the straight wall section at strain gage rosette location 6 under 5300 psig internal pressure. Hoop stress at this point was 25,000 psi tension. The flanges began to separate at 2500 psig internal pressure where internal pressure blow-off load was approximately 25% of the assembly bolt load. Maximum flange separations at the inside diameter wall and seal groove were 0.025 inch and 0.018 inch, respectively, under 5300 psig internal pressure.

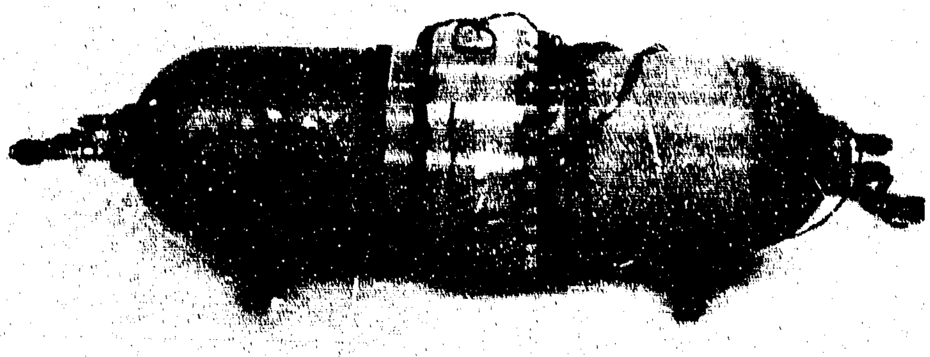

(U) Figure 313. Flange Test Rig FE 78045

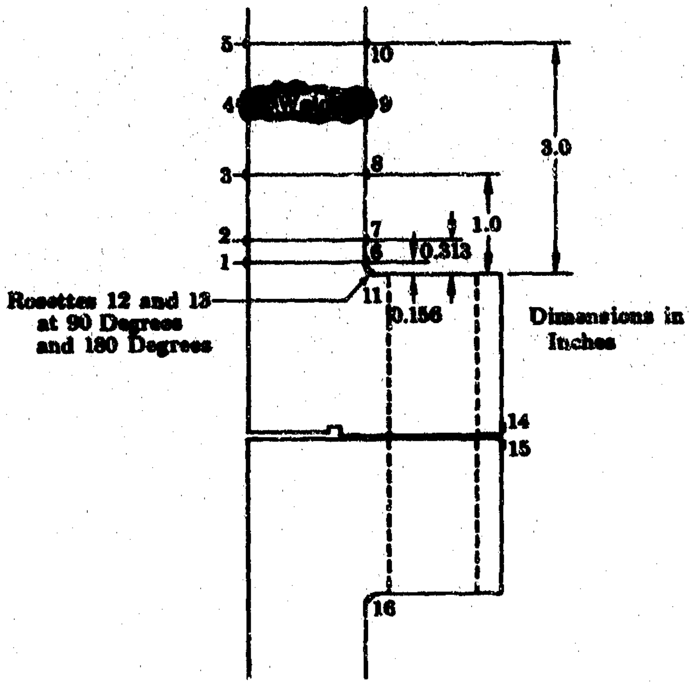

(U) Figure 314. Locations of Strain Gage Rosettes FD 25606

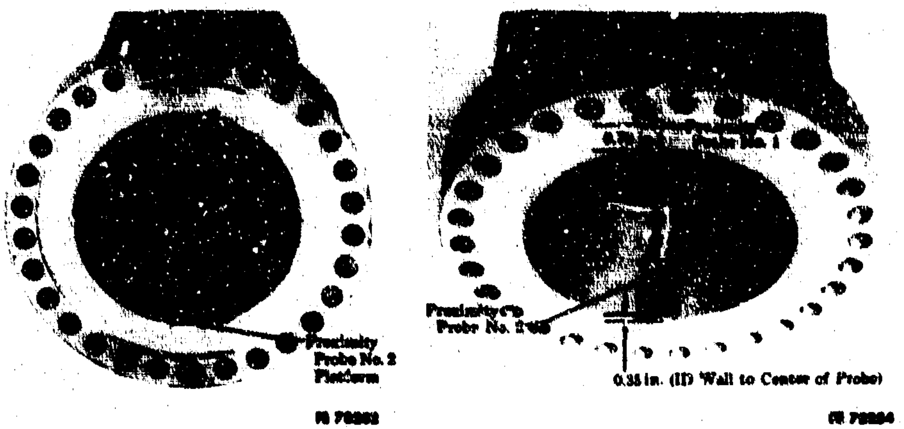

(U) Figure 315. Magnetic Proximity Probe Locations Rig 35120-2 FD 25607

(U) The hydrostatic test rig data indicated reasonably good agreement with the finite element computer program predictions for both stress and deflection as shown in Figure 316. The program was revised to improve matching by expansion to include both coupling members, multipoint bolt loading, and consideration of the effects of the bolt holes. The revised model was used to predict stress and deflection of a cantilevered flange coupling.

(C) The hydrostatic test rig flanges were reworked to the cantilevered design configuration for Rig 35120-3. Sixteen strain gages and six proximity probes were installed, as shown in Figure 317, and the rig was assembled for test. Hydrostatic pressure testing was conducted at ambient temperature up to 5300 psig. Bolt loads were nearly constant and deflection at the inside diameter was essentially as predicted by the finite element program (Figure 318).

(C) Maximum indicated axial tensile stress (above yield) occurred in the flange radius at strain gage rosette location 5 (Figure 317). The flanges did not separate under 5300 psig internal pressure but pivoted at the raised face outer diameter so that deflection at the seal diameter reached a value of approximately 0.004 inch. Maximum flange separation at the inside diameter wall was 0.008 inch at this pressure.

(C) Review of the stress, load, and deflection curves for the cantilevered flange hydrostatic pressure test rig revealed that maximum surface stresses (below yield) near the flange were still somewhat below the finite element program predictions but agreement was improved as shown in Figure 319. Both bolt loads and proximity probes indicated flange separation was imminent at the maximum pressure applied but bolt load was nearly constant up to that point. Bolt loads were then reduced to approximately 4000 pounds and the rig was pressurized to 3800 psig. Bolt loads remained essentially constant up to 3000 psig and calculated joint efficiency (blowoff load/bolt load) was essentially the same as in the previous test.

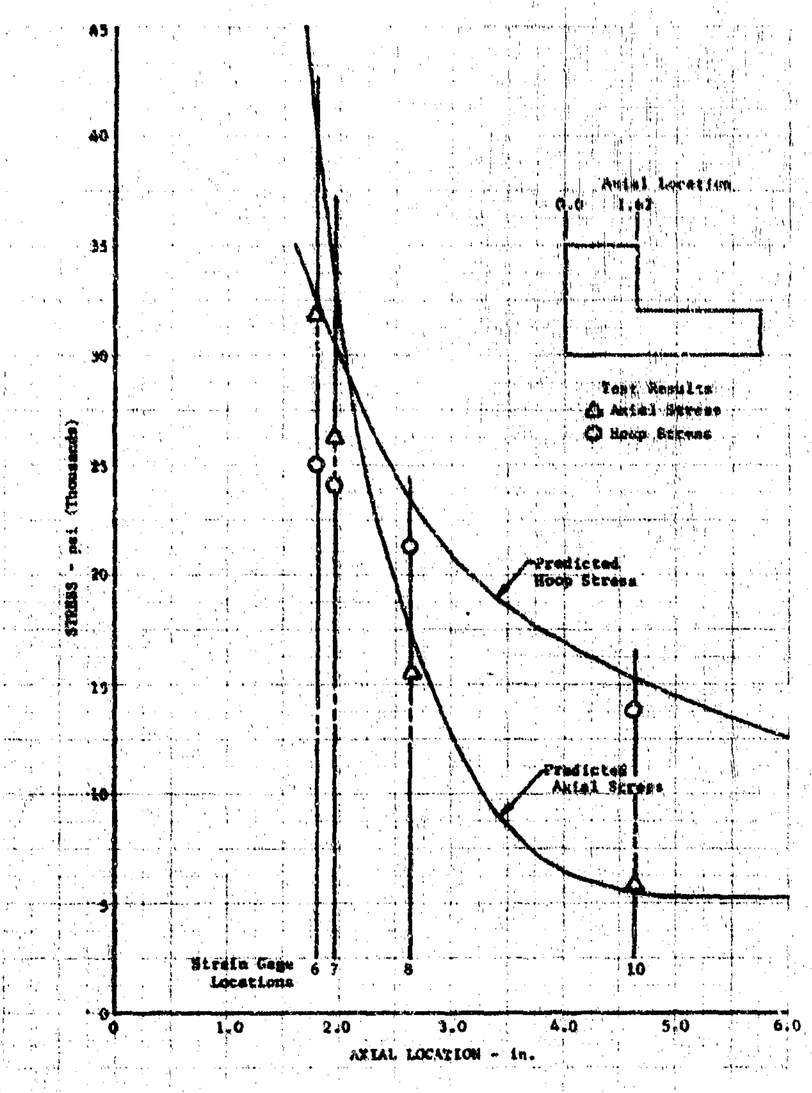

(U) Figure 316. Finite Element Computer Program Predictions DF 68871

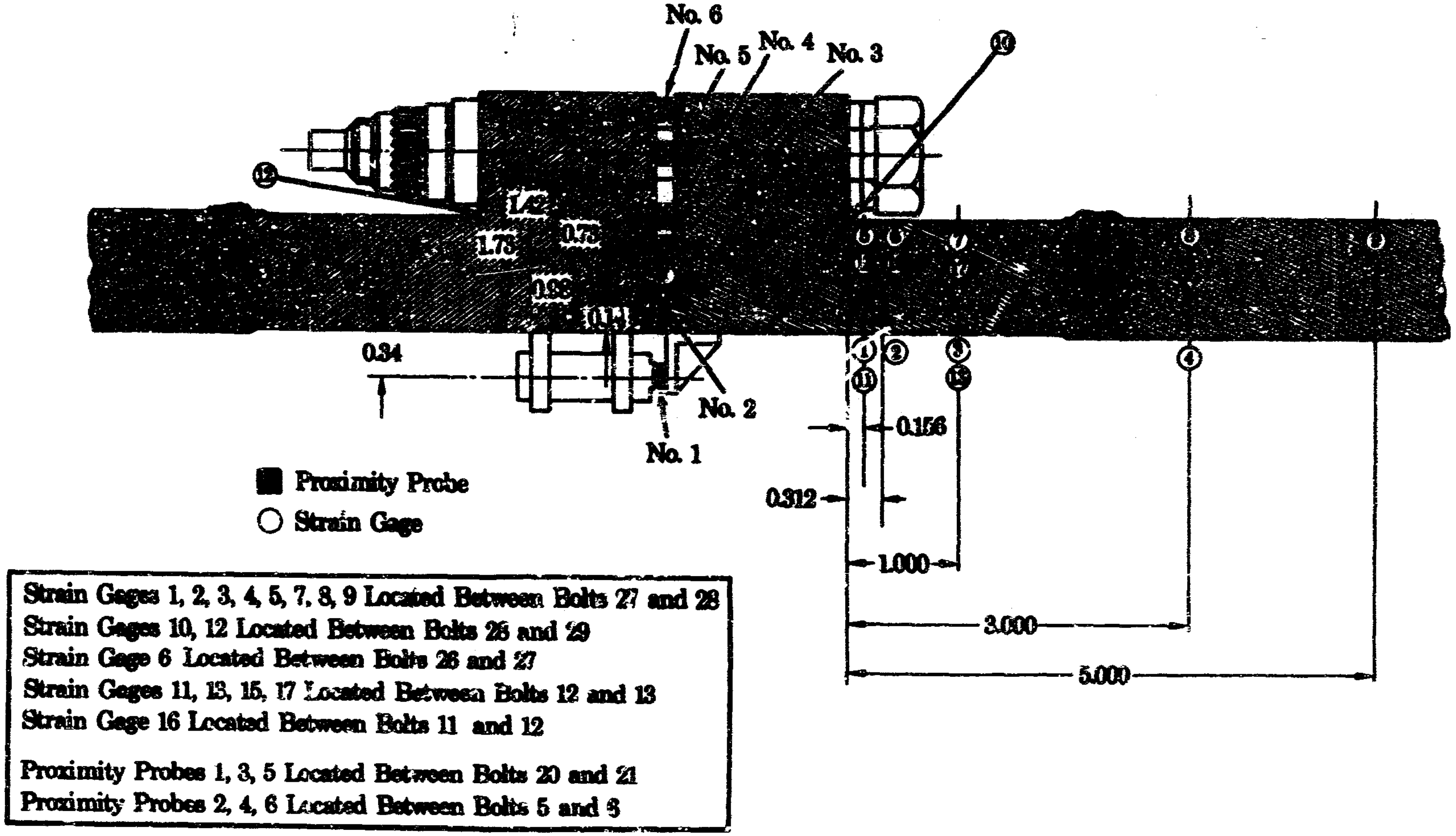

Strain Gages 1, 2, 3, 4, 5, 7, 8, 9 Located Between Bolts 27 and 28
Strain Gages 10, 12 Located Between Bolts 28 and 29
Strain Gage 6 Located Between Bolts 26 and 27
Strain Gages 11, 13, 15, 17 Located Between Bolts 12 and 13
Strain Gage 16 Located Between Bolts 11 and 12

Proximity Probes 1, 3, 5 Located Between Bolts 20 and 21
Proximity Probes 2, 4, 6 Located Between Bolts 5 and 6

(U) Figure 317. Instrumentation Locations Rig 35120-3

FD 25608

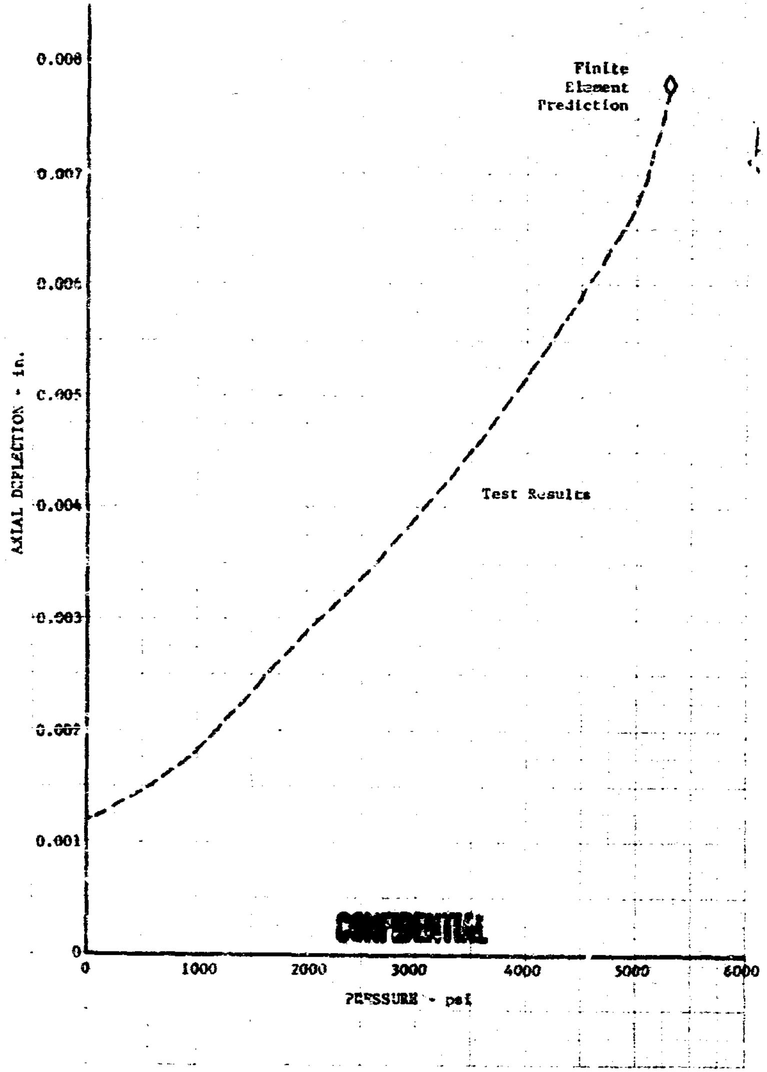

(U) Figure 318. Axial Deflection at ID of Flange Rig 35120-3 DFC 68870

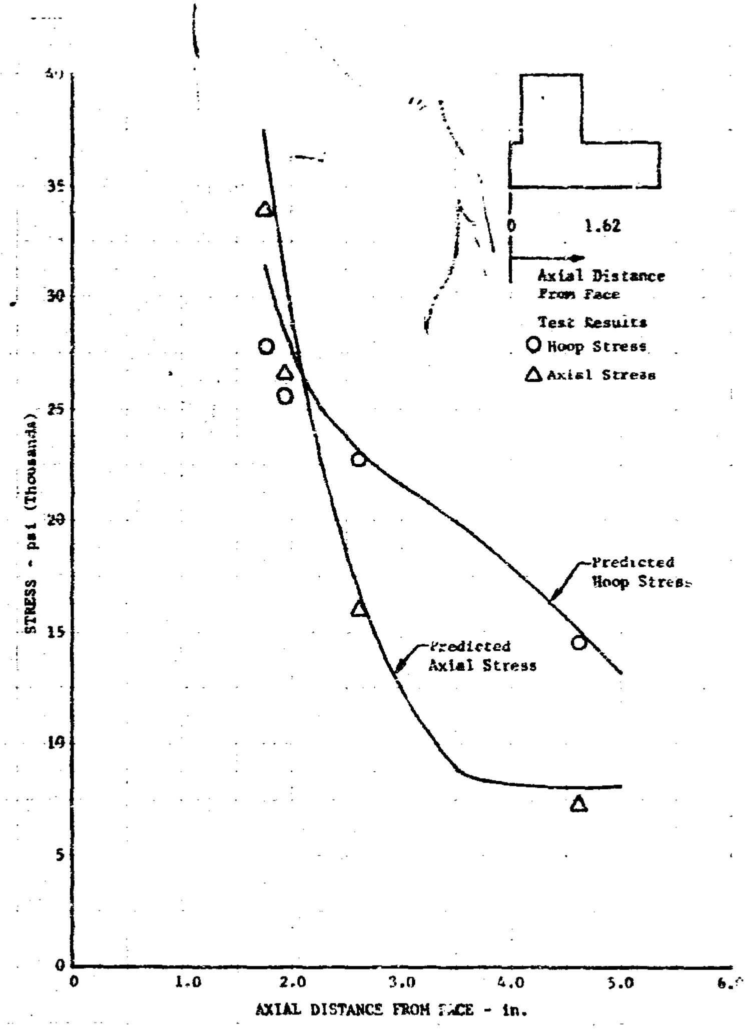

(U) Figure 319. Comparison of Predicted and Measured Stresses on OD Wall Rig 35120-3 DF 68869